Astronomy & Astrophysics manuscript no. Planck˙inflation˙driver2014
February 10, 2015
© ESO 2015

arXiv:1502.02114v1 [astro-ph.CO] 7 Feb 2015

Planck 2015 results. XX. Constraints on inflation

Planck Collaboration: P. A. R. Ade[94], N. Aghanim[66], M. Arnaud[80], F. Arroja[73,86], M. Ashdown[76,6], J. Aumont[66], C. Baccigalupi[93], M. Ballardini[54,56,35], A. J. Banday[106,10], R. B. Barreiro[72], N. Bartolo[34,73], E. Battaner[108,109], K. Benabed[67,105], A. Benoît[64], A. Benoit-Lévy[26,67,105], J.-P. Bernard[106,10], M. Bersanelli[38,55], P. Bielewicz[106,10,93], A. Bonaldi[75], L. Bonavera[72], J. R. Bond[9], J. Borrill[15,99], F. R. Bouchet[67,97], F. Boulanger[66], M. Bucher[1*], C. Burigana[54,36,56], R. C. Butler[54], E. Calabrese[102], J.-F. Cardoso[81,1,67], A. Catalano[82,79], A. Challinor[69,76,13], A. Chamballu[80,17,66], R.-R. Chary[63], H. C. Chiang[30,7], P. R. Christensen[90,42], S. Church[101], D. L. Clements[62], S. Colombi[67,105], L. P. L. Colombo[25,74], C. Combet[82], D. Contreras[24], F. Couchot[77], A. Coulais[79], B. P. Crill[74,12], A. Curto[6,72], F. Cuttaia[54], L. Danese[93], R. D. Davies[75], R. J. Davis[75], P. de Bernardis[37], A. de Rosa[54], G. de Zotti[51,93], J. Delabrouille[1], F.-X. Désert[60], J. M. Diego[72], H. Dole[66,65], S. Donzelli[55], O. Doré[74,12], M. Douspis[66], A. Ducout[67,62], X. Dupac[45], G. Efstathiou[69], F. Elsner[26,67,105], T. A. Enßlin[87], H. K. Eriksen[70], J. Fergusson[13], F. Finelli[54,56⋆], O. Forni[106,10], M. Frailis[53], A. A. Fraisse[30], E. Franceschi[54], A. Frejsel[90], A. Frolov[96], S. Galeotta[53], S. Galli[67], K. Ganga[1], C. Gauthier[1,86], M. Giard[106,10], Y. Giraud-Héraud[1], E. Gjerløw[70], J. González-Nuevo[72,93], K. M. Górski[74,110], S. Gratton[76,69], A. Gregorio[39,53,59], A. Gruppuso[54], J. E. Gudmundsson[30], J. Hamann[104,103], W. Handley[76,6], F. K. Hansen[70], D. Hanson[88,74,9], D. L. Harrison[69,76], S. Henrot-Versillé[77], C. Hernández-Monteagudo[14,87], D. Herranz[72], S. R. Hildebrandt[74,12], E. Hivon[67,105], M. Hobson[6], W. A. Holmes[74], A. Hornstrup[18], W. Hovest[87], Z. Huang[9], K. M. Huffenberger[28], G. Hurier[66], A. H. Jaffe[62], T. R. Jaffe[106,10], W. C. Jones[30], M. Juvela[29], E. Keihänen[29], R. Keskitalo[15], J. Kim[87], T. S. Kisner[84], R. Kneissl[44,8], J. Knoche[87], M. Kunz[19,66,3], H. Kurki-Suonio[29,50], G. Lagache[5,66], A. Lähteenmäki[2,50], J.-M. Lamarre[79], A. Lasenby[6,76], M. Lattanzi[36], C. R. Lawrence[74], R. Leonardi[45], J. Lesgourgues[104,92,78], F. Levrier[79], A. Lewis[27], M. Liguori[34,73], P. B. Lilje[70], M. Linden-Vørnle[18], M. López-Caniego[45,72], P. M. Lubin[32], Y.-Z. Ma[24,75], J. F. Macías-Pérez[82], G. Maggio[53], D. Maino[38,55], N. Mandolesi[54,36], A. Mangilli[66,77], P. G. Martin[9], E. Martínez-González[72], S. Masi[37], S. Matarrese[34,73,48], P. Mazzotta[40], P. McGehee[63], P. R. Meinhold[32], A. Melchiorri[37,57], L. Mendes[45], A. Mennella[38,55], M. Migliaccio[69,76], S. Mitra[61,74], M.-A. Miville-Deschênes[66,9], D. Molinari[72,54], A. Moneti[67], L. Montier[106,10], G. Morgante[54], D. Mortlock[62], A. Moss[95], M. Münchmeyer[67], D. Munshi[94], J. A. Murphy[89], P. Naselsky[90,42], F. Nati[30], P. Natoli[36,4,54], C. B. Netterfield[22], H. U. Nørgaard-Nielsen[18], F. Noviello[75], D. Novikov[85], I. Novikov[90,85], C. A. Oxborrow[18], F. Paci[93], L. Pagano[37,57], F. Pajot[66], R. Paladini[63], S. Pandolfi[20], D. Paoletti[54,56], F. Pasian[53], G. Patanchon[1], T. J. Pearson[12,63], H. V. Peiris[26], O. Perdereau[77], L. Perotto[82], F. Perrotta[93], V. Pettorino[49], F. Piacentini[37], M. Piat[1], E. Pierpaoli[25], D. Pietrobon[74], S. Plaszczynski[77], E. Pointecouteau[106,10], G. Polenta[4,52], L. Popa[68], G. W. Pratt[80], G. Prézeau[12,74], S. Prunet[67,105], J.-L. Puget[66], J. P. Rachen[23,87], W. T. Reach[107], R. Rebolo[71,16,43], M. Reinecke[87], M. Remazeilles[75,66,1], C. Renault[82], A. Renzi[41,58], I. Ristorcelli[106,10], G. Rocha[74,12], C. Rosset[1], M. Rossetti[38,55], G. Roudier[1,79,74], M. Rowan-Robinson[62], J. A. Rubiño-Martín[71,43], B. Rusholme[63], M. Sandri[54], D. Santos[82], M. Savelainen[29,50], G. Savini[91], D. Scott[24], M. D. Seiffert[74,12], E. P. S. Shellard[13], M. Shiraishi[34,73], L. D. Spencer[94], V. Stolyarov[6,76,100], R. Stompor[1], R. Sudiwala[94], R. Sunyaev[87,98], D. Sutton[69,76], A.-S. Suur-Uski[29,50], J.-F. Sygnet[67], J. A. Tauber[46], L. Terenzi[47,54], L. Toffolatti[21,72,54], M. Tomasi[38,55], M. Tristram[77], T. Trombetti[54], M. Tucci[19], J. Tuovinen[11], L. Valenziano[54], J. Valiviita[29,50], B. Van Tent[83], P. Vielva[72], F. Villa[54], L. A. Wade[74], B. D. Wandelt[67,105,33], I. K. Wehus[74], M. White[31], D. Yvon[17], A. Zacchei[53], J. P. Zibin[24], and A. Zonca[32]

(Affiliations can be found after the references)

Preprint online version: February 10, 2015

ABSTRACT

We present the implications for cosmic inflation of the *Planck* measurements of the cosmic microwave background (CMB) anisotropies in both temperature and polarization based on the full *Planck* survey, which includes more than twice the integration time of the nominal survey used for the 2013 Release papers. The *Planck* full mission temperature data and a first release of polarization data on large angular scales measure the spectral index of curvature perturbations to be $n_s = 0.968 \pm 0.006$ and tightly constrain its scale dependence to $dn_s/d\ln k = -0.003 \pm 0.007$ when combined with the *Planck* lensing likelihood. When the *Planck* high-ℓ polarization data is included, the results are consistent and uncertainties are further reduced. The upper bound on the tensor-to-scalar ratio is $r_{0.002} < 0.11$ (95 % CL). This upper limit is consistent with the B-mode polarization constraint $r < 0.12$ (95 % CL) obtained from a joint analysis of the BICEP2/Keck Array and *Planck* data. These results imply that $V(\phi) \propto \phi^2$ and natural inflation are now disfavoured compared to models predicting a smaller tensor-to-scalar ratio, such as R^2 inflation. We search for several physically motivated deviations from a simple power-law spectrum of curvature perturbations, including those motivated by a reconstruction of the inflaton potential not relying on the slow-roll approximation. We find that such models are not preferred, either according to a Bayesian model comparison or according to a frequentist simulation-based analysis. Three independent methods reconstructing the primordial power spectrum consistently recover a featureless and smooth $\mathcal{P}_{\mathcal{R}}(k)$ over the range of scales $0.008\,\mathrm{Mpc}^{-1} \lesssim k \lesssim 0.1\,\mathrm{Mpc}^{-1}$. At large scales, each method finds deviations from a power law, connected to a deficit at multipoles $\ell \approx 20$–40 in the temperature power spectrum, but at an uncompelling statistical significance owing to the large cosmic variance present at these multipoles. By combining power spectrum and non-Gaussianity bounds, we constrain models with generalized Lagrangians, including Galileon models and axion monodromy models. The *Planck* data are consistent with adiabatic primordial perturbations, and the estimated values for the parameters of the base ΛCDM model are not significantly altered when more general initial conditions are admitted. In correlated mixed adiabatic and isocurvature models, the 95 % CL upper bound for the non-adiabatic contribution to the observed CMB temperature variance is $|\alpha_{\text{non-adi}}| < 1.9\,\%$, 4.0 %, and 2.9 % for cold dark matter (CDM), neutrino density, and neutrino velocity isocurvature modes, respectively. We have tested inflationary models producing an anisotropic modulation of the primordial curvature power spectrum finding that the dipolar modulation in the CMB temperature field induced by a CDM isocurvature perturbation is not preferred at a statistically significant level. We also establish tight constraints on a possible quadrupolar modulation of the curvature perturbation. These results are consistent with the *Planck* 2013 analysis based on the nominal mission data and further constrain slow-roll single-field inflationary models, as expected from the increased precision of *Planck* data using the full set of observations.

Key words. Cosmology: theory – early Universe – inflation

1. Introduction

The precise measurements by *Planck*[1] of the cosmic microwave background (CMB) anisotropies covering the entire sky and over a broad range of scales, from the largest visible down to a resolution of approximately 5′, provide a powerful probe of cosmic inflation, as detailed in the *Planck* 2013 inflation paper (Planck Collaboration XXII, 2014, hereafter PCI13). In the 2013 results, the robust detection of the departure of the scalar spectral index from exact scale invariance, i.e., $n_s < 1$, at more than $5\,\sigma$ confidence, as well as the lack of the observation of any statistically significant running of the spectral index, were found to be consistent with simple slow-roll models of inflation. Single-field inflationary models with a standard kinetic term were also found compatible with the new tight upper bounds on the primordial non-Gaussianity parameters $f_{\rm NL}$ reported in Planck Collaboration XXVI (2014). No evidence of isocurvature perturbations as generated in multi-field inflationary models (PCI13) or by cosmic strings or topological defects was found (Planck Collaboration XXV, 2014). The *Planck* 2013 results overall favoured the simplest inflationary models. However, we noted an amplitude deficit for $\ell \lesssim 40$ whose statistical significance relative to the six-parameter base Λ cold dark matter (ΛCDM) model is only about $2\,\sigma$, as well as other anomalies on large angular scales but also without compelling statistical significance. The constraint on the tensor-to-scalar ratio, $r < 0.12$ at 95 % CL, inferred from the temperature power spectrum alone, combined with the determination of n_s, suggested models with concave potentials.

This paper updates the implications for inflation in the light of the *Planck* full mission temperature and polarization data. The *Planck* 2013 cosmology results included only the nominal mission, comprising the first 14 months of the data taken, and used only the temperature data. However, the full mission includes the full 29 months of scientific data taken by the cryogenically cooled high frequency instrument (HFI) (which ended when the ^{3}He/^{4}He supply for the final stage of the cooling chain ran out) and the approximately four years of data taken by the low frequency instrument (LFI), which covered a longer period than the HFI because the LFI did not rely on cooling down to 100 mK for its operation. For a detailed discussion of the new likelihood and a comparison with the 2013 likelihood, we refer the reader to Planck Collaboration XI (2015) and Planck Collaboration XIII (2015), but we mention here some highlights of the differences between the 2013 and 2015 data processing and likelihoods: (1) Improvements in the data processing such as beam characterization and absolute calibration at each frequency result in a better removal of systematic effects. (2) The 2015 temperature high-ℓ likelihood uses half-mission cross-power spectra over more of the sky, owing to less aggressive Galactic cuts. The use of polarization information in the 2015 likelihood release contributes to the constraining power of *Planck* in two principal ways: (1) The measurement of the E-mode polarization at large angular scales (presently based on the 70 GHz channel) constrains the reionization optical depth, τ, independently of other estimates using ancillary data; and (2) the measurement of the TE and EE spectra at $\ell \geq 30$ at the same frequencies used for the TT spectra (100, 143, and 217 GHz) helps break parameter degeneracies, particularly for extended cosmological models (beyond the baseline six-parameter model). A full analysis of the *Planck* low-ℓ polarization is still in progress and will be the subject of another forthcoming set of *Planck* publications.

The *Planck* 2013 results have sparked a revival of interest in several aspects of inflationary models. We mention here a few examples without the ambition to be exhaustive. A lively debate arose on the conceptual problems of some of the inflationary models favoured by the *Planck* 2013 data (Ijjas et al., 2013; Guth et al., 2014; Linde, 2014; Ijjas et al., 2014). The interest in the R^2 inflationary model originally proposed by Starobinsky (1980) increased, since its predictions for cosmological fluctuations (Starobinsky, 1980; Mukhanov & Chibisov, 1981) are compatible with the *Planck* 2013 results (PCI13). It has been shown that supergravity motivates a potential similar to the Einstein gravity conformal representation of the R^2 inflationary model in different contexts (Ellis et al., 2013a,b; Buchmüller et al., 2013; Farakos et al., 2013; Ferrara et al., 2013b). A similar potential can also be generated by spontaneous breaking of conformal symmetry (Kallosh & Linde, 2013).

The constraining power of *Planck* also motivated a comparison between large numbers of inflationary models (Martin et al., 2014) and stimulated different perspectives on how best to compare theoretical inflationary predictions with observations based on the parameterized dependence of the Hubble parameter on the scale factor during inflation (Mukhanov, 2013; Binétruy et al., 2014; Garcia-Bellido & Roest, 2014). The interpretation of the asymmetries on large angular scales (Planck Collaboration XXIII, 2014) also prompted a re-analysis of the primordial dipole modulation (Lyth, 2013; Liddle & Cortês, 2013; Kanno et al., 2013) of curvature perturbations during inflation.

Another recent development has been the renewed interest in possible tensor modes generated during inflation, sparked by the BICEP2 results (BICEP2 Collaboration, 2014a,b). The BICEP2 team suggested that the B-mode polarization signal detected at $50 < \ell < 150$ at a single frequency (150 GHz) might be of primordial origin. However, a crucial step in this possible interpretation was excluding an explanation based on polarized thermal dust emission from our Galaxy. The BICEP2 team put forward a number of models to estimate the likely contribution from dust, but at the time relevant observational data were lacking, and this modelling involved a high degree of extrapolation. If dust polarization were negligible in the observed patch of 380 deg^2, this interpretation would lead to a tensor-to-scalar ratio $r = 0.2^{+0.07}_{-0.05}$ for a scale-invariant spectrum. A value of $r \approx 0.2$, as suggested by BICEP2 Collaboration (2014b), would have obviously changed the *Planck* 2013 perspective from which slow-roll inflationary models are favoured, and such a high value of r would also have required a strong running of the scalar spectral index, or some other modification from a simple power-law spectrum, to reconcile the contribution of gravitational waves to temperature anisotropies at low multipoles with the observed TT spectrum.

The interpretation of the B-mode signal in terms of gravitational waves *alone* presented in BICEP2 Collaboration (2014b) was later cast in doubt by *Planck* measurements of dust polarization at 353 GHz (Planck Collaboration Int. XIX, 2014; Planck Collaboration Int. XX, 2014; Planck Collaboration Int. XXI, 2014; Planck Collaboration Int. XXII, 2014). The *Planck* measurements characterized the frequency dependence of intensity and polarization of the Galactic dust emission, and moreover showed that the polarization fraction is higher than expected in regions of low dust emission. With the help of the *Planck* mea-

* Corresponding authors: Martin Bucher, bucher@apc.univ-paris7.fr; Fabio Finelli, finelli@iasfbo.inaf.it

[1] *Planck* (http://www.esa.int/Planck) is a project of the European Space Agency (ESA) with instruments provided by two scientific consortia funded by ESA member states and led by Principal Investigators from France and Italy, telescope reflectors provided through a collaboration between ESA and a scientific consortium led and funded by Denmark, and additional contributions from NASA (USA).

surements of Galactic dust properties (Planck Collaboration Int. XIX, 2014), it was shown that the interpretation of the B-mode polarization signal in terms of a primordial tensor signal plus a lensing contribution was not statistically preferred to an explanation based on the expected dust signal at 150 GHz plus a lensing contribution (see also Flauger et al., 2014a; Mortonson & Seljak, 2014). Subsequently, Planck Collaboration XXX (2014) extrapolated the *Planck* B-mode power spectrum of dust polarization at 353 GHz over the multipole range $40 < \ell < 120$ to 150 GHz, showing that the B-mode polarization signal detected by BICEP2 could be entirely due to dust.

More recently, a BICEP2/Keck Array-*Planck* (BKP) joint analysis (BICEP2/Keck Array and Planck Collaborations, 2015, herafter BKP) combined the high sensitivity B-mode maps from BICEP2 and Keck Array with the *Planck* maps at higher frequencies where dust emission dominates. A study of the cross-correlations of all these maps in the BICEP2 field found the absence of any statistically significant evidence for primordial gravitational waves, setting an upper limit of $r < 0.12$ at 95 % CL (BKP). Although this upper limit is numerically almost identical to the *Planck* 2013 result obtained combining the nominal mission temperature data with WMAP polarization to remove parameter degeneracies (Planck Collaboration XVI, 2014; Planck Collaboration XXII, 2014), the BKP upper bound is much more robust against modifications of the inflationary model, since B-modes are insensitive to the shape of the predicted scalar anisotropy pattern. In Sect. 13 we explore how the recent BKP analysis constrains inflationary models.

This paper is organized as follows. Section 2 briefly reviews the additional information on the primordial cosmological fluctuations encoded in the polarization angular power spectrum. Section 3 describes the statistical methodology as well as the *Planck* and other likelihoods used throughout the paper. Sections 4 and 5 discuss the *Planck* 2015 constraints on scalar and tensor fluctuations, respectively. Section 6 is dedicated to constraints on the slow-roll parameters and provides a Bayesian comparison of selected slow-roll inflationary models. In Sect. 7 we reconstruct the inflaton potential and the Hubble parameter as a Taylor expansion of the inflaton in the observable range without relying on the slow-roll approximation. The reconstruction of the curvature perturbation power spectrum is presented in Sect. 8. The search for parameterized features is presented in Sect. 9, and combined constraints from the *Planck* 2015 power spectrum and primordial non-Gaussianity derived in Planck Collaboration XVII (2015) are presented in Sect. 10. The analysis of isocurvature perturbations combined and correlated with curvature perturbations is presented in Sect. 11. In Sect. 12 we study the implications of relaxing the assumption of the statistical isotropy of the power spectrum of primordial fluctuations. We discuss two examples of *anisotropic* inflation in light of the tests of isotropy performed in Planck Collaboration XVI (2015). Section 14 presents some concluding remarks.

2. What new information does polarization provide?

This section provides a short theoretical overview of the extra information provided by polarization data over that of temperature alone. (More details can be found in White et al. (1994); Ma & Bertschinger (1995); Bucher (2014), and references therein.) In Sect. 2 of the *Planck* 2013 inflation paper (PCI13), we gave an overview of the relation between the inflationary potential and the three-dimensional primordial scalar and tensor power spectra, denoted as $\mathcal{P}_{\mathcal{R}}(k)$ and $\mathcal{P}_{\rm t}(k)$, respectively. (The scalar variable

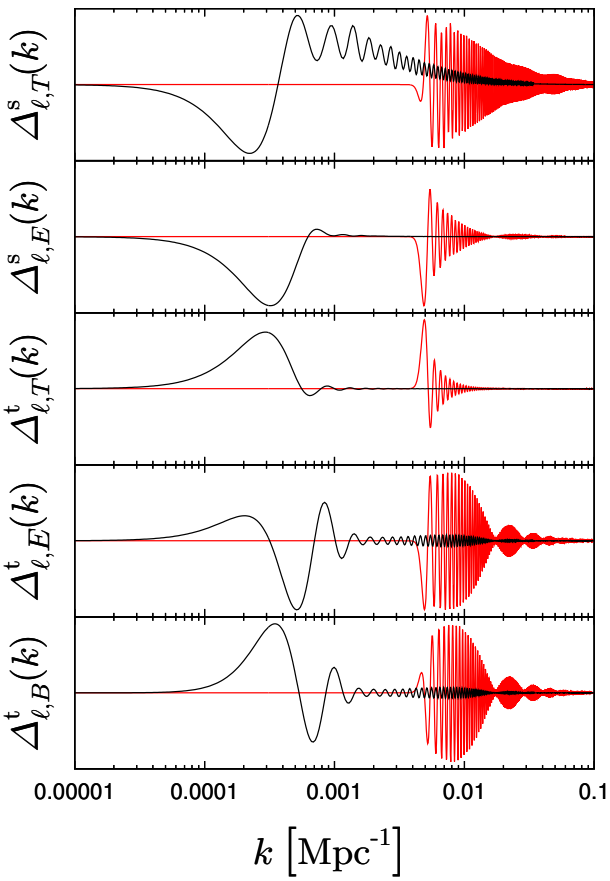

Fig. 1. Comparison of transfer functions for the scalar and tensor modes. The CMB transfer functions $\Delta^{\rm s}_{\ell,\mathcal{A}}(k)$ and $\Delta^{\rm t}_{\ell,\mathcal{A}}(k)$, where $\mathcal{A} = T, E, B$, define the linear transformations mapping the primordial scalar and tensor cosmological perturbations to the CMB anisotropies as seen by us on the sky today. These functions are plotted for two representative values of the multipole number: $\ell = 2$ (in black) and $\ell = 65$ (in red).

$\mathcal{R}$ is defined precisely in Sect. 3). We shall not repeat the discussion there, instead referring the reader to PCI13 and references therein.

Under the assumption of statistical isotropy, which is predicted in all simple models of inflation, the two-point correlations of the CMB anisotropies are described by the angular power spectra C_ℓ^{TT}, C_ℓ^{TE}, C_ℓ^{EE}, and C_ℓ^{BB}, where ℓ is the multipole number. (See Kamionkowski et al. (1997); Zaldarriaga & Seljak (1997); Seljak & Zaldarriaga (1997); Hu & White (1997); Hu et al. (1998) and references therein for early discussions elucidating the role of polarization.) In principle, one could also envisage measuring C_ℓ^{BT} and C_ℓ^{BE}, but in theories where parity symmetry is not explicitly or spontaneously broken, the expectation values for these cross spectra (i.e., theoretical cross spectra) vanish, although the observed realizations of the cross spectra are not exactly zero because of cosmic variance.

The CMB angular power spectra are related to the three-dimensional scalar and tensor power spectra via the transfer functions $\Delta^{\rm s}_{\ell,\mathcal{A}}(k)$ and $\Delta^{\rm t}_{\ell,\mathcal{A}}(k)$, so that the contributions from scalar and tensor perturbations are

$$C_\ell^{\mathcal{AB},\rm s} = \int_0^\infty \frac{{\rm d}k}{k}\, \Delta^{\rm s}_{\ell,\mathcal{A}}(k)\, \Delta^{\rm s}_{\ell,\mathcal{B}}(k)\, \mathcal{P}_{\mathcal{R}}(k) \qquad (1)$$

and

$$C_\ell^{\mathcal{AB},\mathrm{t}} = \int_0^\infty \frac{\mathrm{d}k}{k}\, \Delta^{\mathrm{t}}_{\ell,\mathcal{A}}(k)\, \Delta^{\mathrm{t}}_{\ell,\mathcal{B}}(k)\, \mathcal{P}_{\mathrm{t}}(k), \tag{2}$$

respectively, where $\mathcal{A}, \mathcal{B} = T, E, B$. The scalar and tensor primordial perturbations are uncorrelated in the simplest models, so the scalar and tensor power spectra add in quadrature, meaning that

$$C_\ell^{\mathcal{AB},\mathrm{tot}} = C_\ell^{\mathcal{AB},\mathrm{s}} + C_\ell^{\mathcal{AB},\mathrm{t}}. \tag{3}$$

Roughly speaking, the form of the linear transformations encapsulated in the transfer functions $\Delta^{\mathrm{s}}_{\ell,\mathcal{A}}(k)$ and $\Delta^{\mathrm{t}}_{\ell,\mathcal{A}}(k)$ probe the late-time physics, whereas the primordial power spectra $\mathcal{P}_\mathcal{R}(k)$ and $\mathcal{P}_{\mathrm{t}}(k)$ are solely determined by the primordial universe, perhaps not so far below the Planck scale if large-field inflation turns out to be correct.

To better understand this connection, it is useful to plot and compare the shapes of the transfer functions for representative values of ℓ and characterize their qualitative behavior. Referring to Fig. 1, we emphasize the following qualitative features:

1. For the scalar mode transfer functions, of which only $\Delta^{\mathrm{s}}_{\ell,T}(k)$ and $\Delta^{\mathrm{s}}_{\ell,E}(k)$ are non-vanishing (because to linear order, a three-dimensional scalar mode cannot contribute to the B mode of the polarization), both transfer functions start to rise at more or less the same small values of k (due to the centrifugal barrier in the Bessel differential equation), but $\Delta^{\mathrm{s}}_{\ell,E}(k)$ falls off much faster at large k, and thus smooths sharp features in $\mathcal{P}_\mathcal{R}(k)$ to a smaller extent, than $\Delta^{\mathrm{s}}_{\ell,T}(k)$. This means that polarization is more powerful for reconstructing possible sharp features in the scalar primordial power spectrum than temperature, provided that the required signal-to-noise is available.
2. For the tensor modes, $\Delta^{\mathrm{t}}_{\ell,T}(k)$ starts rising at about the same small k as $\Delta^{\mathrm{s}}_{\ell,T}(k)$ and $\Delta^{\mathrm{s}}_{\ell,E}(k)$ but falls off faster with increasing k than $\Delta^{\mathrm{s}}_{\ell,T}(k)$. On the other hand, the polarization components, $\Delta^{\mathrm{t}}_{\ell,E}(k)$ and $\Delta^{\mathrm{t}}_{\ell,B}(k)$,, have a shape completely different from any of the other transfer functions. The shape of $\Delta^{\mathrm{t}}_{\ell,E}(k)$ and $\Delta^{\mathrm{t}}_{\ell,B}(k)$ is much wider in $\ln(k)$ than the scalar polarization transfer function, with a variance ranging from 0.5 to 1.0 decades. These functions exhibit several acoustic oscillations which appear as an envelope to a rapidly varying carrier frequency.

Regarding the scalar primordial cosmological perturbations, the power spectrum of the E-mode polarization provides an important consistency check. As we explore in Sects. 8 and 9, to some extent the fit of the temperature power spectrum can be improved by allowing a complicated form for the primordial power spectrum (relative to a simple power law), but the C_ℓ^{TE} and C_ℓ^{EE} power spectra provide an important cross-check. Moreover, in multi-field inflationary models, in which isocurvature modes may have been excited (possibily correlated amongst themselves as well as with the adiabatic mode), polarization information provides a powerful way for breaking degeneracies (see, e.g., Bucher et al. (2001)).

The inability of scalar modes to generate B-mode polarization (apart from the effects of lensing) has an important consequence. For the primordial tensor modes, polarization information, especially information concerning the B-mode polarization, offers powerful potential for discovery or for establishing upper bounds. *Planck* 2013 and WMAP established upper bounds on a possible tensor mode contribution using C_ℓ^{TT} alone, but these bounds crucially relied on an assumed simple form for the scalar primordial power spectrum. For example, as reported in PCI13, when a simple power law was generalized to allow for running, the bound on the tensor contribution degraded by approximately a factor of two. The new joint BICEP2/Keck Array-*Planck* upper bound (see Sect. 13), however, is much more robust and cannot be avoided by postulating baroque models that alter the scale dependence of the scalar power spectrum.

3. Methodology

This section describes updates to the formalism used to describe cosmological models and the likelihoods used with respect to the *Planck* 2013 inflation paper (PCI13).

3.1. Cosmological model

The cosmological models that predict observables, such as the CMB anisotropies, rely on inputs specifying the conditions and physics at play during different epochs of the history of the Universe. The primordial inputs describe the power spectrum of the cosmological perturbations at a time when all the observable modes were situated outside the Hubble radius. The inputs from this epoch consist of the primordial power spectra, which may include scalar curvature perturbations, tensor perturbations, and possibly also isocurvature modes and their correlations. The late time (i.e., $z \lesssim 10^4$) cosmological inputs include parameters such as ω_{b}, ω_{c}, Ω_Λ, and τ, which determine the conditions when the primordial perturbations become imprinted on the CMB and also the evolution of the Universe between last scattering and today, affecting primarily the angular diameter distance. Finally, there is a so-called "nuisance" component, consisting of parameters that determine how the measured CMB spectra are contaminated by unsubtracted Galactic and extragalactic foreground contamination. The focus of this paper is on the primordial inputs and how they are constrained by the observed CMB anisotropy, but we cannot completely ignore the other non-primordial parameters because their presence and uncertainties must be dealt with in order to correctly extract the primordial information of interest here.

As in PCI13, we adopt the minimal six-parameter spatially flat base ΛCDM cosmological model as our baseline for the late-time cosmology, mainly altering the primordial inputs, i.e., the simple power-law spectrum parameterized by the scalar amplitude and spectral index for the adiabatic growing mode, which in this minimal model is the only late-time mode excited. This model has four free non-primordial cosmological parameters $(\omega_{\mathrm{b}}, \omega_{\mathrm{c}}, \theta_{\mathrm{MC}}, \tau)$ (for a more detailed account of this model, we refer the reader to Planck Collaboration XIII (2015)). On occasion, this assumption will be relaxed in order to consider the impact of more complex alternative late-time cosmologies on our conclusions about inflation. Some of the commonly used cosmological parameters are defined in Table 1.

3.2. Primordial spectra of cosmological fluctuations

In inflationary models, comoving curvature ($\mathcal{R}$) and tensor (h) fluctuations are amplified by the nearly exponential expansion from quantum vacuum fluctuations to become highly squeezed states resembling classical states. Formally, this quantum mechanical phenomenon is most simply described by the evolution in conformal time, η, of the mode functions for the gauge-invariant inflaton fluctuation, $\delta\phi$, and for the tensor fluctuation,

Table 1. Primordial, baseline, and optional late-time cosmological parameters.

Parameter	Definition
A_s	Scalar power spectrum amplitude (at $k_* = 0.05\,\mathrm{Mpc}^{-1}$)
n_s	Scalar spectral index (at $k_* = 0.05\,\mathrm{Mpc}^{-1}$, unless otherwise stated)
$\mathrm{d}n_s/\mathrm{d}\ln k$	Running of scalar spectral index (at $k_* = 0.05\,\mathrm{Mpc}^{-1}$, unless otherwise stated)
$\mathrm{d}^2n_s/\mathrm{d}\ln k^2$	Running of running of scalar spectral index (at $k_* = 0.05\,\mathrm{Mpc}^{-1}$)
r	Tensor-to-scalar power ratio (at $k_* = 0.05\,\mathrm{Mpc}^{-1}$, unless otherwise stated)
n_t	Tensor spectrum spectral index (at $k_* = 0.05\,\mathrm{Mpc}^{-1}$)
ω_b	Baryon density today
ω_c	Cold dark matter density today
θ_{MC}	Approximation to the angular size of sound horizon at last scattering
τ	Thomson scattering optical depth of reionized intergalactic medium
N_{eff}	Effective number of massive and massless neutrinos
Σm_ν	Sum of neutrino masses
Y_P	Fraction of baryonic mass in primordial helium
Ω_K	Spatial curvature parameter
w_{de}	Dark energy equation of state parameter (i.e., p_{de}/ρ_{de}) (assumed constant)

h:

$$(ay_k)'' + \left(k^2 - \frac{x''}{x}\right) ay_k = 0, \tag{4}$$

with $(x\,,y) = (a\dot{\phi}/H\,,\delta\phi)$ for scalars, and $(x\,,y) = (a\,,h)$ for tensors. Here a is the scale factor, primes indicate derivatives with respect to η, and $\dot{\phi}$ and $H = \dot{a}/a$ are the proper time derivative of the inflaton and the Hubble parameter, respectively. The curvature fluctuation, $\mathcal{R}$, and the inflaton fluctuation, $\delta\phi$, are related via $\mathcal{R} = H\delta\phi/\dot{\phi}$. Analytic and numerical calculations of the predictions for the primordial spectra of cosmological fluctuations generated during inflation have reached high standards of precision, which are more than adequate for our purposes, and the largest uncertainty in testing specific inflationary models arises from our lack of knowledge of the history of the Universe between the end of inflation and the present time, during the so-called "epoch of entropy generation."

This paper uses three different methods to compare inflationary predictions with *Planck* data. The first method consists of a phenomenological parameterization of the primordial spectra of scalar and tensor perturbations as:

$$\mathcal{P}_\mathcal{R}(k) = \frac{k^3}{2\pi^2}|\mathcal{R}_k|^2 = A_s\left(\frac{k}{k_*}\right)^{n_s-1+\frac{1}{2}\,\mathrm{d}n_s/\mathrm{d}\ln k\,\ln(k/k_*)+\frac{1}{6}\,\mathrm{d}^2n_s/\mathrm{d}\ln k^2(\ln(k/k_*))^2+\ldots}, \tag{5}$$

$$\mathcal{P}_t(k) = \frac{k^3}{2\pi^2}\left(|h_k^+|^2 + |h_k^\times|^2\right) = A_t\left(\frac{k}{k_*}\right)^{n_t+\frac{1}{2}\,\mathrm{d}n_t/\mathrm{d}\ln k\,\ln(k/k_*)+\ldots}, \tag{6}$$

where $A_s\,(A_t)$ is the scalar (tensor) amplitude and $n_s\,(n_t)$, $\mathrm{d}n_s/\mathrm{d}\ln k\,(\mathrm{d}n_t/\mathrm{d}\ln k)$, and $\mathrm{d}^2n_s/\mathrm{d}\ln k^2$ are the scalar (tensor) spectral index, the running of the scalar (tensor) spectral index, and the running of the running of the scalar spectral index, respectively. $\mathcal{R}$ denotes the comoving curvature perturbation for adiabatic initial conditions, h the amplitude of the two polarization states $(+,\times)$ of gravitational waves, and k_* the pivot scale. Unless otherwise stated, the tensor-to-scalar ratio,

$$r = \frac{\mathcal{P}_t(k_*)}{\mathcal{P}_\mathcal{R}(k_*)}, \tag{7}$$

is fixed to $-8n_t$,[2] which is the relation that holds when inflation is driven by a single slow-rolling scalar field with a standard kinetic term. We will use a parameterization analogous to Eq. (5) with no running for the power spectra of isocurvature modes and their correlations in Sect. 11.

The second method exploits the analytic dependence of the slow-roll power spectra of primordial perturbations in Eqs. (5) and (6) on the values of the Hubble parameter and the hierarchy of its time derivatives, known as the Hubble flow-functions (HFF): $\epsilon_1 = -\dot{H}/H^2$, $\epsilon_{i+1} \equiv \dot{\epsilon}_i/(H\epsilon_i)$, with $i \geq 1$. We will use the analytic power spectra calculated up to second order using the Green's function method (Gong & Stewart, 2001; Leach et al., 2002) (see Habib et al. 2002, Martin & Schwarz 2003, and Casadio et al. 2006 for alternative derivations). The spectral indices and the relative scale dependence in Eqs. (5) and (6) are given in terms of the HFFs by:

$$n_s - 1 = -2\epsilon_1 - \epsilon_2 - 2\epsilon_1^2 - (2\,C+3)\,\epsilon_1\,\epsilon_2 - C\epsilon_2\epsilon_3, \tag{8}$$

$$\mathrm{d}n_s/\mathrm{d}\ln k = -2\epsilon_1\epsilon_2 - \epsilon_2\epsilon_3, \tag{9}$$

$$n_t = -2\epsilon_1 - 2\epsilon_1^2 - 2\,(C+1)\,\epsilon_1\,\epsilon_2, \tag{10}$$

$$\mathrm{d}n_t/\mathrm{d}\ln k = -2\epsilon_1\epsilon_2\,, \tag{11}$$

where $C \equiv \ln 2 + \gamma_E - 2 \approx -0.7296$ (γ_E is the Euler-Mascheroni constant). See Appendix of PCI13 for more details. Primordial spectra as functions of the ϵ_i will be employed in Sect. 6, and the expressions generalizing Eqs. (8) to (11) for a general Lagrangian $p(\phi, X)$, where $X \equiv -g^{\mu\nu}\partial_\mu\phi\partial_\nu\phi/2$, will be used in Sect. 10. The good agreement between the first and second method as well as with alternative approximations of slow-roll spectra is illustrated in the Appendix of PCI13.

The third method is fully numerical, suitable for models where the slow-roll conditions are not well satisfied and analytical approximations for the primordial fluctuations are not available. Two different numerical codes, the inflation module of Lesgourgues & Valkenburg (2007) as implemented in `CLASS` (Lesgourgues, 2011; Blas et al., 2011) and `ModeCode` (Adams et al., 2001; Peiris et al., 2003; Mortonson et al., 2009; Easther & Peiris, 2012), are used in Sects. 7 and 10, respectively.[3]

Conventions for the functions and symbols used to describe inflationary physics are defined in Table 2.

3.3. Planck data

The *Planck* data processing proceeding from time-ordered data (TOD) to maps has been improved for this 2015 re-

[2] When running is considered, we fix $n_t = -r(2 - r/8 - n_s)/8$ and $\mathrm{d}n_t/\mathrm{d}\ln k = r(r/8 + n_s - 1)/8$.

[3] http://class-code.net, http://modecode.org

Table 2. Conventions and definitions for inflation physics

Parameter	Definition
ϕ	Inflaton
$V(\phi)$	Inflaton potential
a	Scale factor
t	Cosmic (proper) time
δX	Fluctuation of X
$\dot{X} = dX/dt$	Derivative with respect to proper time
$X' = dX/d\eta$	Derivative with respect to conformal time
$X_\phi = \partial X/\partial\phi$	Partial derivative with respect to ϕ
$M_{\rm pl}$	Reduced Planck mass (= 2.435×10^{18} GeV)
Q	Scalar perturbation variable
$h^{+,\times}$	Gravitational wave amplitude of $(+,\times)$-polarization component
X_*	X evaluated at Hubble exit during inflation of mode with wavenumber k_*
$X_{\rm e}$	X evaluated at end of inflation
$\epsilon_V = M_{\rm pl}^2 V_\phi^2/2V^2$	First slow-roll parameter for $V(\phi)$
$\eta_V = M_{\rm pl}^2 V_{\phi\phi}/V^2$	Second slow-roll parameter for $V(\phi)$
$\xi_V^2 = M_{\rm pl}^4 V_\phi V_{\phi\phi\phi}/V^2$	Third slow-roll parameter for $V(\phi)$
$\varpi_V^3 = M_{\rm pl}^6 V_\phi^2 V_{\phi\phi\phi\phi}/V^3$	Fourth slow-roll parameter for $V(\phi)$
$\epsilon_1 = -\dot{H}/H^2$	First Hubble hierarchy parameter
$\epsilon_{n+1} = \dot{\epsilon}_n/H\epsilon_n$	$(n+1)$st Hubble hierarchy parameter (where $n \geq 1$)
$N(t) = \int_t^{t_{\rm e}} {\rm d}t\, H$	Number of e-folds to end of inflation

lease in various aspects (Planck Collaboration II, 2015; Planck Collaboration VII, 2015). We refer the interested reader to Planck Collaboration II (2015) and Planck Collaboration VII (2015) for details, and we describe here two of these improvements. The absolute calibration has been improved using the orbital dipole and more accurate characterization of the *Planck* beams. The calibration discrepancy between *Planck* and WMAP described in Planck Collaboration XXXI (2014) for the 2013 release has now been greatly reduced. At the time of that release, a blind analysis for primordial power spectrum reconstruction described a broad feature at $\ell \approx 1800$ in the temperature power spectrum, which was most prominent in the 217×217 GHz auto-spectra (PCI13). In work done after the *Planck* 2013 data release, this feature was shown to be associated with imperfectly subtracted systematic effects associated with the 4-K cooler lines, which were particularly strong in the first survey. This systematic effect was shown to potentially lead to $0.5\,\sigma$ shifts in the cosmological parameters, slightly increasing $n_{\rm s}$ and H_0, similarly to the case in which the 217×217 channel was excised from the likelihood (Planck Collaboration XV, 2014; Planck Collaboration XVI, 2014). The *Planck* likelihood (Planck Collaboration XI, 2015) is based on the full mission data and comprises temperature and polarization data (see Fig. 2).

Planck low-ℓ likelihood

The *Planck* low-ℓ temperature-polarization likelihood uses foreground-cleaned LFI 70 GHz polarization maps together with the temperature map obtained from the *Planck* 30 to 353 GHz channels by the `Commander` component separation algorithm over 94 % of the sky (see Planck Collaboration IX (2015) for further details). The *Planck* polarization map uses the LFI 70 GHz (excluding Surveys 2 and 4) low-resolution maps of Q and U polarization from which polarized synchrotron and thermal dust emission components have been removed using the LFI 30 GHz and HFI 353 GHz maps as templates, respectively. (See Planck Collaboration XI (2015) for more details.) The polarization map covers the 46 % of the sky outside the lowP polarization mask.

The low-ℓ likelihood is pixel-based and treats the temperature and polarization at the same resolution of 3°.6, or `HEALpix` (Górski et al., 2005) $N_{\rm side} = 16$. Its multipole range extends from $\ell = 2$ to $\ell = 29$ in TT, TE, EE, and BB. In the 2015 *Planck* papers the polarization part of this likelihood is denoted as "lowP."[4] This *Planck* low-ℓ likelihood replaces the *Planck* temperature low-ℓ Gibbs module combined with the WMAP 9-year low-ℓ polarization module used in the *Planck* 2013 cosmology papers (denoted by WP), which used lower resolution polarization maps at $N_{\rm side} = 8$ (about 7°.3). With this *Planck*-only low-ℓ likelihood module, the basic *Planck* results presented in this release are completely independent of external information.

The *Planck* low multipole likelihood alone implies $\tau = 0.067 \pm 0.022$ (Planck Collaboration XI, 2015), a value smaller than the value inferred using the WP polarization likelihood, $\tau = 0.089 \pm 0.013$, used in the *Planck* 2013 papers (Planck Collaboration XV, 2014). See Planck Collaboration XIII (2015) for the important implications of this decrease in τ for reionization. However, the LFI 70 GHz and WMAP polarization maps are in very good agreement when both are foreground-cleaned using the HFI 353 GHz map as a polarized dust template (see Planck Collaboration XI (2015) for further details). Therefore, it is useful to construct a noise-weighted combination to obtain a joint *Planck*/WMAP low-resolution polarization data set, also described in Planck Collaboration XI (2015), using as a polariza-

[4] In this paper we use the conventions introduced in Planck Collaboration XIII (2015). We adopt the following labels for likelihoods: (i) *Planck* TT denotes the combination of the TT likelihood at multipoles $\ell \geq 30$ and a low-ℓ temperature-only likelihood based on the CMB map recovered with `Commander`; (ii) *Planck* TT–lowT denotes the TT likelihood at multipoles $\ell \geq 30$; (iii) *Planck* TT+lowP further includes the *Planck* polarization data in the low-ℓ likelihood, as described in the main text; (iv) *Planck* TE denotes the likelihood at $\ell \geq 30$ using the TE spectrum; and (v) *Planck* TT,TE,EE+lowP denotes the combination of the likelihood at $\ell \geq 30$ using TT, TE, and EE spectra and the low-ℓ multipole likelihood. The label "τ prior" denotes the use of a Gaussian prior $\tau = 0.07 \pm 0.02$. The labels "lowT,P" and "lowEB" denote the low-ℓ multipole likelihood and the Q, U pixel likelihood only, respectively.

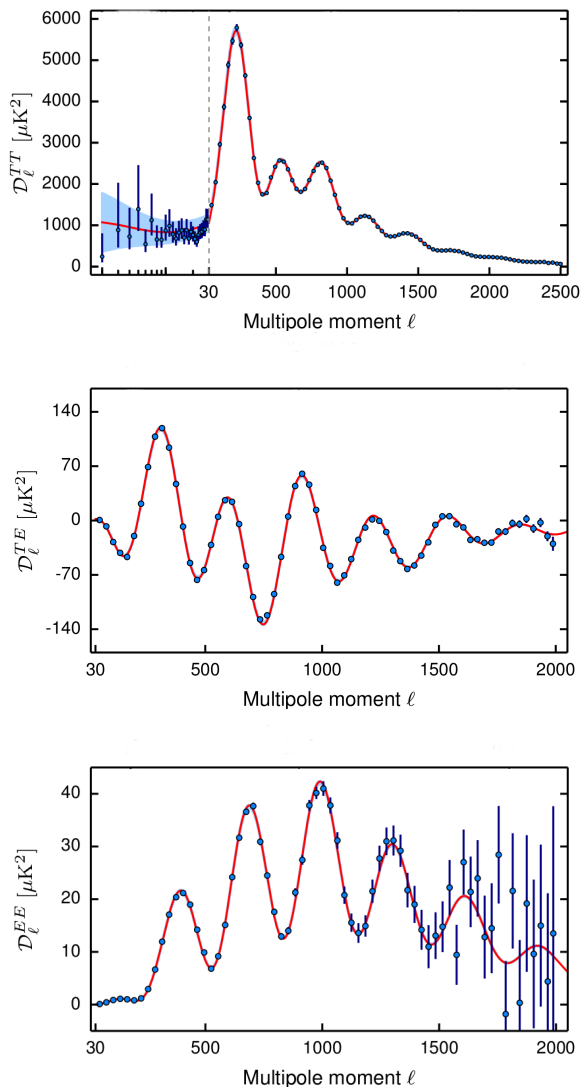

Fig. 2. *Planck* TT (top), high-ℓ TE (centre), and high-ℓ EE (bottom) angular power spectra. Here $\mathcal{D}_\ell \equiv \ell(\ell+1)C_\ell/(2\pi)$.

tion mask the union of the WMAP P06 and *Planck* lowP polarization masks and keeping 74 % of the sky. The polarization part of the combined low-multipole likelihood is called lowP+WP. This combined low-multipole likelihood gives $\tau = 0.071^{+0.011}_{-0.013}$ (Planck Collaboration XI, 2015).

Planck high-ℓ likelihood

Following Planck Collaboration XV (2014), and Planck Collaboration XI (2015) for polarization, we use a Gaussian approximation for the high-ℓ part of the likelihood ($30 < \ell < 2500$), so that

$$-\log\mathcal{L}\big(\hat{C}|C(\boldsymbol{\theta})\big) = \frac{1}{2}\big(\hat{C} - C(\boldsymbol{\theta})\big)^T \mathcal{M}^{-1}\big(\hat{C} - C(\boldsymbol{\theta})\big), \qquad (12)$$

where a constant offset has been discarded. Here $\hat{C}$ is the data vector, $C(\boldsymbol{\theta})$ is the model prediction for the parameter value vector $\boldsymbol{\theta}$, and $\mathcal{M}$ is the covariance matrix. For the data vector, we use 100 GHz, 143 GHz, and 217 GHz half-mission cross-power spectra, avoiding the Galactic plane as well as the brightest point sources and the regions where the CO emission is the strongest. We retain 66 % of the sky for 100 GHz, 57 % for 143 GHz, and 47 % for 217 GHz for the T masks, and respectively 70 %, 50 %, and 41 % for the Q, U masks. Following Planck Collaboration XXX (2014), we do not mask for any other Galactic polarized emission. All the spectra are corrected for the beam and pixel window functions using the same beam for temperature and polarization. (For details see Planck Collaboration XI (2015).)

The model for the cross-spectra can be written as

$$C_{\mu,\nu}(\theta) = \frac{C^{\rm cmb}(\theta) + C^{\rm fg}_{\mu,\nu}(\theta)}{\sqrt{{\rm c}_\mu {\rm c}_\nu}}, \qquad (13)$$

where $C^{\rm cmb}(\theta)$ is the CMB power spectrum, which is independent of the frequency, $C^{\rm fg}_{\mu,\nu}(\theta)$ is the foreground model contribution for the cross-frequency spectrum $\mu \times \nu$, and ${\rm c}_\mu$ is the calibration factor for the $\mu \times \mu$ spectrum. The model for the foreground residuals includes the following components: Galactic dust, clustered CIB, tSZ, kSZ, tSZ correlations with CIB, and point sources, for the TT foreground modeling; and for polarization, only dust is included. All the components are modelled by smooth C_ℓ templates with free amplitudes, which are determined along with the cosmological parameters as the likelihood is explored. The tSZ and kSZ models are the same as in 2013 (see Planck Collaboration XV, 2014), while the CIB and tSZ-CIB correlation models use the updated CIB models described in Planck Collaboration XXX (2014). The point source contamination is modelled as Poisson noise with an independent amplitude for each frequency pair. Finally, the dust contribution uses an effective smooth model measured from high frequency maps. Details of our dust and noise modelling can be found in Planck Collaboration XI (2015). The dust is the dominant foreground component for TT at $\ell < 500$, while the point source component, and for 217×217 also the CIB component, dominate at high ℓ. The other foreground components are poorly determined by *Planck*. Finally, our treatment of the calibration factors and beam uncertainties and mismatch are described in Planck Collaboration XI (2015).

The covariance matrix accounts for the correlation due to the mask and is computed following the equations in Planck Collaboration XV (2014), extended to polarization in Planck Collaboration XI (2015) and references therein. The fiducial model used to compute the covariance is based on a joint fit of base ΛCDM and nuisance parameters obtained with a previous version of the matrix. We iterate the process until the parameters stop changing. For more details, see Planck Collaboration XI (2015).

The joint unbinned covariance matrix is approximately of size 23 000 × 23 000. The memory and speed requirements for dealing with such a huge matrix are significant, so to reduce its size, we bin the data and the covariance matrix to compress the data vector size by a factor of 10. The binning uses varying bin width with $\Delta\ell = 5$ for $29 < \ell < 100$, $\Delta\ell = 9$ for $99 < \ell < 2014$, and $\Delta\ell = 33$ for $2013 < \ell < 2509$, and a weighting in $\ell(\ell+1)$ to flatten the spectrum. Where a higher resolution is desirable, we also use a more finely binned version ("bin3", unbinned up to $\ell = 80$ and $\Delta\ell = 3$ beyond that) as well as a completely unbinned version ("bin1"). We use odd bin sizes, since for an azimuthally symmetric mask, the correlation between a multipole and its neighbours is symmetric, oscillating between positive and negative values. Using the base ΛCDM model and single parameter classical extensions, we confirmed that the cosmological and nuisance parameter fits with or without binning are indistinguishable.

Planck CMB bispectrum

We use measurements of the non-Gaussianity amplitude $f_{\rm NL}$ from the CMB bispectrum presented in Planck Collaboration XVII (2015). Non-Gaussianity constraints have been obtained using three optimal bispectrum estimators (separable template fitting (also known as "KSW"), binned, and modal). The maps analysed are the *Planck* 2015 full mission sky maps, both in temperature and in E polarization, as cleaned with the four component separation methods SMICA, SEVEM, NILC, and Commander. The map is masked to remove the brightest parts of the Galaxy as well as the brightest point sources and covers approximately 70 % of the sky. In this paper we mainly exploit the joint constraints on equilateral and orthogonal non-Gaussianity (after removing the ISW-lensing bias), $f_{\rm NL}^{\rm equil} = -16 \pm 70$, $f_{\rm NL}^{\rm ortho} = -34 \pm 33$ from T only, and $f_{\rm NL}^{\rm equil} = -3.7 \pm 43$, $f_{\rm NL}^{\rm ortho} = -26 \pm 21$ from T and E (68 % CL). For reference, the constraints on local non-Gaussianity are $f_{\rm NL}^{\rm local} = 2.5 \pm 5.7$ from T only, and $f_{\rm NL}^{\rm local} = 0.8 \pm 5.0$ from T and E (68 % CL). Starting from a Gaussian $f_{\rm NL}$-likelihood, which is an accurate assumption in the regime of small primordial non-Gaussianity, we use these constraints to derive limits on the sound speed of the inflaton fluctuations (or other microscopic parameters of inflationary models) (Planck Collaboration XXIV, 2014). The bounds on the sound speed for various models are then used in combination with *Planck* power spectrum data.

Planck CMB lensing data

Some of our analysis includes the *Planck* 2015 lensing likelihood, presented in Planck Collaboration XV (2015), which utilizes the non-Gaussian trispectrum induced by lensing to estimate the power spectrum of the lensing potential, $C_\ell^{\phi\phi}$. This signal is extracted using a full set of temperature- and polarization-based quadratic lensing estimators (Okamoto & Hu, 2003) applied to the SMICA CMB map over approximately 70 % of the sky, as described in Planck Collaboration IX (2015). We have used the conservative bandpower likelihood, covering multipoles $40 \le \ell \le 400$. This provides a measurement of the lensing potential power at the $40\,\sigma$ level, giving a 2.5 %-accurate constraint on the overall lensing power in this multipole range. The measurement of the lensing power spectrum used here is approximately twice as powerful as the measurement used in our previous 2013 analysis (Planck Collaboration XXII, 2014; Planck Collaboration XVII, 2014), which used temperature-only data from the *Planck* nominal mission data set.

3.4. Non-Planck data

BAO data

Baryon acoustic oscillations (BAO) are the counterpart in the late-time matter power spectrum of the acoustic oscillations seen in the CMB multipole spectrum (Eisenstein et al., 2005). Both originate from coherent oscillations of the photon-baryon plasma before these two components become decoupled at recombination. Measuring the position of these oscillations in the matter power spectra at different redshifts constrains the expansion history of the universe after decoupling, thus removing degeneracies in the interpretation of the CMB anisotropies.

In this paper, we combine constraints on $D_V(\bar{z})/r_{\rm s}$ (the ratio between the spherically averaged distance scale D_V to the effective survey redshift, $\bar{z}$, and the sound horizon, $r_{\rm s}$) inferred from 6dFGRS data (Beutler et al., 2011) at $\bar{z} = 0.106$, the SDSS-MGS data (Ross et al., 2014) at $\bar{z} = 0.15$, and the SDSS-DR11 CMASS and LOWZ data (Anderson et al., 2014) at redshifts $\bar{z} = 0.57$ and 0.32. (For details see Planck Collaboration XIII (2015).)

Joint BICEP2/Keck Array and *Planck* constraint on r

Since the *Planck* temperature constraints on the tensor-to-scalar ratio are close to the cosmic variance limit, the inclusion of data sets sensitive to the expected B-mode signal of primordial gravitational waves is particularly useful. In this paper, we provide results including the joint analysis cross-correlating BICEP2/Keck Array observations and *Planck* (BICEP2/Keck Array and Planck Collaborations, 2015, hereafter BKP). Combining the more sensitive BICEP2/Keck Array B-mode polarization maps in the approximately 400 deg^2 BICEP2 field with the *Planck* maps at higher frequencies where dust dominates allows a statistical analysis taking into account foreground contamination. Using BB auto- and cross-frequency spectra between BICEP2/Keck Array (150 GHz) and *Planck* (217 and 353 GHz), BKP find a 95 % upper limit of $r_{0.05} < 0.12$.

3.5. Parameter estimation and model comparison

Much of this paper uses a Bayesian approach to parameter estimation, and unless otherwise specified, we assign broad top-hat prior probability distributions to the cosmological parameters listed in Table 1. We generate posterior probability distributions of the parameters using either the Metropolis-Hastings algorithm implemented in CosmoMC (Lewis & Bridle, 2002) or MontePython (Audren et al., 2013), the nested sampling algorithm MultiNest (Feroz & Hobson, 2008; Feroz et al., 2009, 2013), or PolyChord, which combines nested sampling with slice sampling (Handley et al., 2015). The latter two also compute Bayesian evidences needed for model comparison. Nevertheless, χ^2 values are often provided as well (using CosmoMC's implementation of the BOBYQA algorithm (Powell, 2009) for maximizing the likelihood), and other parts of the paper employ frequentist methods when appropriate.

4. Constraints on the primordial spectrum of curvature perturbations

One of the most important results of the *Planck* nominal mission was the determination of the departure from scale invariance for the spectrum of scalar perturbations at high statistical significance (Planck Collaboration XVI, 2014; Planck Collaboration XXII, 2014). We now update these measurements with the *Planck* full mission data in temperature and polarization.

4.1. Tilt of the curvature power spectrum

For the base ΛCDM model with a power-law power spectrum of curvature perturbations, the constraint on the scalar spectral index, $n_{\rm s}$, with the *Planck* full mission temperature data is

$$n_{\rm s} = 0.9655 \pm 0.0062 \ (68\,\%\ \text{CL}, \textit{Planck}\ \text{TT+lowP})\,. \qquad (14)$$

This result is compatible with the *Planck* 2013 results ($n_{\rm s} = 0.9603 \pm 0.0073$ (Planck Collaboration XV, 2014; Planck Collaboration XVI, 2014); see Fig. 3 for the accompanying changes in τ, $\Omega_{\rm b}h^2$, and $\theta_{\rm MC}$). The shift towards higher values

Parameter	TT+lowP	TT+lowP+lensing	TT+lowP+BAO	TT,TE,EE+lowP
$\Omega_b h^2$	0.02222 ± 0.00023	0.02226 ± 0.00023	0.02226 ± 0.00020	0.02225 ± 0.00016
$\Omega_c h^2$	0.1197 ± 0.0022	0.1186 ± 0.0020	0.1190 ± 0.0013	0.1198 ± 0.0015
$100\theta_{MC}$	1.04085 ± 0.00047	1.04103 ± 0.00046	1.04095 ± 0.00041	1.04077 ± 0.00032
τ	0.078 ± 0.019	0.066 ± 0.016	0.080 ± 0.017	0.079 ± 0.017
$\ln(10^{10}A_s)$	3.089 ± 0.036	3.062 ± 0.029	3.093 ± 0.034	3.094 ± 0.034
n_s	0.9655 ± 0.0062	0.9677 ± 0.0060	0.9673 ± 0.0045	0.9645 ± 0.0049
H_0	67.31 ± 0.96	67.81 ± 0.92	67.63 ± 0.57	67.27 ± 0.66
Ω_m	0.315 ± 0.013	0.308 ± 0.012	0.3104 ± 0.0076	0.3156 ± 0.0091

Table 3. Confidence limits on the parameters of the base ΛCDM model, for various combinations of *Planck* 2015 data, at the 68% confidence level.

for n_s with respect to the nominal mission results is due to several improvements in the data processing and likelihood which are discussed in Sect. 3, including the removal of the 4-K cooler systematics. For the values of other cosmological parameters in the base ΛCDM model, see Table 3. We also provide the results for the base ΛCDM model and extended models online.[5]

When the *Planck* high-ℓ polarization is combined with temperature, we obtain

$$n_s = 0.9645 \pm 0.0049 \ (68\,\%\ \mathrm{CL},\ \textit{Planck}\ \mathrm{TT,TE,EE+lowP}), \tag{15}$$

together with $\tau = 0.079 \pm 0.017$ (68 % CL), which is consistent with the TT+lowP results. The *Planck* high-ℓ polarization pulls up τ to a slightly higher value. When the *Planck* lensing measurement is added to the temperature data, we obtain

$$n_s = 0.9677 \pm 0.0060 \ (68\,\%\ \mathrm{CL},\ \textit{Planck}\ \mathrm{TT+lowP+lensing}), \tag{16}$$

with $\tau = 0.066 \pm 0.016$ (68 % CL). The shift towards slightly smaller values of the optical depth is driven by a marginal preference for a smaller primordial amplitude, A_s, in the *Planck* lensing data (Planck Collaboration XV, 2015). Given that the temperature data provide a sharp constraint on the combination $e^{-2\tau}A_s$, a slightly lower A_s requires a smaller optical depth to reionization.

4.2. Viability of the Harrison-Zeldovich spectrum

Even though the estimated scalar spectral index has risen slightly with respect to the *Planck* 2013 release, the assumption of a Harrison-Zeldovich (HZ) scale-invariant spectrum (Harrison, 1970; Peebles & Yu, 1970; Zeldovich, 1972) continues to be disfavoured (with a modest increase in significance, from $5.1\,\sigma$ in 2013 to $5.6\,\sigma$ today), because the error bar on n_s has decreased. The value of n_s inferred from the *Planck* 2015 temperature plus large-scale polarization data lies 5.6 standard deviations away from unity (with a corresponding $\Delta\chi^2 = 29.9$), if one assumes the base ΛCDM late-time cosmological model. If we consider more general reionization models, parameterized by a principal component analysis (Mortonson & Hu, 2008) instead of τ (where reionization is assumed to have occured instantaneously), we find $\Delta\chi^2 = 14.9$ for $n_s = 1$. Previously, simple one-parameter extensions of the base model, such as ΛCDM+$N_{\rm eff}$ (where $N_{\rm eff}$ is the effective number of neutrino flavours) or ΛCDM+Y_P (where Y_P is the primordial value of the helium mass fraction), could nearly reconcile the *Planck* temperature data with $n_s = 1$. They now lead to $\Delta\chi^2 = 7.6$ and 9.3, respectively. For any of the cosmological models that we have considered, the $\Delta\chi^2$ by which the HZ model is penalized with respect to the tilted model has increased since the 2013 analysis (PCI13) thanks to the constraining power of the full mission temperature data. Adding *Planck* high-ℓ polarization data further disfavours the HZ model: in ΛCDM, the χ^2 increases by 57.8, for general reionization we obtain $\Delta\chi^2 = 41.3$, and for ΛCDM+$N_{\rm eff}$ and ΛCDM+Y_P we find $\Delta\chi^2 = 22.5$ and 24.0, respectively.

[5] http://www.cosmos.esa.int/web/planck/pla

4.3. Running of the spectral index

The running of the scalar spectral index is constrained by the *Planck* 2015 full mission temperature data to

$$\frac{dn_s}{d\ln k} = -0.0084 \pm 0.0082 \ (68\,\%\ \mathrm{CL},\ \textit{Planck}\ \mathrm{TT+lowP})\,. \tag{17}$$

The combined constraint including high-ℓ polarization is

$$\frac{dn_s}{d\ln k} = -0.0057 \pm 0.0071 \ (68\,\%\ \mathrm{CL},\ \textit{Planck}\ \mathrm{TT,TE,EE+lowP})\,. \tag{18}$$

Adding the *Planck* CMB lensing data to the temperature data further reduces the central value for the running, i.e., $dn_s/d\ln k = -0.0033 \pm 0.0074$ (68 % CL, *Planck* TT+lowP+lensing).

The central value for the running has decreased in magntude with respect to the *Planck* 2013 nominal mission (Planck Collaboration XVI (2014) found $dn_s/d\ln k = -0.013 \pm 0.009$; see Fig. 4), and the improvement of the maximum likelihood with respect to a power-law spectrum is smaller, $\Delta\chi^2 \approx -0.8$. Among the different effects contributing to the decrease in the central value of the running with respect to the *Planck* 2013 result, we mention a change in HFI beams at $\ell \lesssim 200$ (Planck Collaboration XIII, 2015). Nevertheless, the deficit of power at low multipoles in the *Planck* 2015 temperature power spectrum contributes to a preference for slightly negative values of the running, but with low statistical significance.

The *Planck* constraints on n_s and $dn_s/d\ln k$ are remarkably stable against the addition of the BAO likelihood. The combination with BAO shifts n_s to slighly higher values and shrinks its uncertainty by about 30 % when only high-ℓ temperature is considered, and by only about 15 % when high-ℓ temperature and polarization are combined. In slow-roll inflation, the running of the scalar spectral index is connected to the third derivative of the potential (Kosowsky & Turner, 1995). As was the case for the nominal mission results, values of the running compatible with the *Planck* 2015 constraints can be obtained in viable inflationary models (Kobayashi & Takahashi, 2011).

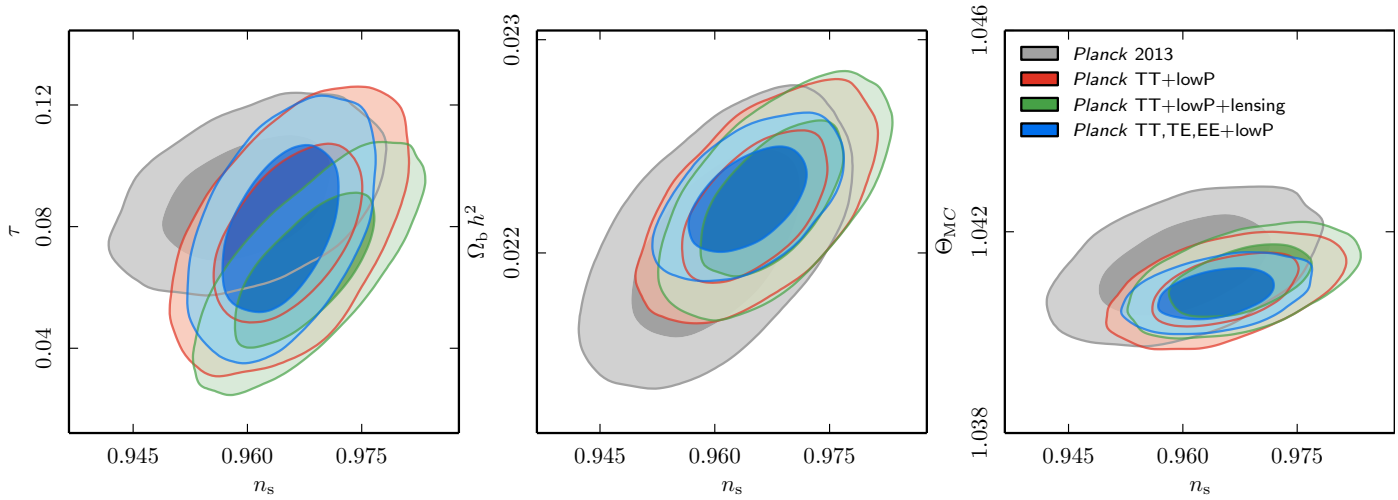

Fig. 3. Comparison of the marginalized joint 68 % and 95 % CL constraints on (n_s, τ) (left panel), $(n_s, \Omega_b h^2)$ (middle panel), and (n_s, θ_{MC}) (right panel), for *Planck* 2013 (grey contours), *Planck* TT+lowP (red contours), *Planck* TT+lowP+lensing (green contours), and *Planck* TT,TE,EE+lowP (blue contours).

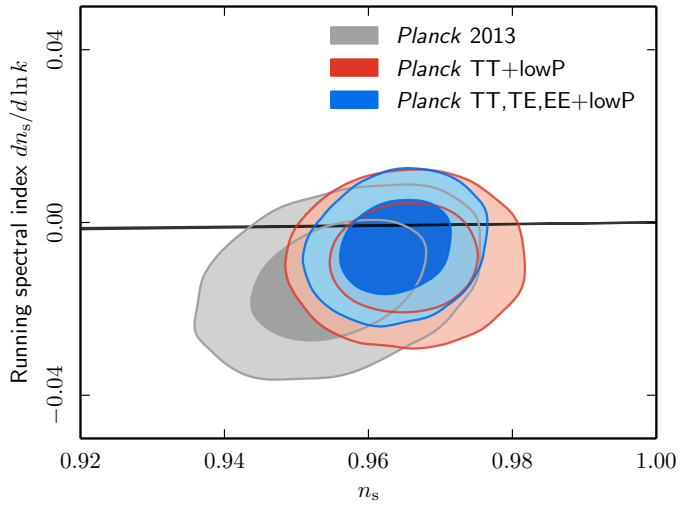

Fig. 4. Marginalized joint 68 % and 95 % CL for $(n_s, \mathrm{d}n_s/\mathrm{d}\ln k)$ using *Planck* TT+lowP and *Planck* TT,TE,EE+lowP. For comparison, the thin black stripe shows the prediction for single-field monomial chaotic inflationary models with $50 < N_* < 60$.

When the running of the running is allowed to float, the *Planck* TT+lowP (*Planck* TT,TE,EE+lowP) data give:

$$\begin{aligned} n_s &= 0.9569 \pm 0.0077 \;\; (0.9586 \pm 0.0056)\,, \\ dn_s/d\ln k &= 0.011^{+0.014}_{-0.013} \;\; (0.009 \pm 0.010)\,, \qquad (68\,\%\ \mathrm{CL}) \\ d^2n_s/d\ln k^2 &= 0.029^{+0.015}_{-0.016} \;\; (0.025 \pm 0.013)\,, \end{aligned} \tag{19}$$

at the pivot scale $k_* = 0.05\,\mathrm{Mpc}^{-1}$. Allowing for running of the running provides a better fit to the temperature spectrum at low multipoles, such that $\Delta\chi^2 \approx -4.8$ (-4.9) for TT+lowP (TT,TE,EE+lowP).

Note that the inclusion of small-scale data such as Lyα might further constrain the running of the spectral index and its derivative. The recent analysis of the BOSS one-dimensional Lyα flux power spectrum presented in Palanque-Delabrouille et al. (2014) and Rossi et al. (2014) was optimised for measuring the neutrino mass. It does not include constraints on the spectral index running, which would require new dedicated N-body simulations. Hence we do not include Lyα constraints here.

The fact that the data cannot accommodate a significant running, but are compatible with a larger running of the running, will also be discussed in the inflaton potential reconstructions of Sect. 7.

4.4. Suppression of power on the largest scales

Although not statistically significant, the trend for a negative running or positive running of the running observed in the last subsection was driven by the lack of power in the *Planck* temperature power spectrum at low multipoles, already mentioned in the *Planck* 2013 release. This deficit could potentially be explained by a primordial spectrum featuring a depletion of power *only* at large wavelengths. Here we investigate two examples of such models.

We first update the analysis (already presented in PCI13) of a power-law spectrum multiplied by an exponential cut-off:

$$\mathcal{P}_{\mathcal{R}}(k) = \mathcal{P}_0(k)\left\{1 - \exp\left[-\left(\frac{k}{k_c}\right)^{\lambda_c}\right]\right\}. \tag{20}$$

This simple parameterization is motivated by models with a short inflationary stage in which the onset of the slow-roll phase coincides with the time when the largest observable scales exited the Hubble radius during inflation. The curvature spectrum is then strongly suppressed on those scales. We apply top-hat priors on the parameter λ_c, controlling the steepness of the cut-off, and on the logarithm of the cut-off scale, k_c. We choose prior ranges $\lambda_c \in [0, 10]$ and $\ln(k_c/\mathrm{Mpc}^{-1}) \in [-12, -3]$. For *Planck* TT+lowP (*Planck* TT,TE,EE+lowP), the best-fit model has $\lambda_c = 0.50$ (0.53), $\ln(k_c/\mathrm{Mpc}^{-1}) = -7.98$ (-7.98), $n_s = 0.9647$ (0.9649), and improves the effective χ^2 by a modest amount, $\Delta\chi^2 \approx -3.4$ (-3.4).

As a second model, we consider a broken-power-law spectrum for curvature perturbations:

$$\mathcal{P}_{\mathcal{R}}(k) = \begin{cases} A_{\mathrm{low}}\left(\frac{k}{k_*}\right)^{n_s-1+\delta} & \text{if } k \le k_b, \\ A_s\left(\frac{k}{k_*}\right)^{n_s-1} & \text{if } k \ge k_b, \end{cases} \tag{21}$$

with $A_{\rm low} = A_{\rm s}(k_{\rm b}/k_*)^{-\delta}$ to ensure continuity at $k = k_{\rm b}$. Hence this model, like the previous one, has two parameters, and also suppresses power at large wavelengths when $\delta > 0$. We assume top-hat priors on $\delta \in [0, 2]$ and $\ln(k_{\rm b}/{\rm Mpc}^{-1}) \in [-12, -3]$, and standard uniform priors for $\ln(10^{10}A_{\rm s})$ and $n_{\rm s}$. The best fit to *Planck* TT+lowP (*Planck* TT,TE,EE+lowP) is found for $n_{\rm s} = 0.9658$ (0.9647), $\delta = 1.14$ (1.14), and $\ln(k_{\rm b}/{\rm Mpc}^{-1}) = -7.55$ (−7.57), with a very small χ^2 improvement of $\Delta\chi^2 \approx -1.9$ (−1.6).

We conclude that neither of these two models with two extra parameters is preferred over the base ΛCDM model. (See also the discussion of a step inflationary potential in Sect. 9.1.1.)

5. Constraints on tensor modes

In this section, we focus on the *Planck* 2015 constraints on tensor perturbations. Unless otherwise stated, we consider that the tensor spectral index satisfies the standard inflationary consistency condition to lowest order in slow-roll, $n_{\rm t} = -r/8$. We recall that r is defined at the pivot scale $k_* = 0.05\,{\rm Mpc}^{-1}$. However, for comparison with other studies, we also report our bounds in terms of the tensor-to-scalar ratio $r_{0.002}$ at $k_* = 0.002\,{\rm Mpc}^{-1}$.

5.1. Planck 2015 upper bound on r

The constraints on the tensor-to-scalar ratio infered from the *Planck* full mission data for the ΛCDM+r model are:

$$r_{0.002} < 0.10 \quad (95\,\%\ {\rm CL},\ \textit{Planck}\ {\rm TT+lowP})\,, \tag{22}$$
$$r_{0.002} < 0.11 \quad (95\,\%\ {\rm CL},\ \textit{Planck}\ {\rm TT+lowP+lensing})\,, \tag{23}$$
$$r_{0.002} < 0.11 \quad (95\,\%\ {\rm CL},\ \textit{Planck}\ {\rm TT+lowP+BAO})\,, \tag{24}$$
$$r_{0.002} < 0.10 \quad (95\,\%\ {\rm CL},\ \textit{Planck}\ {\rm TT,TE,EE+lowP})\,. \tag{25}$$

Table 4 also shows the bounds on $n_{\rm s}$ in each of these cases.

These results slightly improve over the constraint $r_{0.002} < 0.12$ (95 % CL) derived from the *Planck* 2013 temperature data in combination with WMAP large-scale polarization data (Planck Collaboration XVI, 2014; Planck Collaboration XXII, 2014). The constraint obtained by *Planck* temperature and polarization on large scales is tighter than *Planck* B-mode 95 % CL upper limit from the 100 and 143 GHz HFI channels, $r < 0.27$ (Planck Collaboration XI, 2015). The constraints on r reported in Table 4 can be translated into upper bounds on the energy scale of inflation at the time when the pivot scale exits the Hubble radius, using

$$V_* = \frac{3\pi^2 A_{\rm s}}{2}\, r\, M_{\rm pl}^4 = (1.88\times 10^{16}\ {\rm GeV})^4 \frac{r}{0.10}\,. \tag{26}$$

This gives an upper bound on the Hubble parameter during inflation of $H_*/M_{\rm pl} < 3.6\times 10^{-5}$ (95 % CL) for *Planck* TT+lowP.

These bounds are relaxed when allowing for a scale dependence of the scalar and tensor spectral indices. In that case, we assume that the tensor spectral index and its running are fixed by the standard inflationary consistency condition at second order in slow-roll. We obtain

$$r_{0.002} < 0.18 \quad (95\,\%\ {\rm CL},\ \textit{Planck}\ {\rm TT+lowP}), \tag{27}$$
$$\frac{dn_{\rm s}}{d\ln k} = -0.013^{+0.010}_{-0.009} \quad (68\,\%\ {\rm CL},\ \textit{Planck}\ {\rm TT+lowP}), \tag{28}$$

with $n_{\rm s} = 0.9667 \pm 0.0066$ (68 % CL). At the standard pivot scale, $k_* = 0.05\,{\rm Mpc}^{-1}$, the bound is stronger ($r < 0.17$ at 95 % CL), because k_* is closer to the scale at which $n_{\rm s}$ and r decorrelate. The constraint on $r_{0.002}$ in Eq. (27) is 21 % tighter compared with the *Planck* 2013 results. The mean value of the running in Eq. (28) is higher (lower in absolute value) than with *Planck* 2013 by 45 %. Figures 5 and 6 clearly illustrate this significant improvement with respect to the previous *Planck* data release. Table 4 shows how bounds on (r, $n_{\rm s}$, $dn_{\rm s}/d\ln k$) are affected by the lensing reconstruction, BAO, or high-ℓ polarization data. The tightest bounds are obtained in combination with polarization:

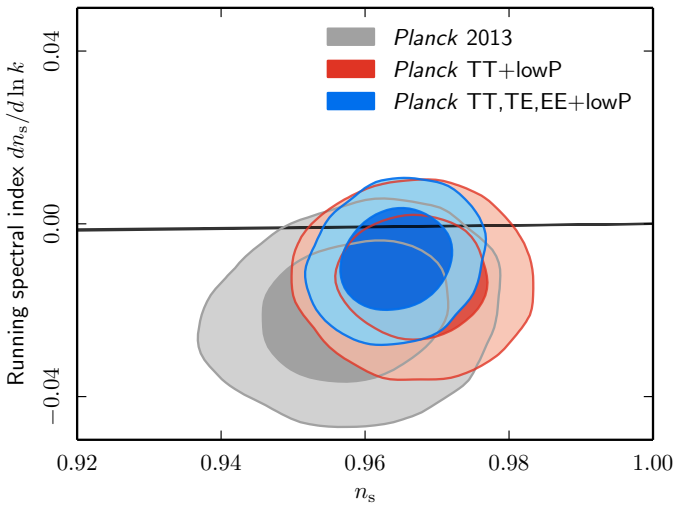

Fig. 5. Marginalized joint confidence contours for ($n_{\rm s}$, $dn_{\rm s}/d\ln k$), at the 68 % and 95 % CL, in the presence of a non-zero tensor contribution, and using *Planck* TT+lowP or *Planck* TT,TE,EE+lowP. Constraints from the *Planck* 2013 data release are also shown for comparison. The thin black stripe shows the prediction of single-field monomial inflation models with $50 < N_* < 60$.

$$r_{0.002} < 0.15 \quad (95\,\%\ {\rm CL},\ \textit{Planck}\ {\rm TT,TE,EE+lowP}), \tag{29}$$
$$\frac{dn_{\rm s}}{d\ln k} = -0.009 \pm 0.008 \quad (68\,\%\ {\rm CL},\ \textit{Planck}\ {\rm TT,TE,EE+lowP}), \tag{30}$$

with $n_{\rm s} = 0.9644 \pm 0.0049$ (68 % CL).

Neither the *Planck* full mission constraints in Eqs. (22)–(25), nor those including a running in Eqs. (27) and (29), are compatible with the interpretation of the BICEP2 B-mode polarization data in terms of primordial gravitational waves (BICEP2 Collaboration, 2014b). Instead, they are in excellent agreement with the results of the BICEP2/Keck Array-*Planck* cross-correlation analysis, as discussed in Sect. 13.

5.2. Dependence of the r constraints on the low-ℓ likelihood

The constraints on r discussed above are further tightened by adding WMAP polarization information on large angular scales. The *Planck* measurement of CMB polarization on large angular scales at 70 GHz is consistent with the WMAP 9-year one, based on the K, Q, and V bands (at 30, 40, and 60 GHz, respectively), once the *Planck* 353 GHz channel is used to remove the dust contamination, instead of the theoretical dust model used by the WMAP team (Page et al., 2007). (For a detailed dicussion, see Planck Collaboration XI (2015).) By combining *Planck* TT data with LFI 70 GHz and WMAP polarization data on large angular scales, we obtain a 35 % reduction of uncertainty, giving $\tau = 0.074 \pm 0.012$ (68 % CL) and $n_{\rm s} = 0.9660 \pm 0.060$ (68 % CL)

Model	Parameter	*Planck* TT+lowP	*Planck* TT+lowP+lensing	*Planck* TT+lowP+BAO	*Planck* TT,TE,EE+lowP
ΛCDM+r	n_s	0.9666 ± 0.0062	0.9688 ± 0.0061	0.9680 ± 0.0045	0.9652 ± 0.0047
	$r_{0.002}$	< 0.103	< 0.114	< 0.113	< 0.099
	$-2\Delta \ln \mathcal{L}_{max}$	0	0	0	0
ΛCDM+r +dn_s/d ln k	n_s	0.9667 ± 0.0066	0.9690 ± 0.0063	0.9673 ± 0.0043	0.9644 ± 0.0049
	$r_{0.002}$	< 0.180	< 0.186	< 0.176	< 0.152
	r	< 0.168	< 0.176	< 0.166	< 0.149
	$dn_s/d\ln k$	$-0.0126^{+0.0098}_{-0.0087}$	$-0.0076^{+0.0092}_{-0.0080}$	-0.0125 ± 0.0091	-0.0085 ± 0.0076
	$-2\Delta \ln \mathcal{L}_{max}$	-0.81	-0.08	-0.87	-0.38

Table 4. Constraints on the primordial perturbation parameters for ΛCDM+r and ΛCDM+r+dn_s/d ln k models from *Planck*. Constraints on the spectral index and its dependence on the wavelength are given at the pivot scale of $k_* = 0.05$ Mpc^{-1}.

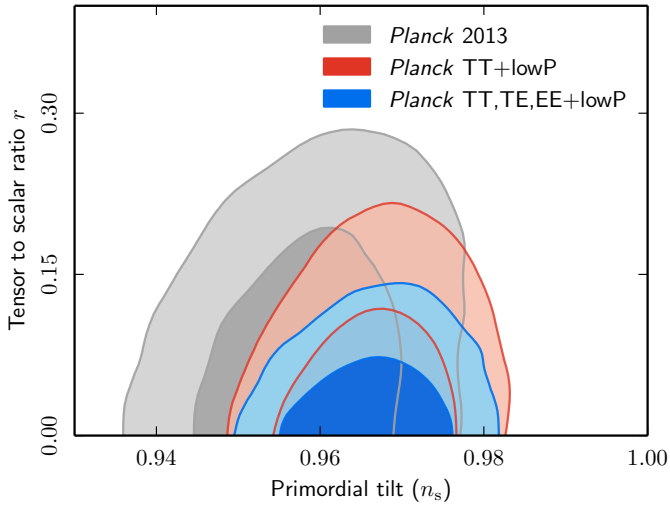

Fig. 6. Marginalized joint confidence contours for (n_s , r), at the 68 % and 95 % CL, in the presence of running of the spectral indices, and for the same data combinations as in the previous figure.

for the base ΛCDM model. When tensors are added, the bounds become

$$r_{0.002} < 0.09 \quad (95\,\%\ \text{CL, } \textit{Planck}\ \text{TT+lowP+WP}), \tag{31}$$
$$n_s = 0.9655 \pm 0.058 \quad (68\,\%\ \text{CL, } \textit{Planck}\ \text{TT+lowP+WP}), \tag{32}$$
$$\tau = 0.073^{+0.011}_{-0.013} \quad (68\,\%\ \text{CL, } \textit{Planck}\ \text{TT+lowP+WP}). \tag{33}$$

When tensors and running are both varied, we obtain $r_{0.002} < 0.14$ (95 % CL) and $dn_s/d\ln k = -0.010 \pm 0.008$ (68 % CL) for *Planck* TT+lowP+WP. These constraints are all tighter than those based on *Planck* TT+lowP only.

5.3. The tensor-to-scalar ratio and the low-ℓ deficit in temperature

As noted previously (Planck Collaboration XV, 2014; Planck Collaboration XVI, 2014; Planck Collaboration XXII, 2014), the low-ℓ temperature data display a slight lack of power compared to the expectation of the best-fit tensor-free base ΛCDM model. Since tensor fluctuations add power on small scales, the effect will be exacerbated in models allowing $r > 0$.

In order to quantify this tension, we compare the observed constraint on r to that inferred from simulated *Planck* data. In the simulations, we assume the underlying fiducial model to be tensor-free, with parameters close to the base ΛCDM best-fit values. We limit the simulations to mock temperature power spectra only and fit these spectra with an exact low-ℓ likelihood for $2 \leq \ell \leq 29$ (see Perotto et al. (2006)), and a high-ℓ Gaussian likelihood for $30 \leq \ell \leq 2508$ based on the frequency-combined, foreground-marginalized, unbinned *Planck* temperature power spectrum covariance matrix. Additionally, we impose a Gaussian prior of $\tau = 0.07 \pm 0.02$.

Based on 100 simulated data sets, we find an expectation value for the 95 % CL upper limit on the tensor-to-scalar ratio of $\bar{r}_{2\sigma} \approx 0.260$. The corresponding constraint from real data (using low-ℓ `Commander` temperature data, the frequency-combined, foreground-marginalized, unbinned *Planck* high-ℓ TT power spectrum, and the same prior on τ as above) reads $r < 0.123$, confirming that the actual constraint is tighter than what one would have expected. However, the actual constraint is not excessively unusual: out of the 100 simulations, 4 lead to an even tighter bound, corresponding to a significance of about $2\,\sigma$. Thus, under the hypothesis of the base ΛCDM cosmology, the upper limit on r that we get from the data is not implausible as a chance fluctuation of the low multipole power.

To illustrate the contribution of the low-ℓ temperature power deficit to the estimates of cosmological parameters, we show as an example in Fig. 7 how n_s shifts towards lower values when the $\ell < 30$ temperature information is discarded (we will refer to this case as "*Planck* TT−lowT"). The shift in n_s is approximately −0.005 (or −0.003 when the lowP likelihood is replaced by a Gaussian prior $\tau = 0.07 \pm 0.02$). Comparing with Sect. 4.4, we notice that these shifts are larger than when fitting a primordial spectrum suppressed on large scales to the data.

Figure 8 displays the posterior probability for r for various combinations of data sets, some of which exclude the $\ell < 30$ TT data. This leads to the very conservative bounds $r \lesssim 0.24$ and $r \lesssim 0.23$ at 95 % CL when combined with the lowP likelihood or with the Gaussian prior $\tau = 0.07 \pm 0.020$, respectively.

5.4. Relaxing assumptions on the late-time cosmological evolution

As in the *Planck* 2013 release (PCI13), we now ask how robust the *Planck* results on the tensor-to-scalar ratio are against assumptions on the late-time cosmological evolution. The results are summarized in Table 5, and some particular cases are illustrated in Fig. 9. Constraints on r turn out to be remarkably stable for one-parameter extensions of the ΛCDM+r model, with the only exception the ΛCDM+r+Ω_K case in the absence of the late-time information from *Planck* lensing or BAO data. The weak trend towards $\Omega_K < 0$, i.e. towards a positively curved (closed)

Extended model, ΛCDM+r+	Parameter	*Planck* TT+lowP +lensing	*Planck* TT+lowP +BAO	*Planck* TT,TE,EE +lowP
+general reionization	r	$r < 0.11$	$r < 0.10$	< 0.10
	n_s	0.975 ± 0.006	0.971 ± 0.005	0.968 ± 0.005
$+N_{\rm eff}$	r	< 0.14	< 0.12	< 0.11
	n_s	$0.977^{+0.016}_{-0.017}$	0.972 ± 0.009	0.964 ± 0.010
	$N_{\rm eff}$	$3.24^{+0.30}_{-0.35}$	3.19 ± 0.24	$3.02^{+0.20}_{-0.21}$
$+Y_{\rm He}$	r	< 0.14	< 0.12	< 0.12
	n_s	0.975 ± 0.007	0.973 ± 0.009	0.969 ± 0.008
	$Y_{\rm He}$	0.258 ± 0.022	0.257 ± 0.022	0.252 ± 0.014
$+m_\nu$	r	< 0.11	< 0.11	< 0.11
	n_s	0.963 ± 0.007	0.967 ± 0.005	0.962 ± 0.005
	m_ν	< 0.67	< 0.21	< 0.58
$+\Omega_K$	r	< 0.15	$r < 0.11$	< 0.15
	n_s	0.971 ± 0.007	0.971 ± 0.007	0.969 ± 0.005
	Ω_K	$-0.008^{+0.010}_{-0.008}$	-0.001 ± 0.003	$-0.045^{+0.016}_{-0.020}$
$+w$	r	< 0.14	< 0.11	< 0.12
	n_s	0.969 ± 0.006	0.967 ± 0.006	0.966 ± 0.005
	w	$-1.46^{+0.20}_{-0.40}$	$-1.02^{+0.08}_{-0.07}$	$-1.57^{+0.17}_{-0.37}$
$+\Omega_K+dn_s/d\ln k$	r	< 0.20	< 0.18	< 0.19
	n_s	0.971 ± 0.007	0.969 ± 0.007	0.969 ± 0.005
	$dn_s/d\ln k$	-0.006 ± 0.009	-0.013 ± 0.009	-0.004 ± 0.008
	Ω_K	$-0.006^{+0.010}_{-0.009}$	-0.001 ± 0.003	$-0.043^{+0.011}_{-0.020}$
$+N_{\rm eff}+m_{\rm eff}$	r	$r < 0.14$	$r < 0.13$	< 0.12
	n_s	$0.980^{+0.010}_{-0.014}$	$0.978^{+0.008}_{-0.011}$	$0.968^{+0.006}_{-0.008}$
	$m_{\rm eff}$	< 0.27	< 0.21	< 0.83
	$N_{\rm eff}$	< 3.45	< 3.73	< 3.47

Table 5. Constraints on extensions of the ΛCDM+r cosmological model for *Planck* TT+lowP+lensing, *Planck* TT+lowP+BAO, and *Planck* TT,TE,EE+lowP. For each model we quote 68 % CL, unless 95 % CL upper bounds are reported.

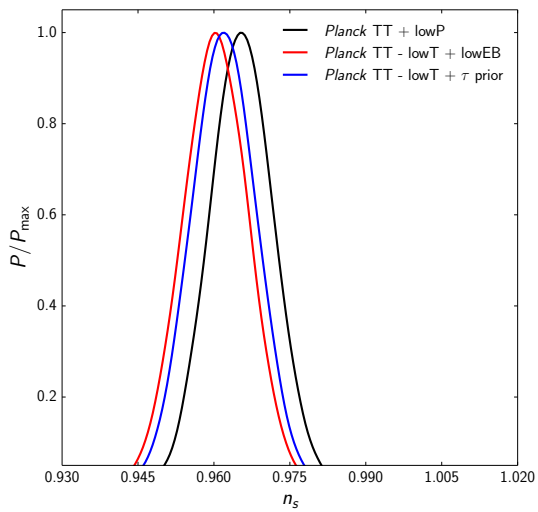

Fig. 7. One dimensional posterior probabilities for n_s for the base ΛCDM model obtained by excluding temperature multipoles for $\ell < 30$ ("TT−lowT"), while either keeping low-ℓ polarization data, or in addition replacing them with a Gaussian prior on τ.

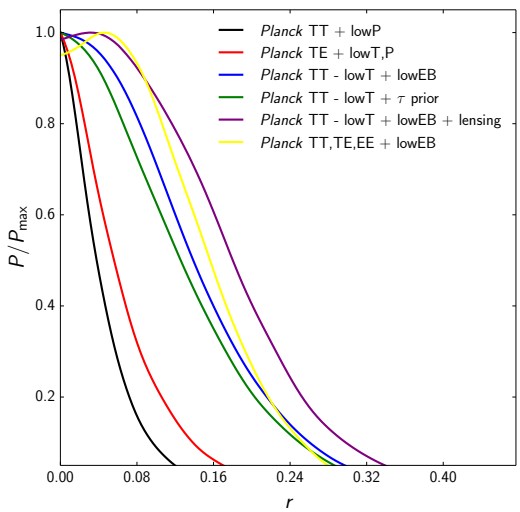

Fig. 8. One dimensional posterior probabilities for r for various data combinations, either including or not including temperature multipoles for $\ell < 30$, and compared with the baseline choice (*Planck* TT+lowP, black curve).

universe from the temperature and polarization data alone, and the well-known degeneracy between Ω_K and $H_0/\Omega_{\rm m}$ lead to a slight suppression of the Sachs-Wolfe plateau in the scalar temperature spectrum. This leaves more room for a tensor component.

This further degeneracy when r is added builds on the negative values for the curvature allowed by *Planck* TT+lowP, $\Omega_K = -0.052^{+0.049}_{-0.055}$ at 95 % CL (Planck Collaboration XIII, 2015). The exploitation of the information contained in the *Planck* lensing likelihood leads to a tighter constraint, $\Omega_K = -0.005^{+0.016}_{-0.017}$ at 95 % CL, which improves on the *Planck*

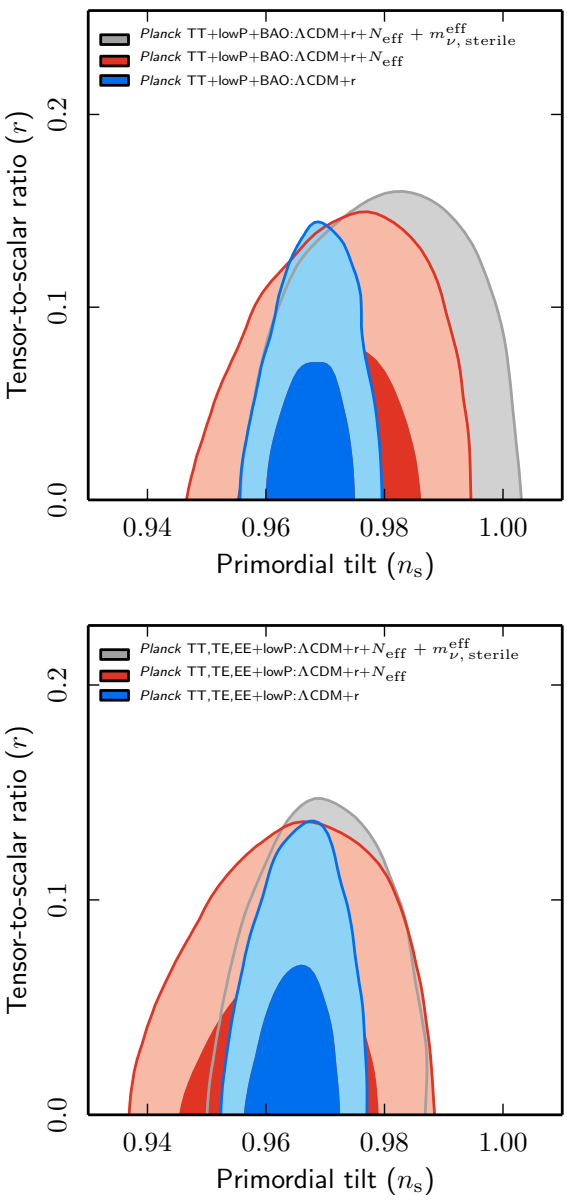

Fig. 9. Marginalized joint 68 % and 95 % CL for $(n_{\rm s}\,, r_{0.002})$ using *Planck* TT+lowP+BAO (upper panel) and *Planck* TT,TE,EE+lowP (lower panel).

2013 results ($\Omega_K = -0.007^{+0.018}_{-0.019}$ at 95 % CL). However, due to the remaining degeneracies left by the uncertainties in polarization on large angular scales, a full appreciation of the improvement due to the full mission temperature and lensing data can be obtained by using lowP+WP, which leads to $\Omega_K = -0.003^{+0.012}_{-0.014}$ at 95 % CL. Let us also finally note that negative values allowed for the curvature are decreased when the running is combined, showing that the low-ℓ temperature deficit could also contribute to the estimate of these parameters.

The trend found for ΛCDM+r+Ω_K is even clearer when spatial curvature and the running of the spectral index are varied at the same time. Then, the *Planck* temperature plus polarization data are compatible with r values as large as 0.19 (95 % CL), at the cost of an almost 4 σ deviation from spatial flatness (which, however, disappears as soon as lensing or BAO data are considered).

6. Implications for single-field slow-roll inflation

In this section we study the implications of *Planck* 2015 constraints on standard slow-roll single-field inflationary models.

6.1. Constraints on slow-roll parameters

We first present the *Planck* 2015 constraints on slow-roll parameters obtained through the analytic perturbative expansion in terms of the Hubble flow functions (HFFs) ϵ_i for the primordial spectra of cosmological fluctuations during slow-roll inflation (Stewart & Lyth, 1993; Gong & Stewart, 2001; Leach et al., 2002). When restricting to first order in ϵ_i, we obtain

$$\epsilon_1 < 0.0068 \qquad (95\,\%\ \text{CL, } \textit{Planck}\ \text{TT+lowP})\,, \tag{34}$$

$$\epsilon_2 = 0.029^{+0.008}_{-0.007} \qquad (68\,\%\ \text{CL, } \textit{Planck}\ \text{TT+lowP})\,. \tag{35}$$

When high-ℓ polarization is included we obtain $\epsilon_1 < 0.0066$ at 95 % CL and $\epsilon_2 = 0.030^{+0.007}_{-0.006}$ at 68 % CL. When second-order contributions in the HFFs are included, we obtain

$$\epsilon_1 < 0.012 \qquad (95\,\%\ \text{CL, } \textit{Planck}\ \text{TT+lowP})\,, \tag{36}$$

$$\epsilon_2 = 0.031^{+0.013}_{-0.011} \qquad (68\,\%\ \text{CL, } \textit{Planck}\ \text{TT+lowP})\,, \tag{37}$$

$$-0.41 < \epsilon_3 < 1.38 \qquad (95\,\%\ \text{CL, } \textit{Planck}\ \text{TT+lowP})\,. \tag{38}$$

When high-ℓ polarization is included we obtain $\epsilon_1 < 0.011$ at 95 % CL, $\epsilon_2 = 0.032^{+0.011}_{-0.009}$ at 68 % CL, and $-0.32 < \epsilon_3 < 0.89$ at 95 % CL.

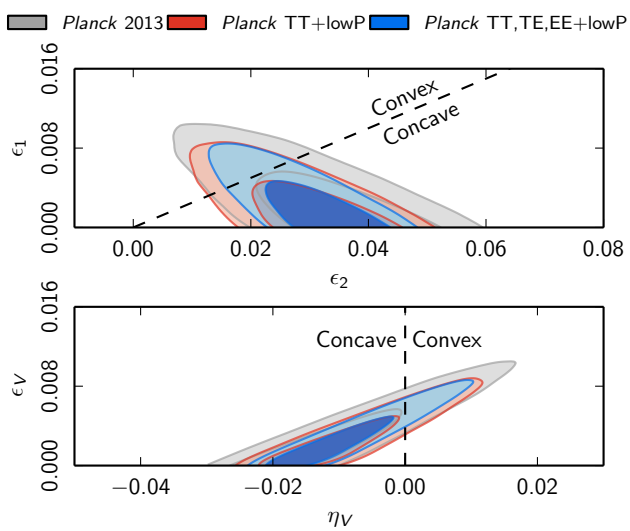

Fig. 10. Marginalized joint 68 % and 95 % CL regions for $(\epsilon_1\,, \epsilon_2)$ (top panel) and $(\epsilon_V\,, \eta_V)$ (bottom panel) for *Planck* TT+lowP (red contours), *Planck* TT,TE,EE+lowP (blue contours), and compared with the *Planck* 2013 results (grey contours).

The potential slow-roll parameters are obtained as derived parameters by using their exact expressions as function of ϵ_i (Leach et al., 2002; Finelli et al., 2010):

$$\epsilon_V = \frac{V_\phi^2 M_{\rm pl}^2}{2V^2} = \epsilon_1 \frac{\left(1 - \frac{\epsilon_1}{3} + \frac{\epsilon_2}{6}\right)^2}{\left(1 - \frac{\epsilon_1}{3}\right)^2}\,, \tag{39}$$

$$\eta_V = \frac{V_{\phi\phi} M_{\rm pl}^2}{V} = \frac{2\epsilon_1 - \frac{\epsilon_2}{2} - \frac{2\epsilon_1^2}{3} + \frac{5\epsilon_1\epsilon_2}{6} - \frac{\epsilon_2^2}{12} - \frac{\epsilon_2\epsilon_3}{6}}{1 - \frac{\epsilon_1}{3}}\,, \tag{40}$$

$$\xi_V^2 = \frac{V_{\phi\phi\phi}V_\phi M_{\rm pl}^4}{V^2} = \frac{1-\frac{\epsilon_1}{3}+\frac{\epsilon_2}{6}}{\left(1-\frac{\epsilon_1}{3}\right)^2}\left(4\epsilon_1^2 - 3\epsilon_1\epsilon_2 + \frac{\epsilon_2\epsilon_3}{2} - \epsilon_1\epsilon_2^2 + 3\epsilon_1^2\epsilon_2 - \frac{4}{3}\epsilon_1^3 - \frac{7}{6}\epsilon_1\epsilon_2\epsilon_3 + \frac{\epsilon_2^2\epsilon_3}{6} + \frac{\epsilon_2\epsilon_3^2}{6} + \frac{\epsilon_2\epsilon_3\epsilon_4}{6}\right), \quad (41)$$

where $V(\phi)$ is the inflaton potential, the subscript ϕ denotes the derivative with respect to ϕ, and $M_{\rm pl} = (8\pi G)^{-1/2}$ is the reduced Planck mass (see also Table 2).

By using Eqs. (39) and (40) with $\epsilon_3 = \epsilon_4 = 0$ and the primordial power spectra to lowest order in the HFFs, the derived constraints for the first two slow-roll potential parameters are:

$$\epsilon_V < 0.0068 \qquad (95\,\%\ \text{CL, } \textit{Planck}\ \text{TT+lowP}), \quad (42)$$
$$\eta_V = -0.010^{+0.005}_{-0.009} \qquad (68\,\%\ \text{CL, } \textit{Planck}\ \text{TT+lowP}). \quad (43)$$

When high-ℓ polarization is included we obtain $\epsilon_V < 0.0067$ at 95 % CL and $\eta_V = -0.010^{+0.004}_{-0.009}$ at 68 % CL. By using Eqs. (39), (40), and (41) with $\epsilon_4 = 0$ and the primordial power spectra to second order in the HFFs, the derived constraints for the slow-roll potential parameters are:

$$\epsilon_V < 0.012 \qquad (95\,\%\ \text{CL, } \textit{Planck}\ \text{TT+lowP}), \quad (44)$$
$$\eta_V = -0.0080^{+0.0088}_{-0.0146} \qquad (68\,\%\ \text{CL, } \textit{Planck}\ \text{TT+lowP}), \quad (45)$$
$$\xi_V = 0.0070^{+0.0045}_{-0.0069} \qquad (68\,\%\ \text{CL, } \textit{Planck}\ \text{TT+lowP}). \quad (46)$$

When high-ℓ polarization is included we obtain $\epsilon_V < 0.011$ at 95 % CL, and $\eta_V = -0.0092^{+0.0074}_{-0.0127}$ and $\xi_V^2 = 0.0044^{+0.0037}_{-0.0050}$, both at 68 % CL.

In Figs. 10 and 11 we show the 68 % CL and 95 % CL of the HFFs and the derived potential slow-roll parameters with and without the inclusion of high-ℓ polarization, comparing with the *Planck* 2013 results.

6.2. Implications for selected inflationary models

The predictions to lowest order in the slow-roll approximation for (n_s, r) of a few inflationary models with a representative uncertainty for the entropy generation stage ($50 < N_* < 60$) are shown in Fig. 12.

In the following we discuss the implications of *Planck* TT+lowP+BAO data for selected slow-roll inflationary models by taking into account the uncertainties in the entropy generation stage. We model these uncertainties by two parameters, as in PCI13: the energy scale $\rho_{\rm th}$ by which the Universe has thermalized, and the parameter $w_{\rm int}$ which characterizes the effective equation of state between the end of inflation and the energy scale specified by $\rho_{\rm th}$. For each inflationary model we provide in Table 6 and in the main text the $\Delta\chi^2$ value with respect to the base ΛCDM model and the Bayesian evidence with respect to the R^2 inflationary model (Starobinsky, 1980), computed by `CosmoMC` connected to `CAMB` using `MultiNest` as the sampler. We use the primordial power spectra of cosmological fluctuations generated during slow-roll inflation parameterized by the HFFs, ϵ_i, to second order, which can be expressed in terms of the number of e-folds to the end of inflation, N_*, and the parameters of the considered inflationary model, using modified routines of the public code `ASPIC`[6] (Martin et al., 2014). For the number of e-folds to the end of inflation (Liddle & Leach, 2003; Martin & Ringeval, 2010) we use the expression (PCI13)

$$N_* \approx 67 - \ln\left(\frac{k_*}{a_0H_0}\right) + \frac{1}{4}\ln\left(\frac{V_*^2}{M_{\rm pl}^4\rho_{\rm end}}\right) + \frac{1-3w_{\rm int}}{12(1+w_{\rm int})}\ln\left(\frac{\rho_{\rm th}}{\rho_{\rm end}}\right) - \frac{1}{12}\ln(g_{\rm th}), \quad (47)$$

where $\rho_{\rm end}$ is the energy density at the end of inflation, a_0H_0 is the present Hubble scale, V_* is the potential energy when k_* left the Hubble radius during inflation, and $g_{\rm th}$ is the number of effective bosonic degrees of freedom at the energy scale $\rho_{\rm th}$. We consider the pivot scale $k_* = 0.002\,{\rm Mpc}^{-1}$, $g_{\rm th} = 10^3$, $\epsilon_{\rm end} = 1$, and a logarithmic prior on $\rho_{\rm th}$ (in the interval $[(10^3\ {\rm GeV})^4, \rho_{\rm end}]$). We have validated the slow-roll approach by cross-checking the Bayes factor computations against the fully numerical inflationary mode equation solver `ModeCode` coupled to the `PolyChord` sampler.

Power-law potentials

We first investigate the class of inflationary models with a single monomial potential (Linde, 1983):

$$V(\phi) = \lambda M_{\rm pl}^4\left(\frac{\phi}{M_{\rm pl}}\right)^n, \quad (48)$$

in which inflation occurs for large values of the inflaton $\phi > M_{\rm pl}$. The predictions for the scalar spectral index and the tensor-to-scalar ratio at first order in the slow-roll approximation are $n_s - 1 \approx -2(n+2)/(4N_* + n)$ and $r \approx 16n/(4N_* + n)$, respectively. By assuming a dust equation of state (i.e., $w_{\rm int} = 0$) prior to thermalization, the cubic and quartic potentials are strongly disfavoured by $\ln B = -11.6$ and $\ln B = -23.3$, respectively. The quadratic potential is moderately disfavoured by $\ln B = -4.7$. Other values, such as $n = 4/3$, 1, and 2/3, motivated by axion monodromy (Silverstein & Westphal, 2008; McAllister et al., 2010), are compatible with *Planck* data with $w_{\rm int} = 0$.

Small modifications occur when considering the effective equation of state parameter, $w_{\rm int} = (n-2)/(n+2)$, defined by averaging over the coherent oscillation regime which follows inflation (Turner, 1983). The Bayes factors are slightly modified when $w_{\rm int}$ is allowed to float, as can be seen from Table 6.

Hilltop models

In hilltop models (Boubekeur & Lyth, 2005), with potential

$$V(\phi) \approx \Lambda^4\left(1 - \frac{\phi^p}{\mu^p} + \ldots\right), \quad (49)$$

the inflaton rolls away from an unstable equilibrium. The predictions to first order in the slow-roll approximation are $r \approx 8p^2(M_{\rm pl}/\mu)^2x^{2p-2}/(1-x^p)^2$ and $n_s - 1 \approx -2p(p-1)(M_{\rm pl}/\mu)^2x^{p-2}/(1-x^p) - 3r/8$, where $x = \phi_*/\mu$. As in PCI13, the ellipsis in Eq. (49) and in what follows indicates higher-order terms that are negligible during inflation but ensure positiveness of the potential.

By sampling $\log_{10}(\mu/M_{\rm pl})$ within the prior $[0.30, 4.85]$ for $p = 2$, we obtain $\log_{10}(\mu/M_{\rm pl}) > 1.02$ (1.05) at 95 % CL and $\ln B = -2.6$ (−2.4) for $w_{\rm int} = 0$ (allowing $w_{\rm int}$ to float).

An exact potential which could also apply after inflation, instead of the approximated one in Eq. (49), might be needed for a better comparison among different models. Hilltop models in Eq. (49) approximate a linear potential $V(\phi) \propto \phi$ for

[6] http://cp3.irmp.ucl.ac.be/~ringeval/aspic.html

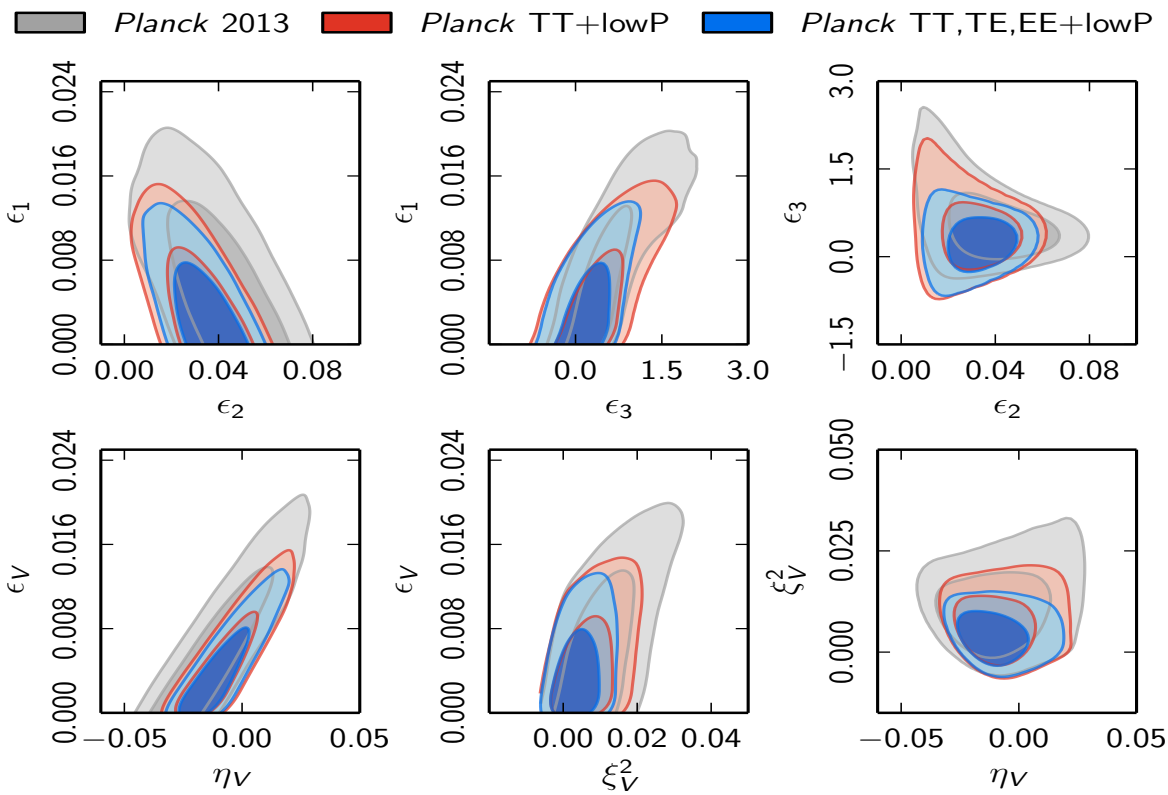

Fig. 11. Marginalized joint 68 % and 95 % CL regions for $(\epsilon_1, \epsilon_2, \epsilon_3)$ (top panels) and $(\epsilon_V, \eta_V, \xi_V^2)$ (bottom panels) for *Planck* TT+lowP (red contours), *Planck* TT,TE,EE+lowP (blue contours), and compared with the *Planck* 2013 results (grey contours).

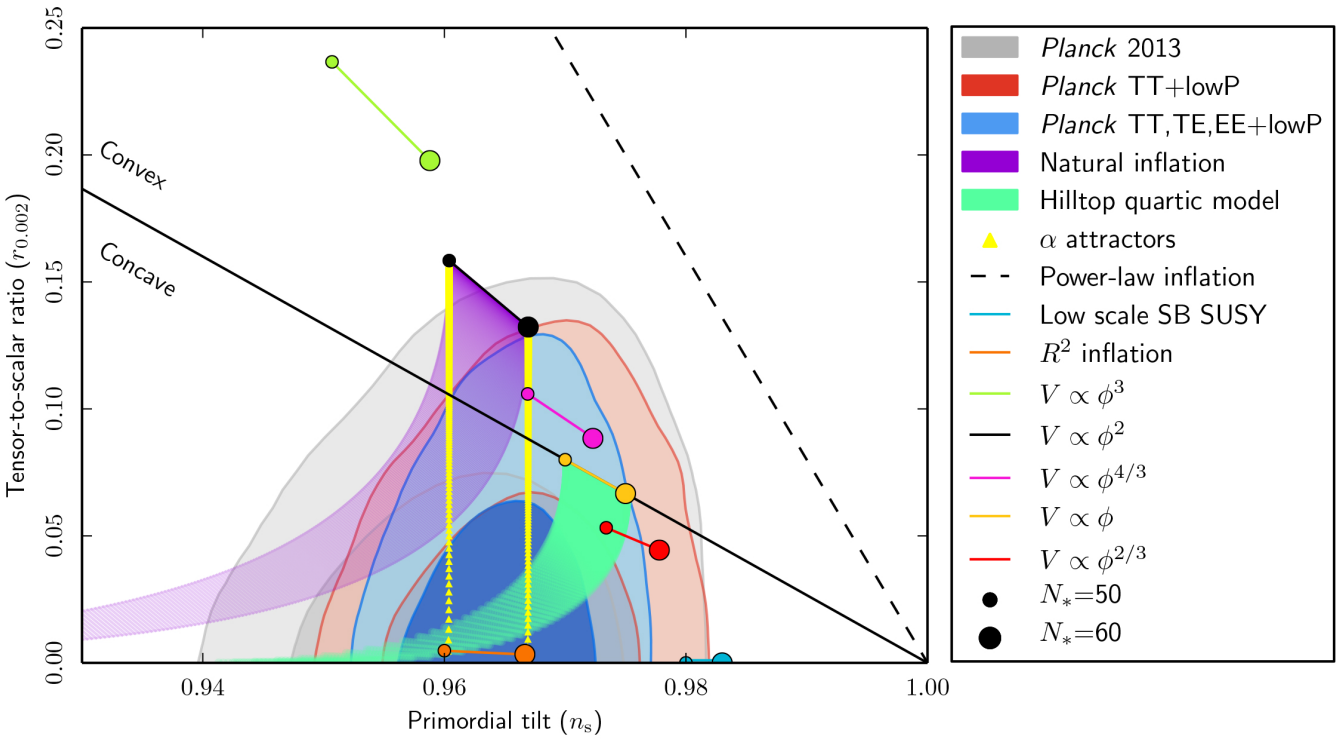

Fig. 12. Marginalized joint 68 % and 95 % CL regions for n_s and $r_{0.002}$ from *Planck* in combination with other data sets, compared to the theoretical predictions of selected inflationary models.

$\mu/M_{\rm pl} \gg 1$. By considering a double-well potential, $V(\phi) = \Lambda^4[1-\phi^2/(2\mu^2)]^2$, instead, we obtain a slightly worse Bayes factor than the hilltop $p = 2$ model, $\ln B = -3.1$ (-2.3) for $w_{\rm int} = 0$ ($w_{\rm int}$ allowed to vary). This different result can be easily understood. Although the double-well potential is equal to the hilltop model for $\phi \ll \mu$, it approximates $V(\phi) \propto \phi^2$ for $\mu/M_{\rm pl} \gg 1$. Since a linear potential is a better fit to *Planck* than ϕ^2, the fit of the double-well potential is therefore worse than the hilltop $p = 2$ case for $\mu/M_{\rm pl} \gg 1$, and this partially explains the slightly different Bayes factors obtained.

In the $p = 4$ case, we obtain $\log_{10}(\mu/M_{\rm pl}) > 1.05$ (1.02) at 95 % CL and $\ln B = -2.8$ (-2.6) for $w_{\rm int} = 0$ (allowing $w_{\rm int}$ to float), assuming a prior range $[-2, 2]$ for $\log_{10}(\mu/M_{\rm pl})$.

Natural inflation

In *natural* inflation (Freese et al., 1990; Adams et al., 1993) a non-perturbative shift symmetry is invoked to suppress radiative corrections, leading to the periodic potential

$$V(\phi) = \Lambda^4 \left[1 + \cos\left(\frac{\phi}{f}\right)\right], \tag{50}$$

where f is the scale which determines the curvature of the potential. We sample $\log_{10}(f/M_{\rm pl})$ within the prior $[0.3, 2.5]$ as in PCI13. We obtain $\log_{10}(f/M_{\rm pl}) > 0.84$ (> 0.83) at 95 % CL and $\ln B = -2.4$ (-2.3) for $w_{\rm int} = 0$ (allowing $w_{\rm int}$ to vary).

Note that the super-Planckian value for f required by observations is not necessarily a problem for this class of models. When several fields ϕ_i with a cosine potential as in Eq. (50) and scales f_i appear in the Lagrangian, an effective single field inflationary trajectory can be found for a suitable choice of parameters (Kim et al., 2005). In such a setting, the super-Planckian value of the effective scale f required by observations can be obtained even if the original scales statisfy $f_i \ll M_{\rm pl}$ (Kim et al., 2005).

D-brane inflation

Inflation can be caused by physics in extra dimensions. If the standard model of particle physics is confined to our 3-dimensional brane, the distance between our brane and anti-brane can drive inflation. We consider the following parameterization for the effective potential driving inflation:

$$V(\phi) = \Lambda^4 \left(1 - \frac{\mu^p}{\phi^p} + ...\right). \tag{51}$$

We sample $\log_{10}(\mu/M_{\rm pl})$ within the prior $[-6, 0.3]$. We consider $p = 4$ (Kachru et al., 2003; Dvali et al., 2001) and $p = 2$ (Garcia-Bellido et al., 2002). The predictions for r and $n_{\rm s}$ can be obtained from the hilltop case with the substitution $p \to -p$. These models agree with the *Planck* data with a Bayes factor of $\ln B = -0.4$ (-0.6) and $\ln B = -0.7$ (-0.9) for $p = 4$ and $p = 2$, respectively, for $w_{\rm int} = 0$ (allowing $w_{\rm int}$ to vary).

Exponential potentials

Exponential potentials are ubiquitous in inflationary models motivated by supergravity and string theory (Goncharov & Linde, 1984; Stewart, 1995; Dvali & Tye, 1999; Burgess et al., 2002; Cicoli et al., 2009). We restrict ourselves to the analysis of the following class of potentials:

$$V(\phi) = \Lambda^4 \left(1 - e^{-q\phi/M_{\rm pl}} + ...\right). \tag{52}$$

As for the hilltop models described earlier, the ellipsis indicates possible higher-order terms that are negligible during inflation but ensure positiveness of the potential. These models predict $r \approx 8q^2 e^{-2q\phi/M_{\rm pl}}/(1 - e^{-q\phi/M_{\rm pl}})^2$ and $n_s - 1 \approx -q^2 e^{-q\phi/M_{\rm pl}}(2 + e^{-q\phi/M_{\rm pl}})/(1 - e^{-q\phi/M_{\rm pl}})^2$ in a slow-roll trajectory characterized by $N \approx f(\phi/M_{\rm pl}) - f(\phi_{\rm end}/M_{\rm pl})$, with $f(x) = (e^{qx} - qx)/q^2$. By sampling $\log_{10}(q/M_{\rm pl})$ within the prior $[-3, 3]$, we obtain a Bayes factor of -0.6 for $w_{\rm int} = 0$ $(-0.9$ when $w_{\rm int}$ is allowed to vary).

Spontaneously broken SUSY

Hybrid models (Copeland et al., 1994; Linde, 1994) predicting $n_{\rm s} > 1$ are strongly disfavoured by the *Planck* data, as for the first cosmological release (PCI13). An example of a hybrid model predicting $n_{\rm s} < 1$ is the case in which slow-roll inflation is driven by loop corrections in spontaneously broken supersymmetric (SUSY) grand unified theories (Dvali et al., 1994) described by the potential

$$V(\phi) = \Lambda^4 \left[1 + \alpha_h \log(\phi/M_{\rm pl})\right], \tag{53}$$

where $\alpha_h > 0$ is a dimensionless parameter. Note that for $\alpha_h \ll 1$, this model leads to the same predictions as the power-law potential for $p \ll 1$ to lowest order in the slow-roll approximation. By sampling $\log_{10}(\alpha_h)$ on a flat prior $[-2.5, 1]$, we obtain a Bayes factor of -2.2 for $w_{\rm int} = 0$ $(-1.7$ when $w_{\rm int}$ is allowed to vary).

R^2 inflation

The first inflationary model proposed (Starobinsky, 1980), with action

$$S = \int {\rm d}^4x \sqrt{-g}\frac{M_{\rm pl}^2}{2}\left(R + \frac{R^2}{6M^2}\right), \tag{54}$$

is still within the *Planck* 68 % CL constraints, as it was for the *Planck* 2013 release (PCI13). This model corresponds to the potential

$$V(\phi) = \Lambda^4 \left(1 - e^{-\sqrt{2/3}\phi/M_{\rm pl}}\right)^2 \tag{55}$$

in the Einstein frame, which leads to the slow-roll predictions $n_{\rm s} - 1 \approx -2/N$ and $r \approx 12/N^2$ (Starobinsky, 1980; Mukhanov & Chibisov, 1981).

After the *Planck* 2013 release, several theoretical developments supported the model in Eq. (54) beyond the original motivation of including quantum effects at one-loop (Starobinsky, 1980). No-scale supergravity (Ellis et al., 2013a), the large field regime of superconformal D-term inflation (Buchmüller et al., 2013), or recent developments in minimal supergravity (Farakos et al., 2013; Ferrara et al., 2013b) can lead to a generalization of the potential in Eq. (55) (see Ketov & Starobinsky (2011) for a previous embedding of R^2 inflation in $F(\mathcal{R})$ supergravity). The potential in Eq. (55) can also be generated by spontaneous breaking of conformal symmetry (Kallosh & Linde, 2013). This inflationary model has $\Delta\chi^2 \approx 0.8$ (0.3) larger than the base ΛCDM model with no tensors for $w_{\rm int} = 0$ (for $w_{\rm int}$ allowed to vary). We obtain $54 < N_* < 62$ $(53 < N_* < 64)$ at 95 % CL for $w_{\rm int} = 0$ (for $w_{\rm int}$ allowed to vary), compatible with the theoretical prediction, $N_* = 54$ (Starobinsky, 1980; Vilenkin, 1985; Gorbunov & Panin, 2011).

α attractors

We now study two classes of inflationary models motivated by recent developments in conformal symmetry and supergravity (Kallosh et al., 2013). The first class has been motivated by considering a vector rather than a chiral multiplet for the inflaton in supergravity (Ferrara et al., 2013a) and corresponds to the potential (Kallosh et al., 2013)

$$V(\phi) = \Lambda^4 \left(1 - e^{-\sqrt{2}\phi/(\sqrt{3\alpha}M_{\rm pl})}\right)^2 . \quad (56)$$

To lowest order in the slow-roll approximation, these models predict $r \approx 64/[3\alpha(1 - e^{\sqrt{2}\phi/(\sqrt{3\alpha}M_{\rm pl})})^2]$ and $n_s - 1 \approx -8(1 + e^{\sqrt{2}\phi/(\sqrt{3\alpha}M_{\rm pl})})/[3\alpha(1 - e^{\sqrt{2}\phi/(\sqrt{3\alpha}M_{\rm pl})})^2]$ on an inflationary trajectory characterized by $N \approx g(\phi/M_{\rm pl}) - g(\phi_{\rm end}/M_{\rm pl})$ with $g(x) = (3\alpha^4 e^{\sqrt{2}x/(\sqrt{3\alpha})} - \sqrt{6\alpha}x)/4$. The relation between N and ϕ can be inverted through the use of the Lambert functions, as done for other potentials (Martin et al., 2014). By sampling $\log_{10}(\alpha^2)$ on a flat prior $[0, 4]$, we obtain $\log_{10}(\alpha^2) < 1.7$ (2.0) at 95 % CL and a Bayes factor of -1.8 (-2) for $w_{\rm int} = 0$ (for $w_{\rm int}$ allowed to vary).

The second class of models has been called super-conformal α attractors (Kallosh et al., 2013) and can be seen as originating from a different generating function with respect to the first class. This second class is described by the following potential (Kallosh et al., 2013):

$$V(\phi) = \Lambda^4 \tanh^{2m}\left(\frac{\phi}{\sqrt{6\alpha}M_{\rm pl}}\right) . \quad (57)$$

This is the simplest class of models with spontaneous breaking of conformal symmetry, and for $\alpha = m = 1$ reduces to the original model introduced by Kallosh & Linde (2013). The potential in Eq. (57) leads to the following slow-roll predictions (Kallosh et al., 2013):

$$r \approx \frac{48\alpha m}{4mN^2 + 2Ng(\alpha, m) + 3\alpha m} , \quad (58)$$

$$n_s - 1 \approx \frac{-8mN - 6\alpha m + 2Ng(\alpha, m)}{4mN^2 + 2Ng(\alpha, m) + 3\alpha m} , \quad (59)$$

where $g(\alpha, m) = \sqrt{3\alpha(4m^2 + 3\alpha)}$. The predictions of this second class of models interpolate between those of a large-field chaotic model, $V(\phi) \propto \phi^{2m}$, for $\alpha \gg 1$ and the R^2 model for $\alpha \ll 1$.

For α we adopt the same priors as the previous class in Eq. (56). By fixing $m = 1$, we obtain $\log_{10}(\alpha^2) < 2.3$ (2.5) at 95 % CL and a Bayes factor of -2.3 (-2.2) for $w_{\rm int} = 0$ (when $w_{\rm int}$ is allowed to vary). When m is allowed to vary as well with a flat prior in the range $[0, 2]$, we obtain $0.02 < m < 1$ ($m < 1$) at 95 % CL for $w_{\rm int} = 0$ (when $w_{\rm int}$ is allowed to vary).

Non-minimally coupled inflaton

Inflationary predictions are quite sensitive to a non-minimal coupling, $\xi R\phi^2$, of the inflaton to the Ricci scalar. One of the most interesting effects due to $\xi \neq 0$ is to reconcile the quartic potential $V(\phi) = \lambda\phi^4/4$ with *Planck* observations, even for $\xi \ll 1$.

The Higgs inflation model (Bezrukov & Shaposhnikov, 2008), in which inflation occurs with $V(\phi) = \lambda(\phi^2 - \phi_0^2)^2/4$ and $\xi \gg 1$ for $\phi \gg \phi_0$, leads to the same predictions as the R^2 model to lowest order in the slow-roll approximation at tree level (see Barvinsky et al. (2008) and Bezrukov & Shaposhnikov (2009) for the inclusion of loop corrections). It is therefore in agreement with the *Planck* constraints, as for the first cosmological data release (PCI13).

Table 6. Results of the inflationary model comparison. We provide $\Delta\chi^2$ with respect to base ΛCDM and Bayes factors with respect to R^2 inflation.

Inflationary model	$\Delta\chi^2$		$\ln B_{0X}$	
	$w_{\rm int} = 0$	$w_{\rm int} \neq 0$	$w_{\rm int} = 0$	$w_{\rm int} \neq 0$
$R + R^2/(6M^2)$	+0.8	+0.3	...	+0.7
$n = 2/3$	+6.5	+3.5	−2.4	−2.3
$n = 1$	+6.2	+5.5	−2.1	−1.9
$n = 4/3$	+6.4	+5.5	−2.6	−2.4
$n = 2$	+8.6	+8.1	−4.7	−4.6
$n = 3$	+22.8	+21.7	−11.6	−11.4
$n = 4$	+43.3	+41.7	−23.3	−22.7
Natural	+7.2	+6.5	−2.4	−2.3
Hilltop ($p = 2$)	+4.4	+3.9	−2.6	−2.4
Hilltop ($p = 4$)	+3.7	+3.3	−2.8	−2.6
Double well	+5.5	+5.3	−3.1	−2.3
Brane inflation ($p = 2$)	+3.0	+2.3	−0.7	−0.9
Brane inflation ($p = 4$)	+2.8	+2.3	−0.4	−0.6
Exponential inflation	+0.8	+0.3	−0.7	−0.9
SB SUSY	+0.7	+0.4	−2.2	−1.7
Supersymmetric α-model	+0.7	+0.1	−1.8	−2.0
Superconformal ($m = 1$)	+0.9	+0.8	−2.3	−2.2
Superconformal ($m \neq 1$)	+0.7	+0.5	−2.4	−2.6

Let us summarize our findings for *Planck* lowP+BAO:

- Monomial potentials with integer $n > 2$ are strongly disfavoured with respect to R^2.
- The Bayes factor prefers R^2 over chaotic inflation with monomial quadratic potential by odds of 110:1 under the assumption of a dust equation of state during the entropy generation stage.
- R^2 inflation has the strongest evidence among the models considered here. However, care must be taken not to overinterpret small differences in likelihood lacking statistical significance.
- The models closest to R^2 in terms of evidence are brane inflation and exponential inflation, which have one more parameter than R^2. Both brane inflation considered in Eq. (51) and exponential inflation in Eq. (52) approximate the linear potential for a large portion of parameter space (for $\mu/M_{\rm pl} \gg 1$ and $q \gg 1$, respectively). For this reason these models have a higher evidence (although not at a statistically significant level) compared to those approximate a quadratic potential, as do α-attractors, for instance.
- In the models considered here, the $\Delta\chi^2$ obtained by allowing w to vary is modest, i.e., less than approximately 1.6 (with respect to $w_{\rm int} = 0$). The gain in the logarithm of the Bayesian evidence is even smaller, since an extra parameter is added.

7. Reconstruction of the potential and analysis beyond slow-roll approximation

In the previous section, we derived constraints on several types of inflationary potentials, assumed to account for the inflaton dynamics between the time at which the largest observable scales

crossed the Hubble radius during inflation and the end of inflation. The full shape of the potential was used in order to identify when inflation ends, and thus the field value ϕ_* when the pivot scale crosses the Hubble radius.

In section 6 of PCI13, we explored another approach, consisting of reconstructing the inflationary potential within its observable range without making any assumptions concerning the inflationary dynamics outside that range. Indeed, given that the number of e-folds between the observable range and the end of inflation can always be adjusted to take a realistic value, any potential shape giving a primordial spectrum of scalar and tensor perturbations in agreement with observations is a valid candidate. Inflation can end abruptly by a phase transition, or can last a long time if the potential becomes very flat after the observable region has been crossed. Moreover, there could be a short inflationary stage responsible for the origin of observable cosmological perturbations, and another inflationary stage later on (but before nucleosynthesis), thus contributing to the total N_*.

In section 6 of PCI13, we performed this analysis with a full integration of the inflaton and metric perturbation modes, so that no slow-roll approximation was made. The only assumption was that primordial scalar perturbations are generated by the fluctuations of a single inflaton field with a canonical kinetic term. Since, in this approach, one is only interested in the potential over a narrow range of observable scales (centered around the field value ϕ_* when the pivot scale crosses the Hubble radius), it is reasonable to test relatively simple potential shapes, described by a small number of free parameters.

This approach gave very similar results to calculations based on the standard slow-roll analysis. This agreement can be explained by the fact that the *Planck* 2013 data already preferred a primordial spectrum very close to a power law, at least over most of the observable range. Hence the 2013 data excluded strong deviations from slow-roll inflation, which would either produce a large running of the spectral index or imprint more complicated features on the primordial spectrum. However, this conclusion did not apply to the largest scales observable by *Planck*, for which cosmic variance and slightly anomalous data points remained compatible with significant deviations from a simple power-law spectrum. The most striking result in section 6 of PCI13 was the fact that, when giving enough freedom to the functional form of the inflation potential, the results were compatible with a rather steep potential at the beginning of the observable window, leading to "not-so-slow" roll during the first few observable e-folds. This explains the shape of the potential in figure 14 of PCI13 for a Taylor expansion at order $n = 4$ and in the region where $\phi - \phi_* \leq -0.2$. However, such features were only partially explored because the method used for potential reconstruction did not allow for an arbitrary value of the inflation velocity $\dot{\phi}$ at the beginning of the observable window. Instead, our code imposed that the inflaton already tracked the inflationary attractor solution when the largest observable modes crossed the Hubble scale.

Given that the *Planck* 2015 data establish even stronger constraints on the primordial power spectrum than the 2013 results, it is interesting to revisit the reconstruction of the potential $V(\phi)$. Section 7.1 presents some new results following the same approach as in PCI13 (explained previously in Lesgourgues & Valkenburg (2007) and Mortonson et al. (2011)). But in the present work, we also present some more general results, independent of any assumption concerning the initial field velocity $\dot{\phi}$ when the inflaton enters the observable window. Following previous studies (Kinney, 2002; Kinney et al., 2006; Peiris & Easther, 2006a; Easther & Peiris, 2006; Peiris & Easther, 2006b, 2008; Lesgourgues et al., 2008; Powell & Kinney, 2007; Hamann et al., 2008; Norena et al., 2012), we reconstruct the Hubble function $H(\phi)$, which determines both the potential, $V(\phi)$, through

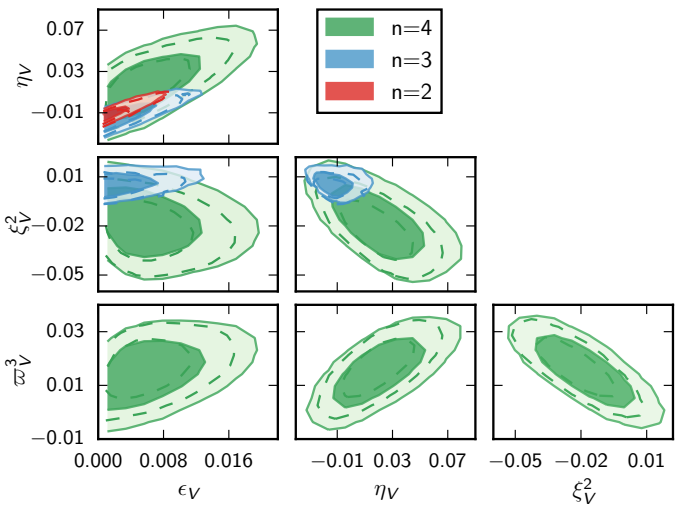

Fig. 13. Posterior distributions for the first four potential slow-roll parameters when the potential is Taylor-expanded to nth order, using *Planck* TT+lowP+BAO (filled contours) or TT,TE,EE+lowP (dashed contours). The primordial spectra are computed *beyond* any slow-roll approximation.

$$V(\phi) = 3M_{\rm Pl}^2\, H^2(\phi) - 2M_{\rm Pl}^4\, [H'(\phi)]^2 \ , \tag{60}$$

and the solution $\phi(t)$, through

$$\dot{\phi} = -2M_{\rm Pl}^2 H'(\phi) \ , \tag{61}$$

with $H'(\phi) = \partial H/\partial\phi$. Note that these two relations are exact. In Sect. 7.2, we fit $H(\phi)$ directly to the data, implicitly including all canonical single-field models in which the inflaton is rolling not very slowly (ϵ not much smaller than one) just before entering the observable window, and the issue of having to start sufficiently early in order to allow the initial transient to decay is avoided. The only drawback in reconstructing $H(\phi)$ is that one cannot systematically test the most simple analytic forms for $V(\phi)$ in the observable range (for instance, polynomials of order $n = 1, 3, 5, \ldots$ in $(\phi - \phi_*)$). But our goal in this section is to check how much one can deviate from slow-roll inflation in general, independently of the shape of the underlying inflation potential.

7.1. Reconstruction of a smooth inflation potential

Following exactly the approach of PCI13, we Taylor-expand the inflaton potential around $\phi = \phi_*$ to order $n = 2, 3, 4$. To obtain faster converging Markov chains, instead of imposing flat priors on the Taylor coefficients $\{V, V_\phi, \ldots, V_{\phi\phi\phi\phi}\}$, we sample the potential slow-roll (PSR) parameters $\{\epsilon_V, \eta_V, \xi_V^2, \varpi_V^3\}$, related to the former as indicated in Table 2. We stress that this is just a choice of prior, and does not imply that we are using any kind of slow-roll approximation in the calculation of the primordial spectra.

The results are given in Table 7 (for *Planck* TT+lowP+BAO) and Fig. 13 (for the same data set, and also for *Planck* TT,TE,EE+lowP). The second part of Table 7 shows the corresponding values of the spectral parameters $n_{\rm s}$, $dn_{\rm s}/d\ln k$, and

n	2	3	4
ϵ_V	< 0.0074	< 0.010	$0.0072^{+0.0093}_{-0.0069}$
η_V	$-0.007^{+0.014}_{-0.012}$	$-0.020^{+0.021}_{-0.018}$	$0.021^{+0.044}_{-0.042}$
ξ^2_V	...	$0.006^{+0.010}_{-0.010}$	$-0.018^{+0.028}_{-0.027}$
ϖ^3_V	...	...	$0.015^{+0.016}_{-0.017}$
τ	$0.083^{+0.036}_{-0.036}$	$0.096^{+0.046}_{-0.044}$	$0.102^{+0.046}_{-0.045}$
n_s	$0.9692^{+0.0094}_{-0.0093}$	$0.9689^{+0.0097}_{-0.0097}$	$0.964^{+0.011}_{-0.011}$
$dn_s/d\ln k$	$-0.00034^{+0.00055}_{-0.00059}$	$-0.013^{+0.019}_{-0.019}$	$0.003^{+0.026}_{-0.026}$
$r_{0.002}$	< 0.11	< 0.16	$0.11^{+0.16}_{-0.11}$
$\Delta\chi^2_{\rm eff}$	...	$\Delta\chi^2_{3/2} = -1.2$	$\Delta\chi^2_{4/3} = -2.1$
$\Delta\ln B$	...	$\Delta\ln B_{3/2} = -4.3$	$\Delta\ln B_{4/3} = -2.9$

Table 7. Numerical reconstruction of the potential slow-roll parameters *beyond* any slow-roll approximation, when the potential is Taylor-expanded to nth order, using *Planck* TT+lowP+BAO. We also show the corresponding bounds on some related parameters (here n_s, $dn_s/d\ln k$, and $r_{0.002}$ are derived from the numerically computed primordial spectra). All error bars are at the 95 % CL. The effective χ^2 value and Bayesian evidence logarithm ($\ln B$) of model n are given relative to model $n-1$ (assuming flat priors for ξ^2_V and ϖ^3_V in the range $[-1, 1]$).

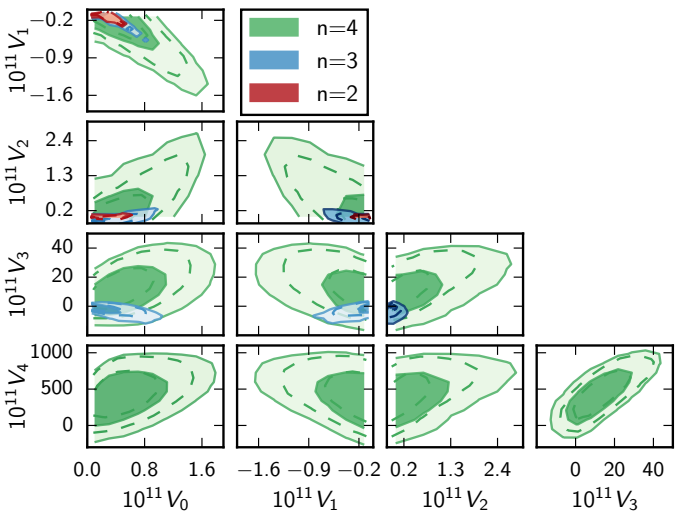

Fig. 14. Posterior distribution for the coefficients of the inflation potential Taylor-expanded to nth order, in natural units (where $\sqrt{8\pi}M_{\rm pl} = 1$), reconstructed *beyond* any slow-roll approximation, using *Planck* TT+lowP+BAO (filled contours) or TT,TE,EE+lowP (dashed contours). The plot shows only half of the results; the other half is symmetric, with opposite signs for V_ϕ and $V_{\phi\phi\phi}$. Note that, unlike Fig. 13, the parameters shown here do *not* have flat priors, since they are mapped from the slow-roll parameters.

$r_{0.002}$, as measured for each numerical primordial spectrum (at the pivot scales $k = 0.05\,{\rm Mpc}^{-1}$ for the scalar and $0.002\,{\rm Mpc}^{-1}$ for the tensor spectra), as well as the reionization optical depth. We also show in Fig. 14 the derived distribution of each coefficient V_i (with a non-flat prior), and in Fig. 15 the reconstructed shape of the best-fit inflation potentials in the observable window. Finally, the posterior distribution of the derived parameters $r_{0.002}$ and n_s is displayed in Fig. 16.

Figure 13 shows that bounds are very similar when temperature data are combined with either high-ℓ polarization data or BAO data. This gives a hint of the robustness of these results. For both data sets, the error bars on the PSR parameters are typically smaller by a factor of 1.5 than in PCI13.

Since potentials with $n = 2$ cannot generate a significant running, the bounds on (n_s, $r_{0.002}$) and the best-fit models are very similar to those obtained with the ΛCDM+r model in Sect. 5 and Table 4. On the other hand, in the $n = 3$ model, results follow the trend of the previous ΛCDM+r+$dn_s/d\ln k$ analysis: the data prefer potentials with V_ϕ and $V_{\phi\phi\phi}$ of the same sign, generating a significant negative running (as can be seen in Fig. 16). This trend for $V_{\phi\phi\phi}$ is driven by the fact that a scalar spectrum with negative running reduces the power on large scales, and provides a better fit to low-ℓ temperature multipoles. However such a running also suppresses power on small scales, so ξ^2_V cannot be too large.

The $n = 4$ case possesses a new feature: the potential has more freedom to generate complicated shapes which would roughly correspond to a running of the running of the tilt (as studied in Sect. 4). The best-fit models now have V_ϕ and $V_{\phi\phi\phi}$ of opposite sign, and a large positive $V_{\phi\phi\phi\phi}$. The preferred combination of these parameters allows for even more suppression of power on large scales, while leaving small scales nearly unchanged. This can be seen very well in the shape of the scalar primordial spectrum corresponding to the best-fit models, for both data sets *Planck* TT+lowP+BAO and *Planck* TT,TE,EE+lowP. These two best-fit models are very similar, but in Fig. 17 we show the one for *Planck* TT,TE,EE+lowP, for which the trend is even more pronounced. Interestingly, the preferred models are such that power on large scales is suppressed in the scalar spectrum and balanced by a small tensor contribution, of roughly $r_{0.002} \sim 0.05$. This particular combination gives the best fit to the low-ℓ data, shown in Fig. 18, while leaving the high-ℓ temperature spectrum identical to the best fit of the base ΛCDM model. Inflation produces such primordial perturbations with the family of green potentials displayed in Fig. 15. At the beginning of the observable range, the potential is very steep ($\epsilon_V(\phi)$ decreases from $O(1)$ to $O(10^{-2})$), and produces a low amplitude of curvature perturbations (allowing a rather large tensor contribution, up to $r_{0.002} \sim 0.3$). Then there is a transition towards a second region with a much smaller slope, leading to a nearly power-law curvature spectrum with the usual tilt value $n_s \approx 0.96$. In Fig. 15, one can check that the height of the $n = 4$ potentials varies in a definite range, while the $n = 2$ and 3 potentials can have arbitrarily small amplitude at the pivot scale, reflecting the posteriors on ϵ_V or r.

However, the improvement in $\chi^2_{\rm eff}$ between the base ΛCDM and $n = 4$ models is only 2.2 (for *Planck* TT+lowP+BAO) or 4.3 (for *Planck* TT,TE,EE+lowP). This is very marginal and brings no significant evidence for these complicated models. This conclusion is also supported by the calculation of the Bayesian evidence ratios, shown in the last line of Table 7 (under the assumption of flat priors in the range [−1,1] for ξ^2_V and ϖ^3_V): the evidence decreases each time that a new free parameter is added to the potential. At the 95 % CL, $r_{0.002}$ is still compatible with zero, and so are the higher order PSR parameters ξ^2_V and ϖ^3_V. More freedom in the inflaton potential allows fitting the data better, but under the assumption of a smooth potential in the observable range, a simple quadratic form provides the best explanation of the *Planck* observations.

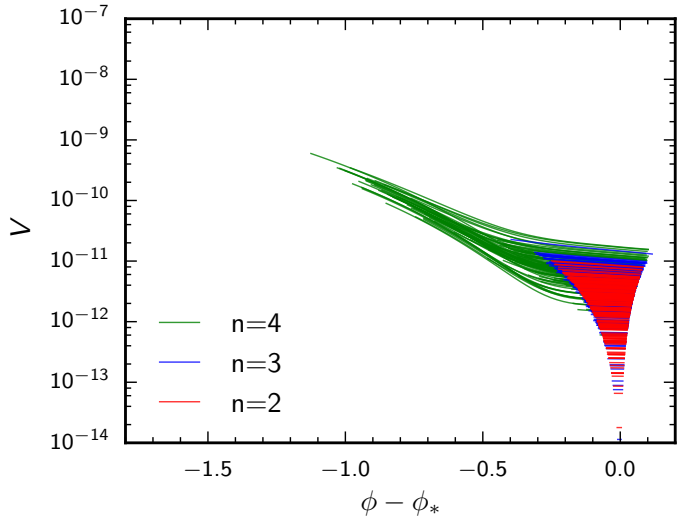

Fig. 15. Observable range of the best-fit inflaton potentials, when $V(\phi)$ is Taylor expanded to the nth order around the pivot value ϕ_*, in natural units (where $\sqrt{8\pi}M_{\rm pl} = 1$), assuming a flat prior on ϵ_V, η_V, ξ_V^2, and ϖ_V^3, and using *Planck* TT+lowP+BAO. Potentials obtained under the transformation $(\phi - \phi_*) \to (\phi_* - \phi)$ leave the same observable signature and are also allowed. The sparsity of potentials with a small $V_0 = V(\phi_*)$ comes from the flat prior on ϵ_V rather than on $\ln(V_0)$; in fact, V_0 is unbounded from below in the $n = 2$ and 3 results. The axis ranges are identical to those in Fig. 20, to make the comparison easier.

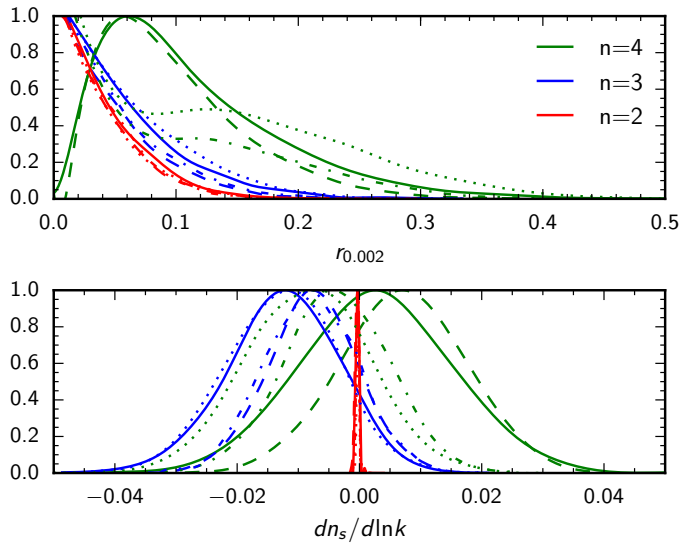

Fig. 16. Posterior distribution for the tensor-to-scalar ratio (at $k = 0.002\,\mathrm{Mpc}^{-1}$) and for the running parameter $dn_s/d\ln k$ (at $k = 0.05\,\mathrm{Mpc}^{-1}$), for the potential reconstructions in Sects. 7.1 and 7.2. The $V(\phi)$ reconstruction gives the solid curves for *Planck* TT+lowP+BAO, or dashed for TT,TE,EE+lowP. The $H(\phi)$ reconstruction gives the dotted curves for *Planck* TT+lowP+BAO, or dashed-dotted for TT,TE,EE+lowP. The tensor-to-scalar ratio appears as a derived parameter, but by taking a flat prior on either ϵ_V or ϵ_H, we implicitly also take a nearly flat prior on r. The same applies to $dn_s/d\ln k$.

With the *Planck* TT+lowP+BAO and TT,TE,EE+lowP datasets, models with a large running or running of the running can be compatible with an unusually large value of the optical depth, as can be seen in Table 7. Including lensing information allows breaking the degeneracy between the optical depth and the primordial amplitude of scalar perturbations. Hence the *Planck* lensing data could be used to strengthen the conclusions of this section.

Since in the $n = 4$ model, slow roll is marginally satisfied at the beginning of observable inflation, the reconstruction is very sensitive to the condition that there is an attractor solution at that time. Hence this case can in principle be investigated in a more conservative way using the $H(\phi)$ reconstruction method of the next section.

7.2. Reconstruction of a smooth Hubble function

In this section, we assume that the shape of the function $H(\phi)$ is well captured within the observable window by a polynomial of order n (corresponding to a polynomial inflaton potential of order $2n$):

$$H(\phi) = \sum_{i=0}^{n} H_i \frac{\phi^i}{i!} \,. \tag{62}$$

We vary n between 2 and 4. To avoid parameter degeneracies, as in the previous section we assume flat priors not on the Taylor coefficient H_i, but on the Hubble slow-roll (HSR) parameters, which are related according to

$$\epsilon_H = 2M_{\rm pl}^2 \left(\frac{H_1}{H_0}\right)^2 , \qquad \eta_H = 2M_{\rm pl}^2 \frac{H_2}{H_0} , \tag{63}$$

$$\xi_H^2 = (2M_{\rm pl}^2)^2 \frac{H_1 H_3}{H_0^2} , \qquad \varpi_H^3 = (2M_{\rm pl}^2)^3 \frac{H_1^2 H_4}{H_0^3} . \tag{64}$$

n	2	3	4
ϵ_H	< 0.0073	< 0.011	< 0.020
η_H	$-0.010^{+0.011}_{-0.009}$	$-0.012^{+0.015}_{-0.013}$	$-0.001^{+0.033}_{-0.027}$
ξ_H^2	...	$0.08^{+0.12}_{-0.12}$	$-0.01^{+0.19}_{-0.19}$
ϖ_H^3	...	...	$1.0^{+2.3}_{-1.8}$
τ	$0.082^{+0.038}_{-0.036}$	$0.096^{+0.042}_{-0.043}$	$0.096^{+0.042}_{-0.042}$
n_s	$0.9693^{+0.0094}_{-0.0093}$	$0.9680^{+0.0096}_{-0.0096}$	$0.967^{+0.010}_{-0.010}$
$10^3 dn_s/d\ln k$	$-0.251^{+0.41}_{-0.41}$	-13^{+18}_{-19}	-8^{+21}_{-21}
$r_{0.002}$	< 0.11	< 0.16	< 0.32
$\Delta\chi^2_{\rm eff}$	...	$\Delta\chi^2_{3/2} = -0.6$	$\Delta\chi^2_{4/3} = -2.3$

Table 8. Numerical reconstruction of the Hubble slow-roll parameters *beyond* any slow-roll approximation, using *Planck* TT+lowP+BAO. We also show the corresponding bounds on some related parameters (here n_s, $dn_s/d\ln k$, and $r_{0.002}$ are derived from the numerically computed primordial spectra). All error bars are at the 95 % CL. The effective χ^2 value of model n is given relative to model $n - 1$.

This is just a choice of prior. This analysis does not rely on the slow-roll approximation.

Table 8 and Fig. 19 show our results for the reconstructed HSR parameters. Figure 20 shows a representative sample of potential shapes $V(\phi - \phi_*)$ derived using Eq. (60), for a sample of models drawn randomly from the chains, for the three cases $n = 1, 2, 3$.

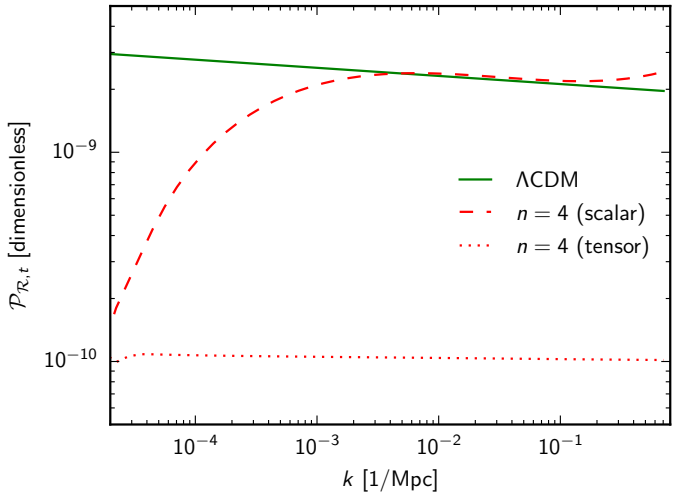

Fig. 17. Primordial spectra (scalar and tensor) of the best-fit $V(\phi)$ model with $n = 4$, for the *Planck* TT,TE,EE+lowP data set, compared to the primordial spectrum (scalar only) of the best-fit base ΛCDM model. The best-fit potential is initially very steep, as can be seen in Fig. 15 (note the typical shape of the green curves). The transition from "marginal slow roll" ($\epsilon_V(\phi)$ between 0.01 and 1) to "full slow roll" ($\epsilon_V(\phi)$ of order 0.01 or smaller) is responsible for the suppression of the large-scale scalar spectrum.

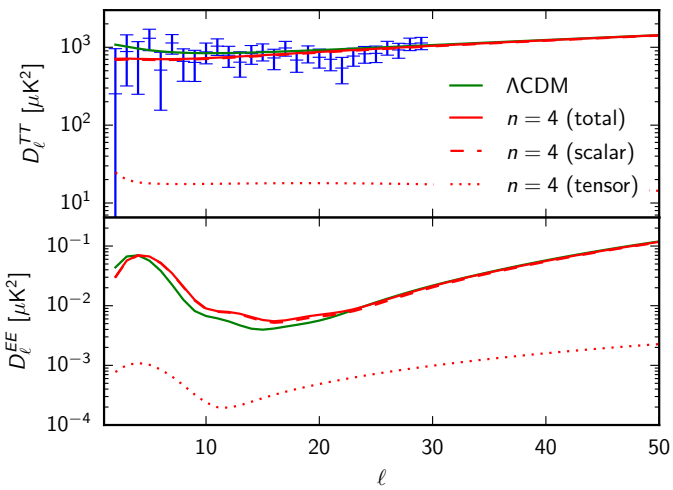

Fig. 18. Temperature spectrum (total, scalar contribution, tensor contribution) of the best-fit $V(\phi)$ model with $n = 4$, for the *Planck* TT,TE,EE+lowP data set, compared to the temperature spectrum (scalar contribution only) of the best-fit base model. We also show the *Planck* low-ℓ temperature data, which is driving the small differences between the two best-fit models.

Most of the discussion of Sect. 7.1 also applies to this section, and so will not be repeated. Results for *Planck* TT+lowP+BAO and TT,TE,EE+lowP are still very similar. The $n = 2$ case still gives results close to ΛCDM+r, and the $n = 3$ case to ΛCDM+r+$dn_s/d\ln k$. The type of potential preferred in the $n = 4$ case is very similar to the $n = 4$ analysis of the previous section, for the reasons explained in Sect. 7.1. There are, however, small differences, because the range of parametric forms for the potential explored by the two analyses differ. In the $H(\phi)$

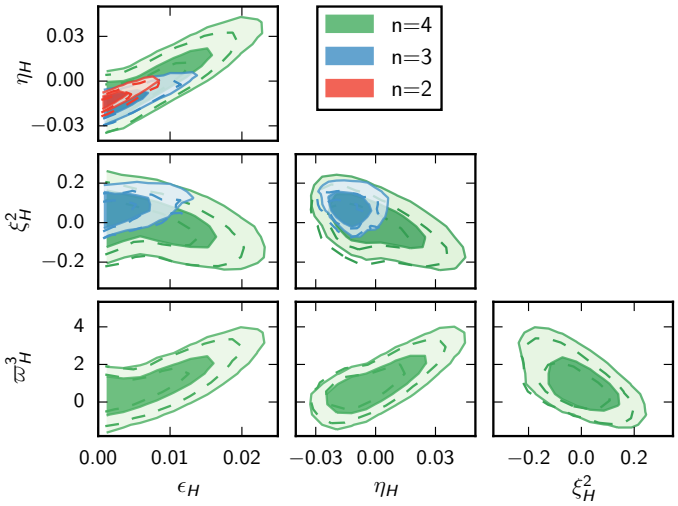

Fig. 19. Posterior distributions for the first four Hubble slow-roll parameters, when $H(\phi)$ is Taylor-expanded to nth order, using *Planck* TT+lowP+BAO (filled contours) or TT,TE,EE+lowP (dashed contours). The primordial spectra are computed *beyond* any slow-roll approximation.

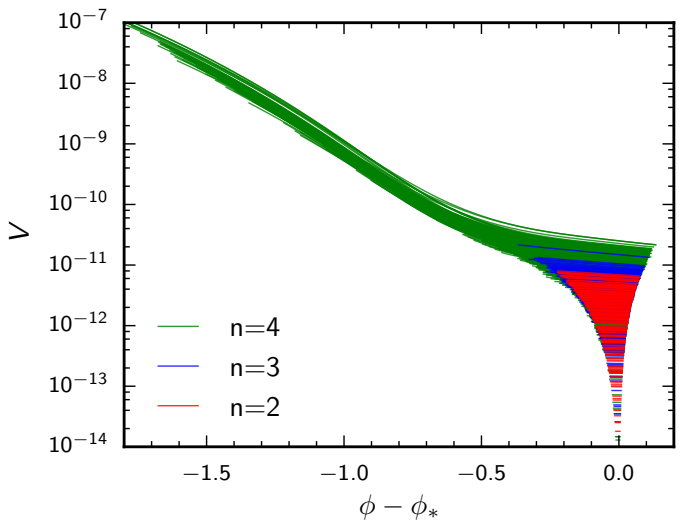

Fig. 20. Same as Fig. 15, when the Taylor expansion to nth order is performed on $H(\phi)$ instead of $V(\phi)$, and the potential is inferred from Eq. (60).

reconstruction, the underlying potentials $V(\phi)$ are not polynomials. In the first approximation, they are close to polynomials of order $2n$, but with constraints between the various coefficients. The main two differences with respect to the results of Sect. 7.1 are as follows:

- The reconstructed potential shape for $n = 4$ at the beginning of the observable window. Figure 20 shows that even steeper potentials are allowed than for the $V(\phi)$ method, with an even greater excursion of the inflaton field between Hubble crossing for the largest observable wavelengths and the pivot scale. This is because the $H(\phi)$ reconstruction does not rely on attractor solutions and automatically explores all valid potentials regardless of their initial field velocity.
- The best-fit models are different, since they do not explore the same parametric families of potentials. In particular, for $n = 4$, the best-fit models have a negligible tensor contri-

bution, but still have a thick distribution tail towards large tensor-to-scalar ratios, so that the upper bound on $r_{0.002}$ is as high as in the previous $n = 4$ models, $r_{0.002} < 0.32$.

Note that ϖ_H^3 can be significantly larger than unity for $n = 4$. This does not imply violation of slow roll within the observable range. By assumption, for all accepted models, ϵ_H must remain smaller than unity over that range. In fact, for most of the green potentials visible in Fig. 20, we checked that ϵ_H either has a maximum very close to unity near the beginning of the observable range or starts from unity. So the best-fit models (maximizing the power suppression at low multipoles) correspond either to inflation of short duration, or to models nearly violating slow roll just before the observable window. However, such peculiar models are not necessary for a good fit. Table 8 shows that the improvement in χ^2 as n increases is negligible.

In summary, this section further establishes the robustness of our potential reconstruction and two main conclusions. Firstly, under the assumption that the inflaton potential is smooth over the observable range, we showed that the simplest parametric forms (involving only three free parameters including the amplitude $V(\phi_*)$, no deviation from slow roll, and nearly power-law primordial spectra) are sufficient to explain the data. No high-order derivatives or deviations from slow roll are required. Secondly, if one allows more freedom in the potential—typically, two more parameters—it is easy to decrease the large-scale primordial spectrum amplitude with an initial stage of "marginal slow roll" along a steep branch of the potential followed by a transition to a less steep branch. This type of model can accommodate a large tensor-to-scalar ratio, as high as $r_{0.002} \approx 0.3$.

8. $\mathcal{P}(k)$ reconstruction

In PCI13 (section 7) we presented the results of a penalized likelihood reconstruction, seeking to detect any possible deviations from a homogeneous power-law form (i.e., $\mathcal{P}(k) \propto k^{n_s-1}$) for the primordial power spectrum (PPS) for various values of a smoothing parameter, λ. In the initial March 2013 preprint version of that paper, we reported evidence for a feature at moderate statistical significance around $k \approx 0.15$ Mpc^{-1}. However, in the November 2013 revision we retracted this finding, because subsequent tests indicated that the feature was no longer statistically significant when more aggressive cuts were made to exclude sky survey rings where contamination from electromagnetic interference from the 4-K cooler were largest, as indicated in the November 2013 "Note Added."

In this section we report on results using the 2015 C_{TT} likelihood (Sect. 8.1) using essentially the same methodology as described in PCI13. (See Gauthier & Bucher (2012) and references therein for more technical details.) This method is also extended to include the EE and TE likelihoods in Sect. 8.1.2. As part of this 2015 release, we include the results of two other methods (see Sects. 8.2 and 8.3) to search for features. We find that all three methods yield broadly consistent reconstructions and reach the following main conclusion: there is no statistically significant evidence for any features departing from a simple power-law (i.e., $\mathcal{P}(k) \propto k^{n_s-1}$) PPS. Given the substantial differences between these methods, it is satisfying to observe this convergence.

8.1. Method I: penalized likelihood

8.1.1. Update with 2015 temperature likelihood

We repeated the same maximum likelihood analysis used to reconstruct the PPS in PCI13 using the updated *Planck* TT likelihood. Since we are interested in deviations from the nearly scale invariant model currently favoured by the parametric approach, we replaced the true PPS $\mathcal{P}_\mathcal{R}(k)$ by a fiducial power-law spectrum $\mathcal{P}_\mathcal{R}^{(0)}(k) = A_s(k/k_*)^{n_s-1}$, modulated by a small deviation function $f(k)$:

$$\mathcal{P}_\mathcal{R}(k) = \mathcal{P}_\mathcal{R}^{(0)}(k) \exp\left[f(k)\right]. \tag{65}$$

The deviation function $f(k)$[7] was represented by B-spline basis functions parameterized by $n_{\rm knot}$ control points $\mathbf{f} = \{f_i\}_{i=1}^{n_{\rm knot}}$, which are the values of $f(k)$ along a grid of knot points $\kappa_i = \ln k_i$.

Naively, maximizing the *Planck* likelihood with respect to $\mathbf{f}$ results in over-fitting to cosmic variance and noise in the data. Furthermore, due to the limited range of scales over which *Planck* measures the anisotropy power spectrum, the likelihood is very weakly dependent on $f(k)$ at extremely small and large scales. To address these issues, the following two penalty functions were added to the *Planck* likelihood:

$$\begin{aligned}\mathbf{f}^{\rm T}\mathbf{R}(\lambda,\alpha)\mathbf{f} \equiv \lambda \int {\rm d}\kappa \left(\frac{\partial^2 f(\kappa)}{\partial\kappa^2}\right)^2 \\ + \alpha \int_{-\infty}^{\kappa_{\rm min}} {\rm d}\kappa\, f^2(\kappa) + \alpha \int_{\kappa_{\rm max}}^{+\infty} {\rm d}\kappa\, f^2(\kappa).\end{aligned} \tag{66}$$

The first term on the right-hand side of Eq. (66) is a roughness penalty, which disfavours $f(\kappa)$ that "wiggle" too much. The last two terms drive $f(\kappa)$ to zero for scales below $\kappa_{\rm min}$ and above $\kappa_{\rm max}$. The values of λ and α represent the strengths of the respective penalties. The exact value of α is unimportant as long as it is large enough to drive $f(\kappa)$ close to zero on scales outside $[\kappa_{\rm min}, \kappa_{\rm max}]$. However, the magnitude of the roughness penalty, λ, controls the smoothness of the reconstruction.

Since the anisotropy spectrum depends linearly on the PPS, the Newton-Raphson method is well suited to optimizing with respect to $\mathbf{f}$. However, a maximum likelihood analysis also has to take into account the cosmological parameters, $\mathbf{\Theta} \equiv \{H_0, \Omega_{\rm b}h^2, \Omega_{\rm c}h^2\}$.[8] These additional parameters are not easy to include in the Newton-Raphson method since it is difficult to evaluate the derivatives $\partial C_\ell/\partial\mathbf{\Theta}$, $\partial^2 C_\ell/\partial\mathbf{\Theta}^2$, etc., to the accuracy required by the method. Therefore a non-derivative method, such as the downhill simplex algorithm, is best suited to optimization over these parameters. Unfortunately the downhill simplex method is inefficient given the large number of control points in our parameter space. Since each method has its drawbacks, we combined the two methods to draw on their respective strengths. We define the function $\mathcal{M}$ as

$$\mathcal{M}(\mathbf{\Theta}) = \min_{f_i\in[-1,1]} \left\{-2\ln\mathcal{L}(\mathbf{\Theta},\mathbf{f}) + \mathbf{f}^T\mathbf{R}(\lambda,\alpha)\mathbf{f}\right\}. \tag{67}$$

Given a set of non-PPS cosmological parameters $\mathbf{\Theta}$, $\mathcal{M}$ is the value of the penalized log likelihood, minimized with respect to $\mathbf{f}$ using the Newton-Raphson method. The function $\mathcal{M}$ is in

[7] The definition of $f(k)$ used here differs from that of PCI13 in that $\exp(f)$ is used in place of $1 + f$, to ensure that the reconstructed primordial power spectrum is always non-negative.

[8] Due to the high correlation between τ and A_s, τ is not included as a free parameter. Any change in τ can be almost exactly compensated for by a change in A_s. We fix τ to its best-fit fiducial model value.

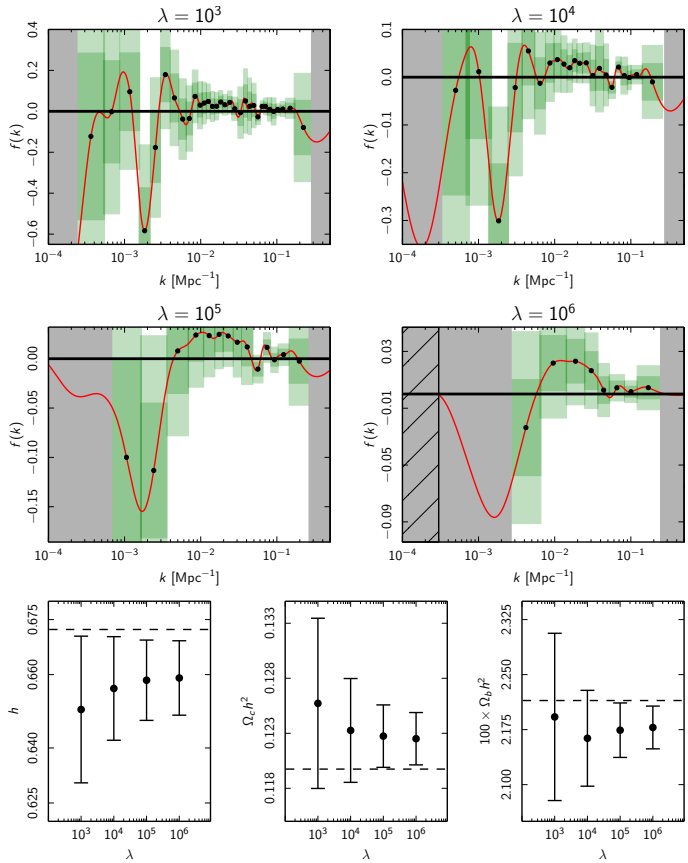

Fig. 21. *Planck* TT likelihood primordial power spectrum (PPS) reconstruction results. *Top four panels*: Reconstruction of the deviation $f(k)$ using four different roughness penalties. The red curves represent the best-fit deviation $f(k)$ using the *Planck* TT likelihood. $f(k) = 0$ would represent a perfectly featureless spectrum with respect to the fiducial PPS model, which is obtained from the best-fit base ΛCDM model with a power-law PPS. The vertical extent of the dark and light green error bars indicates the $\pm 1\,\sigma$ and $\pm 2\,\sigma$ errors, respectively. The width of the error bars represents the minimum reconstructible width (the minimum width for a Gaussian feature so that the mean square deviation of the reconstruction is less than 10 %). The grey regions indicate where the minimum reconstructible width is undefined, indicating that the reconstruction in these regions is untrustworthy. The hatched region in the $\lambda = 10^6$ plot shows where the fixing penalty has been applied. These hashed regions are not visible in the other three reconstructions, for which $\kappa_{\rm min}$ lies outside the range shown in the plots. For all values of the roughness penalty, all data points are within $2\,\sigma$ of the fiducial PPS except for the deviations around $k \approx 0.002\,{\rm Mpc}^{-1}$ in the $\lambda = 10^3$ and $\lambda = 10^4$ reconstructions. *Lower three panels:* $\pm 1\,\sigma$ error bars of the three non-PPS cosmological parameters included in the maximum likelihood reconstruction. All values are consistent with their respective best-fit fiducial model values indicated by the dashed lines.

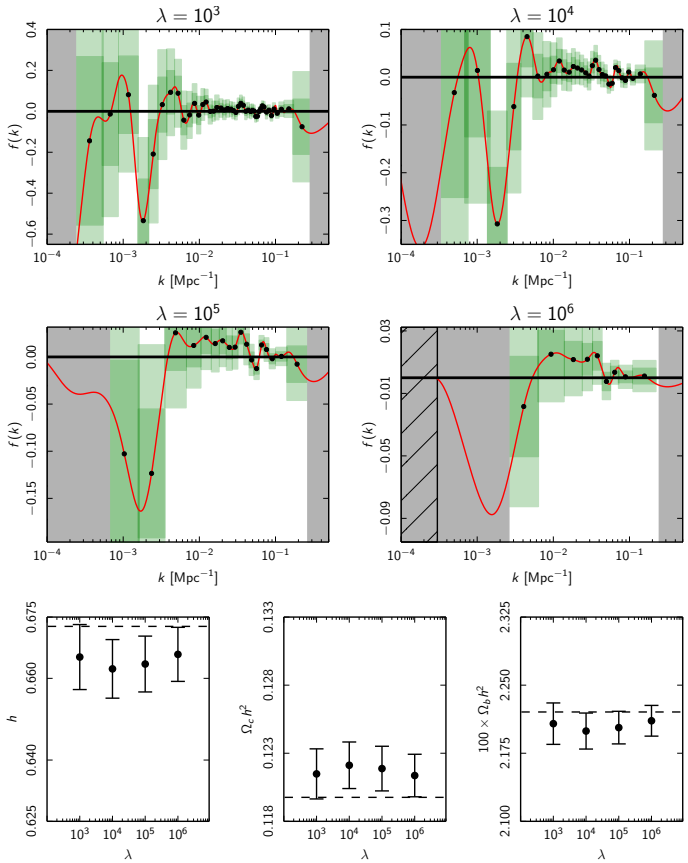

Fig. 22. *Planck* TT,TE,EE+lowTEB likelihood primordial power spectrum reconstruction results. *Top four panels*: Reconstruction of the deviation $f(k)$ using four different roughness penalties. As in Fig. 21, the red curves represent the best-fit deviation $f(k)$ and the height and width of the green error bars represent the error and minimum reconstructible width, respectively. For all values of the roughness penalty, the deviations are consistent with a featureless spectrum. *Lower three panels:* $\pm 1\,\sigma$ error bars of the three non-PPS cosmological parameters included in the maximum likelihood reconstruction. All values are consistent with their respective best-fit fiducial model values (indicated by the dashed lines).

turn minimized with respect to $\boldsymbol{\Theta}$ using the downhill simplex method. In contrast to the analysis done in PCI13, the *Planck* low-ℓ likelihood has been modified so that it can be included in the Newton-Raphson minimization. Thus the reconstructions presented here extend to larger scales than were considered in 2013.

Figure 21 shows the best-fit PPS reconstruction using the *Planck* TT+lowTEB likelihood. The penalties in Eq. (66) introduce a bias in the reconstruction by smoothing and otherwise deforming potential features in the power spectrum. To assess this bias, we define the "minimum reconstructible width" (MRW) to be the minimum width of a Gaussian feature needed so that the integrated squared difference between the feature and its reconstruction is less than 1 % of the integrated square of the input Gaussian, which is equivalent to 10 % rms. Due to the combination of the roughness and fixing penalties, it is impossible to satisfy the MRW criterion too close to $\kappa_{\rm min}$ and $\kappa_{\rm max}$. Wherever the MRW is undefined, the reconstruction is substantially biased and therefore suspect. An MRW cannot be defined too close to the endpoints $\kappa_{\rm min}$ and $\kappa_{\rm max}$ for two reasons: (1) lack of data; and (2) if a feature is too close to where the fixing penalty has been applied, the fixing penalty distorts the reconstruction. Consequently a larger roughness penalty decreases the range over which an MRW is well defined. The grey shaded areas in Fig. 21 show where the MRW is undefined and thus the reconstruction cannot be trusted. The cutoffs $\kappa_{\rm min}$ and $\kappa_{\rm max}$ have

been chosen to maximize the range over which an MRW is defined for a given value of λ. The $1\,\sigma$ and $2\,\sigma$ error bars in Fig. 21 are estimated using the Hessian of the log-likelihood evaluated at the best-fit PPS reconstruction. More detailed MC investigations suggest that the nonlinear corrections to these error bars are small.

For the $\lambda = 10^5$ and 10^6 cases of the TT reconstruction, no deviation exceeds $2\,\sigma$, so we do not comment on the probability of obtaining a worse fit. For the other cases, we use the maximum of the deviation, expressed in σ, of the plotted points as a metric of the quality of fit; then using Monte Carlo simulations we compute the p-value, or the probability to obtain a worse fit, according to this metric. For $\lambda = 10^3$ and 10^4, we obtain p-values of 0.304 and 0.142, respectively, corresponding to 1.03 and $1.47\,\sigma$. We thus conclude that the observed deviations are not statistically significant.

8.1.2. Penalized likelihood results with polarization

In Fig. 22 the best-fit reconstruction of the PPS from the *Planck* TT,TE,EE likelihood is shown. We observe that the reconstruction including polarization broadly agrees with the reconstruction obtained using temperature only. For the *Planck* TT,TE,EE likelihood, we obtain for $\lambda = 10^3, 10^4$, and 10^5 the p-values 0.166, 0.107, and 0.045, respectively, corresponding to 1.38, 1.61, and $2.00\,\sigma$, and likewise conclude the absence of any statistically significant evidence for deviations from a simple power-law scalar primordial power spectrum.

8.2. Method II: Bayesian model comparison

In this section we model the PPS $\mathcal{P}_{\mathcal{R}}(k)$ using a nested family of models where $\mathcal{P}_{\mathcal{R}}(k)$ is piecewise linear in the $\ln(\mathcal{P})$-$\ln(k)$ plane between a number of knots, $N_{\rm knots}$, that is allowed to vary. The question arises as to how many knots one should use, and we address this question using Bayesian model comparison. A family of priors is chosen where both the horizontal and vertical positions of the knots are allowed to vary. We examine the "Bayes factor" or "Bayesian evidence" as a function of $N_{\rm knots}$ to decide

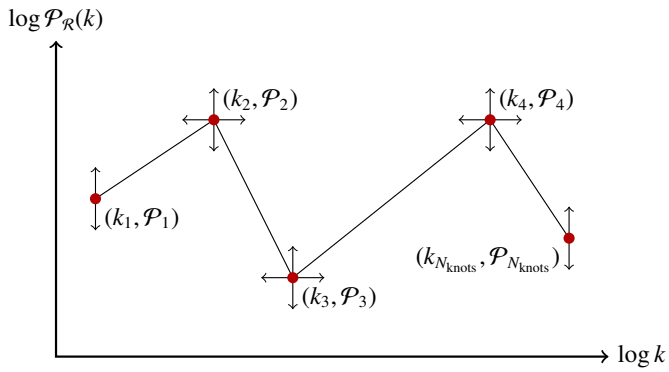

Fig. 23. Linear spline reconstruction. The primordial power spectrum is reconstructed using $N_{\rm knots}$ interpolation points $\{(k_i, \mathcal{P}_i) : i = 1, 2, \ldots N_{\rm knots}\}$. The end knots are fixed in k but allowed to vary in $\mathcal{P}$, whereas the internal knots can vary subject to the constraint that $k_1 < k_2 < \cdots < k_{N_{\rm knots}}$. The function $\mathcal{P}_{\mathcal{R}}(k)$ is constructed within the range $[k_1, k_{N_{\rm knots}}]$ by interpolating logarithmically between adjacent knots (i.e., linearly in log-log space). Outside this range the function is extrapolated logarithmically. The function $\mathcal{P}_{\mathcal{R}}(k; \{k_i, \mathcal{P}_i\})$ thus has $2N_{\rm knots} - 2$ parameters.

Parameter range	Prior type
$10^{-4}\,\mathrm{Mpc}^{-1} = k_1 < k_2 < \ldots < k_{N_{\rm knots}} = 0.3\,\mathrm{Mpc}^{-1}$	log uniform (sorted)
$2 < \ln\left(10^{10}\mathcal{P}_1\right), \ldots, \ln\left(10^{10}\mathcal{P}_{N_{\rm knots}}\right) < 4$	log uniform
$2 \le N_{\rm knots} \le 10$	integer uniform
$0.019 < \Omega_{\rm b}h^2 < 0.025$	uniform
$0.095 < \Omega_{\rm c}h^2 < 0.145$	uniform
$1.03 < 100\theta_{\rm MC} < 1.05$	uniform
$0.01 < \tau < 0.4$	uniform

Table 9. Prior for moveable knot positions. The $\mathcal{P}_{\mathcal{R}}$ positions are distributed in a log-uniform manner across a wide range. The k positions are also log-uniformly distributed across the entire range needed by `CosmoMC` and are sorted so that $k_1 < \ldots < k_{N_{\rm knots}}$. When we marginalize over the number of knots, $N_{\rm knots}$, we assume a uniform prior between 2 and 10.

how many knots are statistically justified. A similar analysis has been performed by Vázquez et al. (2012) and Aslanyan et al. (2014). In addition, we marginalize over all possible numbers of knots to obtain an averaged reconstruction weighted according to the Bayesian evidence.

The generic prescription is illustrated in Fig. 23. $N_{\rm knots}$ knots $\{(k_i, \mathcal{P}_i) : i = 1, \ldots, N_{\rm knots}\}$ are placed in the $(k, \mathcal{P}_{\mathcal{R}})$ plane and the function $\mathcal{P}_{\mathcal{R}}(k)$ is constructed by logarithmic interpolation (a linear interpolation in log-log space) between adjacent points. Outside the horizontal range $[k_1, k_N]$ the function is extrapolated using the outermost interval.

Within this framework, base ΛCDM arises when $N_{\rm knots} = 2$—in other words, when there are two boundary knots and no internal knots, and the parameters $\mathcal{P}_1$ and $\mathcal{P}_2$ (in place of $A_{\rm s}$ and $n_{\rm s}$) parameterize the simple power-law PPS. There are also, of course, the four standard cosmological parameters ($\Omega_{\rm b}h^2$, $\Omega_{\rm c}h^2$, $100\theta_{\rm MC}$, and τ), as well the numerous foreground parameters associated with the *Planck* high-ℓ likelihood, all of which are unrelated to the PPS. This simplest model can be extended iteratively by successively inserting an additional internal knot, thus requiring with each iteration two more variables to parameterize the new knot position.

We run models for a variety of numbers of internal knots, $N_{\rm int} = N_{\rm knots} - 2$, evaluating the evidence for $N_{\rm int}$. Under the assumption that the prior is justified, the most likely, or preferred, model is the one with the highest evidence. Evidences are evaluated using the `PolyChord` sampler (Handley et al., 2015) in `CAMB` and `CosmoMC`. The use of `PolyChord` is essential, as the posteriors in this parameterization are often multi-modal. Also, the ordered log-uniform priors on the k_i are easy to implement within the `PolyChord` framework. All runs were performed with 1000 live points, oversampling the semi-slow and fast parameters by a factor of 5 and 100, respectively.

Priors for the reconstruction and cosmological parameters are detailed in Table 8.2. We report evidence ratios with respect to the base ΛCDM case. The cosmological priors remain the same for all models, and this part of the prior has almost no impact on the evidence ratios. The choice of prior on the reconstruction parameters $\{\mathcal{P}_i\}$ does affect the Bayes factor. `CosmoMC`, however, puts an implicit prior on all models by excluding parameter choices that render the internal computational approximations in `CAMB` invalid. The baseline prior for the vertical position of the knots includes all of the range allowed by `CosmoMC`, so slighly increasing this prior range will not affect

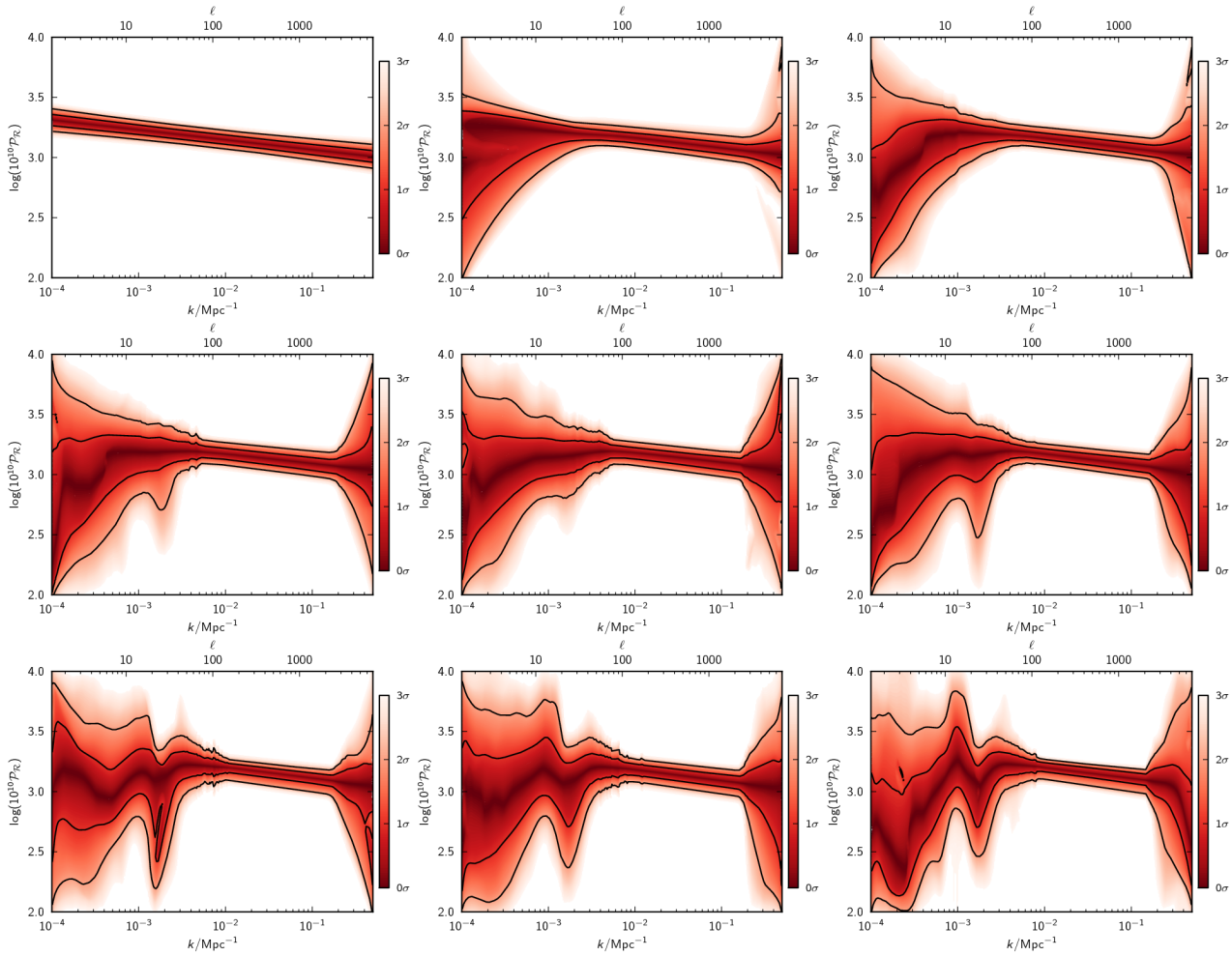

Fig. 24. Bayesian movable knot reconstructions of the primordial power spectrum $\mathcal{P}_{\mathcal{R}}(k)$ using *Planck* TT data. The plots indicate our knowledge of the PPS $P(\mathcal{P}_{\mathcal{R}}(k)|k, N)$ for a given number of knots. The number of internal knots $N_{\rm int}$ increases (left to right and top to bottom) from 0 to 8. For each k-slice, equal colours have equal probabilities. The colour scale is chosen so that darker regions correspond to lower-σ confidence intervals. 1 σ and 2 σ confidence intervals are also sketched (black curves). The upper horizontal axes give the approximate corresponding multipoles via $\ell \approx k/D_{\rm rec}$, where $D_{\rm rec}$ is the comoving distance to recombination.

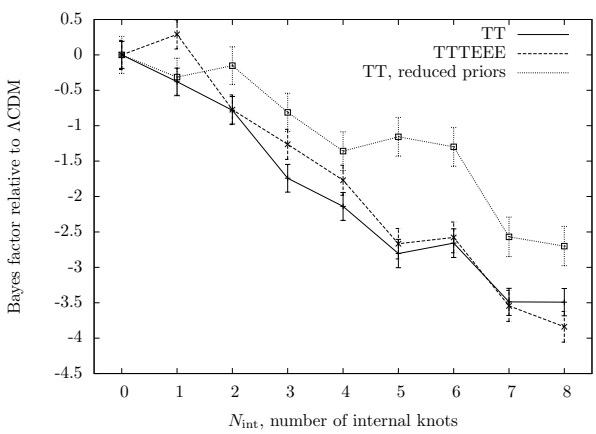

Fig. 25. Bayes factor (relative to the base ΛCDM model) as a function of the number of knots for three separate runs. Solid line: *Planck* TT. Dashed line: *Planck* TT,TE,EE. Dotted line: *Planck* TT, with priors on the $\mathcal{P}$ parameters reduced in width by a factor of 2 ($2.5 < \ln(10^{10}\mathcal{P}) < 3.5$).

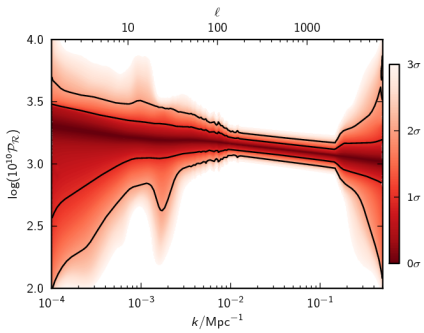

Fig. 26. Bayesian reconstruction of the primordial power spectrum averaged over different values of $N_{\rm int}$ (as shown in Fig. 24), weighted according to the Bayesian evidence. The region $30 < \ell < 2300$ is highly constrained, but the resolution is lacking to say anything precise about higher ℓ. At lower ℓ, cosmic variance reduces our knowledge of $\mathcal{P}_{\mathcal{R}}(k)$. The weights assigned to the lower $N_{\rm int}$ models outweigh those of the higher models, so no oscillatory features are visible here.

the evidence ratios. If one were to reduce the prior widths significantly, the evidence ratios would be increased. The allowed horizontal range includes all k-scales accessible to *Planck*. Thus, altering this width would be unphysical.

After completion of an evidence calculation, `PolyChord` generates a representative set of samples of the posterior for each model $P(\Theta) \equiv P(\Theta|\text{data}, N_{\text{int}})$. We may use this to calculate a marginalized probability distribution for the PPS:

$$P(\log \mathcal{P}_{\mathcal{R}}|k, N_{\text{int}}) = \int \delta\left(\log \mathcal{P}_{\mathcal{R}} - \log \mathcal{P}_{\mathcal{R}}(k;\Theta)\right) P(\Theta)\, d\Theta. \quad (68)$$

This expression encapsulates our knowledge of $\mathcal{P}_{\mathcal{R}}$ at each value of k for a given number of knots. Plots of this PPS posterior are shown in Fig. 24 using *Planck* TT data.

If one considers the Bayesian evidences of each model, Fig. 25 shows that although no model is preferred over base ΛCDM, the case $N_{\text{int}} = 1$ is competitive. This model is analogous to the broken-power-law spectrum of Sect. 4.4, although the models differ significantly in terms of the priors used. In this case, the additional freedom of one knot allows a reconstruction of the suppression of power at low ℓ. Adding polarization data does not alter the evidences significantly, although $N_{\text{int}} = 1$ is strengthened. We also plot a *Planck* TT run, but with the reduced vertical priors $2.5 < \ln\left(10^{10}\mathcal{P}\right) < 3.5$. As expected, this increases the evidence ratios, but does not alter the above conclusion.

For increasing numbers of internal knots, the Bayesian evidence monotonically decreases. Occam's razor dictates, therefore, that these models should not be preferred, due to their higher complexity. However, there is an intriguing stable oscillatory feature, at $20 \lesssim \ell \lesssim 50$, that appears once there are enough knots to reconstruct it. This is a qualitative feature predicted by several inflationary models (discussed in Sect. 9), and a possible hint of new physics, although its statistical significance is not compelling.

A full Bayesian analysis marginalizes over all models weighted according to the normalized evidence $Z_{N_{\text{int}}}$, so that

$$P(\log \mathcal{P}_{\mathcal{R}}|k) = \sum_{N_{\text{int}}} P(\log \mathcal{P}_{\mathcal{R}}|k, N_{\text{int}}) Z_{N_{\text{int}}}, \quad (69)$$

as indicated in Fig. 26. This reconstruction is sensitive to how model complexity is penalized in the prior distribution.

8.3. Method III: cubic spline reconstruction

In this section we investigate another reconstruction algorithm based on cubic splines in the $\ln(k)$-$\ln \mathcal{P}_{\mathcal{R}}$ plane, where (unlike for the approach of the previous subsection) the horizontal positions of the knots are uniformly spaced in $\ln(k)$ and fixed. A prior on the vertical positions (described in detail below) is chosen and the reconstructed power spectrum is calculated using `CosmoMC` for various numbers of knots. This method differs from the method in Sect. 8.1 in that the smoothness is controlled by the number of discrete knots rather than by a continuous parameter of a statistical model having a well-defined continuum limit. With respect to the Bayesian model comparison of Sect. 8.2, the assessment of model complexity differs because here the knots are not movable.

Let the horizontal positions of the n knots be given by k_b, where $b = 1, \ldots, n$, spaced so that k_{b+1}/k_b is independent of b. We single out a "pivot knot" $b = p$, so that $k_p = k_* = 0.05\ \text{Mpc}^{-1}$, which is the standard scalar power spectrum pivot scale. For

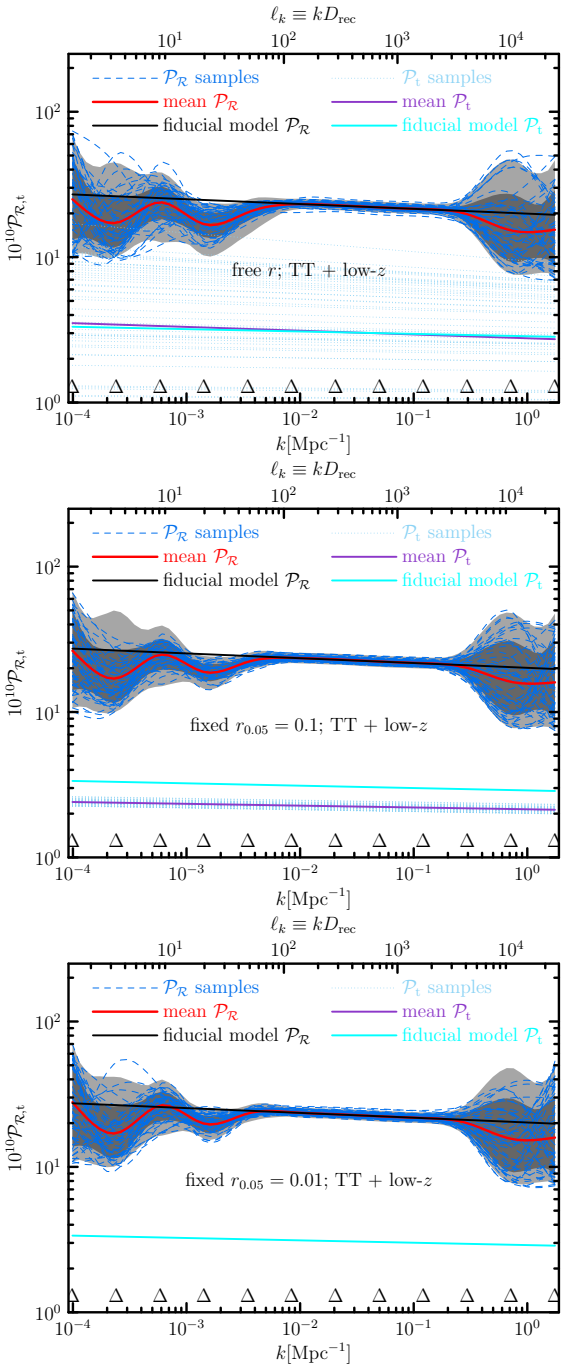

Fig. 27. Reconstructed power spectra applied to the *Planck* 2015 data using 12 knots (with positions marked as Δ at the bottom of each panel) with cubic spline interpolation. Mean spectra as well as sample trajectories are shown for scalars and tensors, and $\pm 1\,\sigma$ and $\pm 2\,\sigma$ limits are shown for the scalars. *Top:* uniform prior $0 \le r \le 1$. *Middle:* fixed $r = 0.1$; *Bottom:* fixed $r = 0.01$. Data sets: *Planck* TT+lowP+BAO+SN+HST+z_{re}>6 prior. D_{rec} is the comoving distance to recombination.

a given number of knots n we choose k_1 and k_n so that the interval of relevant cosmological scales, taken to extend from $10^{-4}\ \text{Mpc}^{-1}$ to $O(1)\ \text{Mpc}^{-1}$, is included. We now define the prior on the vertical knot coordinates. For the pivot point, we define $\ln A_{\text{s}} = \ln \mathcal{P}_{\mathcal{R}}(k_*)$, where $\ln A_{\text{s}}$ has a uniformly distributed prior, and for the other points with $b \neq p$, we define the derived vari-

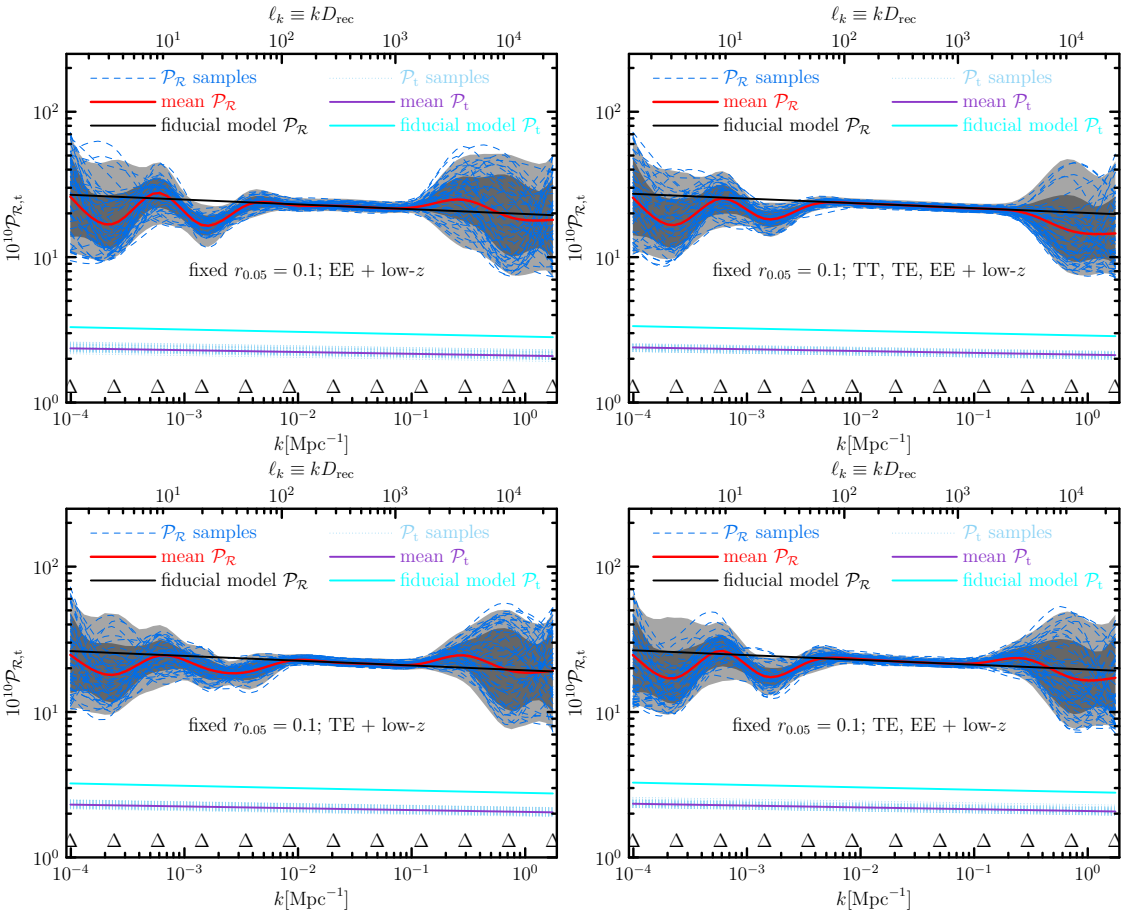

Fig. 28. Reconstructed 12-knot power spectra with polarization included. Data sets in common: lowP+BAO+SN+HST+$z_{\rm re}$>6 prior.

able

$$q_b \equiv \ln\left(\frac{\mathcal{P}_\mathcal{R}(k_b)}{\mathcal{P}_{\mathcal{R},\rm fid}(k_b)}\right), \tag{70}$$

where $\mathcal{P}_{\mathcal{R},\rm fid} \equiv A_{\rm s}(k/k_*)^{n_{\rm s,fid}-1}$. Here the spectral index $n_{\rm s,fid}$ is fixed. A uniform prior is imposed on each variable q_b ($b \neq p$) and the constraint $-1 \leq q_b \leq 1$ is also imposed to force the reconstruction to behave reasonably near the endpoints, where it is hardly constrained by the data. The quantity $\ln \mathcal{P}_\mathcal{R}(k)$ is interpolated between the knots using cubic splines with natural boundary conditions (i.e., the second derivatives vanish at the first and the last knots). Outside $[k_1, k_n]$ we set $\mathcal{P}_\mathcal{R}(k) = e^{q_1}\mathcal{P}_{\mathcal{R},\rm fid}(k)$ (for $k < k_1$) and $\mathcal{P}_\mathcal{R}(k) = e^{q_n}\mathcal{P}_{\mathcal{R},\rm fid}(k)$ (for $k > k_n$). For most knots, we found that the upper and lower bounds of the q_b prior hardly affect the reconstruction, since the data sharpens the allowed range significantly. However, for superhorizon scales (i.e., $k \lesssim 10^{-4}$ Mpc^{-1}) and very small scales (i.e., $k \gtrsim 0.2$ Mpc^{-1}), which are only weakly constrained by the cosmological data, the prior dominates the reconstruction. For the results here, a fiducial spectral index $n_{\rm s,fid} = 0.967$ for $\mathcal{P}_{\mathcal{R},\rm fid}$ was chosen, which is close to the estimate from *Planck* TT+lowP+BAO. A different choice of $n_{\rm s,fid}$ leads to a trivial linear shift in the q_b.

The possible presence of tensor modes (see Sect. 5) has the potential to bias and introduce additional uncertainty in the reconstruction of the primordial scalar power spectrum as parameterized above. Obviously, in the absence of a detection of tensors at high statistical significance, it is not sensible to model a possible tensor contribution with more than a few degrees of freedom. A complicated model would lead to prior-dominated results. We therefore use the power-law parameterization, $\mathcal{P}_{\rm t}(k) = rA_{\rm s}(k/k_*)^{n_{\rm t}}$, where the consistency relation $n_{\rm t} = -r/8$ is enforced as a constraint.

Primordial tensor fluctuations contribute to CMB temperature and polarization angular power spectra, in particular at spatial scales larger than the recombination Hubble length, $k \lesssim (aH)_{\rm rec} \approx 0.005$ Mpc^{-1}. If a large number of knots in $\ln \mathcal{P}_\mathcal{R}(k)$ is included over that range, then a modified $\mathcal{P}_\mathcal{R}$ can mimic a tensor contribution, leading to a near-degeneracy. This can lead to large uncertainty in the tensor amplitude, r. Once r is measured or tightly constrained in B-mode experiments, this near degeneracy will be broken. As examples here, we do allow r to float, but also show what happens when r is constrained to take the values $r = 0.1$ and $r = 0.01$ in the reconstruction.

Figure 27 shows the reconstruction obtained using the 2015 *Planck* TT+lowP likelihood, BAO, SNIa, HST, and a $z_{\rm re} > 6$ prior. Including these ancillary likelihoods improves the constraint on the PPS by helping to fix the cosmological parameters (e.g., H_0, τ, and the late-time expansion history), which in this context may be regarded as nuisance parameters. These results were obtained by modifying `CosmoMC` to incorporate the n-knot parameterization of the PPS. Here 12 knots were used and the mean reconstruction as well as the $1\,\sigma$ and $2\,\sigma$ limits are shown. Some $1\,\sigma$ sample trajectories (dashed curves) are also shown to illustrate the degree of correlation or smoothing of the reconstruction. The tensor trajectories are also shown, but, as explained above, have been constrained to be straight lines.

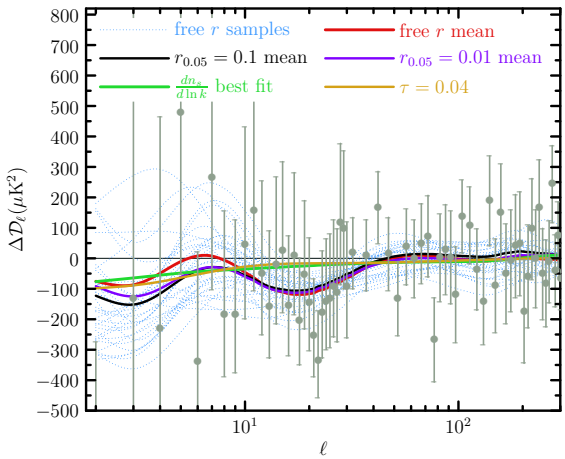

Fig. 29. Reconstructed $\mathcal{D}_\ell^{TT}$ power spectra with the base ΛCDM best-fit subtracted. The mean spectra shown are for the floating r and the two fixed r cases with 12 cubic spline knots. These should be contrasted with the running best-fit mean (green) and the similar looking uniform n_s case in which τ has been lowered from its best-fit base ΛCDM value to 0.04. Data points are the *Planck* 2015 `Commander` ($\ell < 30$) and `Plik` ($\ell \geq 30$) temperature power spectrum.

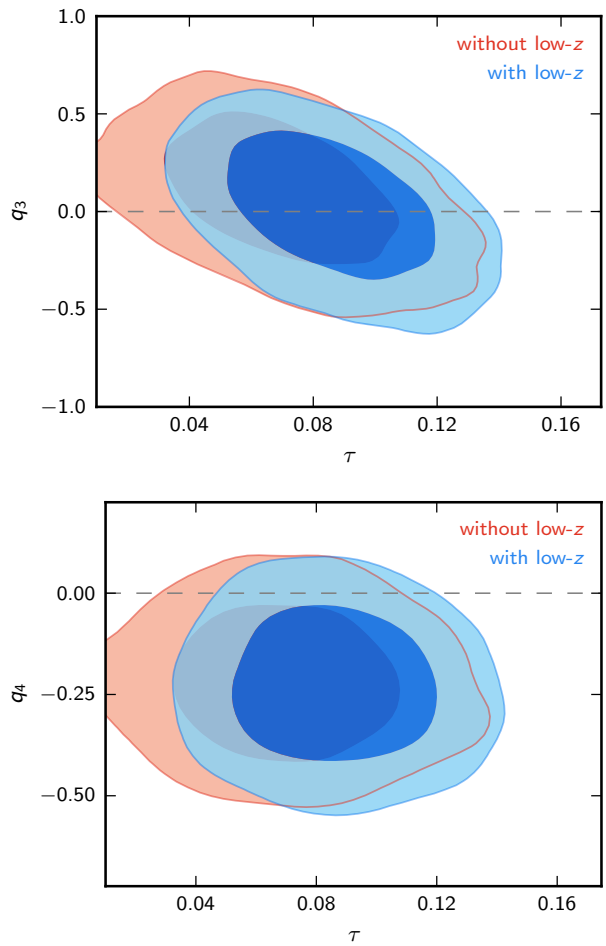

Fig. 30. The degeneracy between τ and the knot variables q_3 and q_4 in the 12-knot case shown in Fig. 27.

In the top panel r is allowed to freely float, and a wide range of r is allowed because of the near-degeneracy with the low-k scalar power. Two illustrative values of fixed r (i.e., $r = 0.1$ and $r = 0.01$) are also shown, to give an idea of how much the reconstruction is sensitive to variations in r within the range of presently plausible values.

The reconstructions using the 2013 *Planck* likelihood in place of the 2015 likelihood are broadly consistent with the reconstruction shown in Fig. 27. To demonstrate robustness with respect to the interpolation scheme we tried using linear interpolation instead of cubic splines and found that the reconstruction was consistent provided enough knots (i.e., $n_{\rm knot} \approx 14$) were used. At intermediate k the reconstruction is consistent with a simple power law, corresponding to a straight line in Fig. 27. We observe that once k drops, so that the effective multipole being probed is below about 60, deviations from a power law appear, but the dispersion in allowed trajectories also rises as a consequence of cosmic variance. The power deficit dip at $k \sim 0.002$ Mpc^{-1} (i.e., $\ell_k \equiv kD_{\rm rec} \sim 30$, where $D_{\rm rec}$ is the comoving distance to recombination) is largely driven by the power spectrum anomaly in the $\ell \approx 20$–30 range that has been evident since the early spectra from WMAP (Bennett et al., 2011), and verified by *Planck*.

We also explore the impact of including the *Planck* polarization likelihood in the reconstruction. Figure 28 shows the reconstructed power spectra using various combinations of the polarization and temperature data. The $\ell < 30$ treatments are the same in all cases, so this is mainly a test of the higher k region. What is seen is that, except at high k, the EE polarization data also enforce a nearly uniform n_s, consistent with that from TT, over a broad k-range. When TE is used alone, or TE and EE are used in combination, the result is also very similar. The upper right panel shows the constraints from all three spectra together, and the errors on the reconstruction are now better than those from TT alone.

It is interesting to examine how the TT power spectrum obtained using the above reconstructions compares to the CMB data, in particular around the range $\ell \approx 20$–30, corresponding roughly to $k_4 \approx 1.5 \times 10^{-3}$ Mpc^{-1}. In Fig. 29 the differences in $\mathcal{D}_\ell^{TT}$ from the best-fit simple power-law model are plotted for various assumptions concerning r. We see that a better fit than the power-law model can apparently be obtained around $\ell \approx 20$–30. We quantify this improvement below.

Due to the degeneracy of scalar and tensor contributions to $\mathcal{D}_\ell^{TT}$, the significance of the low-ℓ anomaly depends on the tensor prior and whether polarization data are used. For $k < 10^{-3}$, once more degeneracy appears: the shape of $\mathcal{D}_\ell^{TT}$ also depends on the reionization optical depth, τ. In Fig. 29 we also show the effect of replacing the best-fit τ for tilted base ΛCDM with a low value, while keeping $A_s e^{-2\tau}$ unchanged. A low τ bends $\mathcal{D}_\ell^{TT}$ downward at $\ell \lesssim 10$. For the 12-knot (or similar) runs, if τ is allowed to run into (nonphysically) small values $\tau \lesssim 0.04$, a slight rise in $\mathcal{P}_\mathcal{R}(k)$ at $k \sim 3 \times 10^{-4}$ Mpc^{-1} is preferred to compensate the low-τ effect. This degeneracy can be broken to a certain extent using low-redshift data: $z_{\rm re} > 6$ from quasar observations (Becker et al., 2001), BAO (SDSS), Supernova (JLA), and HST.

It is evident that allowing n_s to run is not what the $\mathcal{D}_\ell^{TT}$ data prefer. The best-fit running is also shown in Fig. 29. The k-space $\mathcal{P}_\mathcal{R}(k)$-response shown in Fig. 27 shows that running does not capture the shape of the low-ℓ residuals.

We have shown that the cubic spline reconstruction studied in this section consistently produces a dip in q_4, corresponding to

Table 10. Reduced χ^2 and p-values for low-k knots (5 knots) and high-k knots (6 knots, pivot knot excluded), with the null hypothesis being the best-fit power law spectrum. Low-z data refers to BAO+SN+HST+$z_{\rm re}$>6 prior. In all cases lowP data are used.

r prior	low-z data	*Planck* data	low-k $\chi^2_{\rm reduced}$	low-k p-value	high-k $\chi^2_{\rm reduced}$	high-k p-value	q_3 constraint	q_4 constraint
$0 \le r \le 1$	used	TT	0.95	0.45	0.17	0.98	-0.07 ± 0.28	-0.39 ± 0.20
$r = 0.01$	used	TT	1.13	0.34	0.09	0.997	0.01 ± 0.24	-0.23 ± 0.12
$r = 0.01$	not used	TT	0.89	0.49	0.36	0.90	0.10 ± 0.24	-0.23 ± 0.12
$r = 0.1$	used	TT	1.70	0.13	0.12	0.994	-0.04 ± 0.26	-0.28 ± 0.13
$r = 0.1$	not used	TT	1.46	0.20	0.38	0.89	0.05 ± 0.27	-0.28 ± 0.13
$r = 0.1$	used	TT,TE,EE	1.71	0.13	0.17	0.985	-0.02 ± 0.25	-0.30 ± 0.12
$r = 0.1$	used	TE,EE	1.72	0.13	0.38	0.89	0.06 ± 0.25	-0.32 ± 0.15
$r = 0.1$	used	TE	1.80	0.11	0.26	0.95	-0.02 ± 0.27	-0.17 ± 0.16
$r = 0.1$	used	EE	1.78	0.11	0.18	0.98	0.09 ± 0.25	-0.39 ± 0.16
$r = 0.1$	used	TT+lensing	1.54	0.17	0.05	0.9995	0.05 ± 0.25	-0.27 ± 0.13

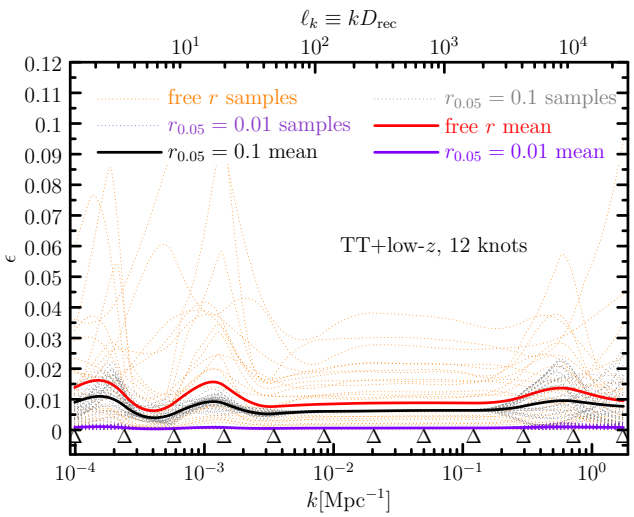

Fig. 31. Slow-roll parameter ϵ for reconstructed trajectories using 12 knots (marked as Δ at the bottom of the figure) with cubic spline interpolation. The mean values are shown for floating r and r fixed to be 0.1 and 0.01. Sample 1 σ trajectories shown for the floating r case show wide variability, which is significantly diminished if r is fixed to $r = 0.1$, as shown.

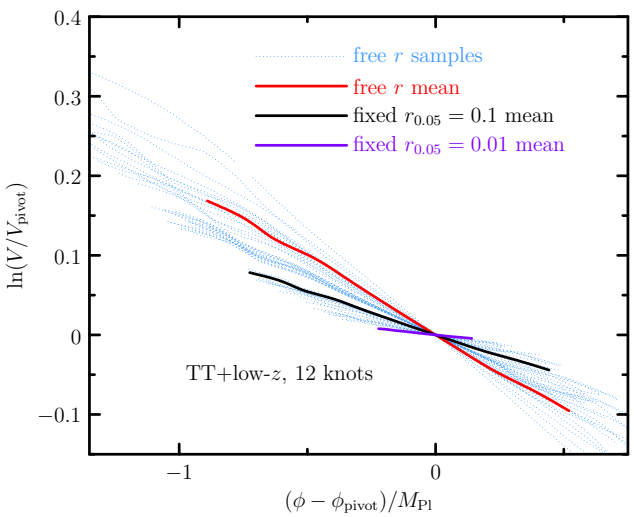

Fig. 32. Reconstructed single-field inflaton potentials from the cubic spline power spectra mode expansion using 12 knots.

$k \approx 1.5 \times 10^{-3}$ Mpc. We now turn to the question of whether this result is real or simply the result of cosmic variance. To assess the statistical significance of the departures of the mean reconstruction from a simple power law, we calculate the low-k and high-k reduced χ^2 for the five q_b values for scales below and six q_b values ($b \neq p$) for scales above $50/D_{\rm rec}$, respectively, indicating the corresponding p-values (i.e., probability to exceed), for various data combinations, in Table 10. The high-k fit is better than expected for reasons that we do not understand, but we attribute this situation to chance. The low-k region shows a poor fit, but in no case does the p-value fall below 10 %. Therefore, even though the low-k dip is robust against the various choices made for the reconstruction, we conclude that it is not statistically significant. The plot for the knot position of the dip (corresponding to q_4) in Fig. 30 does not contradict this conclusion.

Because of the r degeneracy associated with the scalar power, it is best when quoting statistics to use the fixed r cases, although for completeness we show the floating r case as well. There is also a smaller effect associated with the τ degeneracy, and the values quoted have restricted the redshift of reionization to exceed 6. The value $z_{\rm re} = 6.5$ was used in Planck Collaboration XIII (2015). The significance of the low-k anomaly is meaningful only if an explicit r prior and low-redshift constraint on τ have been applied.

Finally, we relate the reconstructed $\mathcal{P}_{\mathcal{R}}(k)$ calculated above to the trajectories of the slow-roll parameter $\epsilon = -\dot{H}/H^2|_{k=aH}$ plotted as a function of k (see Fig. 31). We also plot in Fig. 32 the reconstructed inflationary potential in the region over which the inflationary potential is constrained by the data. Here canonical single-field inflation is assumed, and the value of r enters solely to fix the height of the potential at the pivot scale. This is not entirely self-consistent, but justified by the lack of constraining power on the tensors at present.

8.4. Power spectrum reconstruction summary

The three non-parametric methods for reconstructing the primordial power spectrum explored here support the following two conclusions:

1. Except possibly at low k, over the range of k where the CMB data best constrains the form of the primordial power spectrum, none of the three methods find any statistically significant evidence for deviations from a simple power law form. The fluctuations seen in this regime are entirely consistent with the expectations from cosmic variance and noise.

2. At low k, all three methods reconstruct a power deficit at $k \approx 1.5$–$2.0 \times 10^{-3}\,\mathrm{Mpc}^{-1}$, which can be linked to the dip in the TT angular power spectrum at $\ell \approx 20$–30. This agreement suggests that the reconstruction of this "anomaly" is not an artefact of any of the methods, but rather inherent in the CMB data itself. However, the evidence for this feature is marginal since it is in a region of the spectrum where the fluctuations from cosmic variance are large.

9. Search for parameterized features

In this section, we explore the possibility of a radical departure from the near-scale-invariant power-law spectrum, $\mathcal{P}^0_{\mathcal{R}}(k) = A_s(k/k_*)^{n_s-1}$, of the standard slow-roll scenario for a selection of theoretically motivated parameterizations of the spectrum.

9.1. Models

9.1.1. Step in the inflaton potential

A sudden, step-like feature in the inflaton potential (Adams et al., 2001) or the sound speed (Achúcarro et al., 2011) will lead to a localized oscillatory burst in the scalar primordial power spectrum. A general parameterization describing both a tanh-step in the potential and in the warp term of a DBI model was proposed in Miranda & Hu (2014):

$$\ln \mathcal{P}^s_{\mathcal{R}}(k) = \exp\left[\ln \mathcal{P}^0_{\mathcal{R}}(k) + \mathcal{I}_0(k) + \ln\left(1 + \mathcal{I}_1^2(k)\right)\right], \tag{71}$$

where the first- and second-order terms are given by

$$\mathcal{I}_0 = \mathcal{A}_s\, \mathcal{W}_0(k/k_s)\, \mathcal{D}\left(\frac{k/k_s}{x_s}\right), \tag{72}$$

$$\mathcal{I}_1 = \frac{1}{\sqrt{2}}\left[\frac{\pi}{2}(1-n_s) + [\mathcal{A}_s\, \mathcal{W}_1(k/k_s) + \mathcal{A}_2\, \mathcal{W}_2(k/k_s) + \mathcal{A}_3\, \mathcal{W}_3(k/k_s)]\, \mathcal{D}\left(\frac{k/k_s}{x_s}\right)\right], \tag{73}$$

with window functions

$$\mathcal{W}_0(x) = \frac{1}{2x^4}\left[\left(18x - 6x^3\right)\cos 2x + \left(15x^2 - 9\right)\sin 2x\right], \tag{74}$$

$$\mathcal{W}_1(x) = -\frac{1}{x^4}\left\{3(x\cos x - \sin x)\left[3x\cos x + \left(2x^2 - 3\right)\sin x\right]\right\}, \tag{75}$$

$$\mathcal{W}_2(x) = \frac{3}{x^3}\left(\sin x - x\cos x\right)^2, \tag{76}$$

$$\mathcal{W}_3(x) = -\frac{1}{x^3}\left[3 + 2x^2 - \left(3 - 4x^2\right)\cos(2x) - 6x\sin(2x)\right], \tag{77}$$

and damping function

$$\mathcal{D}(x) = \frac{x}{\sinh x}. \tag{78}$$

Due to the high complexity of this model, we focus on the limiting case of a step in the potential ($\mathcal{A}_2 = \mathcal{A}_3 = 0$).

9.1.2. Logarithmic oscillations

Logarithmic modulations of the primordial power spectrum generically appear, e.g., in models with non-Bunch-Davies initial conditions (Martin & Brandenberger, 2001; Danielsson, 2002; Bozza et al., 2003), or, approximately, in the axion monodromy model, explored in more detail in Sect. 10. We assume a constant modulation amplitude and use

$$\mathcal{P}^{\log}_{\mathcal{R}}(k) = \mathcal{P}^0_{\mathcal{R}}(k)\left\{1 + \mathcal{A}_{\log}\cos\left[\omega_{\log}\ln\left(\frac{k}{k_*}\right) + \varphi_{\log}\right]\right\}. \tag{79}$$

Model	Parameter	Prior range
Step	$\mathcal{A}_s$	$[0, 2]$
	$\log_{10}\left(k_s/\mathrm{Mpc}^{-1}\right)$	$[-5, 0]$
	$\ln x_s$	$[-1, 5]$
Log osc.	$\mathcal{A}_{\log}$	$[0, 0.5]$
	$\log_{10}\omega_{\log}$	$[0, 2.1]$
	$\varphi_{\log}$	$[0, 2\pi]$
Linear osc.	$\mathcal{A}_{\mathrm{lin}}$	$[0, 0.5]$
	$\log_{10}\omega_{\mathrm{lin}}$	$[0, 2]$
	n_{lin}	$[-1, 1]$
	φ_{lin}	$[0, 2\pi]$
Cutoff	$\log_{10}\left(k_c/\mathrm{Mpc}^{-1}\right)$	$[-5, -2]$

Table 11. Parameters and prior ranges.

9.1.3. Linear oscillations

A modulation linear in k can be obtained, e.g., in boundary effective field theory models (Jackson & Shiu, 2013), and is typically accompanied by a scale-dependent modulation amplitude. We adopt the parameterization used in Meerburg & Spergel (2014), which allows for a strong scale dependence of the modulation amplitude:

$$\mathcal{P}^{\mathrm{lin}}_{\mathcal{R}}(k) = \mathcal{P}^0_{\mathcal{R}}(k)\left[1 + \mathcal{A}_{\mathrm{lin}}\left(\frac{k}{k_*}\right)^{n_{\mathrm{lin}}}\cos\left(\omega_{\mathrm{lin}}\frac{k}{k_*} + \varphi_{\mathrm{lin}}\right)\right]. \tag{80}$$

9.1.4. Cutoff model

If today's largest observable scales exited the Hubble radius before the inflaton field reached the slow-roll attractor, the amplitude of the primordial power spectrum is typically strongly suppressed at low k. As an example of such a model, we consider a scenario in which slow roll is preceded by a stage of kinetic energy domination. The resulting power spectrum was derived by Contaldi et al. (2003) and can be expressed as

$$\ln \mathcal{P}^c_{\mathcal{R}}(k) = \ln \mathcal{P}^0_{\mathcal{R}}(k) + \ln\left(\frac{\pi}{16}\frac{k}{k_c}\left|C_c - D_c\right|^2\right), \tag{81}$$

with

$$C_c = \exp\left(\frac{-ik}{k_c}\right)\left[H_0^{(2)}\left(\frac{k}{2k_c}\right) - \left(\frac{k_c}{k} + i\right)H_1^{(2)}\left(\frac{k}{2k_c}\right)\right], \tag{82}$$

$$D_c = \exp\left(\frac{ik}{k_c}\right)\left[H_0^{(2)}\left(\frac{k}{2k_c}\right) - \left(\frac{k_c}{k} - i\right)H_1^{(2)}\left(\frac{k}{2k_c}\right)\right], \tag{83}$$

where $H_n^{(2)}$ denotes the Hankel function of the second kind. The power spectrum in this model is exponentially suppressed for wavenumbers smaller than the cutoff scale k_c and converges to a standard power-law spectrum for $k \gg k_c$, with an oscillatory transition region for $k \gtrsim k_c$.

Model	*Planck* TT+lowP		*Planck* TT,TE,EE+lowP		PTE
	$\Delta\chi^2_{\rm eff}$	$\ln B$	$\Delta\chi^2_{\rm eff}$	$\ln B$	
Step	−8.6	−0.3	−7.3	−0.6	0.09
Log osc.	−10.6	−1.9	−10.1	−1.5	0.24
Linear osc.	−8.9	−1.9	−10.9	−1.3	0.50
Cutoff	−2.0	−0.4	−2.2	−0.6	0.12

Table 12. Improvement in fit and Bayes factors with respect to power-law base ΛCDM for *Planck* TT+lowP and *Planck* TT,TE,EE+lowP data, as well as approximate probability to exceed the observed $\Delta\chi^2_{\rm eff}$ (p-value), constructed from simulated *Planck* TT+lowP data. Negative Bayes factors indicate a preference for the power-law model.

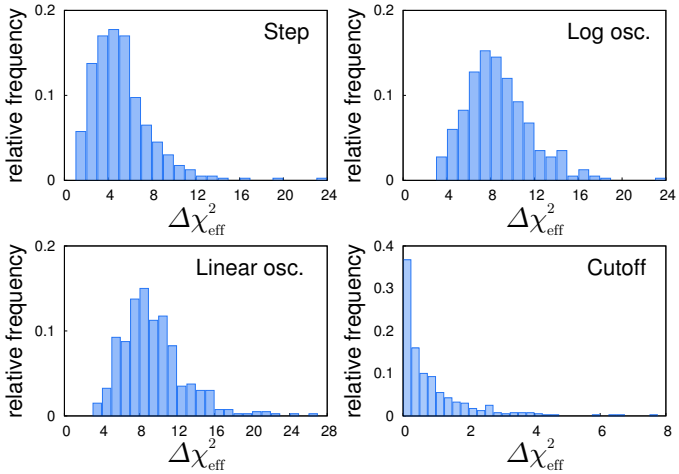

Fig. 33. Distribution of $\Delta\chi^2_{\rm eff}$ from 400 simulated *Planck* TT+lowP data sets.

9.2. Analysis and results

We use `MultiNest` to evaluate the Bayesian evidence for the models and establish parameter constraints, and to roughly identify the global maximum likelihood region of parameter space. The features model best-fit parameters and $\ln\mathcal{L}$ are then obtained with the help of the `CosmoMC` minimization algorithm, taking narrow priors around the `MultiNest` best fit. For the parameters of the features models, we assign flat prior probabilities. The prior ranges are listed in Table 11. Note that throughout this section, for the sake of maximizing sensitivity to very sharp features, the unbinned ("bin1") versions of the high-ℓ TT and TT,TE,EE likelihoods are used instead of the standard, binned versions.

Since the features considered here can lead to broad distortions of the CMB angular power spectrum degenerate with the late-time cosmological parameters (Miranda & Hu, 2014), in all cases we simultaneously vary primordial parameters and all the ΛCDM parameters, but we keep the foreground parameters fixed to their best-fit values for the power-law base ΛCDM model.

We present the Bayes factors with respect to the power-law base ΛCDM model and the improvement in $\chi^2_{\rm eff}$ over the power-law model in Table 12. For our choice of priors, none of the features models are preferred over a power-law spectrum. The best-fit power spectra are plotted in Fig. 34. While the cutoff and step model best fits reproduce the large-scale suppression at $\ell \approx$ 20–30 also obtained by direct power spectrum reconstruction in

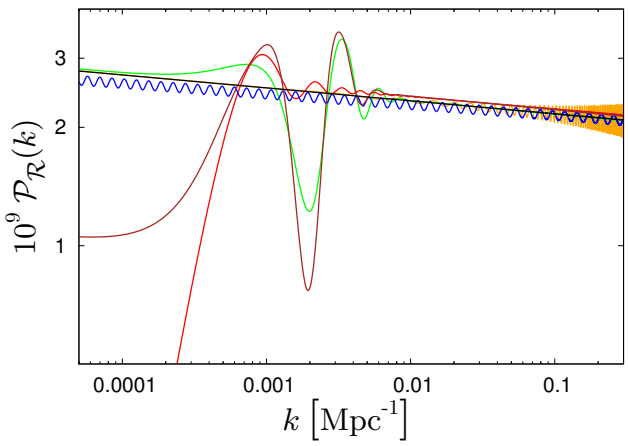

Fig. 34. Best-fit power spectra for the power-law (black curve), step (green), logarithmic oscillation (blue), linear oscillation (orange), and cutoff (red) models using *Planck* TT+lowP data. The brown curve is the best fit for a model with a step in the warp *and* potential (Eqs. (71)–(78)).

Sect. 8, the oscillation models prefer relatively high frequencies that are beyond the resolution of the reconstruction methods.

In addition to the four features models we also show in Fig. 34 the best fit of a model allowing for steps in both inflaton potential and warp (brown line); note particularly the strong resemblance to the reconstructed features of the previous section. The effective $\Delta\chi^2$ for this model is −12.1 (−11.5) for *Planck* TT+lowP (*Planck* TT,TE,EE+lowP) data, at the cost of adding five new parameters, resulting in a ln-Bayes factor of −0.8 (−0.4). A similar phenomenology can be also be found for the case of a sudden change in the slope of the inflaton potential (Starobinsky, 1992; Choe et al., 2004), which yields a best-fit $\Delta\chi^2 = -4.5(-4.9)$ for two extra parameters.

As shown in Table 13, constraints on the remaining cosmological parameters are not significantly affected when allowing for the presence of features.

For the cutoff and step models, the inclusion of *Planck* small-scale polarization data does not add much in terms of direct sensitivity; the best fits lie in the same parameter region as for *Planck* TT+lowP data and the $\Delta\chi^2_{\rm eff}$ and Bayes factors are not subject to major changes. The two oscillation models' *Planck* TT+lowP best fits, on the other hand, also predict a non-negligible signature in the polarization spectra at high ℓ. Therefore, if the features were real, one would expect an additional improvement in $\Delta\chi^2$ for *Planck* TT,TE,EE+lowP. This is not the case here. Though the linear oscillation model's maximum $\Delta\chi^2$ does increase, the local $\Delta\chi^2$ in the *Planck* TT+lowP best-fit regions is in fact reduced for both models, and the global likelihood maxima occur at different frequencies ($\log_{10}\omega_{\rm log} = 1.25$ and $\log_{10}\omega_{\rm lin} = 1.02$) compared to their *Planck* TT+lowP counterparts.

In addition to the Bayesian evidence analysis, we also approach the matter of the statistical relevance of the features models from a frequentist statistics perspective, in order to give the $\Delta\chi^2_{\rm eff}$ numbers a quantitative interpretation. Assuming that the underlying $\mathcal{P}_{\mathcal{R}}(k)$ was actually a featureless power law, we can ask how large an improvement to $\ln\mathcal{L}$ the different features models would yield on average, just by overfitting scatter from cosmic variance and noise. For this purpose, we simulate *Planck* power spectrum data sets consisting of tempera-

Parameter	Step	Log osc.	Linear osc.	Cutoff	Power law
$100\,\omega_b$	2.23 ± 0.02	2.22 ± 0.02	2.23 ± 0.02	2.23 ± 0.02	2.23 ± 0.02
$10\,\omega_c$	1.20 ± 0.02	1.20 ± 0.02	1.20 ± 0.02	1.19 ± 0.02	1.19 ± 0.02
$100\,\theta_{MC}$	1.0409 ± 0.0004	1.0409 ± 0.0004	1.0409 ± 0.0004	1.0410 ± 0.0005	1.0409 ± 0.0005
τ	0.083 ± 0.015	0.082 ± 0.015	0.084 ± 0.014	0.086 ± 0.017	0.085 ± 0.016
$\ln\left(10^{10}A_s\right)$	3.10 ± 0.03	3.10 ± 0.03	3.10 ± 0.03	3.11 ± 0.03	3.10 ± 0.03
n_s	0.966 ± 0.005	0.970 ± 0.007	0.967 ± 0.004	0.968 ± 0.005	0.968 ± 0.005
$\mathcal{A}_s$	0.374	...	...	...	...
$\log_{10}\left(k_s/\mathrm{Mpc}^{-1}\right)$	−3.10	...	...	...	...
$\ln x_s$	0.342	...	...	...	...
$\mathcal{A}_{\log}$	...	0.0278	...	...	...
$\log_{10}\omega_{\log}$	...	1.51	...	...	...
$\varphi_{\log}/2\pi$	...	0.634	...	...	...
$\mathcal{A}_{\mathrm{lin}}$	...	...	0.0292	...	...
$\log_{10}\omega_{\mathrm{lin}}$	...	...	1.73	...	...
n_{lin}	...	...	0.662	...	...
$\varphi_{\mathrm{lin}}/2\pi$	...	...	0.554	...	...
$\log_{10}\left(k_c/\mathrm{Mpc}^{-1}\right)$	...	...	...	−3.44	...

Table 13. Best-fit features parameters and parameter constraints on the remaining cosmological parameters for the four features models for *Planck* TT+lowP data. Note that the foreground parameters have been fixed to their power-law base ΛCDM best-fit values.

ture and polarization up to $\ell = 29$ and unbinned temperature for $30 \leq \ell \leq 2508$, taking as input fiducial spectra the power-law base ΛCDM model's best-fit spectra.

For each of these simulated *Planck* data sets, we perform the following procedure: (i) find the power-law ΛCDM model's best-fit parameters with `CosmoMC`'s minimization algorithm, (ii) fix the non-primordial parameters $(\omega_b, \omega_c, \theta_{MC}, \tau)$ to their respective best-fit values, (iii) using `MultiNest`, find the best fit of the features models,[9] and (iv) extract the effective $\Delta\chi^2$ between power-law and features models.

The resulting distributions are shown in Fig. 33. Compared to the real data $\Delta\chi^2$ values from Table 12, they are biased towards lower values, since we do not vary the late-time cosmological parameters in the analysis of the simulated data. Nonetheless, the observed improvements in the fit do not appear to be extraordinarily large, with the respective (conservative) p-values ranging between 0.09 and 0.50.

These observations lead to the conclusion that even though some of the peculiarities seen in the residuals of the *Planck* data with respect to a power-law primordial spectrum may be explained in terms of primordial features, none of the simple model templates considered here are required by *Planck* data. The simplicity of the power-law spectrum continues to give it an edge over more complicated initial spectra and the most plausible explanation for the apparent features in the data remains that we are just observing fluctuations due to cosmic variance at large scales and noise at small scales.

10. Implications of *Planck* bispectral constraints on inflationary models

The combination of power spectrum constraints and primordial non-Gaussianity (NG) constraints, such as the *Planck* upper bound on the NG amplitude f_{NL} (Planck Collaboration XVII, 2015), can be exploited to limit extensions to the simplest standard single-field models of slow-roll inflation. The next subsection considers inflationary models with a non-standard kinetic term (Garriga & Mukhanov, 1999), where the inflaton Lagrangian is a general function of the scalar inflaton field and its first derivative, $\mathfrak{L} = P(\phi, X)$, where $X = -g^{\mu\nu}\partial_\mu\phi\partial_\nu\phi/2$ (Garriga & Mukhanov, 1999; Chen et al., 2007). Sect. 10.2 focuses on a specific example of a single-field model of inflation with more general higher-derivative operators, the so-called "Galileon inflation." Sect. 10.3 presents constraints on axion monodromy inflation. See Planck Collaboration XVII (2015) for the analysis of other interesting non-standard inflationary models, including warm inflation (Berera, 1995), whose f_{NL} predictions can be constrained by *Planck* .

10.1. Inflation with a non-standard kinetic term

This class of models includes k-inflation (Armendáriz-Picón et al., 1999; Garriga & Mukhanov, 1999) and Dirac-Born-Infield (DBI) models introduced in the context of brane inflation (Silverstein & Tong, 2004; Alishahiha et al., 2004; Chen, 2005b,a). In these models inflation can take place despite a steep potential or may be driven by the kinetic term.

Moreover, one of the main predictions of inflationary models with a non-standard kinetic term is that the inflaton perturbations can propagate with a sound speed $c_s < 1$. We show how the *Planck* combined measurement of the power spectrum and the nonlinearity parameter f_{NL} (Planck Collaboration XVII, 2015) improves constraints on this class of models by breaking degeneracies between the parameters determining the observable power spectra. Such degeneracies (see, e.g., Peiris et al. (2007), Powell et al. (2009), Lorenz et al. (2008), Agarwal & Bean (2009), and Baumann et al. (2015)) are evident from the expressions for the power spectra. We adopt the same notation as Planck Collaboration XXIV (2014). At leading order in the slow-roll parameters the scalar power spectrum depends addi-

[9] Due to the multimodal nature of the posterior, usual minimization routines perform poorly here.

tionally on the sound speed c_s via (Garriga & Mukhanov, 1999)

$$A_s \approx \frac{1}{8\pi^2 M_{pl}^2} \frac{H^2}{c_s \epsilon_1}, \tag{84}$$

which is evaluated at $kc_s = aH$. Correspondingly, the scalar spectral index

$$n_s - 1 = -2\epsilon_1 - \epsilon_2 - s \tag{85}$$

depends on an additional slow-roll parameter, $s = \dot{c}_s/(c_s H)$, which describes the running of the sound speed. The usual consistency relation holding for the standard single-field models of slow-roll inflation ($r = -8n_t$) is modified to $r \approx -8n_t c_s$, with $n_t = -2\epsilon_1$ as usual (Garriga & Mukhanov, 1999).[10]

At lowest order in the slow-roll parameters, there are strong degeneracies between the parameters $(A_s, c_s, \epsilon_1, \epsilon_2, s)$. This makes the constraints on these parameters from the power-spectrum alone not very stringent, and, for parameters like ϵ_1 and ϵ_2, less stringent compared with the standard case. However, combining the constraints on the power spectra observables with those on f_{NL} can also result in a stringent test for this class of inflationary models. Models where the inflaton field has a non-standard kinetic term predict a high level of primordial NG of the scalar perturbations for $c_s \ll 1$, (see, e.g., Chen et al., 2007). Primordial NG is generated by the higher-derivative interaction terms arising from the expansion of the kinetic part of the Lagrangian, $P(\phi, X)$. There are two main contributions to the the amplitude of the NG (i.e., to the nonlinearity parameter f_{NL}) coming from the inflaton field interaction terms $\dot{\delta\phi}(\nabla\delta\phi)^2$ and $(\dot{\delta\phi})^3$ (Chen et al., 2007; Senatore et al., 2010). The NG from the first term scales as c_s^{-2}, while the NG arising from the other term is determined by a second parameter $\tilde{c}_3$ (following the notation of Senatore et al. (2010)). Each of these two interactions produces bispectrum shapes similar to the so-called *equilateral* shape (Babich et al. 2004) for which the signal peaks for equilateral triangles with $k_1 = k_2 = k_3$ (these two shapes are called, respectively, "EFT1" and "EFT2" in Planck Collaboration XVII (2015)). However the difference between the two shapes is such that the total signal is a linear combination of the two, leading to an "orthogonal" bispectral template (Senatore et al., 2010).

The equilateral and orthogonal NG amplitudes can be expressed in terms of the two "microscopic" parameters c_s and $\tilde{c}_3$ (for more details see Planck Collaboration XVII (2015)) according to

$$f_{NL}^{equil} = \frac{1 - c_s^2}{c_s^2}\left[-0.275 - 0.0780 c_s^2 - (2/3) \times 0.780\, \tilde{c}_3\right], \tag{87}$$

$$f_{NL}^{ortho} = \frac{1 - c_s^2}{c_s^2}\left[0.0159 - 0.0167 c_s^2 - (2/3) \times 0.0167\, \tilde{c}_3\right]. \tag{88}$$

Thus the measurements of f_{NL}^{equil} and f_{NL}^{ortho} obtained in the companion paper (Planck Collaboration XVII, 2015) provide a constraint on the sound speed c_s of the inflaton field. Such constraints allow us to combine the NG information with the analyses of the power spectra, since the sound speed is the non-Gaussianity parameter also affecting the power spectra.

[10] We use the more accurate relation

$$r = 16\epsilon_1 c_s^{(1+\epsilon_1)/(1-\epsilon_1)}, \tag{86}$$

accounting for different epochs of freeze-out for the scalar fluctuations (at sound horizon crossing $kc_s = aH$) and tensor perturbations (at horizon crossing $k = aH$) (Peiris et al., 2007; Powell et al., 2009; Lorenz et al., 2008; Agarwal & Bean, 2009; Baumann et al., 2015).

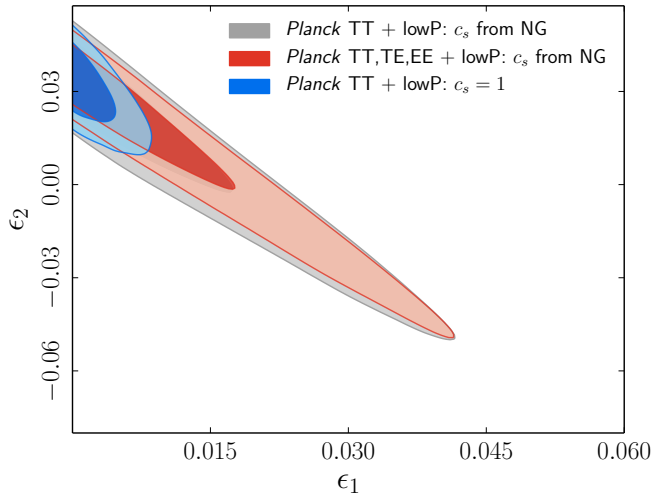

Fig. 35. (ϵ_1, ϵ_2) 68 % and 95 % CL constraints for *Planck* data comparing the canonical Lagrangian case with $c_s = 1$ to the case of varying c_s with a uniform prior $0.024 < c_s < 1$ derived from the *Planck* non-Gaussianity measurements.

In this subsection we consider three cases. In the first case we perform a general analysis as described above (focusing on the simplest case of a constant sound speed, $s = 0$) improving on PCI13 and Planck Collaboration XXIV (2014) by exploiting the full mission temperature and polarization data. The *Planck* constraints on primordial NG in general single-field models of inflation provide the most stringent bound on the inflaton sound speed (Planck Collaboration XVII, 2015) [11]:

$$c_s \geq 0.024 \quad (95\,\%\ \text{CL}). \tag{89}$$

We then use this information on c_s as a uniform prior $0.024 \leq c_s \leq 1$ in Eq. (86) within the HFF formalism, as in PCI13. Fig. 35 shows the joint constraints on ϵ_1 and ϵ_2. *Planck* TT+lowP yields $\epsilon_1 < 0.031$ at 95 % CL. No improvement in the upper bound on ϵ_1 results when using *Planck* TT,TE,EE+lowP. This constraint improves that of the previous analysis in PCI13 and can be compared with the restricted case of $c_s = 1$, also shown in Fig. 35, with $\epsilon_1 < 0.0068$ at 95 % CL. The limits on the sound speed from the constraints on primordial NG are crucial for deriving an upper limit on ϵ_1, because the relation between the tensor-to-scalar ratio and ϵ_1 also involves the sound speed (see, e.g., Eq. (86)). This breaks the degeneracy in the scalar spectral index.

The other two cases analysed involve DBI models. The degeneracy between the different slow-roll parameters can be broken for $s = 0$ or in the case where $s \propto \epsilon_2$. We first consider models defined by an action of the DBI form

$$P(\phi, X) = -f(\phi)^{-1}\sqrt{1 - 2f(\phi)X} + f(\phi)^{-1} - V(\phi), \tag{90}$$

where $V(\phi)$ is the potential and $f(\phi)$ describes the warp factor determined by the geometry of the extra dimensions. We follow an analogous procedure to exploit the NG limits derived in Planck Collaboration XVII (2015) on c_s in the case of DBI models: $c_s \geq 0.087$ (at 95 % CL). Assuming a uniform prior

[11] This section uses results based on f_{NL} constraints from $T + E$ (Planck Collaboration XVII, 2015). In Planck Collaboration XVII (2015) it is shown that although conservatively considered as preliminary, the f_{NL} constraints from $T + E$ are robust, since they pass a extensive battery of validation tests and are in full agreement with T- only constraints.

$0.087 \le c_s \le 1$ and $s = 0$, *Planck* TT+lowP gives $\epsilon_1 < 0.024$ at 95 % CL, a 43 % improvement with respect to PCI13. The addition of high-ℓ TE and EE does not improve the upper bound on ϵ_1 for this DBI case.

Next we update the constraints on the particularly interesting case of infrared DBI models (Chen 2005b,a), where $f(\phi) \approx \lambda/\phi^4$. (For details, see Silverstein & Tong (2004), Alishahiha et al. (2004), Chen et al. (2007) and references therein). In these models the inflaton field moves from the IR to the UV side with an inflaton potential

$$V(\phi) = V_0 - \frac{1}{2}\beta H^2\phi^2 \,. \tag{91}$$

From a theoretical point of view a wide range of values for β is allowed: $0.1 < \beta < 10^9$ (Bean et al., 2008). PCI13 dramatically restricted the allowed parameter space of these models in the limit where stringy effects can be neglected and the usual field theory computation of the primordial curvature perturbation holds (see Chen (2005a,c) and Bean et al. (2008) for more details). In this limit of the IR DBI model, one finds (Chen, 2005c; Chen et al., 2007) $c_s \approx (\beta N_*/3)^{-1}$, $n_s - 1 = -4/N_*$, and $dn_s/d\ln k = -4/N_*^2$. (In this model one can verify that $s \approx 1/N_* \approx \epsilon_2/3$). Combining the uniform prior on c_s with *Planck* TT+lowP, we obtain

$$\beta \le 0.31 \quad (95\,\%\ \mathrm{CL}), \tag{92}$$

and a preference for a high number of e-folds: $78 < N_* < 157$ at 95 % CL.

We now constrain the general case of the IR DBI model, including the "stringy" regime, which occurs when the inflaton extends back in time towards the IR side (Bean et al., 2008). The stringy phase transition is characterized by an interesting phenomenology altering the predictions for cosmological perturbations. A parameterization of the power spectrum of curvature perturbations interpolating between the two regimes is (Bean et al. (2008); see also Ma et al. (2013))

$$\mathcal{P}_{\mathcal{R}}(k) = \frac{A_s}{N_e^{\mathrm{DBI}4}}\left[1 - \frac{1}{(1+x)^2}\right], \tag{93}$$

where $A_s = 324\pi^2/(n_B\beta^4)$ is the amplitude of the perturbations which depends on various microscopic parameters (n_B is the number of branes at the B-throat; see Bean et al. (2008) for more details), while $x = (N_e^{\mathrm{DBI}}/N_c)^8$ sets the stringy phase transition taking place at the critical e-fold N_c. (Here N_e^{DBI} is the number of e-folds to the end of IR DBI inflation). The spectral index and its running are

$$n_s - 1 = \frac{4}{N_e^{\mathrm{DBI}}}\frac{x^2+3x-2}{(x+1)(x+2)}\,, \tag{94a}$$

$$\frac{dn_s}{d\ln k} = \frac{4}{(N_e^{\mathrm{DBI}})^2}\frac{x^4+6x^3-55x^2-96x-4}{(x+1)^2(x+2)^2}\,. \tag{94b}$$

A prediction for the primordial NG in the stringy regime is not available. We assume the standard field-theoretic result for a primordial bispectrum of the equilateral type with an amplitude $f_{\mathrm{NL}}^{\mathrm{DBI}} = -(35/108)\,[(\beta^2\,(N_e^{\mathrm{DBI}})^2/9) - 1]$. By considering the same uniform prior on c_s, we obtain $\beta < 0.77$, $66 < N_e^{\mathrm{DBI}} < 72$, and $x < 0.41$ at 95 % CL, which severely limits the general IR DBI model and strongly restricts the allowed parameter space.

10.2. Galileon inflation

As a further example of the implications of the NG constraints on (non-standard) inflationary models we consider the case of Galileon inflation (Burrage et al., 2011) (see also Kobayashi et al. (2010), Mizuno & Koyama (2010), and Ohashi & Tsujikawa (2012)). This represents a well defined and well motivated model of inflation with more general higher derivatives of the inflaton field compared to the non-standard kinetic term case analyzed above. The Galileon models of inflation are based on the so-called "Galilean symmetry" (Nicolis et al., 2009), and enjoy some well understood stability properties (absence of ghost instabilities and protection from large quantum corrections). This makes the theory also very predictive, since observable quantities (scalar and tensor power spectra and higher-order correlators) depend on a finite number of parameters. From this point of view this class of models shares some of the same properties as the DBI inflationary models (Silverstein & Tong, 2004; Alishahiha et al., 2004). The Galileon field arises naturally within fundamental physics constructions (e.g., de Rham & Gabadadze 2010b,a). These models also offer an interesting example of large-scale modifications to Einstein gravity.

The Galileon model is based on the action (Deffayet et al., 2009a,b)

$$S = \int d^4x\sqrt{-g}\left(\frac{1}{2}R + \sum_{n=0}^{3}\mathcal{L}_n\right), \tag{95}$$

where

$$\begin{aligned}
\mathcal{L}_0 &= c_2 X,\\
\mathcal{L}_1 &= -2(c_3/\Lambda^3)X\Box\phi,\\
\mathcal{L}_2 &= 2(c_4/\Lambda^6)X\left[(\Box\phi)^2 - \left(\nabla_\mu\nabla_\nu\phi\right)^2\right] + (c_4/\Lambda^6)X^2 R,\\
\mathcal{L}_3 &= -2(c_5/\Lambda^9)X\left[(\Box\phi)^3 - 3\Box\phi\left(\nabla_\mu\nabla_\nu\phi\right)^2 + 2\left(\nabla_\mu\nabla_\nu\phi\right)^3\right]\\
&\quad + 6(c_5/\Lambda^9)X^2 G_{\mu\nu}\nabla^\mu\nabla^\nu\phi\,.
\end{aligned} \tag{96}$$

Here $X = -\nabla_\mu\phi\nabla^\mu\phi/2$, $(\nabla_\mu\nabla_\nu\phi)^2 = \nabla_\mu\nabla_\nu\phi\nabla^\mu\nabla^\nu\phi$, and $(\nabla_\mu\nabla_\nu\phi)^3 = \nabla_\mu\nabla_\nu\phi\nabla^\mu\nabla^\rho\phi\nabla^\nu\nabla_\rho\phi$. The coupling coefficients c_i are dimensionless and Λ is the cut-off of the theory. The case of interest includes a potential term $V(\phi) = V_0 + \lambda\phi + (1/2)m^2\phi^2 + \ldots$ to drive inflation.

The predicted scalar power spectrum at leading order is (Ohashi & Tsujikawa (2012); Burrage et al. (2011); Tsujikawa et al. (2013); see also Kobayashi et al. (2011a) and Gao & Steer (2011))[12]

$$\mathcal{P}_{\mathcal{R}} = \left.\frac{H^2}{8\pi^2 M_{\mathrm{Pl}}^2\epsilon_s F c_s}\right|_{c_s k = aH} = \frac{H^4}{8\pi^2 A(\dot\phi_0)^2 c_s^3}, \tag{98}$$

where $F = 1 + \bar{c}_4(\dot\phi_0)^2/(2H^2M_{\mathrm{Pl}}^2)$ and $c_s^2 = -B/A$ is the sound speed of the Galileon field. ϵ_s is different from the usual slow-roll parameter ϵ_1 and at leading order related according to $\epsilon_s = -2(B/1 + 6\bar{c}_3 + 18\bar{c}_4 + 30\bar{c}_5)\epsilon_1$. The scalar spectral index

$$n_s - 1 = -2\epsilon_1 - \eta_s - s \tag{99}$$

[12] For the following expressions it is convenient to define the quantities

$$A = c_2/2 + 6\bar{c}_3 + 27\bar{c}_4 + 60\bar{c}_5, \quad B = -c_2/2 - 4\bar{c}_3 - 13\bar{c}_4 - 24\bar{c}_5, \tag{97}$$

where $\bar{c}_i = c_i Z^{i-2}$ for $i = 2$ to 5, with $Z = H\dot\phi_0/\Lambda^3$. In order to have a healthy model we require $A > 0$ (no ghosts) and $B < 0$ (no gradient instabilities).

depends on the slow-roll parameters ϵ_1, $\eta_s = \dot{\epsilon}_s/(H\epsilon_s)$, and $s = \dot{c}_s/(Hc_s)$. As usual the slow-roll parameter s describes the running of the sound speed. In the following we restrict ourselves to the case of a constant sound speed with $s = 0$. The tensor-to-scalar ratio is

$$r = 16\epsilon_s c_s = 16\epsilon_1 \bar{c}_s\,, \tag{100}$$

where we have introduced the parameter $\bar{c}_s = -[2B/(1 + 6\bar{c}_3 + 18\bar{c}_4 + 30\bar{c}_5)]c_s$, related to the Galileon sound speed. The parameter $\bar{c}_s$ can be either positive or negative. In the negative branch a blue spectral tilt for the primordial gravitational waves is allowed, contrary to the situation for standard slow-roll models of inflation. We introduce such a quantity so that the consistency relation takes the form $r \approx -8n_t\bar{c}_s$, with $n_t = -2\epsilon_1$ analogous to Eq. (86). The measurements of primordial NG constrain $\bar{c}_s$, which in turn constrain ϵ_1 and η_s in Eq. (99). This is analogous to the constraints on ϵ_1 and η of Eq. (85) in the previous subsection.

Galileon models of inflation predict interesting NG signatures (Burrage et al., 2011; Tsujikawa et al., 2013).[13] We have verified (see also Creminelli et al. (2011)) that bispectra can be generated with the same shapes as the "EFT1" and "EFT2" (Senatore et al. (2010); Chen et al. (2007)) constrained in the companion paper (Planck Collaboration XVII, 2015), which usually arise in models of inflation with non-standard kinetic terms, with

$$\begin{aligned} f_{\rm NL}^{\rm EFT1} &= \frac{17}{972}\left(-\frac{5}{c_s^4} + \frac{30}{c_s^2} - \frac{40}{c_s\bar{c}_s} + 15\right), \\ f_{\rm NL}^{\rm EFT2} &= \frac{1}{243}\left(\frac{5}{c_s^4} + \frac{30/A - 55}{c_s^2} + \frac{40}{c_s\bar{c}_s} - 320\frac{c_s}{\bar{c}_s} - \frac{30}{A} + 275\right. \\ &\quad \left. - 225c_s^2 + 280\frac{c_s{}^3}{\bar{c}_s}\right). \end{aligned} \tag{101}$$

As explained in the previous subsection, the linear combinations of these two bispectra produce both equilateral and orthogonal bispectrum templates. Given Eqs. (98)–(101), we can proceed as in the previous section to exploit the limits on primordial NG in a combined analysis with the power spectra analysis. In Planck Collaboration XVII (2015) the constraint $c_s \geq 0.23$ (95 % CL) is obtained based on the constraints on $f_{\rm NL}^{\rm equil}$ and $f_{\rm NL}^{\rm ortho}$. One can proceed as described in Planck Collaboration XVII (2015) to constrain the parameter $\bar{c}_s$ modifying the consistency relation Eq. (100). Adopting a log-uniform prior on A in the interval $10^{-4} \leq A \leq 10^4$ and a uniform prior $10^{-4} \leq c_s \leq 1$, the *Planck* measurements on $f_{\rm NL}^{\rm equil}$ and $f_{\rm NL}^{\rm ortho}$ constrain $\bar{c}_s$ to be $0.038 \leq \bar{c}_s \leq 100$ (95 % CL) (Planck Collaboration XVII, 2015). We also explore the possibility of the negative branch (corresponding to a blue tensor spectral index), finding $-100 \leq \bar{c}_s \leq -0.034$ (95 % CL) (Planck Collaboration XVII, 2015). By allowing a logarithmic prior on $\bar{c}_s$ based on the $f_{\rm NL}$ measurements, Fig. 36 shows the joint constraints on ϵ_1 and η_s for the $n_t < 0$ branch and for the $n_t > 0$ branch. *Planck* TT+lowP+BAO and the NG bounds on $\bar{c}_s$ constrain $\epsilon_1 < 0.036$ at 95 % CL for $n_t < 0$ (and $|\epsilon_1| < 0.041$ for $n_t > 0$).

10.3. Axion monodromy inflation

The mechanism of monodromy inflation (Silverstein & Westphal, 2008; McAllister et al., 2010; Kaloper et al., 2011; Flauger et al., 2014b) in string theory motivates a broad class of inflationary potentials of the form

$$V(\phi) = \mu^{4-p}\phi^p + \Lambda_0^4 e^{-C_0\left(\frac{\phi}{\phi_0}\right)^{p_\Lambda}} \cos\left[\gamma_0 + \frac{\phi_0}{f_0}\left(\frac{\phi}{\phi_0}\right)^{p_f+1}\right]. \tag{102}$$

Here μ, Λ_0, f_0, and ϕ_0 are constants with the dimension of mass and C_0, p, p_Λ, p_f, and γ_0 are dimensionless.

In simpler parameterizations used in prior analyses of oscillations from axion monodromy inflation (Peiris et al., 2013; Planck Collaboration XXII, 2014; Easther & Flauger, 2014; Jackson et al., 2014; Meerburg et al., 2014b; Meerburg & Spergel, 2014; Meerburg et al., 2014a; Meerburg, 2014), one assumes $p_\Lambda = p_f = 0$, corresponding to a sinusoidal term with constant amplitude throughout inflation, taken to be a periodic function of the canonically-normalized inflaton ϕ. Taking $p_\Lambda \neq 0$ and $p_f \neq 0$ allows the *magnitude* and *frequency*, respectively, of the modulation to depend on ϕ. For example, the frequency is always a periodic function of an underlying angular axion field, but its relation to the canonically normalized inflaton field is model dependent.

The microphysical motivation for $p_\Lambda \neq 0$ and $p_f \neq 0$ is that in string theory additional scalar fields, known as "moduli," evolve during inflation. The inflationary potential depends on a subset of these fields. Because the magnitude and frequency of modulations are determined by the vacuum expectation values of moduli, both quantities are then naturally functions of ϕ. The case $p_\Lambda = p_f = 0$ corresponds to when these fields are approximately fixed, stabilized strongly by additional terms in the scalar potential. But in other cases, the axion potential that drives inflation also provides a leading term stabilizing the moduli. The exponential dependence of the magnitude in the potential of Eq. (102) arises because the modulations are generated non-perturbatively, e.g., by instantons. For this reason, the modulations can be undetectably small in this framework, although there are interesting regimes where they could be visible.

Specific examples studied thus far yield exponents p, p_Λ, and p_f which are rational numbers of modest size. For example, models with $p = 3$, 2, 4/3, 1, and 2/3 have been constructed (Silverstein & Westphal, 2008; McAllister et al., 2010, 2014) or in another case $p = 4/3$, $p_\Lambda = -1/3$, and $p_f = -1/3$). Following Flauger et al. (2014b), we investigate the effect of a drift in frequency arising from p_f, neglecting a possible drift in the modulation amplitude by setting $p_\Lambda = C_0 = 0$. Even in this restricted model, a parameter exploration using a fully numerical computation of the primordial power spectrum following the methodology of Peiris et al. (2013) is prohibitive, so we follow Flauger

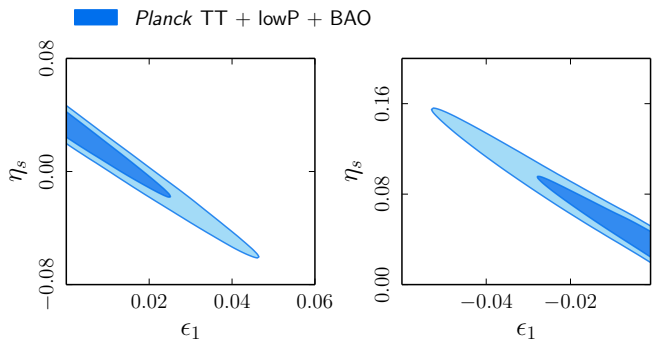

Fig. 36. Marginalized joint 68 % and 95 % CL for the Galileon parameters (ϵ_1, η_s) for $n_t < 0$ (left panel) and $n_t > 0$ (right panel).

[13] See also Mizuno & Koyama (2010), Gao & Steer (2011), Kobayashi et al. (2011b), De Felice & Tsujikawa (2013), and Regan et al. (2014).

et al. (2014b) studying two templates capturing the features of the primordial spectra generated by this potential.

The first template, which we term the "semi-analytic" template, is given by

$$\mathcal{P}_{\mathcal{R}}(k) = \mathcal{P}_{\mathcal{R}}(k_*)\left(\frac{k}{k_*}\right)^{n_s-1}\left\{1+\delta n_s \cos\left[\frac{\phi_0}{f}\left(\frac{\phi_k}{\phi_0}\right)^{p_f+1}+\Delta\phi\right]\right\}. \tag{103}$$

The parameter f is higher than f_0, the underlying axion decay constant in the potential, by a few percent, but this difference will be neglected in this analysis. The quantity ϕ_0 is some fiducial value for the scalar field, and ϕ_k is the value of the scalar field at the time when the mode with comoving momentum k exits the horizon. At leading order in the slow-roll expansion, in units where the reduced Planck mass $M_{\rm Pl} = 1$, $\phi_k = \sqrt{2p\,(N_0 - \ln(k/k_*))}$, where $N_0 = N_* + \phi_{\rm end}^2/(2p)$, and $\phi_{\rm end}$ is the value of the scalar field at the end of inflation.

The second "analytic" template was derived by Flauger et al. (2014b) by expanding the argument of the trigonometric function in Eq. (103) in $\ln(k/k_*)$, leading to

$$\mathcal{P}_{\mathcal{R}}(k) = \mathcal{P}_{\mathcal{R}}(k_*)\left(\frac{k}{k_*}\right)^{n_s-1} \tag{104}$$
$$\times\left\{1+\delta n_s \cos\left[\Delta\phi+\alpha\left(\ln\left(\frac{k}{k_*}\right)+\sum_{n=1}^{2}\frac{c_n}{N_*^n}\ln^{n+1}\left(\frac{k}{k_*}\right)\right)\right]\right\}.$$

The relation between the empirical parameters in the templates and the potential parameters are approximated by $\delta n_s = 3b\sqrt{(2\pi)/\alpha}$, where

$$\alpha = (1+p_f)\frac{\phi_0}{2fN_0}\left(\frac{\sqrt{2pN_0}}{\phi_0}\right)^{1+p_f}, \tag{105}$$

and b is the monotonicity parameter defined in Flauger et al. (2014b), providing relations converting bounds on c_n into bounds on the microphysical parameters of the potential. However, the analytic template can describe more general shapes of primordial spectra than just axion monodromy.

As discussed by Flauger et al. (2014b), there is a degeneracy between p (or alternatively n_s) and f, and for both templates we fix $p = 4/3$ as well as fixing the tensor power spectrum to its form in the absence of oscillations. This is an excellent approximation because tensor oscillations are suppressed relative to the scalar oscillations by a factor $\alpha(f/M_{\rm Pl})^2 \ll 1$. A uniform prior $-\pi < \Delta\phi < \pi$ is adopted for the phase parameter of both templates as well as a prior $0 < \delta n_s < 0.7$ for the modulation amplitude parameter.

In order to specify the semi-analytic template we assume instantaneous reheating, which for $p = 4/3$ corresponds to $N_* \approx 57.5$ for $k_* = 0.05\,{\rm Mpc}^{-1}$. We set $\phi_0 = 12.38\ M_{\rm Pl}$ with $\phi_{\rm end} = 0.59\ M_{\rm Pl}$. We adopt uniform priors $-4 < \log_{10}(f/M_{\rm Pl}) < -1$ and $-0.75 < p_f < 1$ for the remaining parameters. The priors $0 < \ln(\alpha) < 6.9$ and $-2 < c_{1,2} < 2$ specify the *analytic* template. The single-field effective field theory becomes strongly coupled for $\alpha > 200$. However, in principle the string construction remains valid in this regime.

10.3.1. Power spectrum constraints on monodromy inflation

We carry out a Bayesian analysis of axion monodromy inflation using a high-resolution version of CAMB coupled to the PolyChord sampler (see Sect. 8.2). For our baseline analysis we conservatively adopt the PLIK T-only "bin1" likelihood, using only low-ℓ polarization data. In addition to the primordial template priors specified above, we marginalize over the standard priors for the cosmological parameters, the primordial amplitude, and foreground parameters.

The marginalized joint posterior constraints on pairs of primordial parameters for the semi-analytic and analytic templates are shown in Figs. 38 and 37, respectively.

The complex structures seen in these plots arise due to degeneracies in the likelihood frequency "beating" between underlying modulations in the data and the model (Easther et al., 2005). Parameter combinations where "beating" occurs over the largest k ranges lead to discrete local maxima in the likelihood. Fortuitous correlations in the observed realization of the C_ℓ can give the same effect.

The four frequencies picked out by these structures, $\ln(\alpha) \approx \{3.5, 5.4, 6.0, 6.8\}$, show improvements of $\Delta\chi^2_{\rm eff} \approx \{-9.7, -7.1, -12.2, -12.5\}$ relative to ΛCDM, respectively. These frequencies are marked by dotted lines in Fig. 37, and by solid lines in Fig. 38 using Eq. (105). The semi-analytic and analytic templates lead to self-consistent results as expected, with analogous structures being picked out by the likelihood in each template. There is no evidence for a drifting frequency, $p_f \neq 0$ or $c_n \neq 0$. Thus, these parameters serve to smooth out structures in the marginalized posterior.

The improvement in χ^2 is not compelling enough to suggest a primordial origin. Fitting a modulated model to simulations with a smooth spectrum can give rise to $\Delta\chi^2_{\rm eff} \sim -10$ improvements (Flauger et al., 2014b). Furthermore, as the monodromy model contains only a single frequency, at least three of these structures must correspond to spurious fits to the noise. Considering the two models defined by the two templates and the parameter priors specified above, the Bayes factors calculated using PolyChord favours base ΛCDM over both templates by odds of roughly 8:1.

Compared to previous analyses of the linear ($p = 1$) axion monodromy model for WMAP9 (Peiris et al., 2013) and the 2013 *Planck* data (Planck Collaboration XXII, 2014; Easther & Flauger, 2014) the common frequencies are shifted slightly higher. The lower frequency in common appears shifted by a factor of order $\sqrt{p}$, from $\alpha \approx 28.9$ to 31.8, and the higher frequency in common from $\alpha \approx 210$ to 223. Flauger et al. (2014b) suggest that the lower frequency (which had $\Delta\chi^2_{\rm eff} = -9$ in PCI13) was associated with the 4-K cooler line systematic effects in the 2013 *Planck* likelihood. However its presence at similar significance in the 2015 likelihood with improved handling of the cooler line systematics suggests that this explanation is not correct. The second frequency, which appeared with $\Delta\chi^2_{\rm eff} \approx -20$ in WMAP9 (Peiris et al., 2013) is still present but with much reduced significance, suggesting that the high multipoles do not give evidence for this frequency. Additionally, two higher frequencies are present, which, if interpreted as being of primordial origin, correspond to a regime well beyond the validity of the single-field effective field theory. If one of these frequencies were to be confirmed as primordial, a significantly improved understanding of the underlying string construction would need to be undertaken.

In order to check whether the improvement in fit at these four modulation frequencies is responding to residual foregrounds or other systematics, we examine the frequency residuals. Figure 39 shows the residuals of the data minus the model (including the best-fit foreground model) for the four PLIK frequency combinations binned at $\Delta\ell = 30$ for the lowest mod-

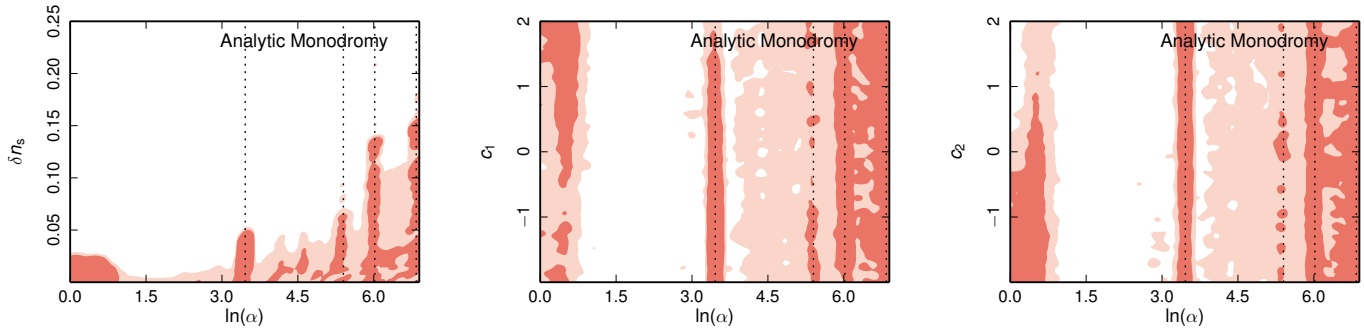

Fig. 37. Constraints on the parameters of the analytic template, showing joint 68 % and 95 % CL. The dotted lines correspond to the frequencies showing the highest likelihood improvements (see text).

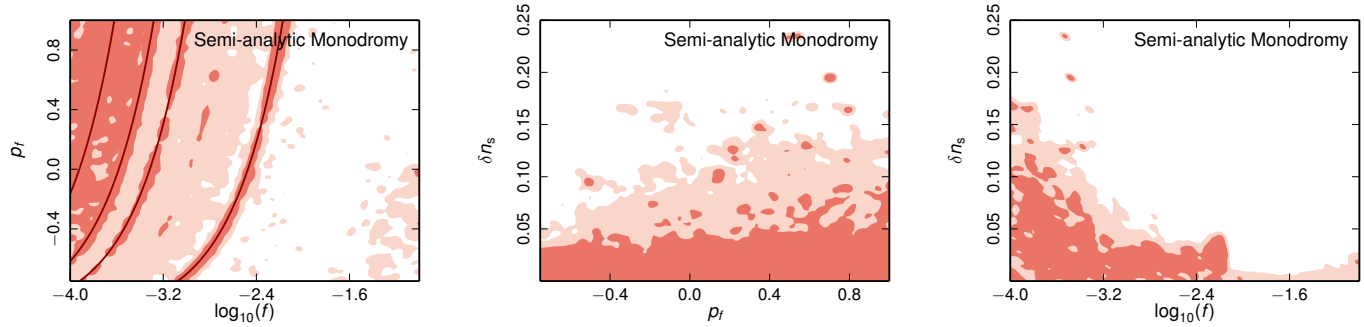

Fig. 38. Constraints on the parameters of the semi-analytic template, showing joint 68 % and 95 % CL. The solid lines on the left-hand panel mark the frequencies showing the highest likelihood improvements (see text).

ulation frequency, $\ln(\alpha) \approx 3.5$. This plot shows no significant frequency dependence, and thus there is no indication that the fit is responding to frequency-dependent systematics. Furthermore, the plot does not show evidence that the improvement for this modulation frequency comes from the feature at $\ell \approx 800$, as suggested by Easther & Flauger (2014). This feature and another at $\ell \approx 1500$ are apparent at all frequency combinations. Similar plots for the three other modulation frequencies also do not show indications of frequency dependence.

In order to confirm whether any of the frequencies picked out here have a primordial origin, one can make use of independent information in the polarization data to perform a cross-check of the temperature prediction which minimizes the "look-elsewhere" effect (Mortonson et al., 2009). Leaving a complete analysis of the independent information in the polarization for future work, we now check whether the temperature-only result remains stable when high-ℓ polarization is added in the likelihood. In Fig. 40 we show a preliminary analysis using the PLIK temperature and polarization "bin1" likelihood plus low-ℓ polarization data. Comparing with the left-hand panels of Figs. 37 and 38, there are slight differences from the T-only analysis. However, all the four frequencies identified in the temperature are present when high-ℓ polarization is added.

10.3.2. Predictions for resonant non-Gaussianity

The left-hand panel of Fig. 41 presents derived constraints on the parameters of the potential, Eq. (102), calculated using the analytic template. Another cross-check of primordial origin is available since the monodromy model predicts resonant non-Gaussianity, generating a bispectrum whose properties would be strongly correlated with that of the power spectrum (Chen et al., 2008; Flauger & Pajer, 2011). Using the mapping

$$f_{\rm NL}^{\rm res} = \frac{\delta n_{\rm s}}{8}\alpha^2, \tag{106}$$

we use the analytic template to derive the posterior probability for the resonant non-Gaussianity signal predicted by constraints from the power spectrum, presented in the middle and right panels of Fig. 41.

Planck Collaboration XVII (2015) use an improved modal estimator to scan for resonant non-Gaussianity. The resolution of this scan is currently limited to $\ln(\alpha) < 3.9$, which is potentially able to probe the lowest frequency picked out in the power spectrum search. However, the modal estimator's sensitivity (imposed by cosmic variance) of $\Delta f_{\rm NL}^{\rm res} \approx 80$ is significantly greater than the predicted value for this frequency from fits to the power spectrum, $f_{\rm NL}^{\rm res} \sim 10$. Efforts to increase the resolution of the modal estimator are ongoing and may allow consistency tests of the significantly higher levels of resonant non-Gaussianity predicted by the higher frequencies in the future.

10.3.3. Power spectrum and bispectrum constraints on axion inflation with a gauge field coupling

We now consider the case where the axion field is coupled to a gauge field. Such a scenario is physically well motivated. From an effective field theory point of view the derivative coupling is natural and must be included since it respects the same shift symmetry that leads to axion models of inflation (Anber & Sorbo,

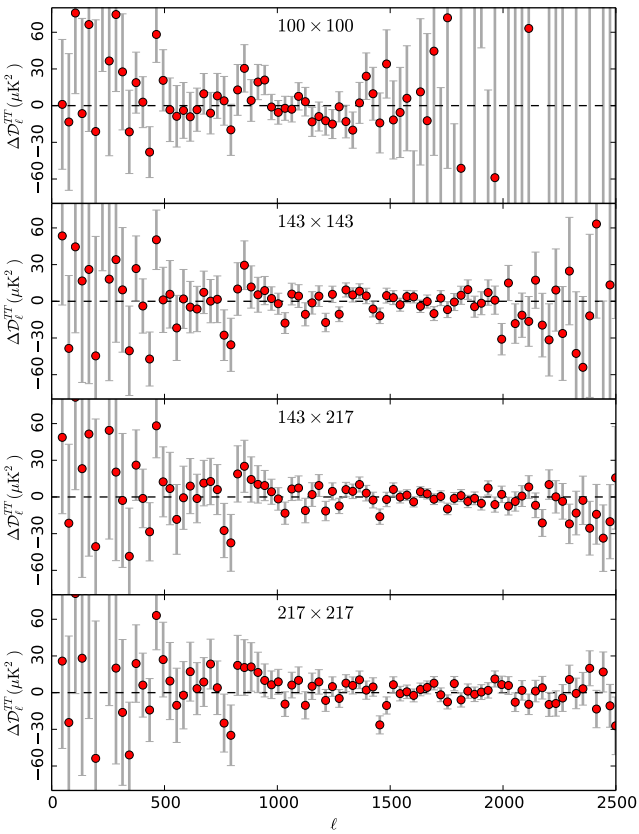

Fig. 39. Frequency residuals for the $\ln(\alpha) \approx 3.5$ likelihood peak, binned at $\Delta\ell = 30$. The $\pm 1\,\sigma$ errors are given by the square root of the diagonal elements of the covariance matrix.

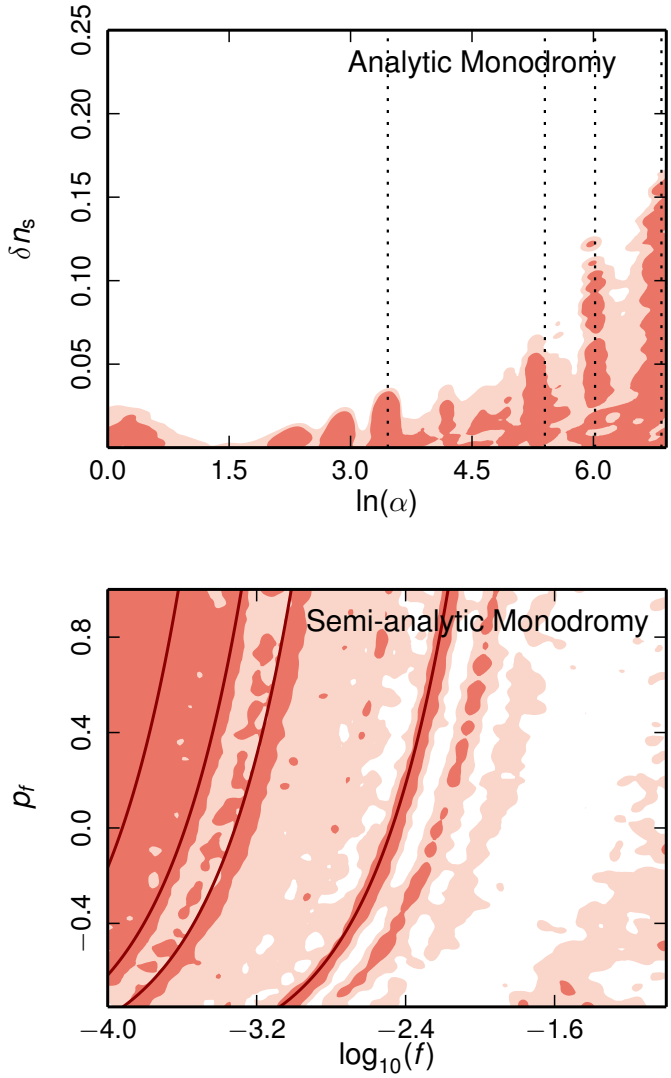

Fig. 40. Constraints on the parameters of the analytic (top) and semi-analytic (bottom) templates with the addition of high-ℓ polarization data in the likelihood, showing joint 68 % and 95 % CL. The lines mark the frequencies showing the highest-likelihood improvements identified in the baseline temperature-only analysis.

2010; Barnaby & Peloso, 2011; Pajer & Peloso, 2013). This type of coupling is also ubiquitous in string theory (see, e.g., Barnaby et al. (2012) and Linde et al. (2013)). The coupling term in the action is (Anber & Sorbo, 2010; Barnaby & Peloso, 2011; Barnaby et al., 2011)

$$S \supset \int d^4x \sqrt{-g}\left(-\frac{\alpha}{4f}\phi F^{\mu\nu}\tilde{F}_{\mu\nu}\right), \tag{107}$$

where $F_{\mu\nu} = \partial_\mu A_\nu - \partial_\nu A_\mu$, its dual is $\tilde{F}^{\mu\nu} = \epsilon^{\mu\nu\alpha\beta}F_{\alpha\beta}/2$, and α is a dimensionless constant which, from an effective field theory perspective, is expected to be of order one. For the potential of the axion field, we will not investigate further the consequences of the oscillatory part of the potential, focusing on the coupling of the axion field to the U(1) gauge field (effectively setting $\Lambda_0 = 0$).

The coupling of a pseudo-scalar axion with the gauge field has interesting phenomenological consequences, both for density perturbations and primordial gravitational waves (Barnaby & Peloso, 2011; Sorbo, 2011; Barnaby et al., 2011, 2012; Meerburg & Pajer, 2013; Ferreira & Sloth, 2014). Gauge field quanta source the axion field via an inverse decay process $\delta A + \delta A \to \delta\varphi$, modifying the usual predictions already at the power-spectrum level. Additionally, the inverse decay can generate a high level of primordial NG.

The parameter

$$\xi = \frac{\alpha|\dot{\phi}|}{2fH} \tag{108}$$

characterizes the strength of the inverse decay effects. If $\xi < 1$ the coupling is too small to produce any modifications to the usual predictions of the uncoupled model. For previous constraints on ξ see Barnaby et al. (2011, 2012) and Meerburg & Pajer (2013). Using the slow-roll approximation and neglecting the small oscillatory part of the potential. One can express

$$\xi = M_{\rm Pl}\frac{\alpha}{f}\sqrt{\frac{p}{8N+2p}}, \tag{109}$$

where N is the number of e-folds to the end of inflation, defined by $\epsilon_{1\rm end} = 1$. The scalar power spectrum of curvature perturbation is given by

$$\mathcal{P}_\mathcal{R}(k) = \mathcal{P}_*\left(\frac{k}{k_*}\right)^{n_s-1}\left[1 + \mathcal{P}_*\left(\frac{k}{k_*}\right)^{n_s-1} f_2(\xi(k))\, e^{4\pi\xi_*}\left(\frac{k}{k_*}\right)^{2\pi\xi_*\eta_*}\right], \tag{110}$$

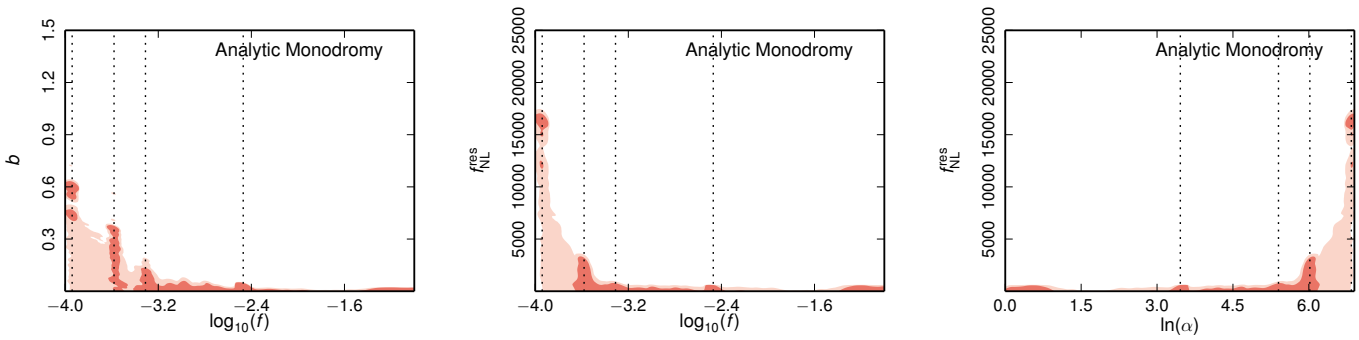

Fig. 41. Derived constraints on the parameters of the potential, Eq. (102), as well as the predicted resonant non-Gaussianity, $f_{\rm NL}^{\rm res}$, using the analytic template, showing joint 68 % and 95 % CL. The dotted lines mark the frequencies showing the highest likelihood improvements (see text).

where (Meerburg & Pajer, 2013)

$$\xi(k) = \xi_* \left[1 + \frac{\eta_*}{2} \ln\left(\frac{k}{k_*}\right)\right] . \tag{111}$$

Here an asterisk indicates evaluation at the pivot scale $k_* = 0.05\,{\rm Mpc}^{-1}$ and $\mathcal{P}_* = H_*^4/(4\pi^2\dot{\phi}_*^2)$ and $n_{\rm s} - 1 = -2\epsilon_* - \eta_*$ are the amplitude and spectral index of the standard slow-roll power spectrum of vacuum-mode curvature perturbations (the usual power spectrum in the absence of the gauge-coupling). Numerically evaluating the function $f_2(\xi)$ (defined in equation (3.27) of Barnaby et al. (2011)), we created an analytical fit to this function, which is accurate to better than 2 % in the range $0.1 < \xi < 7$.[14] In the following, unless stated otherwise, we fix $p = 4/3$ as in the previous subsection and assume instantaneous reheating so that $N_* \approx 57.5$ and the slow-roll parameters ϵ_* and η_* are fixed. For the tensor power spectrum we adopt the approximation (Barnaby et al., 2011)

$$\mathcal{P}_{\rm t}(k) = \mathcal{P}_{\rm t}\left(\frac{k}{k_*}\right)^{n_{\rm t}} \left[1 + \frac{\pi^2}{2}\mathcal{P}_{\rm t} f_{{\rm t},L}(\xi(k)) e^{4\pi\xi_*}\left(\frac{k}{k_*}\right)^{n_{\rm t}+2\pi\eta_*\xi_*}\right] , \tag{112}$$

where

$$f_{{\rm t},L}(\xi(k)) = 2.6 \cdot 10^{-7}\xi^{-5.7}(k) . \tag{113}$$

Here $\mathcal{P}_{\rm t} = 2H_*^2/(\pi^2 M_{\rm Pl}^2)$ and $n_{\rm t} = -2\epsilon_*$ are the "usual" expressions for the tensor amplitude and tensor tilt in standard slow-roll inflation.

The total bispectrum is (Barnaby et al., 2012)

$$B(k_i) = B_{\rm inv.dec.}(k_i) + B_{\rm res}(k_i) \tag{114a}$$

$$= f_{\rm NL}^{\rm inv.dec.}(\xi)\, F_{\rm inv.dec.}(k_i) + B_{\rm res}(k_i), \tag{114b}$$

where the explicit expression for $F_{\rm inv.dec.}(k_i)$ (Barnaby et al. (2011); see also Meerburg & Pajer (2013)) is reported in Planck Collaboration XVII (2015). This shows that the inverse decay effects and the resonant effects (which arise from the oscillatory part of the potential) simply "add up" in the bispectrum. The nonlinearity parameter is

$$f_{\rm NL}^{\rm inv.dec.} = \frac{f_3(\xi_*)\mathcal{P}_*^3 e^{6\pi\xi_*}}{\mathcal{P}_{\mathcal{R}}^2(k_*)} . \tag{115}$$

The function $f_3(\xi_*)$ corresponds to the quantity $f_3(\xi_*; 1, 1)$ defined in equation (3.29) of Barnaby et al. (2011). We have computed $f_3(\xi_*)$ numerically and employed a fit with an accuracy of better than 2 %.[15] We use the observational constraint $f_{\rm NL}^{\rm inv.dec.} = 22.7 \pm 25.5$ (68 % CL) obtained in Planck Collaboration XVII (2015) from an analysis where only the inverse decay type non-Gaussianity is assumed present, so we omit the explicit expression for the resonant bispectrum $B_{\rm res}$, since it will not be used here.

We carried out an MCMC analysis of constraints on the (scalar and tensor) power spectra predicted by this model with the standard PLIK temperature-only likelihood plus low-ℓ polarization, marginalizing over standard priors for the cosmological parameters and foreground parameters, with uniform priors $2.5 \le \ln[10^{10}\mathcal{P}_*] \le 3.7$ and $0.1 \le \xi_* \le 7.0$.

The power spectrum constraint gives

$$0.1 \le \xi_* \le 2.3 \quad (95\,\%\ {\rm CL}). \tag{116}$$

Given that $f_{\rm NL}^{\rm inv.dec.}$ is exponentially sensitive to ξ, this translates into the prediction (using Eq. (115)) $f_{\rm NL}^{\rm inv.dec.} \le 1.2$, which is significantly tighter than the current bispectrum constraint from Planck Collaboration XVII (2015). Indeed, importance sampling with the likelihood for $f_{\rm NL}^{\rm inv.dec.}$, taken to be a Gaussian centred on the NG estimate $f_{\rm NL}^{\rm inv.dec.} = 22.7 \pm 25.5$ (68 % CL) (Planck Collaboration XVII, 2015), changes the limit on ξ_* only at the second decimal place.

We now derive constraints on model parameters using only the observational constraint on $f_{\rm NL}^{\rm inv.dec}$. The constraints thus derived are applicable for generic p and also to the axion monodromy model discussed in Sect. 10.3, even in the case $\Lambda_0 \neq 0$. We follow the procedure described in section 11 of Planck Collaboration XVII (2015). The likelihood for $f_{\rm NL}^{\rm inv.dec.}$ is taken to be a Gaussian centred on the NG estimate $f_{\rm NL}^{\rm inv.dec.} = 22.7 \pm 25.5$ (68 % CL) (Planck Collaboration XVII, 2015). We use the expression of Eq. (115), where $f_3(\xi_*)$ is numerically evaluated. To find the posterior distribution for the parameter ξ_* we choose uniform priors in the intervals $1.5 \times 10^{-9} \le \mathcal{P}_* \le 3.0 \times 10^{-9}$ and $0.1 \le \xi_* \le 7.0$. This yields 95 % CL constraints for ξ_* (for any value of p) of

$$\xi_* \le 2.5 \quad (95\,\%\ {\rm CL}). \tag{117}$$

[14] The fitting function used is $\exp\{-a - b\,\ln(\xi) - c\,[\ln(\xi)]^2 + d\,[\ln(\xi)]^3 + e\,[\ln(\xi)]^4\}$, where the coefficients are $a = 10.8$, $b = 4.58$, $c = 0.51$, $d = 0.01$, and $e = 0.02$.

[15] The fit has the same expression as the one for $f_2(\xi)$ with coefficients $a = 17.0048$, $b = 6.6578$, $c = 0.96479$, $d = 0.0506098$, and $e = 0.039139$.

If we choose a log-constant prior on ξ_* we find

$$\xi_* \leq 2.2 \quad (95\,\%\ \mathrm{CL}). \tag{118}$$

For both cases the results are insensitive to the upper limit chosen for the prior on ξ_* since the likelihood quickly goes to zero for $\xi_* > 3$. As the likelihood for ξ_* is fairly flat, the tighter constraint seen for the log-constant case is mildly prior-driven. The constraints from the bispectrum are consistent with and slightly worse than the result from the power spectrum alone.

Using a similar procedure and Eq. (109) one can also obtain a constraint on α/f. Adopting a log-constant prior $2 \leq \alpha/f \leq 100$[16] and uniform priors $50 \leq N_* \leq 70$ and $1.5 \times 10^{-9} \leq \mathcal{P}_* \leq 3.0 \times 10^{-9}$ we obtain the 95 % CL constraints

$$\alpha/f \leq 48\, M_{\mathrm{Pl}}^{-1} \ \text{ for } \ p = 1, \qquad \alpha/f \leq 35\, M_{\mathrm{Pl}}^{-1} \ \text{ for } \ p = 2, \tag{119}$$

and

$$\alpha/f \leq 42\, M_{\mathrm{Pl}}^{-1} \ \text{ for } \ p = 4/3\,. \tag{120}$$

For example, for a linear potential, $p = 1$, if $\alpha = O(1)$ as suggested by effective field theory, then the axion decay constant f is constrained to be

$$f \geq 0.020\, M_{\mathrm{Pl}} \quad (95\,\%\ \mathrm{CL})\,, \tag{121}$$

while for a potential with $p = 4/3$

$$f \geq 0.023\, M_{\mathrm{Pl}} \quad (95\,\%\ \mathrm{CL}). \tag{122}$$

These limits are complementary to those derived in Sect. 10.3 where a gauge coupling of the axion field is taken into account.

11. Constraints on isocurvature modes

In PCI13, we presented constraints on a number of simple models featuring a mixture of the adiabatic (ADI) mode and one type of isocurvature mode. We covered the cases of CDM density isocurvature (CDI), neutrino density isocurvature (NDI), and neutrino velocity isocurvature (NVI) modes (Bucher et al., 2000), with different assumptions concerning the correlation (Langlois, 1999; Amendola et al., 2002) between the primordial adiabatic and isocurvature perturbations. Isocurvature modes, possibly correlated among themselves and with the adiabatic mode, can be generated in multi-field models of inflation; however, at present a mechanism for exciting the neutrino velocity isocurvature mode is lacking. Section 11.2 shows how these constraints have evolved with the new *Planck* TT+lowP likelihoods, how much including the *Planck* lensing likelihood changes the results, and what extra information the *Planck* high-ℓ polarization contributes. A pure isocurvature mode as a sole source of perturbations has been ruled out (Enqvist et al., 2002), since, as can be seen from Fig. 42, any of the isocurvature modes leads to an acoustic peak structure for the temperature angular power very different from the adiabatic mode, which fits the data very well. The different phases and tilts of the various modes also occur in the polarization spectra, as shown in Fig. 42 for the E mode.[17]

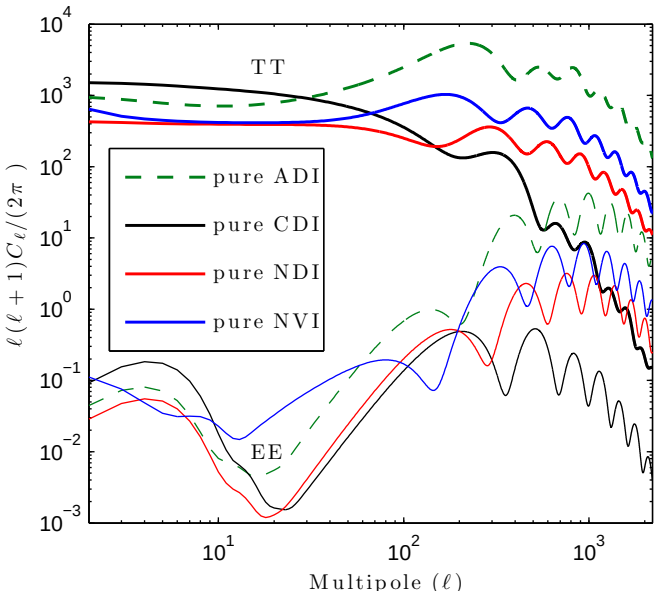

Fig. 42. Angular power spectra for the scale invariant (i.e., $n_{\mathcal{R}\mathcal{R}} = 1$) pure adiabatic mode (ADI, green dashed curves) and for the scale invariant ($n_{\mathcal{I}\mathcal{I}} = 1$) pure isocurvature (CDI, NDI, or NVI) modes, with equal primordial perturbation amplitudes. The thick lines represent the temperature auto-correlation (TT), and the thin lines the E mode polarization auto-correlation (EE).

In Sect. 11.4 we add one extra degree of freedom to the generally-correlated ADI+CDI model by allowing primordial tensor perturbations (assuming the inflationary consistency relation for the tilt of the tensor power spectrum and its running). Our main goal is to explore a possible degeneracy between tensor modes and negatively correlated CDI modes, tending to tilt the large-scale temperature spectrum in opposite directions. In Sect. 11.5, we update the constraints on three special cases motivated by axion or curvaton scenarios.

The goal of this analysis is to test the hypothesis of adiabaticity, and establish the robustness of the base ΛCDM model against different assumptions concerning initial conditions (Sect. 11.3). Adiabaticity is also an important probe of the inflationary paradigm, since any significant detection of isocurvature modes would exclude the possibility that all perturbations in the Universe emerged from quantum fluctuations of a single inflaton field, which can excite only one degree of freedom, the curvature (i.e., adiabatic) perturbation.[18]

[16] We give only the results for a log-constant prior on α/f, which is well-motivated since it corresponds to a log-constant prior on the axion decay constant for some fixed α.

[17] The transfer function mapping the primordial CDI mode to C_ℓ^{TT} is suppressed by a factor $(k/k_{\mathrm{eq}})^{-2} \sim (\ell/\ell_{\mathrm{eq}})^{-2}$ relative to the ADI mode, where k_{eq} is the wavenumber of matter-radiation equality. As seen in Fig. 42, there is a similar damping for the E mode in the CDI versus the ADI case. Therefore, to be observable at high ℓ, a CDI mode should be (highly) blue tilted. So, if the data favoured as small as possible a disturbance by CDI over all scales, then the CDI should have a spectral index, $n_{\mathcal{I}\mathcal{I}}$, of roughly three. In practice, the lowest-ℓ part of the data has very little weight due to cosmic variance, and thus we expect that the data should favour $n_{\mathcal{I}\mathcal{I}}$ less than three, but significantly larger than one. This should be kept in mind when interpreting the results in the CDI case, i.e., one cannot expect strong constraints on the *primordial* CDI fraction at small scales, even if the data are purely adiabatic. The imprint of the baryon density isocurvature (BDI) mode, at least at linear order, in the CMB is indistinguishable from the CDI case, and hence we do not consider it separately as it can be described by $\mathcal{I}_{\mathrm{CDI}}^{\mathrm{effective}} = \mathcal{I}_{\mathrm{CDI}} + (\Omega_{\mathrm{b}}/\Omega_{\mathrm{c}})\mathcal{I}_{\mathrm{BDI}}$. The trispectrum, however, can in principle be used to distinguish the BDI and CDI modes (Grin et al., 2014).

[18] However, conversely, if no isocurvature was detected, the fluctuations could have been seeded either by single- or multi-field inflation, since later processes easily wash out inflationary isocurvature pertur-

In this section, theoretical predictions were obtained with a modified version of the camb code (version Jul14) while parameter exploration was performed with the MultiNest nested sampling algorithm.

11.1. Parameterization and notation

A general mixture of the adiabatic mode and one isocurvature mode is described by the three functions $\mathcal{P}_{\mathcal{RR}}(k)$, $\mathcal{P}_{\mathcal{II}}(k)$, and $\mathcal{P}_{\mathcal{RI}}(k)$, describing the curvature, isocurvature, and cross-correlation power spectra, respectively. Our sign conventions are such that positive values for $\mathcal{P}_{\mathcal{RI}}$ correspond to a positive contribution of the cross-correlation term to the Sachs-Wolfe component of the total temperature spectrum.

As in PCI13, we specify the amplitudes at two scales $k_1 < k_2$ and assume power-law behaviour, so that

$$\mathcal{P}_{\rm ab}(k) = \exp\left[\left(\frac{\ln(k)-\ln(k_2)}{\ln(k_1)-\ln(k_2)}\right)\ln\left(\mathcal{P}^{(1)}_{\rm ab}\right) + \left(\frac{\ln(k)-\ln(k_1)}{\ln(k_2)-\ln(k_1)}\right)\ln\left(\mathcal{P}^{(2)}_{\rm ab}\right)\right], \tag{123}$$

where $\mathrm{a,b} = \mathcal{I},\mathcal{R}$ and $\mathcal{I} = \mathcal{I}_{\rm CDI}$, $\mathcal{I}_{\rm NDI}$, or $\mathcal{I}_{\rm NVI}$. We set $k_1 = 0.002\,{\rm Mpc}^{-1}$ and $k_2 = 0.100\,{\rm Mpc}^{-1}$, so that $[k_1, k_2]$ spans most of the range constrained by the *Planck* data. The positive definiteness of the initial condition matrix imposes a constraint on its elements at any value of k:

$$[\mathcal{P}_{\rm ab}(k)]^2 \le \mathcal{P}_{\rm aa}(k)\mathcal{P}_{\rm bb}(k)\,. \tag{124}$$

We take uniform priors on the positive amplitudes,

$$\mathcal{P}^{(1)}_{\mathcal{RR}}, \mathcal{P}^{(2)}_{\mathcal{RR}} \in (10^{-9},\ 10^{-8})\,, \tag{125}$$

$$\mathcal{P}^{(1)}_{\mathcal{II}}, \mathcal{P}^{(2)}_{\mathcal{II}} \in (0,\ 10^{-8})\,. \tag{126}$$

The correlation spectrum can be positive or negative. For $\mathrm{a} \neq \mathrm{b}$ we apply a uniform prior at large scales (at k_1),

$$\mathcal{P}^{(1)}_{\rm ab} \in (-10^{-8},\ 10^{-8})\,, \tag{127}$$

but reject all parameter combinations violating the constraint in Eq. (124). To ensure that Eq. (124) holds for all k, we restrict ourselves to a scale-independent correlation fraction

$$\cos\Delta_{\rm ab} = \frac{\mathcal{P}_{\rm ab}}{(\mathcal{P}_{\rm aa}\mathcal{P}_{\rm bb})^{1/2}} \in (-1, 1)\,. \tag{128}$$

Thus $\mathcal{P}^{(2)}_{\rm ab}$ is a derived parameter[19] given by

$$\mathcal{P}^{(2)}_{\rm ab} = \mathcal{P}^{(1)}_{\rm ab}\frac{\left(\mathcal{P}^{(2)}_{\rm aa}\mathcal{P}^{(2)}_{\rm bb}\right)^{1/2}}{\left(\mathcal{P}^{(1)}_{\rm aa}\mathcal{P}^{(1)}_{\rm bb}\right)^{1/2}}, \tag{129}$$

which, in terms of spectral indices, is equivalent to

$$n_{\rm ab} = \frac{1}{2}(n_{\rm aa} + n_{\rm bb})\,. \tag{130}$$

The conservative baseline likelihood is *Planck* TT+lowP. The results obtained with *Planck* TT,TE,EE+lowP should be interpreted with caution because the data used in the 2015 release are known to contain some low level systematics, in particular arising from $T \to E$ leakage, and it is possible that such systematics may be fit by the isocurvature auto-correlation and cross-correlation templates. (See Planck Collaboration XIII (2015) for a detailed discussion.)

In what follows, we quote our results in terms of derived parameters identical to those in PCI13. We define the primordial isocurvature fraction as

$$\beta_{\rm iso}(k) = \frac{\mathcal{P}_{\mathcal{II}}(k)}{\mathcal{P}_{\mathcal{RR}}(k) + \mathcal{P}_{\mathcal{II}}(k)}\,. \tag{131}$$

Unlike the primordial correlation fraction $\cos\Delta$ defined in Eq. (128), $\beta_{\rm iso}$ is scale-dependent in the general case. We present bounds on this quantity at $k_{\rm low} = k_1$, $k_{\rm mid} = 0.050\,{\rm Mpc}^{-1}$, and $k_{\rm high} = k_2$.

We report constraints on the relative adiabatic ($\mathrm{ab} = \mathcal{RR}$), isocurvature ($\mathrm{ab} = \mathcal{II}$), and correlation ($\mathrm{ab} = \mathcal{RI}$) according to their contribution to the observed CMB temperature variance in various multipole ranges:

$$\alpha_{\rm ab}(\ell_{\rm min}, \ell_{\rm max}) = \frac{(\Delta T)^2_{\rm ab}(\ell_{\rm min}, \ell_{\rm max})}{(\Delta T)^2_{\rm tot}(\ell_{\rm min}, \ell_{\rm max})}, \tag{132}$$

where

$$(\Delta T)^2_{\rm ab}(\ell_{\rm min}, \ell_{\rm max}) = \sum_{\ell=\ell_{\rm min}}^{\ell_{\rm max}}(2\ell+1)C^{TT}_{{\rm ab},\ell}. \tag{133}$$

The ranges considered are $(\ell_{\rm min}, \ell_{\rm max}) = (2, 20)$, $(21, 200)$, $(201, 2500)$, and $(2, 2500)$, where the last range describes the total contribution to the observed CMB temperature variance. Here $\alpha_{\mathcal{RR}}$ measures the adiabaticity of the temperature angular power spectrum, a value of unity meaning "fully adiabatic initial conditions." Values less than unity mean that some of the observed power comes from the isocurvature or correlation spectrum, while values larger than unity mean that some of the power is "cancelled" by a negatively correlated isocurvature contribution. The relative non-adiabatic contribution can be expressed as $\alpha_{\rm non\text{-}adi} = 1 - \alpha_{\mathcal{RR}} = \alpha_{\mathcal{II}} + \alpha_{\mathcal{RI}}$.

11.2. Results for generally-correlated adiabatic and one isocurvature mode (CDI, NDI, or NVI)

Results are reported as 2D and 1D marginalized posterior probability distributions. Numerical 95 % CL intervals or upper bounds are tabulated in Table 15.

Figure 43 shows the *Planck* 68 % and 95 % CL contours for various 2D combinations of the primordial adiabatic and isocurvature amplitude parameters at large scales ($k_1 = 0.002\,{\rm Mpc}^{-1}$) and small scales ($k_2 = 0.100\,{\rm Mpc}^{-1}$), for (a) the generally-correlated ADI+CDI, (b) ADI+NDI, and (c) ADI+NVI models. Overall, the results using *Planck* TT+lowP are consistent with the nominal mission results in PCI13, but slightly tighter. In the first panels of Figs. 43 (a), (b), and (c), we also show the constraints on the curvature perturbation power in the pure adiabatic case. Comparing the generally-correlated isocurvature case to the pure adiabatic case with the same data combination

bations (Mollerach, 1990; Weinberg, 2004; Beltrán et al., 2005). An example is the curvaton model, in which perturbations can be purely isocurvature at Hubble exit during inflation, but are later converted to ADI if the curvaton or curvaton particles (Linde & Mukhanov, 2006) dominate the energy density at the curvaton's decay. For a summary of various curvaton scenarios, see, e.g., Gordon & Lewis (2003).

[19] Given our ansatz of power-law primordial spectra, if we treated $\mathcal{P}^{(2)}_{\rm ab}$ as an independent parameter as we do with $\mathcal{P}^{(1)}_{\rm ab}$, Eq. (124) would always be violated somewhere outside $[k_1, k_2]$. In PCI13, we dealt with this by assuming that when maximal (anti-)correlation is reached at some scale, the correlation remains at (−)100 % beyond this scale. This introduced a kink in the cross-correlation spectrum, located at a different wavenumber for each model. Even though the range $[k_1, k_2]$ was chosen to span most of the observable scales, this kink tended to impact the smallest (or largest) multipole values used in the analysis. In particular, the kink helped fit the dip in the temperature angular power in the multipole range $\ell \approx 10$–40.

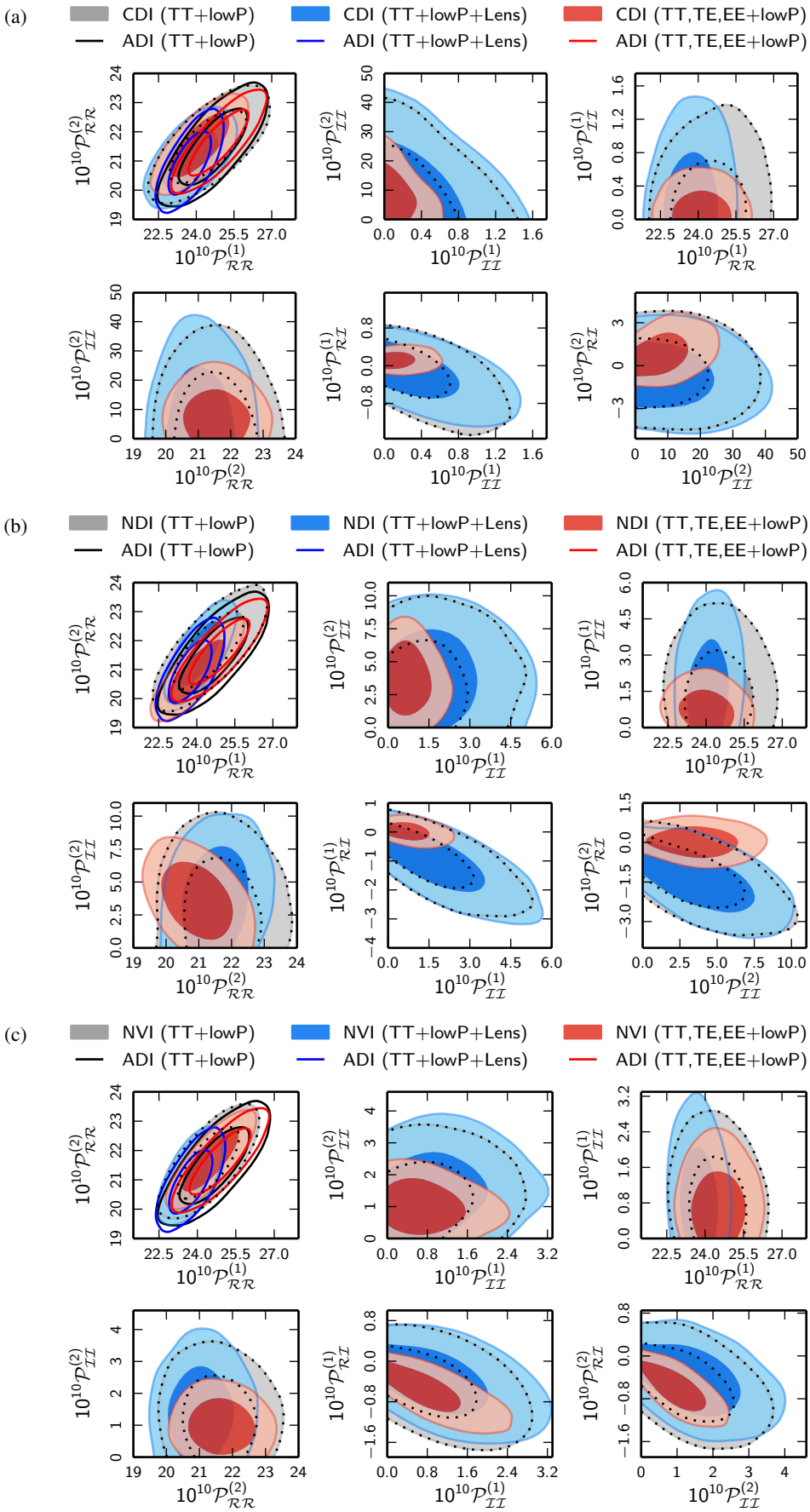

Fig. 43. 68 % and 95 % CL constraints on the primordial perturbation power in general mixed ADI+CDI (a), ADI+NDI (b), and ADI+NVI (c) models at two scales, $k_1 = 0.002\,\mathrm{Mpc}^{-1}$ (1) and $k_2 = 0.100\,\mathrm{Mpc}^{-1}$ (2), for *Planck* TT+lowP (grey regions highlighted by dotted contours), *Planck* TT+lowP+lensing (blue), and *Planck* TT,TE,EE+lowP (red). In the first panels, we also show contours for the pure adiabatic base ΛCDM model, with the corresponding colours of solid lines.

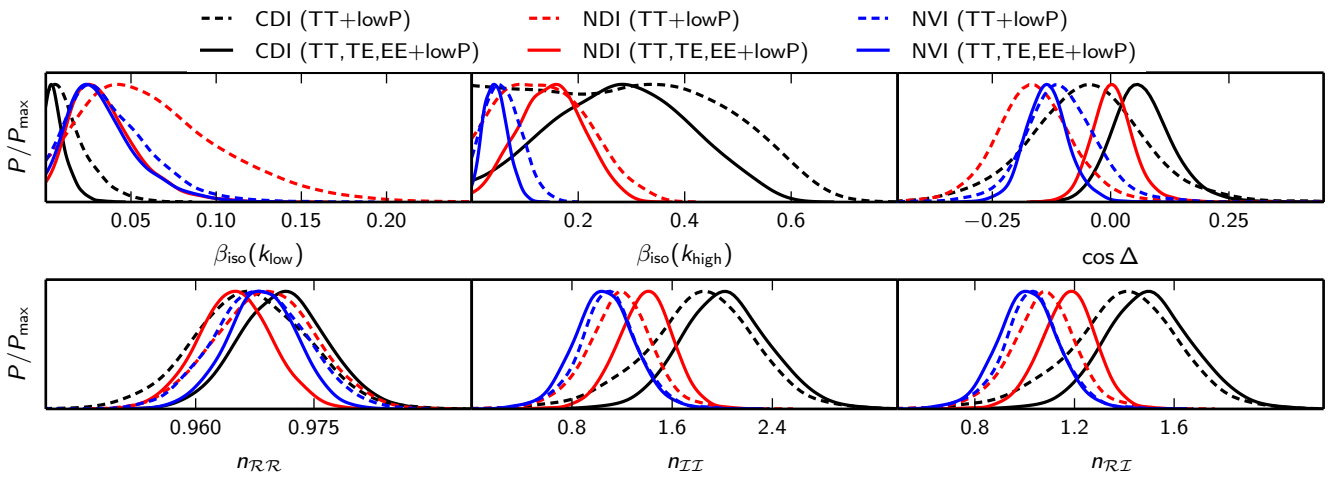

Fig. 44. Constraints on the primordial isocurvature fraction, $\beta_{\rm iso}$, at $k_{\rm low} = 0.002\,{\rm Mpc}^{-1}$ and $k_{\rm high} = 0.100\,{\rm Mpc}^{-1}$, the primordial correlation fraction, $\cos\Delta$, the adiabatic spectral index, $n_{\mathcal{RR}}$, the isocurvature spectral index, $n_{\mathcal{II}}$, and the correlation spectral index, $n_{\mathcal{RI}} = (n_{\mathcal{RR}} + n_{\mathcal{II}})/2$, with *Planck* TT+lowP data (dashed curves) and TT,TE,EE+lowP data (solid curves), for the generally-correlated mixed ADI+CDI (black), ADI+NDI (red), and ADI+NVI (blue) models. All these parameters are derived, and the distributions shown here result from a uniform prior on the primary parameters, as detailed in Eqs. (125)–(127). However, the effect of the non-flat derived-parameter priors is negligible for all parameters except for $n_{\mathcal{II}}$ (and $n_{\mathcal{RI}}$) where the prior biases the distribution toward one. With TT+lowP, the flatness of $\beta_{\rm iso}(k_{\rm high})$ in the CDI case up to a "threshold" value of about 0.5 is a consequence of the $(k/k_{\rm eq})^{-2}$ damping of its transfer function as explained in Footnote 17.

summarizes neatly what the data tell us about the initial conditions. If the contours in the $\mathcal{P}^{(1)}_{\mathcal{RR}}$-$\mathcal{P}^{(2)}_{\mathcal{RR}}$-plane were shifted significantly relative to the pure adiabatic case, the missing power could come either from the isocurvature and postive correlation contributions, or the extra adiabatic power could be cancelled by a negative correlation contribution. We can see that these shifts are small. The low-ℓ temperature data continues to mildly favour a negative correlation (see in particular the bottom middle panel for each of the three models), since compared to the prediction of the best-fit adiabatic base ΛCDM model, the TT angular power at multipoles $\ell \lesssim 40$ is somewhat low. But the dotted grey shaded contours in the three middle top panels show that for *Planck* TT+lowP, the posterior peaks at values $(\mathcal{P}^{(1)}_{\mathcal{II}}, \mathcal{P}^{(2)}_{\mathcal{II}})$ entirely consistent with (0, 0), i.e., the pure adiabatic case is preferred. The best-fit values of $(\mathcal{P}^{(1)}_{\mathcal{II}}, \mathcal{P}^{(2)}_{\mathcal{II}})$ are $(1.4\times10^{-11}, 4.7\times10^{-13})$ for CDI, $(1.2\times10^{-12}, 4.6\times10^{-10})$ for NDI, and $(1.6\times10^{-12}, 2.3\times10^{-10})$ for NVI, while $(\mathcal{P}^{(1)}_{\mathcal{RR}}, \mathcal{P}^{(2)}_{\mathcal{RR}}) \approx (2.4\times10^{-9}, 2.1\times10^{-9})$. It may appear from the bottom-centre panels of Fig. 43 that there is non-zero posterior probability for $\mathcal{P}^{(1)}_{\mathcal{RI}} \neq 0$ when $\mathcal{P}^{(1)}_{\mathcal{II}} = 0$, which would violate the positivity constraint, Eq. (124). However, the left-most pixels of the plots are actually evaluated at values of $\mathcal{P}^{(1)}_{\mathcal{II}}$ large enough so that the constraint is satisfied.

Including the *Planck* lensing likelihood does not significantly affect the non-adiabatic primordial powers, except for tightening the constraints on the adiabatic power (see the blue versus black contours in the first panels of Figs. 43 (a), (b), and (c)). Including the lensing ($C^{\phi\phi}_\ell$) likelihood constrains the optical depth τ more tightly than the high-ℓ temperature and low-ℓ polarization alone (Planck Collaboration XIII, 2015). As there is a strong degeneracy between τ and the primordial (adiabatic) perturbation power $\mathcal{P}_{\mathcal{RR}}$ (denoted in the other sections of this paper by $A_{\rm s}$), it is natural that adding the lensing data leads to stronger constraints on $\mathcal{P}_{\mathcal{RR}}$. Moreover, replacing the low-ℓ likelihood *Planck* lowP by *Planck* lowP+WP constrains τ better (Planck Collaboration XIII, 2015). In the ADI+CDI case the effect of this replacement was very similar to adding the *Planck* lensing data (see also Table 15). Although the *Planck* lensing data do not directly constrain the isocurvature contribution,[20] they can shift and tighten the constraints on some derived isocurvature parameters by affecting the favoured values of the standard parameters (present even in the pure adiabatic model). However, this effect is small, as confirmed by Table 15. Therefore, in the figures we do not show 1D posteriors of the derived isocurvature parameters for *Planck* TT+lowP+lensing, since they would be (almost) indistinguishable from *Planck* TT+lowP, as we see in Fig. 43 for the primary non-adiabatic parameters.

In contrast, the high-ℓ *polarization* data significantly tighten the bounds on isocurvature and cross-correlation parameters, as seen by comparing the dotted grey and red contours in Fig. 43. The significant negative correlation previously allowed by the temperature data in the ADI+CDI and ADI+NDI models is now disfavoured. This is also clearly visible in the 1D posteriors of primordial and observable isocurvature and cross-correlation fractions, shown, respectively, in Fig. 44 and 45; note how the $\cos\Delta$ and $\alpha_{\mathcal{RI}}$ parameters are driven towards zero by the inclusion of the high-ℓ TE,EE data (from the dashed to the solid lines) in the ADI+CDI and ADI+NDI cases. We have also checked that when the lowP data are replaced by a simple Gaussian prior on the reionization optical depth ($\tau = 0.078 \pm 0.019$), the trend is similar: the high-ℓ ($\ell \geq 30$) *Planck* TT data allow a large negative correlation, while the high-ℓ *Planck* TE,EE data prefer positive correlation. This is clearly seen in Fig. 46 for the ADI+CDI case. The best-fit values show an even more dramatic effect; we find $\cos\Delta = -0.55$ with TT+lowP, and +0.15 with TT,TE,EE+lowP.

[20] This is expected, since already with *Planck* TT+lowP, the allowed isocurvature fraction is so small that it hardly affects the lensing potential $C^{\phi\phi}_\ell$.

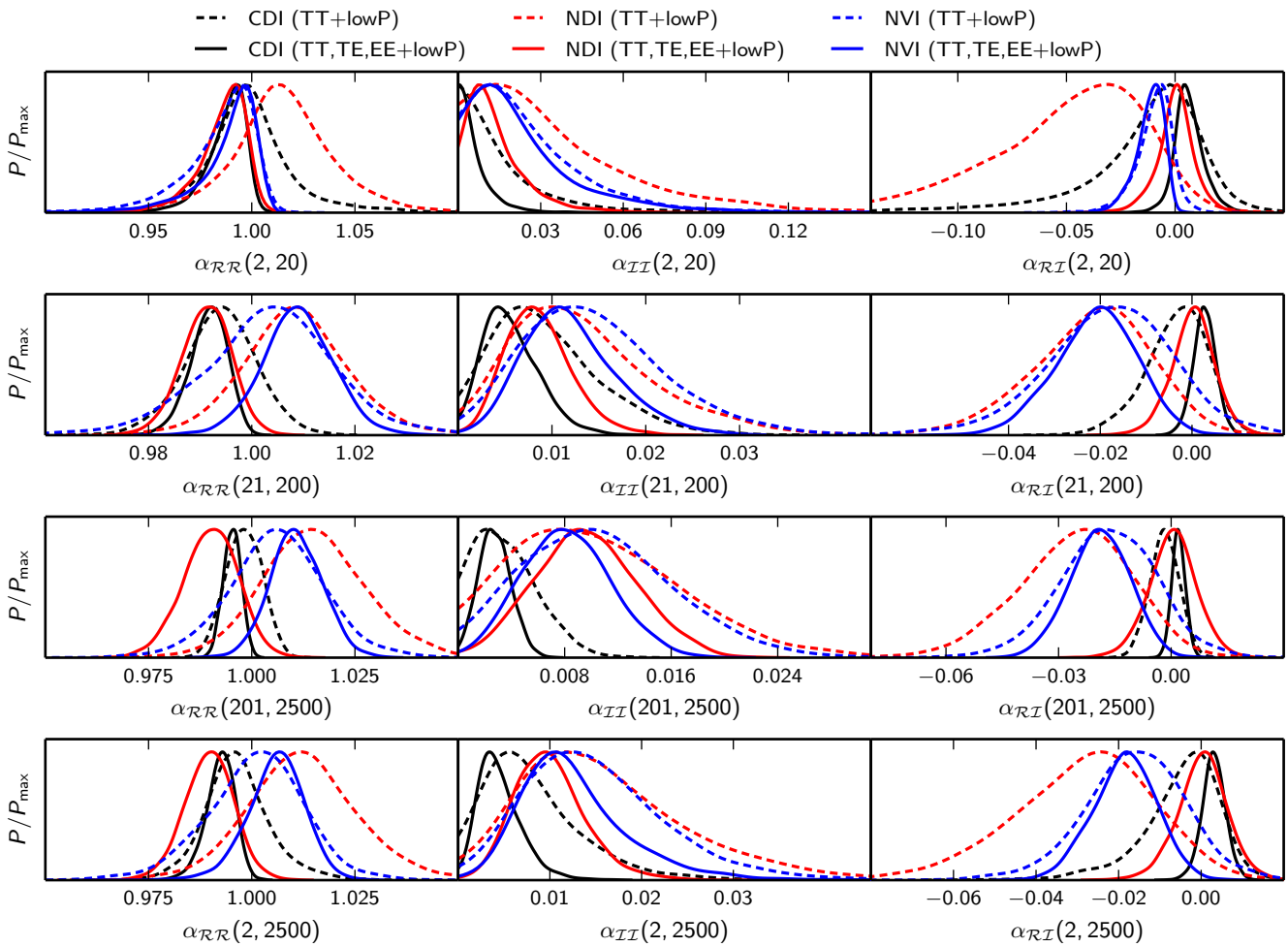

Fig. 45. Constraints on the fractional contribution of the adiabatic ($\mathcal{RR}$), isocurvature ($\mathcal{II}$), and correlation ($\mathcal{RI}$) components to the CMB temperature variance in various multipole ranges, Eq. (132), with *Planck* TT+lowP data (dashed curves) and with *Planck* TT,TE,EE+lowP data (solid curves). These are shown for the generally-correlated mixed ADI+CDI (black), ADI+NDI (red), or ADI+NVI (blue) models.

Hence, there is a competition between the temperature and polarization data that balances out and yields almost symmetric results about zero correlation (except in the ADI+NVI case). The isocurvature auto-correlation amplitude is also strongly reduced, especially in the ADI+CDI case. The best-fit values are slightly offset from $(\mathcal{P}^{(1)}_{\mathcal{II}}, \mathcal{P}^{(2)}_{\mathcal{II}}) = (0, 0)$, but the pure adiabatic model is still well inside the 68 % CL (for ADI+CDI and ADI+NDI) or 95 % CL (for ADI+NVI) regions. In summary, the high-ℓ polarization data exhibit a strong preference for adiabaticity, although one should keep in mind the possibility of unaccounted-for systematic effects in the polarization data, possibly leading to artificially strong constraints. For example, the tendency for polarization to shift the constraints towards positive correlation may be due to particular systematic effects that mimic modified acoustic peak structure, as we discussed in Sect. 11.1.

We also performed a parameter extraction with the *Planck* TT,TE,EE+lowP+lensing data, but this combination did not provide interesting new constraints—only a tightening of bounds on the standard adiabatic parameters, as in the *Planck* TT+lowP+lensing case.

We provide 95 % CL upper limits or ranges for $\beta_{\rm iso}$, $\cos\Delta$, and $\alpha_{\mathcal{RR}}$ in Table 15. With *Planck* TT+lowP, the constraints on the non-adiabatic contribution to the temperature variance, $1 - \alpha_{\mathcal{RR}}(2, 2500)$, are $(-1.5\,\%, 1.9\,\%)$, $(-4.0\,\%, 1.4\,\%)$, and $(-2.3\,\%, 2.4\,\%)$ in the ADI+CDI, ADI+NDI, and ADI+NVI cases, respectively.[21] With *Planck* TT,TE,EE+lowP these tighten to $(0.1\,\%, 1.5\,\%)$, $(-0.1\,\%, 2.2\,\%)$, and $(-2.0\,\%, 0.8\,\%)$. In the ADI+CDI case, zero is not in the 95 % CL interval, but this should not be considered a detection of non-adiabaticity. For example, as mentioned above, $(\mathcal{P}^{(1)}_{\mathcal{II}}, \mathcal{P}^{(2)}_{\mathcal{II}}) = (0, 0)$ is in the 68 % CL region, and the best-fit values are $(\mathcal{P}^{(1)}_{\mathcal{II}}, \mathcal{P}^{(2)}_{\mathcal{II}}) = (1.0 \times 10^{-13}, 3.5 \times 10^{-9})$. Moreover, the improvement in χ^2 with respect to the adiabatic model is only 5.3 with 3 extra parameters, so this is not a significant improvement of fit. Indeed, for all generally-correlated mixed models the improvement in χ^2 is very small. In particular, with *Planck* TT+lowP it does not even exceed the number of extra degrees of freedom, which is three (see Table 15).

Finally, we checked whether there is any Bayesian evidence for the presence of generally-correlated adiabatic and isocurva-

[21] It should be noted that these numbers can be positive even if the correlation contribution is negative. This happens whenever $\alpha_{\mathcal{II}} > |\alpha_{\mathcal{RI}}|$. Thus, in the observational non-adiabaticity estimator, $1 - \alpha_{\mathcal{RR}}(2, 2500)$, the negative numbers are not as pronounced as in the primordial correlation fraction, $\cos\Delta$.

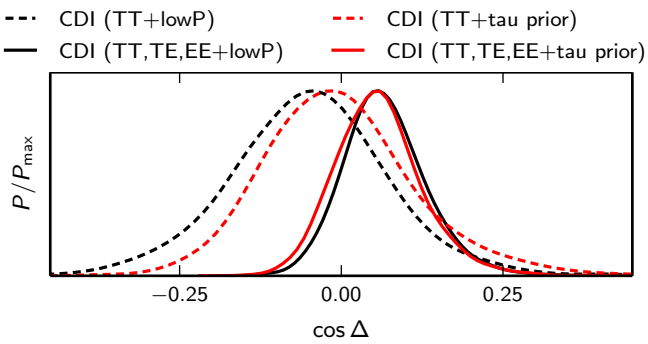

Fig. 46. Constraints on the primordial correlation fraction $\cos\Delta$ in the mixed ADI+CDI model with *Planck* TT+lowP data (dashed black curve) compared to the case where *Planck* lowP data are not used, but replaced by a Gaussian prior $\tau = 0.078 \pm 0.019$ (dashed red curve). The same exercise is repeated with *Planck* TT,TE,EE data (solid curves), demonstrating that, to a great extent, the preferred value of $\cos\Delta$ is driven by the high-ℓ data.

ture modes. In all cases, and with all data combinations studied, the Bayesian model comparison supports the null hypothesis, i.e., adiabaticity. Indeed, the logarithm of the evidence ratio is $\ln B = \ln(P_{\rm ISO}/P_{\rm ADI}) < -5$ (i.e., "decisive" evidence, or odds of much greater than 150:1, in favour of pure adiabaticity within *Planck*'s accuracy and given the parameterization and prior ranges used in our analysis), except for ADI+NDI with *Planck* TT+lowP+lensing, for which the evidence ratio is slightly larger, −4.6, corresponding to odds of 1:100 for the ADI+NDI model compared to the pure adiabatic model.

11.3. Robustness of the determination of standard cosmological parameters

Another spectacular outcome of our analysis is the robustness of the determination of the standard cosmological parameters against assumptions on initial conditions. Figure 47 shows the 1D marginalized posteriors for several cosmological parameters (not all independent of each other) with the *Planck* TT+lowP data alone. For the first time, we observe that in the presence of one generally-correlated isocurvature mode (CDI, NDI, or NVI), predictions for these parameters remain very stable with respect to the pure adiabatic case. Except for the ADI+NDI case, the posteriors neither broaden nor shift significantly. A small broadening is only observed in the case of the sound horizon angle, $\theta_{\rm MC}$, which is naturally the most sensitive parameter to tiny disturbances of the acoustic peak structure. In the ADI+NDI case, the peak of the posterior distribution for some parameters shifts slightly, but the largest shift (for $\Omega_c h^2$) is less than $1\,\sigma$.

It is particularly striking that the case of a scale-invariant adiabatic spectrum ($n_{\mathcal{RR}} = 1$) is excluded at many σ even when isocurvature modes are present: at $4.7\,\sigma$ (ADI+CDI), $5.0\,\sigma$ (ADI+NDI), $5.4\,\sigma$ (ADI+NVI). This illustrates how much the constraining power of the CMB has improved. With WMAP data, there was still a strong degeneracy between, e.g., the primordial isocurvature fraction and the adiabatic spectral index (Valiviita & Giannantonio, 2009; Savelainen et al., 2013). This degeneracy nearly disappears with *Planck* TT+lowP, and even more so with *Planck* TT,TE,EE+lowP, as shown in the upper panel of Fig. 48. Contours in the ($n_{\mathcal{RR}}$, $\cos\Delta$) space also shrink considerably, with some correlation remaining between these parameters in the ADI+CDI and ADI+NVI cases (Fig. 48, lower panel).

11.4. CDI and primordial tensor perturbations

A primordial tensor contribution adds extra temperature angular power at low multipoles, where the adiabatic base ΛCDM model predicts slightly more power than seen in the data. Hence, allowing for a non-zero tensor-to-scalar ratio, r, might tighten the constraints on positively correlated isocurvature, but degrade them in negatively correlated models. We test how treating r as a free parameter affects the constraints on isocurvature, and, on the other hand, how allowing for the generally-correlated CDI mode affects the constraints on r. These cases are denoted as "CDI+r." For comparison, we examine the pure adiabatic case in the same parameterization, and call it "ADI+r." We also consider another approach where we fix $r = 0.1$. These cases are named as "CDI+r=0.1" and "ADI+r=0.1."

In the pure adiabatic case (where the curvature and tensor perturbations stay constant on super-Hubble scales) the primordial r is the same as the tensor-to-scalar ratio at the Hubble radius exit of perturbations during inflation, which we call $\tilde{r}$. However, in the presence of an isocurvature component, $\mathcal{P}_{\mathcal{RR}}$ is not constant in time even on super-Hubble scales (García-Bellido & Wands, 1996). Instead, the isocurvature component may source $\mathcal{P}_{\mathcal{RR}}$, for example, if the background trajectory in the field space is curved between Hubble exit and the end of inflation (Langlois, 1999; Langlois & Riazuelo, 2000; Gordon et al., 2001; Amendola et al., 2002). As a result, we will have at the primordial time $\mathcal{P}_{\mathcal{RR}} = \tilde{\mathcal{P}}_{\mathcal{RR}}/(1-\cos^2\Delta)$, where $\tilde{\mathcal{P}}_{\mathcal{RR}}$ is the curvature power at Hubble exit. That is, by the primordial time the curvature perturbation power is larger than at the Hubble radius exit time (Bartolo et al., 2001; Wands et al., 2002; Byrnes & Wands, 2006). Thus we find a relation (Savelainen et al., 2013; Valiviita et al., 2012; Kawasaki & Sekiguchi, 2008):

$$r = (1-\cos^2\Delta)\tilde{r}\,, \tag{134}$$

i.e., the tensor-to-scalar ratio at the primordial time (r) is smaller than the ratio at the Hubble radius exit time ($\tilde{r}$).

The derivation of Eq. (134) assumes that the adiabatic and isocurvature perturbations are uncorrelated at Hubble radius exit ($\cos\tilde{\Delta} = 0$), and that all the possible primordial correlation ($\cos\Delta \neq 0$) appears from the evolution of super-Hubble perturbations between Hubble exit and the primordial time. This is true to leading order in the slow-roll parameters, but inflationary models that break slow roll might produce perturbations that are strongly correlated already at the Hubble radius exit time. In these cases the correlation would depend on the details of the particular model, such as the detailed shape of the potential and the interactions of the fields. However, a generic prediction of slow-roll inflation is that, at Hubble radius exit, the cross-correlation $\tilde{\mathcal{P}}_{\mathcal{RI}}$ is very weak, and indeed is of the order of the slow-roll parameters compared to the auto-correlations $\tilde{\mathcal{P}}_{\mathcal{RR}}$ and $\tilde{\mathcal{P}}_{\mathcal{II}}$ (see, e.g., Byrnes & Wands, 2006). Thus, for slow-roll models, $|\cos\tilde{\Delta}| = O(\text{slow-roll parameters}) \ll 1$.

In our analysis, we fix the tensor spectral index by the leading-order inflationary consistency relation, which now reads (Wands et al., 2002)

$$n_{\rm t} = -\frac{\tilde{r}}{8} = -\frac{r}{8(1-\cos^2\Delta)}\,. \tag{135}$$

Assuming a uniform prior for r would lead to huge negative $n_{\rm t}$ whenever $\cos^2\Delta$ was close to one. Therefore, when studying the

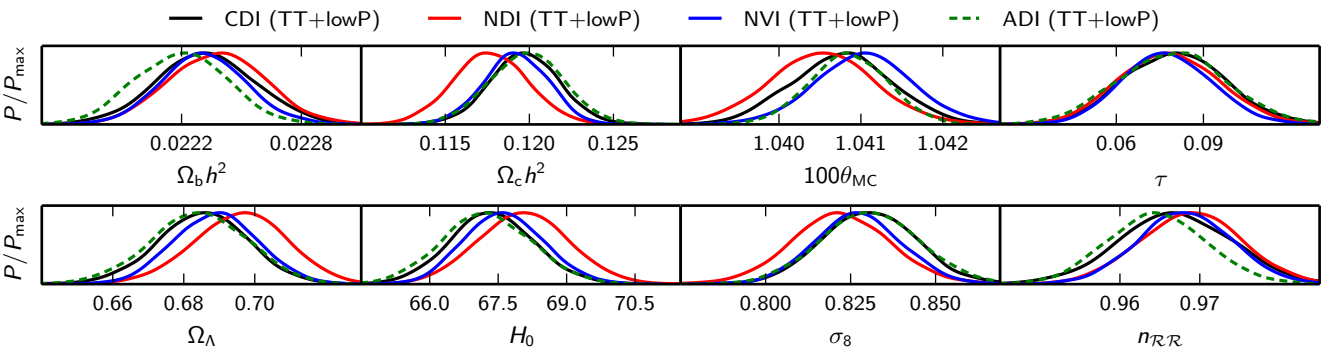

Fig. 47. Constraints on selected "standard" cosmological parameters with *Planck* TT+lowP data for the generally-correlated ADI+CDI (black), ADI+NDI (red), and ADI+NVI (blue) models compared to the pure adiabatic case (ADI, green dashed curves).

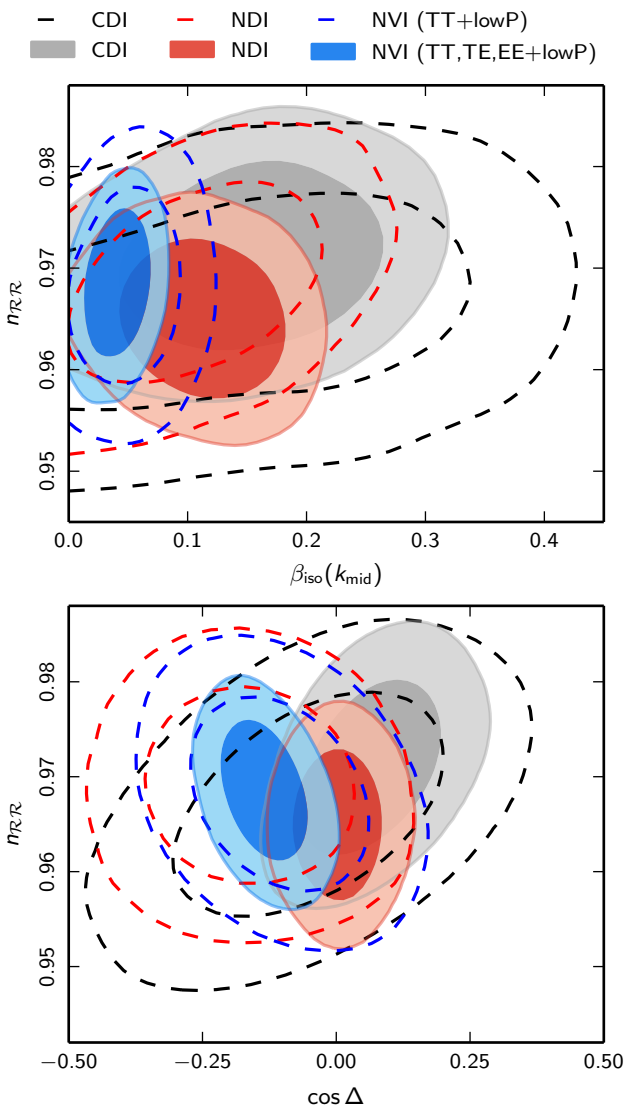

Fig. 48. Dependence of the determination of the adiabatic spectral index $n_{\mathcal{RR}}$ (called n_s in the other sections of this paper) on the primordial isocurvature fraction $\beta_{\rm iso}$ and correlation fraction $\cos\Delta$, with *Planck* TT+lowP data (dashed contours) and with *Planck* TT,TE,EE+lowP data (shaded regions).

CDI+r case we assume a uniform prior on $\tilde{r}$ at $k = 0.05\,{\rm Mpc}^{-1}$ (for details, see Savelainen et al., 2013).

Surprisingly, allowing for a generally-correlated CDI mode (i.e., three extra parameters) hardly changes the constraints on r from those obtained in the pure adiabatic model. In Fig. 49 we demonstrate this in a "standard" plot of $r_{0.002}$ versus adiabatic spectral index.

From Table 15 we notice that, with *Planck* TT+lowP and TT,TE,EE+lowP, fixing r to 0.1 tightens constraints on the primordial isocurvature fraction at large scales. This is as we expected, since both tensor and isocurvature perturbations add power at low ℓ, and the data do not prefer this. However, the shape of the tensor spectrum and correlation spectrum are such that negative correlation cannot efficiently cancel the unwanted extra power over all scales produced by tensor perturbations (at $\ell \lesssim 70$). Therefore, the correlation fraction $\cos\Delta$ is almost unaffected. However, when we allow r to vary, the cancelation mechanism works to some degree when using *Planck* TT+lowP data, leading to more negative $\cos\Delta$ than without r: with varying r we have $\cos\Delta$ in the range $(-0.43, 0.20)$, while without r it is in $(-0.30, 0.20)$, at 95 % CL. As there is now some cancellation of power at large scales, the constraint on $\beta_{\rm iso}(k_{\rm low})$ weakens slightly from 0.041 without r to 0.043 with r. On the other hand, the high-ℓ polarization data constrain the correlation to be so close to zero that with *Planck* TT,TE,EE+lowP the results for $\cos\Delta$ with and without r are almost identical.

The mean value of $\cos\Delta$ in the CDI+r cases is -0.071 (TT+lowP) and -0.076 (TT,TE,EE+lowP). Therefore, $1 - \cos^2\Delta \approx 0.99$, and so we do not expect a large difference between the primordial r and the Hubble radius exit value, $\tilde{r}$. The smallness of the difference is evident in Table 14. To summarize, CDI hardly affects the determination of r from the *Planck* data, and allowing for tensor perturbations hardly affects the determination of the non-adiabaticity parameters.

11.5. Special CDI cases

Next we study three one-parameter CDI extensions to the adiabatic model. In all these extensions the isocurvature mode modifies only the largest angular scales, since we either fix n_{II} to unity ("axion") or to the adiabatic spectral index ("curvaton I/II"). As can be seen from Fig. 42, the polarization E mode at multipoles $\ell \gtrsim 200$ will not be significantly affected by this type of CDI mode. Therefore, these models are much less sensitive to residual systematic effects in the high-ℓ polarization data than the generally correlated models.

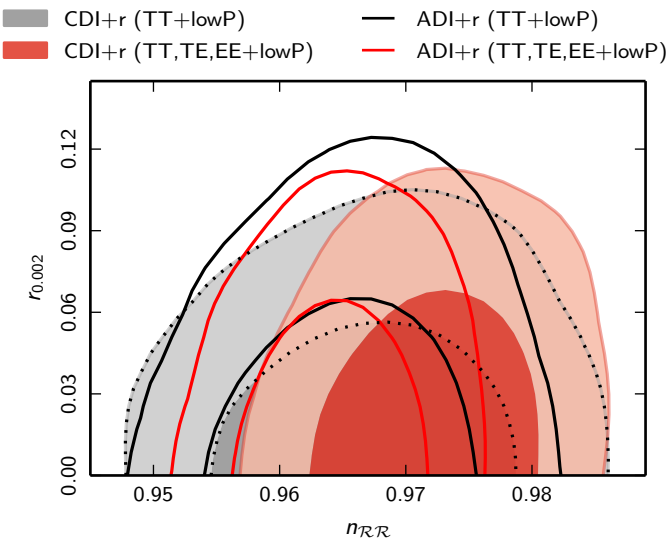

Fig. 49. 68 % and 95 % CL constraints on the primordial adiabatic spectral index $n_{\mathcal{RR}}$ and the primordial tensor-to-scalar ratio r (more accurately, in the CDI+r model, the primordial tensor-to-curvature power ratio) at $k = 0.002\,\mathrm{Mpc}^{-1}$. Filled contours are for generally-correlated ADI+CDI and solid contours for the pure adiabatic model.

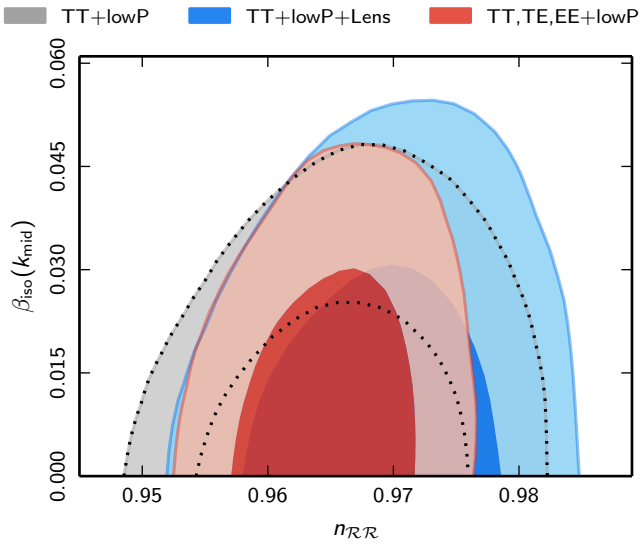

Fig. 50. Uncorrelated ADI+CDI with $n_{\mathcal{II}} = 1$ ("axion").

Model (and data)	$r_{0.05}$	$\tilde{r}_{0.05}$	$C_{10}^{\rm tens}/C_{10}^{\rm scal}$
CDI+r (TT+lowP)	0.086	0.089	0.041
ADI+r (TT+lowP)	0.101	0.101	0.048
CDI+r (TT,TE,EE+lowP)	0.092	0.092	0.043
ADI+r (TT,TE,EE+lowP)	0.094	0.094	0.044

Table 14. 95 % CL upper bounds on the tensor-to-scalar ratio (actually the tensor-to-curvature power ratio) at the primordial time, r, and earlier, at the Hubble radius exit time during inflation, $\tilde{r}$, at $k = 0.05\,\mathrm{Mpc}^{-1}$. (In the pure adiabatic case r and $\tilde{r}$ are equal.) In the last column $C_{10}^{\rm tens}/C_{10}^{\rm scal}$ indicates the tensor contribution to the temperature angular power at $\ell = 10$ relative to the temperature power from scalar perturbations ($C_{10}^{\rm scal} = C_{10}^{\mathcal{RR}} + C_{10}^{\mathcal{RI}} + C_{10}^{\mathcal{IR}} + C_{10}^{\mathcal{II}}$).

11.5.1. Uncorrelated ADI+CDI ("Axion")

We start with an uncorrelated mixture of adiabatic and CDI modes ($\mathcal{P}_{\mathcal{RI}} = 0$), and make the additional assumption that $\mathcal{P}_{\mathcal{II}}^{(2)} = \mathcal{P}_{\mathcal{II}}^{(1)}$, i.e., we assume unit isocurvature spectral index, $n_{\mathcal{II}} = 1$. Constraints in the ($n_{\mathcal{RR}}$,$\beta_{\rm iso}$) plane are presented in Fig. 50. This model is the only case for which our new results do not improve over bounds from PCI13. At $k_{\rm mid} = 0.050\,\mathrm{Mpc}^{-1}$, we find $\beta_{\rm iso} < 0.038$ (95 % CL, TT,TE,EE+lowP; see Table 15), compared with $\beta_{\rm iso} < 0.039$ using *Planck* 2013 and low-ℓ WMAP data. This is not surprising, since fixing $n_{\mathcal{II}}$ to unity implies that bounds are dominated by measurements on very large angular scales, $\ell \lesssim 30$, as can easily be understood from Fig. 42. Hence the results are insensitive to the addition of better high-ℓ temperature data, or new high-ℓ polarization data.

We summarized in PCI13 why an uncorrelated CDI mode with $n_{\mathcal{II}} \approx 1$ can be produced in axion models, under a number of restrictive assumptions: the Peccei-Quinn symmetry should be broken before inflation; it should not be restored by quantum fluctuations of the inflaton or by thermal fluctuations when the Universe reheats; and axions produced through the misalignement angle should contribute to a sizable fraction (or all) of the dark matter. Under all of these assumptions, limits on $\beta_{\rm iso}$ can be used to infer a bound on the energy scale of inflation, using equation (73) of PCI13. This bound is strongest when all the dark matter is assumed to be in the form of axions. In that case, the limit on $\beta_{\rm iso}(k_{\rm mid})$ for *Planck* TT,TE,EE+lowP gives

$$H_{\rm inf} < 0.86 \times 10^7\,\mathrm{GeV}\left(\frac{f_a}{10^{11}\,\mathrm{GeV}}\right)^{0.408} \qquad (95\,\%\ \mathrm{CL})\,, \quad (136)$$

where $H_{\rm inf}$ is the expansion rate at Hubble radius exit of the scale corresponding to $k_{\rm mid} = 0.050\,\mathrm{Mpc}^{-1}$ and f_a is the Peccei-Quinn symmetry breaking energy scale.

11.5.2. Fully correlated ADI+CDI ("Curvaton I")

Another interesting special case of mixed adiabatic and CDI (or BDI) perturbations is a model where these perturbations are primordially fully correlated and their power spectra have the same shape. These cases are obtained by setting $\mathcal{P}_{\mathcal{RI}}^{(1)} = (\mathcal{P}_{\mathcal{RR}}^{(1)}\mathcal{P}_{\mathcal{II}}^{(1)})^{1/2}$, which, by condition (129), implies that the corresponding statement holds at scale k_2 and indeed at any scale. In addition, we set $\mathcal{P}_{\mathcal{II}}^{(2)} = (\mathcal{P}_{\mathcal{RR}}^{(2)}/\mathcal{P}_{\mathcal{RR}}^{(1)})\mathcal{P}_{\mathcal{II}}^{(1)}$, i.e., $n_{\mathcal{II}} = n_{\mathcal{RR}}$. From this it follows that $\beta_{\rm iso}$ is scale independent. Therefore, this model has only one primary non-adiabaticity parameter, $\mathcal{P}_{\mathcal{II}}^{(1)}$.

A physically motivated example of this type of model is the curvaton model (Mollerach, 1990; Linde & Mukhanov, 1997; Enqvist & Sloth, 2002; Moroi & Takahashi, 2001; Lyth & Wands, 2002; Lyth et al., 2003) with the following assumptions. (1) The average curvaton field value, $\bar{\chi}_*$, is sufficiently below the Planck mass when cosmologically interesting scales exit the Hubble radius during inflation. (2) At Hubble radius exit, the curvature perturbation from the inflaton is negligible compared to the perturbation caused by the curvaton. (3) The same is true for any inflaton decay products after reheating. This means that, after reheating, the Universe is homogeneous, except for the spatially varying entropy (i.e., isocurvature perturbation) due to the curvaton field perturbations. (4) Later, CDM is created from the curvaton decay and baryon number after curvaton decay. This

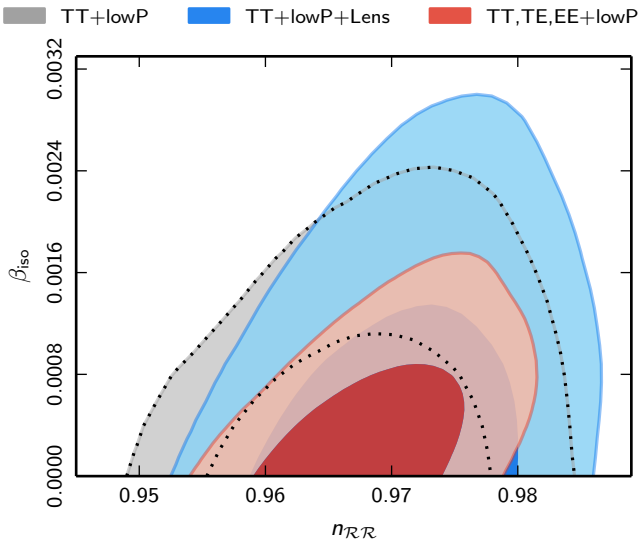

Fig. 51. Fully correlated ADI+CDI with $n_{\mathcal{II}} = n_{\mathcal{RR}}$ ("curvaton I"). Since the spectral indices are equal, the primordial isocurvature fraction $\beta_{\rm iso}$ is scale independent.

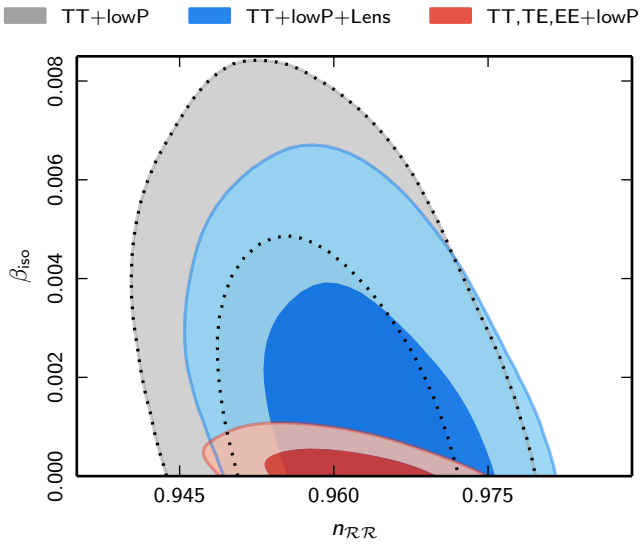

Fig. 52. Fully anticorrelated ADI+CDI with $n_{\mathcal{II}} = n_{\mathcal{RR}}$ ("curvaton II").

corresponds to case 4 presented in Gordon & Lewis (2003). (5) The curvaton contributes a significant amount to the energy density of the Universe at the time of the curvaton's decay to CDM, i.e., the curvaton decays late enough. (6) The energy density of curvaton particles possibly produced during reheating should be sufficiently low (Bartolo & Liddle, 2002; Linde & Mukhanov, 2006). (7) The small-scale variance of curvaton perturbations, $\Delta_s^2 = \langle\delta\chi^2\rangle_s/\bar{\chi}^2$, is negligible, so that it does not significantly contribute to the average energy density on CMB scales; see equation (102) in Sasaki et al. (2006). The last two conditions are necessary in order to have an almost-Gaussian curvature perturbation, as required by the *Planck* observations. Namely, if they are not valid, a large $f_{\rm NL}^{\rm local}$ follows, as discussed below. Indeed, the conditions (6) and (7) are related, since curvaton particles would add a homogeneous component to the average energy density on large scales, and hence we can describe their effect by $\Delta_s^2 = \rho_{\chi,\,\rm particles}/\rho_{\bar{\chi},\,\rm field}$, where $\rho_{\bar{\chi},\,\rm field}$ is the average energy density of the classical curvaton field on large scales; see equation (98) in Sasaki et al. (2006). Then the total energy density carried by the curvaton will be $\bar{\rho}_\chi = \rho_{\bar{\chi},\,\rm field} + \rho_{\chi,\,\rm particles}$.

The amount of isocurvature and non-Gaussianity present after curvaton decay depends on the "curvaton decay fraction",

$$r_D = \frac{3\bar{\rho}_\chi}{3\bar{\rho}_\chi + 4\bar{\rho}_{\rm radiation}}, \tag{137}$$

evaluated at curvaton decay time. If conditions (6) and (7) do not hold, then the isocurvature perturbation disappears.[22]

The curvaton scenario presented here is one of the simplest to test against observations. It should be noted that at least the conditions (1)–(5) listed at the beginning of this subsection should be satisfied simultaneously. Indeed, if we relax some of these conditions, almost any type of correlation can be produced.

[22] Indeed, if curvaton particles are produced during reheating, they can be expected to survive and outweigh other particles at the moment of curvaton decay, but by how much depends on the details of the model. As the curvaton field (during its oscillations) and the curvaton particles have the same equation of state and they decay simultaneously, no isocurvature perturbations are produced.

For example, the relative correlation fraction can be written as $\cos\Delta = \sqrt{\lambda/(1+\lambda)}$, where $\lambda = (8/9)r_D^2\epsilon_*(M_{\rm Pl}/\bar{\chi}_*)^2$. Therefore, the model is fully correlated only if $\lambda \gg 1$. If the slow-roll parameter ϵ_* is very close to zero or the curvaton field value $\bar{\chi}_*$ is large compared to the Planck mass, this model leads to almost uncorrelated perturbations.

As seen in Fig. 51 and Table 15, the upper bound on the primordial isocurvature fraction in the fully correlated ADI+CDI model weakens slightly when we add the *Planck* lensing data to *Planck* TT+lowP, whereas adding high-ℓ TE,EE tightens the upper bound moderately. With all of these three data combinations, the pure adiabatic model gives an equally good best-fit χ^2 as the fully-correlated ADI+CDI model. Bayesian model comparison strengthens the conclusion that the data disfavour this model with respect to the pure adiabatic model.

The isocurvature fraction is connected to the curvaton decay fraction, Eq. (137), by

$$\beta_{\rm iso} \approx \frac{9(1-r_D)^2}{r_D^2 + 9(1-r_D)^2} \tag{138}$$

(see case 4 in Gordon & Lewis, 2003). Reading the constraints on $\beta_{\rm iso}$ from Table 15, we can convert them into constraints on r_D and further into the non-Gaussianity parameter assuming a quadratic potential for the curvaton and instantaneous decay[23] (Sasaki et al., 2006):

$$f_{\rm NL}^{\rm local} = (1+\Delta_s^2)\frac{5}{4r_D} - \frac{5}{3} - \frac{5r_D}{6}. \tag{139}$$

If conditions (6) and (7) hold, i.e., $\Delta_s^2 = 0$, as implicitly assumed, e.g., in Bartolo et al. (2004a,b), then the smallest possible value

[23] It should be noted that, in particular, in the older curvaton literature a formula $f_{\rm NL}^{\rm local} = \frac{5}{4r_D}$ is often quoted or utilized. This result, which follows from considering only squares of first order perturbations, is valid when r_D is close to zero, i.e., when $f_{\rm NL}^{\rm local}$ is very large. However, when r_D is close to unity or $f_{\rm NL}^{\rm local} \lesssim 10$, which is the case with the *Planck* measurements, the second and third terms in Eq. (139) are vitally important. These follow from genuine second order perturbation theory calculations. Coincidentally, if one erroneously uses the expression $\frac{5}{4r_D}$ in the limit $r_D \to 1$, one obtains a result $+5/4$, whereas the correct formula (139), with $\Delta_s^2 = 0$, leads to $-5/4$, when $r_D \to 1$.

of $f_{\rm NL}^{\rm local}$ is $-5/4$, which is obtained when $r_D = 1$, and Eqs. (138) and (139) yield for the various *Planck* data sets (at 95 % CL):[24]

$$\text{TT+lowP:}\quad \beta_{\rm iso} < 0.0018 \Rightarrow 0.9860 < r_D \leq 1 \Rightarrow -1.250 \leq f_{\rm NL}^{\rm local} < -1.220\,, \tag{140}$$

$$\text{TT+lowP+lensing:}\quad \beta_{\rm iso} < 0.0022 \Rightarrow 0.9845 < r_D \leq 1 \Rightarrow -1.250 \leq f_{\rm NL}^{\rm local} < -1.217\,, \tag{141}$$

$$\text{TT,TE,EE+lowP:}\quad \beta_{\rm iso} < 0.0013 \Rightarrow 0.9882 < r_D \leq 1 \Rightarrow -1.250 \leq f_{\rm NL}^{\rm local} < -1.225\,. \tag{142}$$

Thus the results for the simplest curvaton model remain unchanged from those presented in PCI13, i.e., in order to produce almost purely adiabatic perturbations, the curvaton should decay when it dominates the energy density of the Universe ($r_D > 0.98$), and the non-Gaussianity parameter is constrained to close to its smallest possible value ($-5/4 < f_{\rm NL}^{\rm local} < -1.21$), which is consistent with the result $f_{\rm NL}^{\rm local} = 2.5 \pm 5.7$ (68 % CL, from T only) found in Planck Collaboration XVII (2015).

11.5.3. Fully anticorrelated ADI+CDI ("Curvaton II")

The curvaton scenario or some other mechanism could also produce 100 % anticorrelated perturbations, with $n_{II} = n_{\mathcal{RR}}$. The constraints in the $(n_{\mathcal{RR}}, \beta_{\rm iso})$ plane are presented in Fig. 52. Examples of this kind of model are provided by cases 2, 3, and 6 in Gordon & Lewis (2003). These lead to a fixed, large amount of isocurvature, e.g., in case 2 to $\beta_{\rm iso} = 9/10$, and are hence excluded by the data at very high significance. However, case 9 in Gordon & Lewis (2003), with a suitable r_D (i.e., $r_D > R_{\rm c}$, where $R_{\rm c} = \rho_{\rm c}/(\rho_{\rm c} + \rho_{\rm b})$), leads to fully anticorrelated perturbations and might provide a good fit to the data. In this case CDM is produced by curvaton decay while baryons are created earlier from inflaton decay products and do not carry a curvature perturbation. We obtain a very similar expression to Eq. (138), namely

$$\beta_{\rm iso} \approx \frac{9(1 - r_D/R_{\rm c})^2}{r_D^2 + 9(1 - r_D/R_{\rm c})^2}\,. \tag{143}$$

We convert this approximately to a constraint on r_D by fixing $R_{\rm c}$ to its best-fit value, $R_{\rm c} = 0.8437$ (*Planck* TT+lowP), within this model. The results for the various *Planck* data sets are:

$$\text{TT+lowP:}\quad \beta_{\rm iso} < 0.0064 \Rightarrow 0.8437 < r_D < 0.8632 \Rightarrow -0.9379 < f_{\rm NL}^{\rm local} < -0.8882\,, \tag{144}$$

$$\text{TT+lowP+lensing:}\quad \beta_{\rm iso} < 0.0052 \Rightarrow 0.8437 < r_D < 0.8612 \Rightarrow -0.9329 < f_{\rm NL}^{\rm local} < -0.8882\,, \tag{145}$$

$$\text{TT,TE,EE+lowP:}\quad \beta_{\rm iso} < 0.0008 \Rightarrow 0.8437 < r_D < 0.8505 \Rightarrow -0.9056 < f_{\rm NL}^{\rm local} < -0.8882\,. \tag{146}$$

After all the tests conducted in this section, both for the generally correlated CDI, NDI, and NVI cases as well as for the special CDI cases, we conclude that, within the spatially flat base ΛCDM model, the initial conditions of perturbations are consistent with the hypothesis of pure adiabaticity, a conclusion that is also overwhelmingly supported by the Bayesian model comparison. Moreover, Planck Collaboration XVII (2015) report a null detection of *isocurvature non-Gaussianity*, with polarization improving constraints significantly.

[24] However, if Δ_s^2 was non-negligible, then all the constraints on $f_{\rm NL}^{\rm local}$ would shift upward. For example, with $\Delta_s^2 = 1$, our constraints on $\beta_{\rm iso}$ would translate to $0 \leq f_{\rm NL}^{\rm local} \lesssim 0.03$. On the other hand, the *Planck* constraint of $f_{\rm NL}^{\rm local}$ can be converted to an upper bound $\Delta_s^2 = \rho_{\chi,\,\rm particles}/\rho_{\tilde{\chi},\,\rm field} < 8.5$ (95 % CL from T only) as shown in Planck Collaboration XVII (2015).

12. Statistical anisotropy and inflation

A key prediction of standard inflation, which in the present context includes all single field models of inflation as well as many multi-field models, is that the stochastic process generating the primordial cosmological perturbations is completely characterized by its power spectrum, constrained by statistical isotropy to depend only on the multipole number ℓ. This statement applies at least to the accuracy that can be probed using the CMB, given the limitations imposed by cosmic variance, since all models exhibit *some* level of non-Gaussianity. Nevertheless, more general Gaussian stochastic processes can be envisaged for which one or more special directions on the sky are singled out, so that the expectation values for the temperature multipoles take the form

$$\left\langle a^T_{\ell m}\,(a^T_{\ell' m'})^* \right\rangle = C^{TT}_{\ell m;\ell' m'}\,, \tag{147}$$

rather than the very special form

$$\left\langle a^T_{\ell m}\,(a^T_{\ell' m'})^* \right\rangle = C^{TT}_{\ell}\,\delta_{\ell,\ell'}\,\delta_{m,m'}\,, \tag{148}$$

which is the only possibility consistent with statistical isotropy.

The most general form for a Gaussian stochastic process on the sphere violating the hypothesis of statistical isotropy, Eq. (147), is too broad to be useful, especially given the fact that we have only one sky to analyse. For $\ell < \ell_{\rm max}$, there are $O(\ell^2_{\rm max})$ multipole expansion coefficients, compared with $O(\ell^4_{\rm max})$ model parameters. Therefore, in order to make some progress on testing the hypothesis of statistical isotropy, we must restrict ourselves to examining only the simplest models violating statistical isotropy, for which the available data can establish meaningful constraints and for which one can hope to find a simple theoretical motivation.

12.1. Asymmetry: observations versus model building

In one simple class of statistically anisotropic models, we start with a map produced by a process respecting statistical isotropy, which becomes modulated by another field in the following manner to produce the observed sky map:

$$\delta T_{\rm sky}(\hat{\mathbf{\Omega}}) = \left(1 + M(\hat{\mathbf{\Omega}})\right)\delta T_{\rm s\text{-}i}(\hat{\mathbf{\Omega}}), \tag{149}$$

where $\hat{\mathbf{\Omega}}$ denotes a position on the celestial sphere and $\delta T_{\rm s\text{-}i}(\hat{\mathbf{\Omega}})$ is the outcome of the underlying statistically isotropic process before modulation. Roughly speaking, where the modulating field $M(\hat{\mathbf{\Omega}})$ is positive, power on scales smaller than the scale of variation of $M(\hat{\mathbf{\Omega}})$ is enhanced, whereas where $M(\hat{\mathbf{\Omega}})$ is negative, power is suppressed. We refer to this as a "power asymmetry." If $M(\hat{\mathbf{\Omega}}) = A\hat{\mathbf{d}}\cdot\hat{\mathbf{\Omega}}$, we have a model of dipolar modulation with amplitude A and direction $\hat{\mathbf{d}}$, but higher-order or mixed modulation may also be considered, such as a quadrupole modulation or modulation by a scale-invariant field $M(\hat{\mathbf{\Omega}})$, to name just a few special cases.

In Planck Collaboration XXIII (2014) and Planck Collaboration XVI (2015), the details of constructing efficient estimators for statistical anisotropy, in particular in the presence of realistic data involving sky cuts and possibly incompletely removed foreground contamination, are considered in depth. In addition, the question of the statistical significance of any detected "anomalies" from the expectations of base

Model (and data)	$100\beta_{\rm iso}(k_{\rm low})$	$100\beta_{\rm iso}(k_{\rm mid})$	$100\beta_{\rm iso}(k_{\rm high})$	$100\cos\Delta$	$100\alpha_{\mathcal{RR}}(2,2500)$	Δn	$\Delta\chi^2$	$\ln B$
General models:								
CDI (TT+lowP)	4.1	35.4	56.9	[−30:20]	[98.1:101.5]	3	−2.1	−8.8
CDI (TT+lowP+WP)	4.2	35.5	57.2	[−31:23]	[97.9:101.4]	3	−1.8	−9.1
CDI (TT,TE,EE+lowP)	2.0	[3.4:28.1]	[3.1:51.8]	[−6:20]	[98.5: 99.9]	3	−5.3	−8.8
CDI (TT,TE,EE+lowP+WP)	2.1	[2.3:28.4]	[2.6:52.1]	[−7:21]	[98.5: 99.9]	3	−5.5	−8.2
CDI (TT+lowP+lensing)	4.5	37.9	59.4	[−28:17]	[98.1:101.1]	3	−1.2	−8.8
NDI (TT+lowP)	14.3	22.4	27.4	[−33: 1]	[98.6:104.0]	3	−2.0	−5.3
NDI (TT,TE,EE+lowP)	7.3	[3.4:19.3]	[3.5:26.7]	[−9:10]	[97.8:100.1]	3	−5.5	−5.5
NDI (TT+lowP+lensing)	15.8	[1.4:24.1]	[0.3:28.4]	[−32: 0]	[98.6:104.0]	3	−2.8	−4.6
NVI (TT+lowP)	8.3	[0.1:10.2]	11.9	[−26: 6]	[97.6:102.3]	3	−2.8	−6.3
NVI (TT,TE,EE+lowP)	7.4	[0.9: 7.4]	[0.4: 8.8]	[−22:−4]	[99.2:102.0]	3	−6.2	−6.5
NVI (TT+lowP+lensing)	9.7	[0.4:11.6]	13.1	[−23: 7]	[97.1:102.0]	3	−2.5	−6.5
General models + r:								
CDI+r=0.1 (TT+lowP)	3.4	38.7	63.9	[−33:24]	[98.1:101.4]	3	−5.4	−8.9
CDI+r=0.1 (TT,TE,EE+lowP)	1.6	[4.4:31.7]	[6.9:59.2]	[−6:22]	[98.6: 99.9]	3	−6.3	−8.1
CDI+r (TT+lowP)	4.3	34.9	56.2	[−43:20]	[97.9:102.4]	3	−3.3	−7.7
CDI+r (TT,TE,EE+lowP)	1.7	[3.9:29.0]	[5.8:53.8]	[−5:21]	[98.6: 99.9]	3	−5.1	−7.2
Special CDI cases:								
Uncorrelated, $n_{II} = 1$								
"axion" (TT+lowP)	3.3	3.7	3.8	0	[98.5:100]	1	0.0	−5.2
"axion" (TT,TE,EE+lowP)	3.5	3.8	3.9	0	[98.4:100]	1	−0.2	−4.9
"axion" (TT+lowP+lensing)	3.9	4.3	4.4	0	[98.3:100]	1	0.0	−5.0
Fully correlated, $n_{II} = n_{\mathcal{RR}}$								
"curvaton I" (TT+lowP)	0.18	0.18	0.18	100	[97.5:100.0]	1	−0.1	−8.1
"curvaton I" (TT,TE,EE+lowP)	0.13	0.13	0.13	100	[97.8: 99.9]	1	0.0	−7.8
"curvaton I" (TT+lowP+lensing)	0.22	0.22	0.22	100	[97.3: 99.7]	1	0.0	−8.5
Fully anti-correlated, $n_{II} = n_{\mathcal{RR}}$								
"curvaton II" (TT+lowP)	0.64	0.64	0.64	−100	[100.5:105.1]	1	−1.1	−5.4
"curvaton II" (TT,TE,EE+lowP)	0.08	0.08	0.08	−100	[100.1:101.8]	1	0.0	−8.9
"curvaton II" (TT+lowP+lensing)	0.52	0.52	0.52	−100	[100.4:104.4]	1	−0.6	−6.3

Table 15. Constraints on mixed adiabatic and isocurvature models. For each mixed model, we report 95% CL bounds on the fractional primordial contribution of isocurvature modes at three comoving wavenumbers ($k_{\rm low} = 0.002$ Mpc^{-1}, $k_{\rm mid} = 0.050$ Mpc^{-1}, and $k_{\rm high} = 0.100$ Mpc^{-1}), as well as the scale-independent primordial correlation fraction, $\cos\Delta$. The fractional adiabatic contribution to the observed temperature variance is denoted by $\alpha_{\mathcal{RR}}(2,2500)$, and from this the nonadiabatic contribution can be calculated as $\alpha_{\text{non-adi}} = 1 - \alpha_{\mathcal{RR}}(2,2500)$. The number of extra parameters compared with the corresponding pure adiabatic model is denoted by Δn, and $\Delta\chi^2$ is the difference between the χ^2 of the best-fitting mixed and pure adiabatic models. (A negative $\Delta\chi^2$ means that the mixed model is a better fit to the data.) In the last column we give the difference between the logarithm of Bayesian evidences. (A negative $\ln B = \ln(P_{\rm ISO}/P_{\rm ADI})$ means that Bayesian model comparison disfavours the mixed model. With our settings of `MultiNest` the uncertainty in these numbers is about ±0.5.)

ΛCDM is examined in detail. Importantly, in the *absence* of a particular inflationary model for such an observed anomaly, the significance should be corrected for the "multiplicity of tests" that *could* have resulted in similarly significant detections (i.e., for the "look elsewhere effect"), although applying such corrections can be ambiguous. In this paper, however, we consider only forms of statistical anisotropy that are predicted by specific inflationary models, and, hence, such corrections will not be necessary.

Several important questions can be posed regarding the link between statistical isotropy and inflation. In particular, we can ask the following questions. (1) Does a statistically significant finding of a violation of statistical isotropy falsify inflation? (2) If not, what sort of non-standard inflation could produce the required departure from statistical isotropy? (3) What other perhaps non-inflationary models could also account for the violation of statistical isotropy? In this section, we begin to address these questions by assessing the viability of an inflationary model for dipolar asymmetry, as well as by placing new limits on the presence of quadrupolar power asymmetry.

For the case of the dipolar asymmetry reported in Planck Collaboration XVI (2015), there are two aspects that make inflationary model building difficult. First is the problem of obtaining a significant amplitude of dipole modulation. In Planck Collaboration XVI (2015) the asymmetry was found to have amplitude $A \approx 6$–$7\,\%$ on scales $2 \le \ell \le 64$. This compares with the expected value of $A = 2.9\,\%$ on these scales due to cosmic variance in statistically isotropic skies. One basic strategy for incorporating the violation of statistical isotropy into inflation is to consider some form of multi-field inflation and use one of the directions orthogonal to the direction of slow roll as the field responsible for the modulation. Obtaining the required modulation is problematic because most extra fields in multi-field inflation become disordered in a nearly scale-invariant way, just like the fluctuations in the field parallel to the direction of slow roll. What is needed resembles a pure gradient with no fluctuations of shorter wavelength. In Liddle & Cortês (2013) it was proposed that such a field could be produced using the supercurvature mode of open inflation. (See, however, the discussion in Kanno et al. (2013).) Also, in order to respect the $f_{\rm NL}$ con-

straints, one must avoid that the modulating field leave a direct imprint on the temperature anisotropy.

The second aspect which makes model building difficult for dipolar asymmetry is that the measured amplitude is strongly scale dependent, and on scales $\ell \gtrsim 100$ no significant detection of a dipolar modulation amplitude is made (Planck Collaboration XVI, 2015), once our proper motion has been taken into account (Planck Collaboration XXVII, 2014). On the other hand, the simplest models are scale-free and produce statistical anisotropy of the type described by the ansatz in Eq. (149), for which the bulk of the statistical weight should be detected at the resolution of the survey. To resolve this difficulty, Erickcek et al. (2009) proposed modulating CDI fluctuations generated within the framework of a curvaton scenario, because, unlike adiabatic perturbations, CDI perturbations entering the horizon after last scattering contribute negligibly to the CMB fluctuations (recall Fig. 42).

The situation for the quadrupolar power asymmetry is different from the dipolar case in that no detection is currently claimed. Model building is easier than the dipolar case since no pure gradient modes are required, but also more difficult in that anisotropy during inflation is needed. While the isotropy of the recent expansion of the Universe (i.e., since the CMB fluctuations were first imprinted) is tightly constrained, bounds on a possible anisotropic expansion at early times are much weaker. Ackerman et al. (2007) proposed using constraints on the quadrupolar statistical anisotropy of the CMB to probe the isotropy of the expansion during inflation—that is, during the epoch when the perturbations now seen in the CMB first exited the horizon. Assuming an anisotropic expansion during inflation, Ackerman et al. (2007) computed its impact on the three-dimensional power spectrum on superhorizon scales by integrating the mode functions for the perturbations during inflation and beyond. Several sources of such anisotropy have been proposed, such as vector fields during inflation (Dimastrogiovanni et al., 2010; Soda, 2012; Maleknejad et al., 2013; Schmidt & Hui, 2013; Bartolo et al., 2013; Naruko et al., 2014), or an inflating solid or elastic medium (Bartolo et al., 2013).

12.2. Scale-dependent modulation and idealized estimators

The ansatz in Eq. (149) expressed in angular space may be rewritten in terms of the multipole expansion and generalized to include scale-dependent modulation by means of Wigner $3j$ symbols:

$$\left\langle a^T_{\ell m}\, a^T_{\ell' m'} \right\rangle = \sum_{L=0}^{\infty} \sum_{M=-L}^{+L} C^{TT}_{\ell;\ell';L,M} \begin{pmatrix} \ell & \ell' & L \\ m & m' & M \end{pmatrix}. \tag{150}$$

Because of the symmetry of the left-hand side, the coefficients $C^{TT}_{\ell;\ell';L,M}$ acquire a phase $(-1)^{\ell+\ell'+L}$ under interchange of ℓ and ℓ'. This is the most general form consistent with the hypothesis of Gaussianity. The usual isotropic power spectrum, which is the generic prediction of simple models of inflation, includes only the $L = 0$ term, where $C^{TT}_{\ell;\ell';0,0} = C^{TT}_{\ell}$ and the Wigner $3j$ symbol provides the $\delta_{\ell,\ell'}\delta_{m,m'}$ factor. The coefficients $C^{TT}_{\ell;\ell';L,M}$ with $L > 0$ introduce statistical anisotropy.

If we assume that there is a common vector (corresponding to $L = 1$ on the celestial sphere) that defines the direction of the anisotropy of the power spectrum for all the terms of $L = 1$, we may adopt a more restricted ansatz for the bipolar modulation, so that

$$C^{TT}_{\ell;\ell';1,M} = C^{1}_{\ell,\ell'} X^{(1)}_M, \tag{151}$$

where we assume that X_M is normalized (i.e., $\sum_M X_M X_M{}^* = 1$). In such a theory, supposing that $C^1_{\ell,\ell'}$ is theoretically determined, but the orientation of the unit vector X_M is random and isotropically distributed on the celestial sphere, we may construct the following quadratic estimator for the direction:

$$X^{(L)}_M = \sum_{\ell,m} \sum_{\ell',m'} \frac{w_{\ell,\ell'}}{(2L+1)(C_\ell)^{1/2}\,(C_{\ell'})^{1/2}} \times \begin{pmatrix} \ell & \ell' & L \\ m & m' & M \end{pmatrix} a^T_{\ell m}\, a^T_{\ell' m'}, \tag{152}$$

where the weights for the unbiased minimum variance estimator are given by

$$w_{\ell,\ell';L} = c_{\ell,\ell';L} \left(\sum_{\ell,\ell'} c_{\ell,\ell';L} \right)^{-1}. \tag{153}$$

This construction, which for the $L = 1$ case may be found in Moss et al. (2011) and Planck Collaboration XVI (2015), may be readily generalized to $L > 1$ in the above way.

12.3. Constraining inflationary models for dipolar asymmetry

In this section, we confront with *Planck* data the modulated curvaton model of Erickcek et al. (2009), which attempts to explain the observed large-scale power asymmetry via a gradient in the background curvaton field. In this model, the curvaton decays after CDM freeze-out, which results in a nearly scale-invariant isocurvature component between CDM and radiation. In the viable version of this scenario, the curvaton contributes negligibly to the CDM density. A long-wavelength fluctuation in the curvaton field initial value σ_* is assumed, with amplitude $\Delta\sigma_*$ across our observable volume. This modulates the curvaton isocurvature fluctuations according to $S_{\sigma\gamma} \approx 2\delta\sigma_*/\sigma_*$. The curvaton produces all of the final CDI fluctuations, which are nearly scale invariant, as well as a component of the final adiabatic fluctuations. Hence both of these components will be modulated, and the parameter space of the model will be constrained by observations of the power asymmetry on large and small scales, as well as the full-sky CDI fraction. In practice, the very tight constraints on small-scale power asymmetry obtained in Planck Collaboration XVI (2015) imply a small curvaton adiabatic component, which implies that the CDI and adiabatic fluctuations are only weakly correlated. This model easily satisfies constraints due to the CMB dipole, quadrupole, and non-Gaussianity (Erickcek et al., 2009).

There are two main parameters which we constrain for this model. First, the fraction of adiabatic fluctuations due to the curvaton, ξ, is defined as

$$\xi \equiv \frac{\Sigma_\sigma^2 \mathcal{P}_\sigma}{\mathcal{P}_{\mathcal{R}_{\rm inf}} + \Sigma_\sigma^2 \mathcal{P}_\sigma}. \tag{154}$$

Here, $\mathcal{P}_{\mathcal{R}_{\rm inf}}$ and $\mathcal{P}_\sigma$ are the inflaton and curvaton primordial power spectra, respectively, and Σ_σ is the coupling from curvaton isocurvature to adiabatic fluctuations. (Up to a sign, ξ is equal to the correlation parameter.) Next, the coupling of curvaton to CDI, $M_{{\rm CDI}\sigma}$, is determined by the constant $\kappa \equiv M_{{\rm CDI}\sigma}/R \gtrsim -1$, where

$$R \equiv \frac{3\Omega_\sigma}{4\Omega_\gamma + 3\Omega_\sigma + 3\Omega_{\rm CDM}} \tag{155}$$

and all density parameters are evaluated just prior to curvaton decay. The isocurvature fraction can be written in terms of these two parameters by

$$\beta_{\rm iso} = \frac{9\kappa^2\xi}{1+9\kappa^2\xi}. \tag{156}$$

These parameters determine the modulation of the CMB temperature fluctuations via $\Delta C_\ell/C_\ell = 2K_\ell\Delta\sigma_*/\sigma_*$, where (Erickcek et al., 2009)

$$K_\ell \equiv \xi\frac{C_\ell^{\rm ad} + 9\kappa^2 C_\ell^{\rm iso} + 3\kappa C_\ell^{\rm cor}}{C_\ell^{\rm ad} + \xi(9\kappa^2 C_\ell^{\rm iso} + 3\kappa C_\ell^{\rm cor})}. \tag{157}$$

Here $C_\ell^{\rm ad}$, $C_\ell^{\rm iso}$, and $C_\ell^{\rm cor}$ are the adiabatic, CDI, and correlated power spectra calculated for unity primordial spectra.

Note that this modulated curvaton model contains some simple special cases. For $\kappa = 0$, we have a purely adiabatic, i.e., scale-invariant, modulation. This is equivalent to a modulation of the scalar amplitude $A_{\rm s}$. On the other hand, if we take the limit $\kappa \to \infty$, with fixed $\kappa^2\xi$ (i.e., with fixed isocurvature fraction $\beta_{\rm iso}$), we obtain a pure CDI modulation. For $\kappa = \xi = 0$ we have no modulation, i.e., we recover base ΛCDM. Therefore this model is particularly useful for examining a range of possible modulations within the context of a concrete framework.

In order to constrain this model, we use a formalism which was developed to determine the signatures of potential gradients in physical parameters in the CMB (Moss et al., 2011), and which is used to examine dipolar modulation and described in detail in Planck Collaboration XVI (2015). This approach is well suited to testing the modulated curvaton model since it can accommodate scale-dependent modulations. Briefly, we write the temperature anisotropy covariance given a gradient ΔX_M in a parameter X as

$$C_{\ell m\ell' m'} = C_\ell\delta_{\ell\ell'}\delta_{mm'} + (-1)^m\frac{\delta C_{\ell\ell'}}{2}\left[(2\ell+1)(2\ell'+1)\right]^{1/2} \times \begin{pmatrix}\ell & \ell' & 1\\ 0 & 0 & 0\end{pmatrix}\sum_M \Delta X_M \begin{pmatrix}\ell & \ell' & 1\\ -m & m' & M\end{pmatrix}, \tag{158}$$

where $\delta C_{\ell\ell'} \equiv dC_\ell/dX + dC_{\ell'}/dX$. Note that this covariance takes the form of Eqs. (150) and (151), with

$$C^1_{\ell;\ell'} = \frac{\delta C_{\ell\ell'}}{2}\left[(2\ell+1)(2\ell'+1)\right]^{1/2}\begin{pmatrix}\ell & \ell' & 1\\ 0 & 0 & 0\end{pmatrix}. \tag{159}$$

We then construct a maximum likelihood estimator for the gradient components. We use C^{-1} filtered data (Planck Collaboration XV, 2015) and perform a mean-field subtraction, giving

$$\Delta\hat{X}_M = \frac{3}{f_{1M}}\sum_{\ell m\ell' m'}(-1)^m C^1_{\ell;\ell'}\begin{pmatrix}\ell & \ell' & 1\\ -m & m' & M\end{pmatrix} \times \left(T_{\ell m}T^*_{\ell' m'} - \left\langle T_{\ell m}T^*_{\ell' m'}\right\rangle\right)\left[\sum_{\ell\ell'}(C^1_{\ell;\ell'})^2 F_\ell F_{\ell'}\right]^{-1}. \tag{160}$$

Here f_{1M} is a normalization correction due to the applied mask, $M(\Omega)$, and is given by

$$f_{1M} \equiv \int d\Omega\, Y^*_{1M}(\Omega)M(\Omega). \tag{161}$$

The $T_{\ell m}$ are the filtered data and $F_\ell \equiv \left\langle T_{\ell m}T^*_{\ell m}\right\rangle$. In practice, exploring the parameter space of the model is sped up dramatically by binning the estimator, Eq. (160), into bins of width $\Delta\ell = 1$,

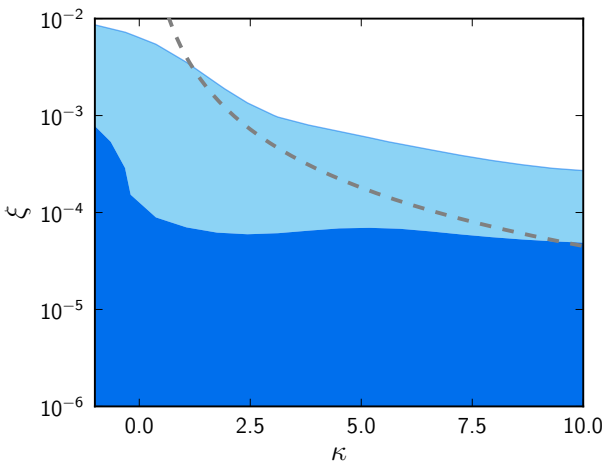

Fig. 53. 68 % and 95 % CL regions in the modulated isocurvature model parameter space using the *Planck* temperature data up to $\ell_{\rm max} = 1000$ (contours). The region above the dashed curve is ruled out by the *Planck* constraint on an uncorrelated, scale-invariant isocurvature component.

which means that the estimators only need to be calculated once (Planck Collaboration XVI, 2015). Finally, for the modulated curvaton model we identify

$$\frac{dC_\ell}{dX} = 2K_\ell C_\ell. \tag{162}$$

Note that, for our constraints, we fix the curvaton gradient to its maximum value, $\Delta\sigma_*/\sigma_* = 1$. Therefore, our constraints are conservative, since smaller $\Delta\sigma_*/\sigma_*$ would only reduce the modulation that this model could produce.

The temperature anisotropies measured by *Planck* constrain the modulated curvaton parameters κ and ξ via Eqs. (157) and (160). Figure 53 shows the constraints in this parameter space evaluating the estimator to $\ell_{\rm max} = 1000$. The maximum likelihood region corresponds to a band at $\kappa \gtrsim 3$. For parameters in this region, the model produces a large-scale asymmetry via a mainly-CDI modulation. However, the *amplitude* of this large-scale asymmetry is lower than the 6–7 % actually observed (Planck Collaboration XVI, 2015). The reason is that, had a CDI modulation produced all of the large-scale asymmetry, the consequent small-scale asymmetry (due to the shape of the scale-invariant CDI spectrum) would be larger than the *Planck* observations allow. The allowed CDI modulation is further reduced by the *Planck* 95 % upper limit on an uncorrelated, scale-invariant ("axion"-type) isocurvature component, $\beta_{\rm iso} < 0.0331$, from Sect. 11. Imposing this constraint reduces the available parameter space in the κ–ξ plane via Eq. (156), as illustrated in Fig. 53.

The best fit in Fig. 53 corresponds to $\Delta\chi^2_{\rm eff} = -6.8$ relative to base ΛCDM, for two extra paramters. In order to assess how likely such an improvement would be in statistically isotropic skies, we note that the best-fit CDI modulation amplitude is very close to the mean amplitude expected due to cosmic variance, as calculated directly from Eq. (160). More precisely, since the amplitude is χ^2 distributed with three degrees of freedom, i.e., Maxwell-Boltzmann distributed, we conclude that about 44 % of statistically isotropic skies will exhibit a measured [via Eq. (160)] isocurvature modulation larger than that of the actual sky.

To summarize, the modulated curvaton model can only produce a small part of the observed large-scale asymmetry, and

what it can produce is entirely consistent with cosmic variance in a statistically isotropic sky. Hence we must favour base ΛCDM over this model. Finally, note that further generalizing the model (e.g., to allow non-scale-invariant CDI spectra) may allow more large-scale asymmetry to be produced and hence result in an improved $\Delta\chi^2_{\rm eff}$, at the expense of more parameters. On the other hand, the neutrino isocurvature modes are not expected to fit the observed asymmetry well, due to their approximate scale invariance (see Fig. 42).

12.4. Constraints on quadrupolar asymmetry generated during inflation ($L = 2$)

In this section, we assume a quadrupolar direction dependence in the primordial power spectrum, which we may expand using spherical harmonics according to

$$g_*(k)\,(\hat{\boldsymbol{k}}\cdot\hat{\boldsymbol{E}}_{\rm cl})^2 = \frac{g_*(k)}{3} + \frac{8\pi}{15}g_*(k)\sum_M Y^*_{2M}(\hat{\boldsymbol{E}}_{\rm cl})\,Y_{2M}(\hat{\boldsymbol{k}}). \quad (163)$$

With this expansion, we then write the power spectrum as

$$P(\boldsymbol{k}) = \tilde{P}_0(k)\left[1 + \sum_M g_{2M}(k)\,Y_{2M}(\hat{\boldsymbol{k}})\right], \quad (164)$$

where we have absorbed $g_*(k)/3$ into the normalization of the isotropic part, $\tilde{P}_0(k) \equiv P_0(k)(1 + g_*(k)/3)$, and defined

$$g_{2M}(k) \equiv \frac{8\pi}{15}\frac{g_*(k)}{1+g_*(k)/3}Y^*_{2M}(\hat{\boldsymbol{E}}_{\rm cl}) \approx \frac{8\pi}{15}g_*(k)\,Y^*_{2M}(\hat{\boldsymbol{E}}_{\rm cl}), \quad (165)$$

with $g_{2M}(k)$ satisfying $g_{2,-M}(k) = (-1)^M g^*_{2,M}(k)$. The approximation on the rightmost side is justified by the fact that the amplitude g_* is observationally constrained to quite a small value, $g_* \lesssim 10^{-2}$ (Kim & Komatsu, 2013). In this analysis, we shall model the scale dependence of $g_*(k)$ with a power law, $g_*\,(k/k_0)^q$, and consider three values of the spectral index, namely $q = 0$, 1, and 2. Here, k_0 is a pivot wavenumber, which we set to $0.05\,{\rm Mpc}^{-1}$. Given the anisotropic power spectrum of Eq. (164), the CMB temperature and polarization fluctuations have the following expectation (Ma et al., 2011):

$$C^{pp'}_{\ell;\ell';L,M} = i^{\ell-\ell'}D^{pp'}_{\ell\ell'}\,g_{2M}(k)\left[\frac{5(2\ell+1)(2\ell'+1)}{4\pi}\right]^{\frac{1}{2}} \times\begin{pmatrix}2 & \ell & \ell'\\ 0 & 0 & 0\end{pmatrix}, \quad (166)$$

where $D^{pp'}_{\ell\ell'} \equiv (2/\pi)\int k^2dk\,\Delta^p_\ell(k)\,\Delta^{p'}_{\ell'}(k)\,\tilde{P}_0(k)(k/k_0)^q$, and $\Delta^T_\ell(k)$ and $\Delta^E_\ell(k)$ denote the temperature and E-mode radiation transfer functions, respectively.

The analysis is made using the foreground-cleaned CMB temperature maps SMICA, NILC, SEVEM, and Commander, where we apply the common mask from the previous *Planck* release (Planck Collaboration XII 2014), which has more conservative foreground masking than the newly available mask. The implementation details of the optimal estimator can be found in the appendix of Planck Collaboration XVI (2015). We estimate g_{LM} from the data at the multipoles $2 \le \ell \le 1200$. The range of multipoles is chosen such that the effect of residual foregrounds on the analysis is insignificant. For the assessment, we use realistic simulations containing residual foregrounds. Apart from that, we estimate the statistical uncertainty of g_{LM} with various $\ell_{\rm max}$ values using simulations. We find that the temperature data at $\ell > 1500$ make little contribution to the reduction of statistical uncertainty, due to the point-source masking of numerous holes.

Table 16. Constraints on g_*, the quadrupolar asymmetry amplitude, determined from the SMICA, NILC, SEVEM, and Commander foreground-cleaned maps. Error bars are 68 % CL.

$g_* \times 10^2$	$q = 0$	$q = 1$	$q = 2$
Commander ...	$0.19^{+1.97}_{-1.40}$	$-0.09^{+1.85}_{-1.83}$	$-0.27^{+1.14}_{-1.10}$
NILC	$0.60^{+1.73}_{-1.62}$	$0.16^{+1.51}_{-0.99}$	$-0.04^{+0.73}_{-0.66}$
SEVEM	$0.13^{+1.55}_{-1.26}$	$0.03^{+1.38}_{-1.04}$	$-0.01^{+0.98}_{-0.71}$
SMICA	$0.23^{+1.70}_{-1.24}$	$0.16^{+1.47}_{-1.00}$	$0.13^{+1.01}_{-0.61}$

Table 16 shows the constraints on g_* obtained after marginalizing over the direction $\hat{\boldsymbol{E}}_{\rm cl}$. Our limits provide a stringent test of rotational symmetry during inflation, with $g_* = 0.23^{+1.70}_{-1.24} \times 10^{-2}$ (68 % CL) for the scale-independent case (i.e. $q = 0$),[25] using the SMICA temperature map data, where the known effects of systematics including the asymmetry of the *Planck* beams are taken into account. We note that the central values for g_* in Table 16 are closer to zero than expected given the errors. The reason for this is not clear, but it might simply be due to chance.

Unlike the results from the temperature data, the analysis of foreground-cleaned polarization data shows a large, apparently highly statistically significant departure from a null value; however, this result is likely due to systematic errors, most notably a temperature-to-polarization leakage associated with the mismatch of elliptical beams, for which at present a reliable estimate is lacking.

13. Combination with BICEP2/Keck Array-*Planck* cross-correlation

We discuss the implications of the recent constraints on the primordial B-mode polarization from the cross-correlation of the BICEP2 and Keck Array data at 150 GHz with the *Planck* maps at higher frequencies to characterize and remove the contribution from polarized thermal dust emission from our Galaxy (BICEP2/Keck Array and Planck Collaborations (2015), hereafter BKP). On its own, the BKP likelihood leads to a 95 % CL upper limit $r < 0.12$, compatible with and independent of the constraints obtained using the 2015 *Planck* temperature and large angular scale polarization in Sect. 5 (note, however, that the BKP likelihood uses the Hamimeche-Lewis approximation (Hamimeche & Lewis, 2008) which requires the assumption of a fiducial model). The BKP results are also compatible with the *Planck* 2013 Results (Planck Collaboration XVI, 2014; Planck Collaboration XXII, 2014). The posterior probability distribution for r obtained by BKP peaks away from zero at $r \approx 0.05$, but the region of large posterior probability includes $r = 0$.

Here we combine the baseline two-parameter BKP likelihood using the lowest five B-mode bandpowers with the *Planck* 2015 likelihoods. The two BKP nuisance parameters are the B-mode amplitude and frequency spectral index of the polarized thermal dust emission. The combined analysis yields the following constraint on the tensor-to-scalar ratio:

$$r_{0.002} < 0.08 \quad (95\,\%\ {\rm CL},\ \textit{Planck}\ {\rm TT+lowP+BKP}), \quad (167)$$

[25] The constraints from the *Planck* 2013 data by Kim & Komatsu (2013) should be multiplied by a factor of $\sqrt{2}$ in our normalization.

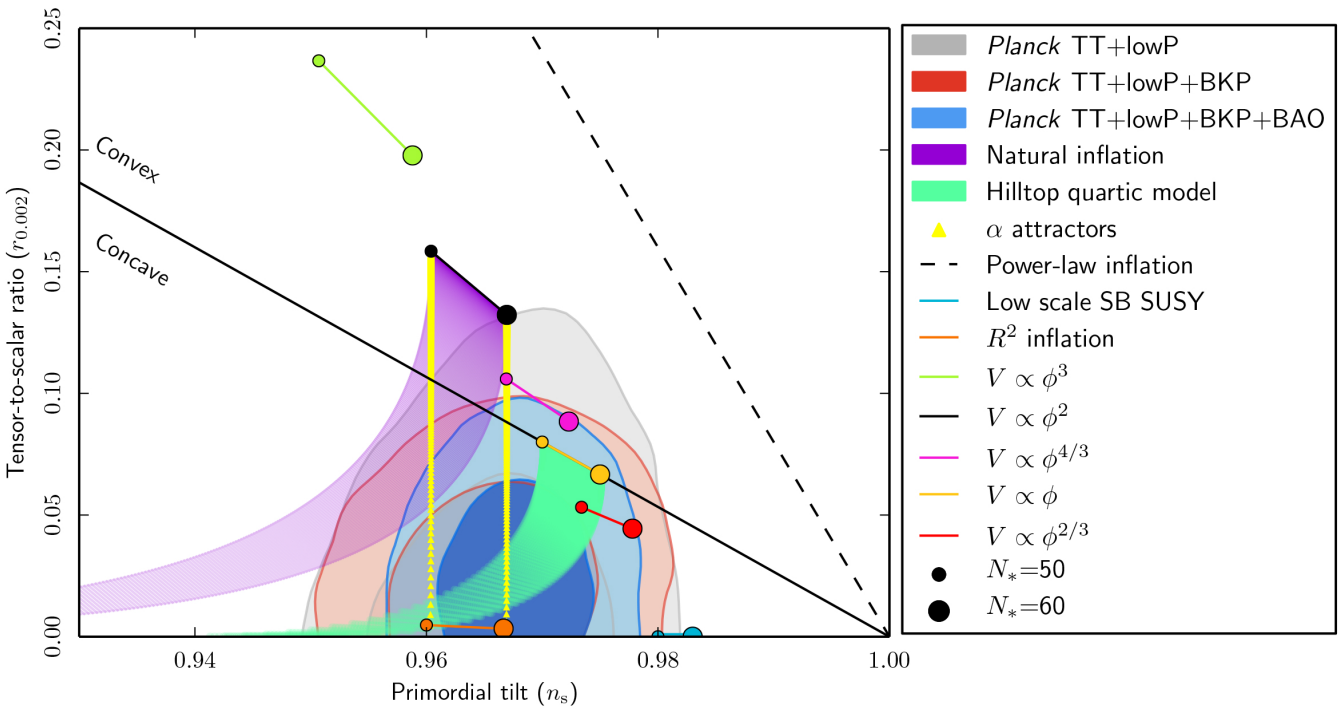

Fig. 54. Marginalized joint 68 % and 95 % CL regions for n_s and $r_{0.002}$ from *Planck* alone and in combination with its cross-correlation with BICEP2/Keck Array and/or BAO data compared with the theoretical predictions of selected inflationary models.

further improving on the upper limits obtained from the different data combinations presented in Sect. 5.

By directly constraining the tensor mode, the BKP likelihood removes degeneracies between the tensor-to-scalar ratio and other parameters. Adding tensors and running, we obtain

$$r_{0.002} < 0.10 \quad (95\,\%\ \text{CL}, \textit{Planck}\ \text{TT+lowP+BKP})\,, \qquad (168)$$

which constitutes almost a 50 % improvement over the *Planck* TT+lowP constraint quoted in Eq. (28). These limits on tensor modes are more robust than the limits using the shape of the C_ℓ^{TT} spectrum alone owing to the fact that scalar perturbations cannot generate B modes irrespective of the shape of the scalar spectrum.

13.1. Implications of BKP on selected inflationary models

Using the BKP likelihood further strengthens the constraints on the inflationary parameters and models discussed in Sect. 6, as seen in Fig. 54. If we set $\epsilon_3 = 0$, the first slow-roll parameter is constrained to $\epsilon_1 < 0.0055$ at 95 % CL by *Planck* TT+lowP+BKP. With the same data combination, concave potentials are preferred over convex potentials with $\log B = 3.8$, which improves on $\log B = 2$ obtained from the *Planck* data alone.

Combining with the BKP likelihood strengthens the constraints on the selected inflationary models studied in Sect. 6. Using the same methodology as in Sect. 6 and adding the BKP likelihood gives a Bayes factor preferring R^2 over chaotic inflation with monomial quadratic potential and natural inflation by odds of 403:1 and 270:1, respectively, under the assumption of a dust equation of state during the entropy generation stage. The combination with the BKP likelihood further penalizes the double-well model compared to R^2 inflation. However, adding BKP reduces the Bayes factor of the hilltop models compared to R^2, because these models can predict a value of the tensor-to-scalar ratio that better fits the statistically insignificant peak at $r \approx 0.05$. See Table 17 for the Bayes factors of other inflationary models with the same two cases of post-inflationary evolution studied in Sect. 6.

Table 17. Results of inflationary model comparison using the cross-correlation between BICEP2/Keck Array and *Planck*. This table is the analogue to Table 6, which did not use the BKP likelihood.

Inflationary Model	$\ln B_{0X}$	
	$w_{\rm int} = 0$	$w_{\rm int} \neq 0$
$R + R^2/6M^2$	...	+0.3
$n = 2$	−6.0	−5.6
Natural	−5.6	−5.0
Hilltop ($p = 2$)	−0.7	−0.4
Hilltop ($p = 4$)	−0.6	−0.9
Double well	−4.3	−4.2
Brane inflation ($p = 2$)	+0.2	0.0
Brane inflation ($p = 4$)	+0.1	−0.1
Exponential inflation	−0.1	0.0
SB SUSY	−1.8	−1.5
Supersymmetric α-model	−1.1	+0.1
Superconformal ($m = 1$)	−1.9	−1.4

13.2. Implications of BKP on scalar power spectrum

The presence of tensors would, at least to some degree, require an enhanced suppression of the scalar power spectrum on large scales to account for the low-ℓ deficit in the C_ℓ^{TT} spectrum. We therefore repeat the analysis of an exponential cut-off studied

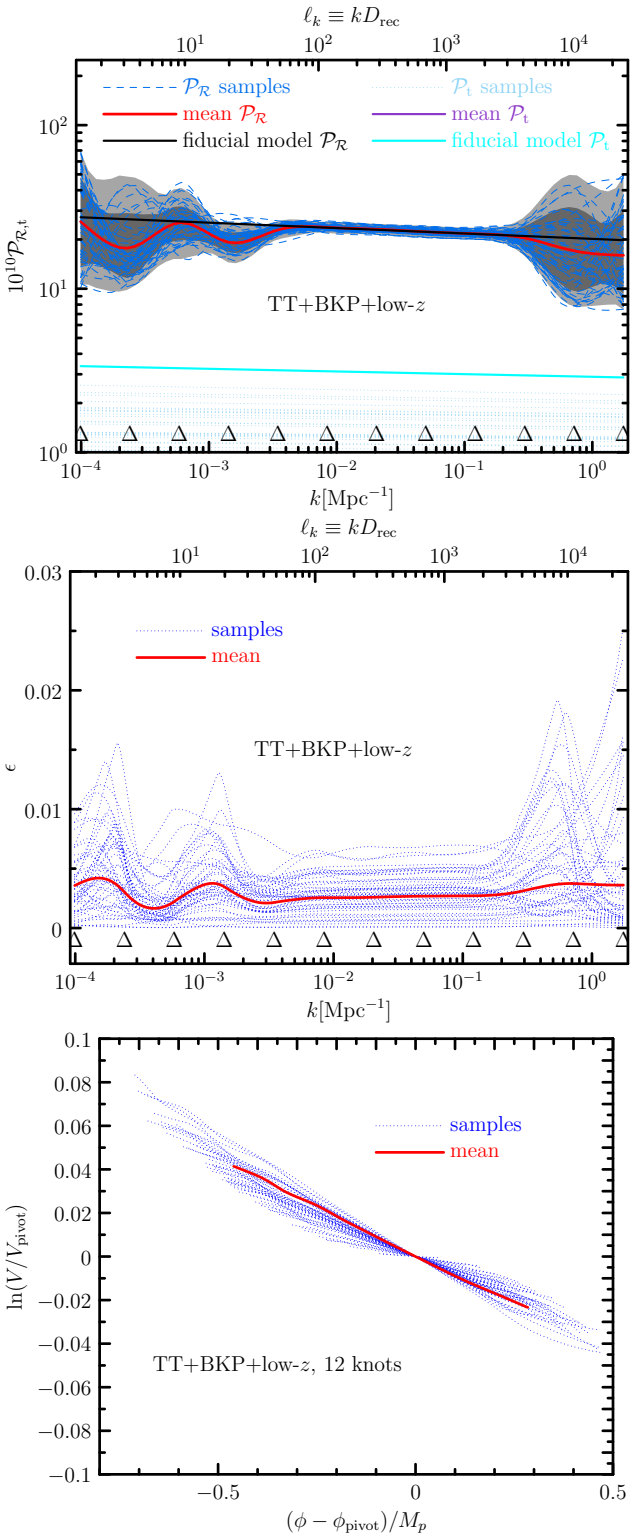

Fig. 55. Impact of BKP likelihood on scalar primordial power spectrum reconstruction. We show how including the BKP likelihood affects the reconstruction in Sect. 8.3. The top panel is to be compared with the reconstructions in Fig. 27, and we observe that including BKP has a minimal impact given the uncertainty in the reconstruction. The middle panel is to be compared with Fig. 31, and here we notice that including BKP excludes the trajectories with large values of ϵ. The bottom panel shows how the inflationary potential reconstructions are modified by BKP (to be compared with Fig. 32).

in Sect. 4.4 with tensor perturbations included and the standard tensor tilt (i.e., $n_{\rm t} = -r/8$). Allowing tensors does not significantly degrade the $\Delta\chi^2$ improvement found in Sect. 4.4 for *Planck* TT+lowP with a best fit at $r \approx 0$. When the BKP likelihood is combined, we obtain $\Delta\chi^2 = -4$ with respect to the base ΛCDM model with a best fit at $r \approx 0.04$. However, since this model contains 3 additional parameters, it is not preferred over the base ΛCDM.

In Fig. 55 we show how the scalar primordial power spectrum reconstruction discussed in Sect. 8.3 is modified when the BKP likelihood is also included. While the power spectrum reconstruction hardly varies given the uncertainties in the method, the trajectories of the slow-roll parameters are significantly closer to slow roll. When the 12-knot reconstruction is carried out, the upper bound on the tensor-to-scalar ratio is $r < 0.11$ at 95 % CL. The χ^2 per degree of freedom for the 5 low-k and 6 high-k knots are 1.14 and 0.22, respectively, corresponding to p-values of 0.33 and 0.97.

13.3. Relaxing the standard single-field consistency condition

We now relax the consistency condition (i.e., $n_{\rm t} = -r/8$) and allow the tensor tilt to be independent of the tensor-to-scalar ratio. This fully phenomenological analysis with the BKP likelihood is complementary to the study of inflationary models with generalized Lagrangians in Sect. 10, which also predict modifications to the consistency condition $n_{\rm t} = -r/8$ for a nearly scale-invariant spectrum of tensor modes. In this subsection we adopt a phenomenological approach, thereby including radical departures from $n_{\rm t} \lesssim 0$, including values predicted in alternative models to inflation (Gasperini & Veneziano, 1993; Boyle et al., 2004; Brandenberger et al., 2007). In Sect. 10 we fold in the *Planck* $f_{\rm NL}$ constraints (Planck Collaboration XVII, 2015), whereas here we consider *Planck* and BKP likelihoods only. Complementary probes such as pulsar timing, direct detection of gravitational waves, and nucleosynthesis bounds could be used to constrain blue values for the tensor spectral index (Stewart & Brandenberger, 2008), but here we are primarily interested in what CMB data can tell us.

We caution the reader that in the absence of a clear detection of a tensor component, joint constraints on r and $n_{\rm t}$ depend strongly on priors, or equivalently on the choice of parameterization. Nevertheless, the BKP likelihood has some constraining power over a range of scales more than a decade wide around $k \approx 0.01\,{\rm Mpc}^{-1}$, so the results are not entirely prior driven.

The commonly used $(r, n_{\rm t})$ parameterization suffers from pathological behavior around $r = 0$, which could be problematic for statistical sampling. We therefore use a parameterization specifying r at two different scales, (r_{k_1}, r_{k_2}) (analogous to the treatment of primordial isocurvature in Sect. 11) as well as the more familiar $(r, n_{\rm t})$ parameterization. We present results based on $k_1 = 0.002\,{\rm Mpc}^{-1}$ and $k_2 = 0.02\,{\rm Mpc}^{-1}$, also quoting the amplitude at $k = 0.01\,{\rm Mpc}^{-1}$ for both parameterizations. This scale is close to the decorrelation scale for $(r, n_{\rm t})$ for the *Planck* +BKP joint constraints. We obtain $r_{0.002} < 0.07$ (0.06) and $r_{0.02} < 0.29$ (0.31) at 95 % CL from the two-scale parameterization with *Planck* TT+lowP+BAO+BKP (TT,TE,EE+lowP+BKP). Figure 56 illustrates the impact of the BKP likelihood on the one-dimensional posterior probabilities for these two parameters. The derived constraint at $k = 0.01\,{\rm Mpc}^{-1}$ is $r_{0.01} < 0.12$ (0.12) at 95 % CL with *Planck* TT+lowP+BAO+BKP (TT,TE,EE+lowP+BKP). The upper panel of Fig. 57 shows the relevant 2D contours for the

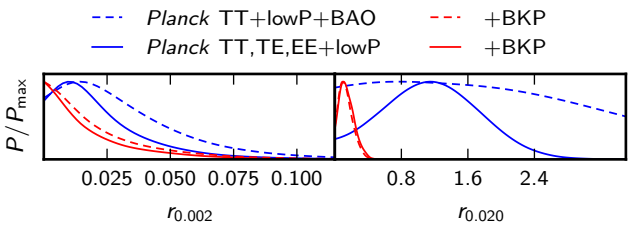

Fig. 56. Posterior probability density of the tensor-to-scalar ratio at two different scales. The inflationary consistency relation is relaxed and $r_{0.002}$ and $r_{0.020}$ are used as sampling parameters, assuming a power-law spectrum for primordial tensor perturbations. When the BKP likelihood is included in the analysis, the results with *Planck* TT+lowP+BAO and *Planck* TT,TE,EE+lowP coincide (red dashed and red solid curves, respectively).

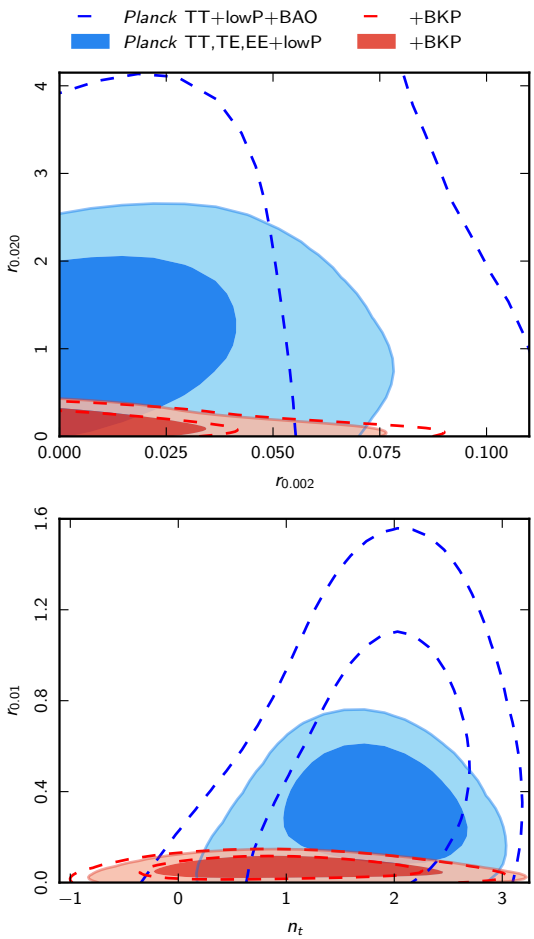

Fig. 57. 68 % and 95 % CL constraints on tensors when the inflationary consistency relation is relaxed, with *Planck* TT+lowP+BAO (blue dashed contours) and TT,TE,EE+lowP (blue shaded regions). The red colours are for the same data plus the BKP joint likelihood. The upper panel shows our independent primary parameters $r_{0.002}$ and $r_{0.020}$. The lower panel shows the derived parameters n_t and $r_{0.01}$. The scale $k = 0.01\,\mathrm{Mpc}^{-1}$ is near the decorrelation scale of (n_t, r) for the *Planck* +BKP data.

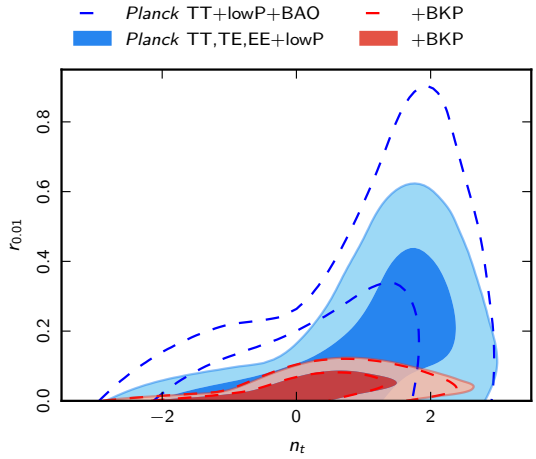

Fig. 58. The same as Fig. 57 lower panel, but using n_t and $r_{0.002}$ as primary parameters.

tensor-to-scalar ratios at the two scales and the improvement due to the combination with the BKP likelihood. The lower panel shows the 2d contours in $(r_{0.01}, n_t)$ obtained by sampling with the two scale parameterization. Figure 58 shows the 2D contours in $(r_{0.01}, n_t)$ obtained by the $(r_{0.002}, n_t)$ parameterization.

We conclude that positive values of the tensor tilt n_t are not statistically significantly preferred by the BKP joint measurement of *B*-mode polarization in combination with *Planck* data, a conclusion at variance with results reported using the BICEP2 data (Lewis, 2014; Gerbino et al., 2014). However, the now firmly established contamination by polarized dust emission could explain the discrepancy. Values of tensor tilt consistent with the standard single-field inflationary consistency relation are compatible with the *Planck* +BKP constraints.

14. Conclusions

The *Planck* full mission temperature and polarization data are consistent with the spatially flat base ΛCDM model, whose perturbations are Gaussian and adiabatic with a spectrum described by a simple power law, as predicted by the simplest inflationary models. For this release, the basic *Planck* results do not rely on external data. The first *Planck* polarization release at large angular scales from the LFI 70 GHz channel determines an optical depth of $\tau = 0.067 \pm 0.022$ (68 % CL, *Planck* low multipole likelihood), a value smaller than the previous *Planck* 2013 result based on the WMAP9 polarization likelihood as delivered by the WMAP team. This *Planck* value of τ is consistent with an analysis of WMAP9 polarization data cleaned for polarized dust emission using the *Planck* 353 GHz data (Planck Collaboration XV, 2014; Planck Collaboration XI, 2015). The estimates of cosmological parameters from the full mission temperature data and polarization on large angular scales are consistent with those of the *Planck* 2013 release. The *TE* and *EE* spectra at $\ell \geq 30$ together with the lensing power spectra lead to cosmological constraints in agreement with those obtained from temperature.

The *Planck* full mission temperature and large angular scale polarization data rule out an exactly scale-invariant spectrum of curvature perturbations at $5.6\,\sigma$. For the base ΛCDM model, the spectral index is measured to be $n_s = 0.965 \pm 0.006$ (68 % CL, *Planck* TT+lowP). No evidence for a running of the spectral index is found, with $dn_s/d\ln k = -0.008 \pm 0.008$ (68 % CL, *Planck* TT+lowP).

The *Planck* full mission data improve the upper bound on the tensor-to-scalar ratio to $r_{0.002} < 0.10$ (95 % CL, *Planck* TT+lowP), a bound that changes only slightly when including the *Planck* lensing likelihood, the high-ℓ polarization likelihood, or the likelihood from the WMAP large angular scale polarization map (dust-cleaned with the *Planck* 353 GHz map). We showed how the low-ℓ deficit in temperature contributes to the *Planck* upper bound on $r_{0.002}$, but this deficit is not a statistically significant anomaly within the base ΛCDM cosmology. Using the full mission *Planck* data, we find the upper bound on $r_{0.002}$ stable, even when extended cosmological models or models with CDM isocurvature are considered. The *Planck* bound on $r_{0.002}$ is consistent with the recent result $r_{0.002} < 0.12$ at 95 % CL obtained by the BKP cross-correlation analysis which accounts for contamination by polarized dust emission (Planck Collaboration XXX, 2014). By combining *Planck* TT+lowP with the BKP cross-correlation likelihood, we obtain $r_{0.002} < 0.08$ at 95 % CL.

The increased precision of the *Planck* full mission data reduces the area enclosed by the 95 % confidence contour in the (n_s, r)-plane by 29 %. We performed a Bayesian model comparison with the same methodology as in PCI13, taking into account reheating uncertainties by marginalizing over two extra parameters: the energy scale at thermalization, $\rho_{\rm th}$, and the parameter $w_{\rm int}$ characterizing the average equation of state between the end of inflation and thermalization. Among the models considered using this approach, the R^2 inflationary model proposed by Starobinsky (1980) is the most preferred. Due to its high tensor-to-scalar ratio, the quadratic model is now strongly disfavoured with respect to R^2 inflation for *Planck* TT+lowP in combination with BAO data. By combining wth the BKP likelihood, this trend is confirmed, and natural inflation is also disfavoured.

We reconstructed the inflaton potential and the Hubble parameter evolution during the observable part of inflation using a Taylor expansion of the inflaton potential or $H(\phi)$. This analysis did not rely on the slow-roll approximation, nor on any assumption about the end of inflation. When higher-order terms were allowed, both reconstructions led to a change in the slope of the potential at the beginning of the observable range, thus better fitting the low-ℓ temperature deficit by turning on a non-zero running of running and accommodating $r_{0.002} \approx 0.2$. These models, however, are not significantly favoured compared to lower order parameterizations that lead to slow-roll evolution at all times.

Three distinct methods were used to reconstruct the primordial power spectrum. All three methods strongly constrain deviations from a featureless power spectrum over the range of scales $0.008\,\mathrm{Mpc}^{-1} \lesssim k \lesssim 0.1\,\mathrm{Mpc}^{-1}$. More interestingly, they also independently find common patterns in the primordial power spectrum of curvature perturbations $\mathcal{P}_{\mathcal{R}}(k)$ at $k \lesssim 0.008\,\mathrm{Mpc}^{-1}$. These patterns are related to the dip at $\ell \approx 20$–40 in the temperature power spectrum. This deviation from a simple power-law spectrum has weak statistical significance due to the large cosmic variance at low ℓ.

This direct reconstruction of the power spectrum is complemented by a search for parameterized features in physically motivated models. The models considered range from the minimal case of a kinetic energy dominated phase preceding a short inflationary stage (with just one extra parameter), to a model with a step-like feature in the potential and in the sound speed (with five extra parameters). As with the *Planck* 2013 nominal mission data, these templates lead to an improved fit, up to $\Delta\chi^2 \approx 12$. However, neither the Bayesian evidence nor a frequentist simulation-based analysis shows any statistically significant preference over a simple power law.

We have updated the analysis that combines power spectrum constraints with those derived from the $f_{\rm NL}$ parameters (Planck Collaboration XVII, 2015). New limits on the sound speed inferred from the full mission temperature and polarization data further constrain the slow-roll parameters for generalized models, including DBI inflation. For the first time, we derived combined constraints on Galileon inflation, including the region of parameter space in which the predicted spectrum of gravitational waves has a blue spectral index.

Several models motivated by the axion monodromy mechanism in string theory predict oscillatory modulations and corresponding non-Gaussianities, potentially detectable by *Planck*. A TT-only analysis picks up four possible modulation frequencies, which remain present when the high-ℓ polarization likelihood is included. An inspection of frequency residuals in the high-ℓ TT likelihood does not reveal evidence of foreground-related systematics at similar frequencies. However, a Bayesian evidence comparison prefers the smooth base ΛCDM model over modulated models, suggesting that the latter could simply be fitting the noise in the data. The monodromy model predicts resonant non-Gaussian features correlated to power spectrum features. A partial analysis beyond the power spectrum was presented. We also constrained a possible pseudo-coupling of the axion to gauge fields by requiring that non-Gaussianities induced by inverse decay satisfy the *Planck* bounds on $f_{\rm NL}$.

Section 11 reports on a search for possible deviations from purely adiabatic initial conditions by studying a range of models including isocurvature modes as well as possible correlations with the adiabatic mode. The *Planck* full mission temperature data are consistent with adiabaticity. The *Planck* TT data place tight constraints on three-parameter extensions to the flat adiabatic base ΛCDM model, allowing arbitrarily correlated mixtures of the adiabatic mode with one isocurvature mode (of either the CDM, baryon, neutrino density, or neutrino velocity type). Adding the high-ℓ TE and EE polarization data further squeezes the constraints, since polarization spectra contain additional shape and phase information on acoustic oscillations. The likelihood with polarization included is in agreement with adiabatic initial conditions. However, the tightening of the constraints after including polarization must be interpreted with caution because of possible systematic effects. For this reason we emphasize the more conservative *Planck* TT+lowP bounds in Table 15. The constraints on the six base-ΛCDM cosmological model parameters remain stable when correlated isocurvature modes are allowed. The largest shifts occur for the neutrino density mode, but these shifts are not significant (i.e., $< 1\,\sigma$). The constraints on the tensor-to-scalar ratio also remain stable when isocurvature modes are allowed.

Finally we examined the connection between inflation and statistical isotropy, a key prediction of the simplest inflationary models. We tested separately the two lowest moments of an anisotropic modulation of the primordial curvature power spectrum. We found that a modulated curvaton model proposed to explain the observed large-scale dipolar power asymmetry cannot account for all of the asymmetry, and hence is not preferred over statistically isotropic base ΛCDM. The full mission temperature data place the tightest constraints to date on a quadrupolar modulation of curvature perturbations.

Acknowledgements. The Planck Collaboration acknowledges the support of: ESA; CNES and CNRS/INSU-IN2P3-INP (France); ASI, CNR, and INAF (Italy); NASA and DoE (USA); STFC and UKSA (UK); CSIC, MINECO, JA, and RES (Spain); Tekes, AoF, and CSC (Finland); DLR and MPG (Germany); CSA (Canada); DTU Space (Denmark); SER/SSO (Switzerland); RCN (Norway); SFI (Ireland); FCT/MCTES (Portugal); ERC and PRACE (EU).

A description of the Planck Collaboration and a list of its members, indicating which technical or scientific activities they have been involved in, can be found at http://www.cosmos.esa.int/web/planck/planck-collaboration. This research used resources of the National Energy Research Scientific Computing Center, a DOE Office of Science User Facility supported by the Office of Science of the U.S. Department of Energy under Contract No. DE-AC02-05CH11231. Part of this work was undertaken at the STFC DiRAC HPC Facilities at the University of Cambridge, funded by UK BIS National E-infrastructure capital grants. We gratefully acknowledge the IN2P3 Computer Center (`http://cc.in2p3.fr`) for providing a significant amount of the computing resources and services needed for this work.

References

Achúcarro, A., Gong, J.-O., Hardeman, S., Palma, G. A., & Patil, S. P., Features of heavy physics in the CMB power spectrum. 2011, JCAP, 1101, 030, arXiv:1010.3693

Ackerman, L., Carroll, S. M., & Wise, M. B., Imprints of a Primordial Preferred Direction on the Microwave Background. 2007, Phys.Rev., D75, 083502, arXiv:astro-ph/0701357

Adams, F. C., Bond, J. R., Freese, K., Frieman, J. A., & Olinto, A. V., Natural inflation: Particle physics models, power law spectra for large scale structure, and constraints from COBE. 1993, Phys.Rev., D47, 426, arXiv:hep-ph/9207245

Adams, J., Cresswell, B., & Easther, R., Inflationary perturbations from a potential with a step. 2001, Phys. Rev. D, 64, 123514, arXiv:astro-ph/0102236

Adams, J. A., Cresswell, B., & Easther, R., Inflationary perturbations from a potential with a step. 2001, Phys.Rev., D64, 123514, arXiv:astro-ph/0102236

Agarwal, N. & Bean, R., Cosmological constraints on general, single field inflation. 2009, Phys. Rev. D, 79, 023503, arXiv:0809.2798

Alishahiha, M., Silverstein, E., & Tong, D., DBI in the sky: Non-Gaussianity from inflation with a speed limit. 2004, Phys. Rev. D, 70, 123505, arXiv:hep-th/0404084

Amendola, L., Gordon, C., Wands, D., & Sasaki, M., Correlated perturbations from inflation and the cosmic microwave background. 2002, Phys.Rev.Lett., 88, 211302, arXiv:astro-ph/0107089

Anber, M. M. & Sorbo, L., Naturally inflating on steep potentials through electromagnetic dissipation. 2010, Phy.Rev.D, 81, 043534, arXiv:0908.4089

Anderson, L. et al., The clustering of galaxies in the SDSS-III Baryon Oscillation Spectroscopic Survey: Baryon Acoustic Oscillations in the Data Release 10 and 11 galaxy samples. 2014, MNRAS, 441, 24, arXiv:1312.4877

Armendáriz-Picón, C., Damour, T., & Mukhanov, V., k-Inflation. 1999, Physics Letters B, 458, 209, arXiv:hep-th/9904075

Aslanyan, G., Price, L. C., Abazajian, K. N., & Easther, R., The Knotted Sky I: Planck constraints on the primordial power spectrum. 2014, ArXiv e-prints, arXiv:1403.5849

Audren, B., Lesgourgues, J., Benabed, K., & Prunet, S., Conservative constraints on early cosmology: an illustration of the Monte Python cosmological parameter inference code. 2013, JCAP, 1302, 001, arXiv:1210.7183

Babich, D., Creminelli, P., & Zaldarriaga, M., The shape of non-Gaussianities. 2004, JCAP, 8, 9, arXiv:astro-ph/0405356

Barnaby, N., Namba, R., & Peloso, M., Phenomenology of a pseudo-scalar inflaton: naturally large nongaussianity. 2011, JCAP, 4, 9, arXiv:1102.4333

Barnaby, N., Pajer, E., & Peloso, M., Gauge field production in axion inflation: Consequences for monodromy, non-Gaussianity in the CMB, and gravitational waves at interferometers. 2012, Phys. Rev. D, 85, 023525, arXiv:1110.3327

Barnaby, N. & Peloso, M., Large Non-Gaussianity in Axion Inflation. 2011, Physical Review Letters, 106, 181301, arXiv:1011.1500

Bartolo, N. & Liddle, A. R., The Simplest curvaton model. 2002, Phys.Rev., D65, 121301, arXiv:astro-ph/0203076

Bartolo, N., Matarrese, S., Peloso, M., & Ricciardone, A., Anisotropy in solid inflation. 2013, JCAP, 1308, 022, arXiv:1306.4160

Bartolo, N., Matarrese, S., & Riotto, A., Adiabatic and isocurvature perturbations from inflation: Power spectra and consistency relations. 2001, Phys.Rev., D64, 123504, arXiv:astro-ph/0107502

Bartolo, N., Matarrese, S., & Riotto, A., Gauge-invariant temperature anisotropies and primordial non-Gaussianity. 2004a, Phys.Rev.Lett., 93, 231301, arXiv:astro-ph/0407505

Bartolo, N., Matarrese, S., & Riotto, A., On nonGaussianity in the curvaton scenario. 2004b, Phys.Rev., D69, 043503, arXiv:hep-ph/0309033

Barvinsky, A. O., Kamenshchik, A. Y., & Starobinsky, A. A., Inflation scenario via the Standard Model Higgs boson and LHC. 2008, JCAP, 0811, 021

Baumann, D., Green, D., & Porto, R. A., B-modes and the nature of inflation. 2015, JCAP, 1, 16, arXiv:1407.2621

Bean, R., Chen, X., Peiris, H., & Xu, J., Comparing infrared Dirac-Born-Infeld brane inflation to observations. 2008, Phys. Rev. D, 77, 023527, arXiv:0710.1812

Becker, R. H., Fan, X., White, R. L., et al., Evidence for Reionization at z~6: Detection of a Gunn-Peterson Trough in a z=6.28 Quasar. 2001, AJ, 122, 2850, arXiv:astro-ph/0108097

Beltrán, M., García-Bellido, J., Lesgourgues, J., & Viel, M., Squeezing the window on isocurvature modes with the lyman-alpha forest. 2005, Phys.Rev., D72, 103515, arXiv:astro-ph/0509209

Bennett, C. L., Hill, R. S., Hinshaw, G., et al., Seven-year Wilkinson Microwave Anisotropy Probe (WMAP) Observations: Are There Cosmic Microwave Background Anomalies? 2011, ApJS, 192, 17, arXiv:1001.4758

Berera, A., Warm inflation. 1995, Phys.Rev.Lett., 75, 3218, arXiv:astro-ph/9509049

Beutler, F., Blake, C., Colless, M., et al., The 6dF Galaxy Survey: Baryon Acoustic Oscillations and the Local Hubble Constant. 2011, MNRAS, 416, 3017, arXiv:1106.3366

Bezrukov, F. & Shaposhnikov, M., The Standard Model Higgs boson as the inflaton. 2008, Phys. Lett., B659, 703

Bezrukov, F. & Shaposhnikov, M., Standard Model Higgs boson mass from inflation: two loop analysis. 2009, JHEP, 07, 089, arXiv:0904.1537

BICEP2 Collaboration, BICEP2 II: Experiment and Three-Year Data Set. 2014a, Astrophys.J., 792, 62, arXiv:1403.4302

BICEP2 Collaboration, Detection of B-Mode Polarization at Degree Angular Scales by BICEP2. 2014b, Phys.Rev.Lett., 112, 241101, arXiv:1403.3985

BICEP2/Keck Array and Planck Collaborations, A joint analysis of BICEP2/Keck Array and Planck data. 2015, submitted to PRL, arXiv:1502.00612

Binétruy, P., Kiritsis, E., Mabillard, J., Pieroni, M., & Rosset, C., Universality classes for models of inflation. 2014, arXiv:1407.0820

Blas, D., Lesgourgues, J., & Tram, T., The Cosmic Linear Anisotropy Solving System (CLASS) II: Approximation schemes. 2011, JCAP, 1107, 034, arXiv:1104.2933

Boubekeur, L. & Lyth, D., Hilltop inflation. 2005, JCAP, 0507, 010, arXiv:hep-ph/0502047

Boyle, L. A., Steinhardt, P. J., & Turok, N., The Cosmic gravitational wave background in a cyclic universe. 2004, Phys.Rev., D69, 127302, arXiv:hep-th/0307170

Bozza, V., Giovannini, M., & Veneziano, G., Cosmological perturbations from a new physics hypersurface. 2003, JCAP, 0305, 001, arXiv:hep-th/0302184

Brandenberger, R. H., Nayeri, A., Patil, S. P., & Vafa, C., Tensor Modes from a Primordial Hagedorn Phase of String Cosmology. 2007, Phys.Rev.Lett., 98, 231302, arXiv:hep-th/0604126

Bucher, M., Physics of the cosmic microwave background anisotropy. 2014, Int. J. Mod. Phys.D, arXiv:1501.04288

Bucher, M., Moodley, K., & Turok, N., The General primordial cosmic perturbation. 2000, Phys.Rev., D62, 083508, arXiv:astro-ph/9904231

Bucher, M., Moodley, K., & Turok, N., Constraining isocurvature perturbations with CMB polarization. 2001, Phys. Rev. Lett., 87, 191301, arXiv:(astro-ph/0012141)

Buchmüller, W., Domcke, V., & Kamada, K., The Starobinsky Model from Superconformal D-Term Inflation. 2013, Phys.Lett., B726, 467, arXiv:1306.3471

Burgess, C., Martineau, P., Quevedo, F., Rajesh, G., & Zhang, R., Brane - anti-brane inflation in orbifold and orientifold models. 2002, JHEP, 0203, 052, arXiv:hep-th/0111025

Burrage, C., de Rham, C., Seery, D., & Tolley, A. J., Galileon inflation. 2011, JCAP, 1, 14, arXiv:1009.2497

Byrnes, C. T. & Wands, D., Curvature and isocurvature perturbations from two-field inflation in a slow-roll expansion. 2006, Phys.Rev., D74, 043529, arXiv:astro-ph/0605679

Casadio, R., Finelli, F., Kamenshchik, A., Luzzi, M., & Venturi, G., Method of comparison equations for cosmological perturbations. 2006, JCAP, 0604, 011, arXiv:gr-qc/0603026

Chen, X., Inflation from warped space. 2005a, JHEP, 8, 45, arXiv:hep-th/0501184

Chen, X., Multithroat brane inflation. 2005b, Phys. Rev. D, 71, 063506, arXiv:hep-th/0408084

Chen, X., Running non-Gaussianities in Dirac-Born-Infeld inflation. 2005c, Phys. Rev. D, 72, 123518, arXiv:astro-ph/0507053

Chen, X., Easther, R., & Lim, E. A., Generation and Characterization of Large Non-Gaussianities in Single Field Inflation. 2008, JCAP, 0804, 010, arXiv:0801.3295

Chen, X., Huang, M.-X., Kachru, S., & Shiu, G., Observational signatures and non-Gaussianities of general single-field inflation. 2007, JCAP, 1, 2, arXiv:hep-th/0605045

Choe, J., Gong, J.-O., & Stewart, E. D., Second order general slow-roll power spectrum. 2004, JCAP, 0407, 012, arXiv:hep-ph/0405155

Cicoli, M., Burgess, C., & Quevedo, F., Fibre Inflation: Observable Gravity Waves from IIB String Compactifications. 2009, JCAP, 0903, 013, arXiv:0808.0691

Contaldi, C. R., Peloso, M., Kofman, L., & Linde, A. D., Suppressing the lower multipoles in the CMB anisotropies. 2003, JCAP, 0307, 002, arXiv:astro-ph/0303636

Copeland, E. J., Liddle, A. R., Lyth, D. H., Stewart, E. D., & Wands, D., False vacuum inflation with Einstein gravity. 1994, Phys.Rev., D49, 6410, arXiv:astro-ph/9401011

Creminelli, P., D'Amico, G., Musso, M., Noreña, J., & Trincherini, E., Galilean symmetry in the effective theory of inflation: new shapes of non-Gaussianity. 2011, JCAP, 2, 6, arXiv:1011.3004

Danielsson, U. H., A Note on inflation and transPlanckian physics. 2002, Phys.Rev., D66, 023511, arXiv:hep-th/0203198

De Felice, A. & Tsujikawa, S., Shapes of primordial non-Gaussianities in the Horndeski's most general scalar-tensor theories. 2013, JCAP, 3, 30, arXiv:1301.5721

de Rham, C. & Gabadadze, G., Generalization of the Fierz-Pauli action. 2010a, Phys. Rev. D, 82, 044020, arXiv:1007.0443

de Rham, C. & Gabadadze, G., Selftuned massive spin-2. 2010b, Physics Letters B, 693, 334, arXiv:1006.4367

Deffayet, C., Deser, S., & Esposito-Farèse, G., Generalized Galileons: All scalar models whose curved background extensions maintain second-order field equations and stress tensors. 2009a, Phys. Rev. D, 80, 064015, arXiv:0906.1967

Deffayet, C., Esposito-Farèse, G., & Vikman, A., Covariant Galileon. 2009b, Phys. Rev. D, 79, 084003, arXiv:0901.1314

Dimastrogiovanni, E., Bartolo, N., Matarrese, S., & Riotto, A., Non-Gaussianity and Statistical Anisotropy from Vector Field Populated Inflationary Models. 2010, Adv.Astron., 2010, 752670, arXiv:1001.4049

Dvali, G., Shafi, Q., & Solganik, S., D-brane inflation. 2001, arXiv:hep-th/0105203

Dvali, G. & Tye, S. H., Brane inflation. 1999, Phys.Lett., B450, 72, arXiv:hep-ph/9812483

Dvali, G. R., Shafi, Q., & Schaefer, R. K., Large scale structure and supersymmetric inflation without fine tuning. 1994, Phys. Rev. Lett., 73, 1886, arXiv:hep-ph/9406319

Easther, R. & Flauger, R., Planck Constraints on Monodromy Inflation. 2014, JCAP, 1402, 037, arXiv:1308.3736

Easther, R., Kinney, W. H., & Peiris, H., Observing trans-Planckian signatures in the cosmic microwave background. 2005, JCAP, 0505, 009, arXiv:astro-ph/0412613

Easther, R. & Peiris, H., Implications of a Running Spectral Index for Slow Roll Inflation. 2006, JCAP, 0609, 010, arXiv:astro-ph/0604214

Easther, R. & Peiris, H. V., Bayesian analysis of inflation. II. Model selection and constraints on reheating. 2012, Phys. Rev. D, 85, 103533, arXiv:1112.0326

Eisenstein, D. J. et al., Detection of the baryon acoustic peak in the large-scale correlation function of SDSS luminous red galaxies. 2005, Astrophys.J., 633, 560, arXiv:astro-ph/0501171

Ellis, J., Nanopoulos, D. V., & Olive, K. A., No-Scale Supergravity Realization of the Starobinsky Model of Inflation. 2013a, Phys.Rev.Lett., 111, 111301, arXiv:1305.1247

Ellis, J., Nanopoulos, D. V., & Olive, K. A., Starobinsky-like Inflationary Models as Avatars of No-Scale Supergravity. 2013b, JCAP, 1310, 009, arXiv:1307.3537

Enqvist, K., Kurki-Suonio, H., & Valiviita, J., Open and closed CDM isocurvature models contrasted with the CMB data. 2002, Phys.Rev., D65, 043002, arXiv:astro-ph/0108422

Enqvist, K. & Sloth, M. S., Adiabatic CMB perturbations in pre - big bang string cosmology. 2002, Nucl.Phys., B626, 395, arXiv:hep-ph/0109214

Erickcek, A. L., Hirata, C. M., & Kamionkowski, M., A Scale-Dependent Power Asymmetry from Isocurvature Perturbations. 2009, Phys. Rev., D80, 083507, arXiv:0907.0705

Farakos, F., Kehagias, A., & Riotto, A., On the Starobinsky Model of Inflation from Supergravity. 2013, Nucl.Phys., B876, 187, arXiv:1307.1137

Feroz, F. & Hobson, M., Multimodal nested sampling: an efficient and robust alternative to MCMC methods for astronomical data analysis. 2008, MNRAS, 384, 449, arXiv:0704.3704

Feroz, F., Hobson, M., & Bridges, M., MultiNest: an efficient and robust Bayesian inference tool for cosmology and particle physics. 2009, MNRAS, 398, 1601, arXiv:0809.3437

Feroz, F., Hobson, M., Cameron, E., & Pettitt, A., Importance Nested Sampling and the MultiNest Algorithm. 2013, arXiv:1306.2144

Ferrara, S., Kallosh, R., Linde, A., & Porrati, M., Minimal Supergravity Models of Inflation. 2013a, Phys.Rev., D88, 085038, arXiv:1307.7696

Ferrara, S., Kallosh, R., & Van Proeyen, A., On the Supersymmetric Completion of $R + R^2$ Gravity and Cosmology. 2013b, JHEP, 1311, 134, arXiv:1309.4052

Ferreira, R. Z. & Sloth, M. S., Universal constraints on axions from inflation. 2014, JHEP, 12, 139, arXiv:1409.5799

Finelli, F., Hamann, J., Leach, S. M., & Lesgourgues, J., Single-field inflation constraints from CMB and SDSS data. 2010, JCAP, 1004, 011, arXiv:0912.0522

Flauger, R., Hill, J. C., & Spergel, D. N., Toward an Understanding of Foreground Emission in the BICEP2 Region. 2014a, JCAP, 1408, 039, arXiv:1405.7351

Flauger, R., McAllister, L., Silverstein, E., & Westphal, A., Drifting Oscillations in Axion Monodromy. 2014b, arXiv:1412.1814

Flauger, R. & Pajer, E., Resonant Non-Gaussianity. 2011, JCAP, 1101, 017, arXiv:1002.0833

Freese, K., Frieman, J. A., & Olinto, A. V., Natural inflation with pseudo Nambu-Goldstone bosons. 1990, Phys. Rev. Lett., 65, 3233

Gao, X. & Steer, D. A., Inflation and primordial non-Gaussianities of "generalized Galileons". 2011, JCAP, 12, 19, arXiv:1107.2642

Garcia-Bellido, J., Rabadan, R., & Zamora, F., Inflationary scenarios from branes at angles. 2002, JHEP, 0201, 036, arXiv:hep-th/0112147

Garcia-Bellido, J. & Roest, D., Large-N running of the spectral index of inflation. 2014, Phys.Rev., D89, 103527, arXiv:1402.2059

García-Bellido, J. & Wands, D., Metric perturbations in two field inflation. 1996, Phys.Rev., D53, 5437, arXiv:astro-ph/9511029

Garriga, J. & Mukhanov, V. F., Perturbations in k-inflation. 1999, Physics Letters B, 458, 219, arXiv:hep-th/9904176

Gasperini, M. & Veneziano, G., Pre - big bang in string cosmology. 1993, Astropart.Phys., 1, 317, arXiv:hep-th/9211021

Gauthier, C. & Bucher, M., Reconstructing the primordial power spectrum from the CMB. 2012, JCAP, 1210, 050, arXiv:astro-ph/1209.2147

Gerbino, M., Marchini, A., Pagano, L., et al., Blue gravity waves from BICEP2? 2014, Phys.Rev., D90, 047301, arXiv:1403.5732

Goncharov, A. & Linde, A. D., Chaotic Inflation of the Universe in Supergravity. 1984, Sov.Phys.JETP, 59, 930

Gong, J.-O. & Stewart, E. D., The Density perturbation power spectrum to second order corrections in the slow roll expansion. 2001, Phys.Lett., B510, 1, arXiv:astro-ph/0101225

Gorbunov, D. & Panin, A., Scalaron the mighty: producing dark matter and baryon asymmetry at reheating. 2011, Phys.Lett., B700, 157, arXiv:1009.2448

Gordon, C. & Lewis, A., Observational constraints on the curvaton model of inflation. 2003, Phys.Rev., D67, 123513, arXiv:astro-ph/0212248

Gordon, C., Wands, D., Bassett, B. A., & Maartens, R., Adiabatic and entropy perturbations from inflation. 2001, Phys.Rev., D63, 023506, arXiv:astro-ph/0009131

Górski, K. M., Hivon, E., Banday, A. J., et al., HEALPix: A Framework for High-Resolution Discretization and Fast Analysis of Data Distributed on the Sphere. 2005, ApJ, 622, 759, arXiv:astro-ph/0409513

Grin, D., Hanson, D., Holder, G. P., Dor, O., & Kamionkowski, M., Baryons do trace dark matter 380,000 years after the big bang: Search for compensated isocurvature perturbations with WMAP 9-year data. 2014, Phys.Rev., D89, 023006, arXiv:1306.4319

Guth, A. H., Kaiser, D. I., & Nomura, Y., Inflationary paradigm after Planck 2013. 2014, Phys.Lett., B733, 112, arXiv:1312.7619

Habib, S., Heitmann, K., Jungman, G., & Molina-Paris, C., The Inflationary perturbation spectrum. 2002, Phys.Rev.Lett., 89, 281301, arXiv:astro-ph/0208443

Hamann, J., Lesgourgues, J., & Valkenburg, W., How to constrain inflationary parameter space with minimal priors. 2008, JCAP, 0804, 016, arXiv:0802.0505

Hamimeche, S. & Lewis, A., Likelihood Analysis of CMB Temperature and Polarization Power Spectra. 2008, Phys.Rev., D77, 103013, arXiv:0801.0554

Handley, W. J., Hobson, M. P., & Lasenby, A. N., PolyChord: Nested Sampling for cosmology. 2015, submitted to MNRAS

Harrison, E. R., Fluctuations at the threshold of classical cosmology. 1970, Phys. Rev., D1, 2726

Hu, W., Seljak, U., White, M. J., & Zaldarriaga, M., A complete treatment of CMB anisotropies in a FRW universe. 1998, Phys.Rev., D57, 3290, arXiv:astro-ph/9709066

Hu, W. & White, M. J., CMB anisotropies: Total angular momentum method. 1997, Phys.Rev., D56, 596, arXiv:astro-ph/9702170

Ijjas, A., Steinhardt, P. J., & Loeb, A., Inflationary paradigm in trouble after Planck2013. 2013, Phys.Lett., B723, 261, arXiv:1304.2785

Ijjas, A., Steinhardt, P. J., & Loeb, A., Inflationary schism after Planck2013. 2014, arXiv:1402.6980

Jackson, M. G. & Shiu, G., Study of the consistency relation for single-field inflation with power spectrum oscillations. 2013, Phys.Rev., D88, 123511,

arXiv:1303.4973
Jackson, M. G., Wandelt, B., & Bouchet, F., Angular Correlation Functions for Models with Logarithmic Oscillations. 2014, Phys.Rev., D89, 023510, arXiv:1303.3499
Kachru, S., Kallosh, R., Linde, A. D., et al., Towards inflation in string theory. 2003, JCAP, 0310, 013, arXiv:hep-th/0308055
Kallosh, R. & Linde, A., Superconformal generalizations of the Starobinsky model. 2013, JCAP, 1306, 028, arXiv:1306.3214
Kallosh, R., Linde, A., & Roest, D., Superconformal Inflationary α-Attractors. 2013, JHEP, 1311, 198, arXiv:1311.0472
Kaloper, N., Lawrence, A., & Sorbo, L., An Ignoble Approach to Large Field Inflation. 2011, JCAP, 1103, 023, arXiv:1101.0026
Kamionkowski, M., Kosowsky, A., & Stebbins, A., Statistics of cosmic microwave background polarization. 1997, Phys.Rev., D55, 7368, arXiv:astro-ph/9611125
Kanno, S., Sasaki, M., & Tanaka, T., A viable explanation of the CMB dipolar statistical anisotropy. 2013, Progr. Theor. Exp. Phys., 2013, 111E01
Kawasaki, M. & Sekiguchi, T., Cosmological Constraints on Isocurvature and Tensor Perturbations. 2008, Prog.Theor.Phys., 120, 995, arXiv:0705.2853
Ketov, S. V. & Starobinsky, A. A., Embedding $(R + R^2)$ Inflation into Supergravity. 2011, Phys.Rev., D83, 063512, arXiv:1011.0240
Kim, J. & Komatsu, E., Limits on anisotropic inflation from the Planck data. 2013, Phys. Rev. D, 88, 101301, arXiv:1310.1605
Kim, J. E., Nilles, H. P., & Peloso, M., Completing natural inflation. 2005, JCAP, 0501, 005, arXiv:hep-ph/0409138
Kinney, W. H., Inflation: Flow, fixed points and observables to arbitrary order in slow roll. 2002, Phys.Rev., D66, 083508, arXiv:astro-ph/0206032
Kinney, W. H., Kolb, E. W., Melchiorri, A., & Riotto, A., Inflation model constraints from the Wilkinson Microwave Anisotropy Probe three-year data. 2006, Phys.Rev., D74, 023502, arXiv:astro-ph/0605338
Kobayashi, T. & Takahashi, F., Running Spectral Index from Inflation with Modulations. 2011, JCAP, 1101, 026, arXiv:1011.3988
Kobayashi, T., Yamaguchi, M., & Yokoyama, J., G-inflation: Inflation driven by the Galileon field. 2010, Phys.Rev.Lett., 105, 231302, arXiv:1008.0603
Kobayashi, T., Yamaguchi, M., & Yokoyama, J., Generalized G-Inflation — Inflation with the Most General Second-Order Field Equations —. 2011a, Progr. Theor. Phys., 126, 511, arXiv:1105.5723
Kobayashi, T., Yamaguchi, M., & Yokoyama, J., Primordial non-Gaussianity from G inflation. 2011b, Phys. Rev. D, 83, 103524, arXiv:1103.1740
Kosowsky, A. & Turner, M. S., CBR anisotropy and the running of the scalar spectral index. 1995, Phys.Rev., D52, 1739, arXiv:astro-ph/9504071
Langlois, D., Correlated adiabatic and isocurvature perturbations from double inflation. 1999, Phys.Rev., D59, 123512, arXiv:astro-ph/9906080
Langlois, D. & Riazuelo, A., Correlated mixtures of adiabatic and isocurvature cosmological perturbations. 2000, Phys.Rev., D62, 043504, arXiv:astro-ph/9912497
Leach, S. M., Liddle, A. R., Martin, J., & Schwarz, D. J., Cosmological parameter estimation and the inflationary cosmology. 2002, Phys.Rev., D66, 023515, arXiv:astro-ph/0202094
Lesgourgues, J., The Cosmic Linear Anisotropy Solving System (CLASS) I: Overview. 2011, arXiv:1104.2932
Lesgourgues, J., Starobinsky, A. A., & Valkenburg, W., What do WMAP and SDSS really tell about inflation? 2008, JCAP, 0801, 010, arXiv:0710.1630
Lesgourgues, J. & Valkenburg, W., New constraints on the observable inflaton potential from WMAP and SDSS. 2007, Phys.Rev., D75, 123519, arXiv:astro-ph/0703625
Lewis, A. & Bridle, S., Cosmological parameters from CMB and other data: A Monte Carlo approach. 2002, Phys.Rev., D66, 103511, arXiv:astro-ph/0205436
Lewis, A. M., *Planck* 2015 results. I. Overview of products and results. 2014, http://cosmocoffee.info/viewtopic.php?t=2302
Liddle, A. R. & Cortês, M., Cosmic microwave background anomalies in an open universe. 2013, Phys. Rev. Lett., 111, 111302, arXiv::1306.5698
Liddle, A. R. & Leach, S. M., How long before the end of inflation were observable perturbations produced? 2003, Phys. Rev., D68, 103503, arXiv:astro-ph/0305263
Linde, A., Inflationary Cosmology after Planck 2013. 2014, arXiv:1402.0526
Linde, A., Mooij, S., & Pajer, E., Gauge field production in supergravity inflation: Local non-Gaussianity and primordial black holes. 2013, Phys. Rev. D, 87, 103506, arXiv:1212.1693
Linde, A. D., Chaotic Inflation. 1983, Phys.Lett., B129, 177
Linde, A. D., Hybrid inflation. 1994, Phys.Rev., D49, 748, arXiv:astro-ph/9307002
Linde, A. D. & Mukhanov, V., The curvaton web. 2006, JCAP, 0604, 009, arXiv:astro-ph/0511736
Linde, A. D. & Mukhanov, V. F., Nongaussian isocurvature perturbations from inflation. 1997, Phys.Rev., D56, 535, arXiv:astro-ph/9610219
Lorenz, L., Martin, J., & Ringeval, C., k-inflationary power spectra in the uniform approximation. 2008, Phys. Rev. D, 78, 083513, arXiv:0807.3037
Lyth, D. H., The CMB modulation from inflation. 2013, JCAP, 1308, 007, arXiv:1304.1270
Lyth, D. H., Ungarelli, C., & Wands, D., The Primordial density perturbation in the curvaton scenario. 2003, Phys.Rev., D67, 023503, arXiv:astro-ph/0208055
Lyth, D. H. & Wands, D., Generating the curvature perturbation without an inflaton. 2002, Phys.Lett., B524, 5, arXiv:hep-ph/0110002
Ma, C.-P. & Bertschinger, E., Cosmological perturbation theory in the synchronous and conformal Newtonian gauges. 1995, Ap.J., 455, 7, arXiv:astro-ph/9506072
Ma, Y.-Z., Efstathiou, G., & Challinor, A., Testing a direction-dependent primordial power spectrum with observations of the cosmic microwave background. 2011, Phys. Rev. D, 83, 083005, arXiv:1102.4961
Ma, Y.-Z., Huang, Q.-G., & Zhang, X., Confronting brane inflation with Planck and pre-Planck data. 2013, Phys. Rev. D, 87, 103516, arXiv:1303.6244
Maleknejad, A., Sheikh-Jabbari, M., & Soda, J., Gauge Fields and Inflation. 2013, Phys.Rept., 528, 161, arXiv:1212.2921
Martin, J. & Brandenberger, R. H., The TransPlanckian problem of inflationary cosmology. 2001, Phys.Rev., D63, 123501, arXiv:hep-th/0005209
Martin, J. & Ringeval, C., First CMB Constraints on the Inflationary Reheating Temperature. 2010, Phys.Rev., D82, 023511, arXiv:1004.5525
Martin, J., Ringeval, C., & Vennin, V., Encyclopdia Inflationaris. 2014, Phys.Dark Univ., arXiv:1303.3787
Martin, J. & Schwarz, D. J., WKB approximation for inflationary cosmological perturbations. 2003, Phys.Rev., D67, 083512, arXiv:astro-ph/0210090
McAllister, L., Silverstein, E., & Westphal, A., Gravity Waves and Linear Inflation from Axion Monodromy. 2010, Phys.Rev., D82, 046003, arXiv:0808.0706
McAllister, L., Silverstein, E., Westphal, A., & Wrase, T., The Powers of Monodromy. 2014, JHEP, 1409, 123, arXiv:1405.3652
Meerburg, P. D., Alleviating the tension at low ℓ through axion monodromy. 2014, Phys.Rev., D90, 063529, arXiv:1406.3243
Meerburg, P. D. & Pajer, E., Observational constraints on gauge field production in axion inflation. 2013, JCAP, 2, 17, arXiv:1203.6076
Meerburg, P. D. & Spergel, D. N., Searching for Oscillations in the Primordial Power Spectrum: Constraints from Planck (Paper II). 2014, Phys.Rev., D89, 063537, arXiv:1308.3705
Meerburg, P. D., Spergel, D. N., & Wandelt, B. D., Searching for oscillations in the primordial power spectrum. 2014a, arXiv:1406.0548
Meerburg, P. D., Spergel, D. N., & Wandelt, B. D., Searching for Oscillations in the Primordial Power Spectrum: Perturbative Approach (Paper I). 2014b, Phys.Rev., D89, 063536, arXiv:1308.3704
Miranda, V. & Hu, W., Inflationary Steps in the Planck Data. 2014, Phys.Rev., D89, 083529, arXiv:1312.0946
Mizuno, S. & Koyama, K., Primordial non-Gaussianity from the DBI Galileons. 2010, Phys. Rev. D, 82, 103518, arXiv:1009.0677
Mollerach, S., Isocurvature baryon perturbations and inflation. 1990, Phys.Rev., D42, 313
Moroi, T. & Takahashi, T., Effects of cosmological moduli fields on cosmic microwave background. 2001, Phys.Lett., B522, 215, arXiv:hep-ph/0110096
Mortonson, M. J., Dvorkin, C., Peiris, H. V., & Hu, W., CMB polarization features from inflation versus reionization. 2009, Phys. Rev. D, 79, 103519, arXiv:0903.4920
Mortonson, M. J. & Hu, W., Model-independent constraints on reionization from large-scale CMB polarization. 2008, Ap.J., 672, 737, arXiv:0705.1132
Mortonson, M. J., Peiris, H. V., & Easther, R., Bayesian analysis of inflation: Parameter estimation for single field models. 2011, Phys. Rev. D, 83, 043505, arXiv:1007.4205
Mortonson, M. J. & Seljak, U., A joint analysis of Planck and BICEP2 B modes including dust polarization uncertainty. 2014, JCAP, 1410, 035, arXiv:1405.5857
Moss, A., Scott, D., Zibin, J. P., & Battye, R., Tilted Physics: A Cosmologically Dipole-Modulated Sky. 2011, Phys. Rev., D84, 023014, arXiv:1011.2990
Mukhanov, V., Quantum Cosmological Perturbations: Predictions and Observations. 2013, Eur.Phys.J., C73, 2486, arXiv:1303.3925
Mukhanov, V. F. & Chibisov, G., Quantum Fluctuation and Nonsingular Universe. (In Russian). 1981, JETP Lett., 33, 532
Naruko, A., Komatsu, E., & Yamaguchi, M., Anisotropic inflation reexamined: upper bound on broken rotational invariance during inflation. 2014, ArXiv e-prints, arXiv:1411.5489
Nicolis, A., Rattazzi, R., & Trincherini, E., Galileon as a local modification of gravity. 2009, Phys. Rev. D, 79, 064036, arXiv:0811.2197
Norena, J., Wagner, C., Verde, L., Peiris, H. V., & Easther, R., Bayesian Analysis of Inflation III: Slow Roll Reconstruction Using Model Selection. 2012, Phys.Rev., D86, 023505, arXiv:1202.0304

Ohashi, J. & Tsujikawa, S., Potential-driven Galileon inflation. 2012, JCAP, 10, 35, arXiv:1207.4879

Okamoto, T. & Hu, W., CMB lensing reconstruction on the full sky. 2003, Phys.Rev., D67, 083002, arXiv:astro-ph/0301031

Page, L., Hinshaw, G., Komatsu, E., et al., Three-Year Wilkinson Microwave Anisotropy Probe (WMAP) Observations: Polarization Analysis. 2007, ApJS, 170, 335, arXiv:astro-ph/0603450

Pajer, E. & Peloso, M., A review of axion inflation in the era of Planck. 2013, Classical and Quantum Gravity, 30, 214002, arXiv:1305.3557

Palanque-Delabrouille, N., Yche, C., Lesgourgues, J., et al., Constraint on neutrino masses from SDSS-III/BOSS Lyα forest and other cosmological probes. 2014, arXiv:1410.7244

Peebles, P. & Yu, J., Primeval adiabatic perturbation in an expanding universe. 1970, Ap.J., 162, 815

Peiris, H., Baumann, D., Friedman, B., & Cooray, A., Phenomenology of D-brane inflation with general speed of sound. 2007, Phys. Rev. D, 76, 103517, arXiv:0706.1240

Peiris, H. & Easther, R., Recovering the Inflationary Potential and Primordial Power Spectrum With a Slow Roll Prior: Methodology and Application to WMAP 3 Year Data. 2006a, JCAP, 0607, 002, arXiv:astro-ph/0603587

Peiris, H. & Easther, R., Slow Roll Reconstruction: Constraints on Inflation from the 3 Year WMAP Dataset. 2006b, JCAP, 0610, 017, arXiv:astro-ph/0609003

Peiris, H., Easther, R., & Flauger, R., Constraining Monodromy Inflation. 2013, JCAP, 1309, 018, arXiv:1303.2616

Peiris, H. V. & Easther, R., Primordial Black Holes, Eternal Inflation, and the Inflationary Parameter Space after WMAP5. 2008, JCAP, 0807, 024, arXiv:0805.2154

Peiris, H. V., Komatsu, E., Verde, L., et al., First-Year Wilkinson Microwave Anisotropy Probe (WMAP) Observations: Implications For Inflation. 2003, ApJS, 148, 213, arXiv:astro-ph/0302225

Perotto, L., Lesgourgues, J., Hannestad, S., Tu, H., & Wong, Y. Y., Probing cosmological parameters with the CMB: Forecasts from full Monte Carlo simulations. 2006, JCAP, 0610, 013, arXiv:astro-ph/0606227

Planck Collaboration XII, *Planck* 2013 results. XII. Diffuse component separation. 2014, A&A, 571, A12, arXiv:1303.5072

Planck Collaboration XV, *Planck* 2013 results. XV. CMB power spectra and likelihood. 2014, A&A, 571, A15, arXiv:1303.5075

Planck Collaboration XVI, *Planck* 2013 results. XVI. Cosmological parameters. 2014, A&A, 571, A16, arXiv:1303.5076

Planck Collaboration XVII, *Planck* 2013 results. XVII. Gravitational lensing by large-scale structure. 2014, A&A, 571, A17, arXiv:1303.5077

Planck Collaboration XXII, *Planck* 2013 results. XXII. Constraints on inflation. 2014, A&A, 571, A22, arXiv:1303.5082

Planck Collaboration XXIII, *Planck* 2013 results. XXIII. Isotropy and statistics of the CMB. 2014, A&A, 571, A23, arXiv:1303.5083

Planck Collaboration XXIV, *Planck* 2013 results. XXIV. Constraints on primordial non-Gaussianity. 2014, A&A, 571, A24, arXiv:1303.5084

Planck Collaboration XXV, *Planck* 2013 results. XXV. Searches for cosmic strings and other topological defects. 2014, A&A, 571, A25, arXiv:1303.5085

Planck Collaboration XXVI, *Planck* 2013 results. XXVI. Background geometry and topology of the Universe. 2014, A&A, 571, A26, arXiv:1303.5086

Planck Collaboration XXVII, *Planck* 2013 results. XXVII. Doppler boosting of the CMB: Eppur si muove. 2014, A&A, 571, A27, arXiv:1303.5087

Planck Collaboration XXX, *Planck* 2013 results. XXX. Cosmic infrared background measurements and implications for star formation. 2014, A&A, 571, A30, arXiv:1309.0382

Planck Collaboration XXXI, *Planck* 2013 results. XXXI. Consistency of the *Planck*data. 2014, A&A, 571, A31

Planck Collaboration II, *Planck* 2015 results. II. Low Frequency Instrument data processing. 2015, in preparation

Planck Collaboration VII, *Planck* 2015 results. VII. High Frequency Instrument data processing: Time-ordered information and beam processing. 2015, in preparation

Planck Collaboration IX, *Planck* 2015 results. IX. Diffuse component separation: CMB maps. 2015, in preparation

Planck Collaboration XI, *Planck* 2015 results. XI. CMB power spectra, likelihood, and consistency of cosmological parameters. 2015, in preparation

Planck Collaboration XIII, *Planck* 2015 results. XIII. Cosmological parameters. 2015, in preparation

Planck Collaboration XV, *Planck* 2015 results. XV. Gravitational lensing. 2015, in preparation

Planck Collaboration XVI, *Planck* 2015 results. XVI. Isotropy and statistics of the CMB. 2015, in preparation

Planck Collaboration XVII, *Planck* 2015 results. I. XVII. Constraints on primordial non-Gaussianity. 2015, in preparation

Planck Collaboration Int. XIX, Planck intermediate results. XIX. An overview of the polarized thermal emission from Galactic dust. 2014, A&A, submitted, arXiv:1405.0871

Planck Collaboration Int. XX, Planck intermediate results. XX. Comparison of polarized thermal emission from Galactic dust with simulations of MHD turbulence. 2014, A&A, submitted, arXiv:1405.0872

Planck Collaboration Int. XXI, Planck intermediate results. XXI. Comparison of polarized thermal emission from Galactic dust at 353 GHz with optical interstellar polarization. 2014, A&A, submitted, arXiv:1405.0873

Planck Collaboration Int. XXII, Planck intermediate results. XXII. Frequency dependence of thermal emission from Galactic dust in intensity and polarization. 2014, A&A, submitted, arXiv:1405.0874

Powell, B. A. & Kinney, W. H., Limits on primordial power spectrum resolution: An inflationary flow analysis. 2007, JCAP, 0708, 006, arXiv:0706.1982

Powell, B. A., Tzirakis, K., & Kinney, W. H., Tensors, non-Gaussianities, and the future of potential reconstruction. 2009, JCAP, 4, 19, arXiv:0812.1797

Powell, M. J. D., The BOBYQA algorithm for bound constrained optimization without derivatives. 2009

Regan, D., Anderson, G. J., Hull, M., & Seery, D., Constraining Galileon Inflation. 2014, ArXiv e-prints, arXiv:1411.4501

Ross, A. J., Samushia, L., Howlett, C., et al., The Clustering of the SDSS DR7 Main Galaxy Sample I: A 4 per cent Distance Measure at z=0.15. 2014, arXiv:1409.3242

Rossi, G., Yeche, C., Palanque-Delabrouille, N., & Lesgourgues, J., Constraints on dark radiation from cosmological probes. 2014, arXiv:1412.6763

Sasaki, M., Valiviita, J., & Wands, D., Non-Gaussianity of the primordial perturbation in the curvaton model. 2006, Phys.Rev., D74, 103003, arXiv:astro-ph/0607627

Savelainen, M., Valiviita, J., Walia, P., Rusak, S., & Kurki-Suonio, H., Constraints on neutrino density and velocity isocurvature modes from WMAP-9 data. 2013, Phys.Rev., D88, 063010, arXiv:1307.4398

Schmidt, F. & Hui, L., Cosmic Microwave Background Power Asymmetry from Non-Gaussian Modulation. 2013, Phys.Rev.Lett., 110, 011301, arXiv:1210.2965

Seljak, U. & Zaldarriaga, M., Signature of gravity waves in polarization of the microwave background. 1997, Phys.Rev.Lett., 78, 2054, arXiv:astro-ph/9609169

Senatore, L., Smith, K. M., & Zaldarriaga, M., Non-Gaussianities in single field inflation and their optimal limits from the WMAP 5-year data. 2010, JCAP, 1, 28, arXiv:0905.3746

Silverstein, E. & Tong, D., Scalar speed limits and cosmology: Acceleration from D-cceleration. 2004, Phys. Rev. D, 70, 103505, arXiv:hep-th/0310221

Silverstein, E. & Westphal, A., Monodromy in the CMB: Gravity Waves and String Inflation. 2008, Phys.Rev., D78, 106003, arXiv:0803.3085

Soda, J., Statistical Anisotropy from Anisotropic Inflation. 2012, Class.Quant.Grav., 29, 083001, arXiv:1201.6434

Sorbo, L., Parity violation in the Cosmic Microwave Background from a pseudoscalar inflaton. 2011, JCAP, 6, 3, arXiv:1101.1525

Starobinsky, A. A., A New Type of Isotropic Cosmological Models Without Singularity. 1980, Phys.Lett., B91, 99

Starobinsky, A. A., Spectrum of adiabatic perturbations in the universe when there are singularities in the inflation potential. 1992, JETP Lett., 55, 489

Stewart, A. & Brandenberger, R., Observational Constraints on Theories with a Blue Spectrum of Tensor Modes. 2008, JCAP, 0808, 012, arXiv:0711.4602

Stewart, E. D., Inflation, supergravity and superstrings. 1995, Phys.Rev., D51, 6847, arXiv:hep-ph/9405389

Stewart, E. D. & Lyth, D. H., A more accurate analytic calculation of the spectrum of cosmological perturbations produced during inflation. 1993, Phys. Lett. B, 302, 171, arXiv:gr-qc/9302019

Tsujikawa, S., Ohashi, J., Kuroyanagi, S., & De Felice, A., Planck constraints on single-field inflation. 2013, Phys. Rev. D, 88, 023529, arXiv:1305.3044

Turner, M. S., Coherent scalar-field oscillations in an expanding universe. 1983, Phys. Rev. D, 28, 1243

Valiviita, J. & Giannantonio, T., Constraints on primordial isocurvature perturbations and spatial curvature by Bayesian model selection. 2009, Phys.Rev., D80, 123516, arXiv:0909.5190

Valiviita, J., Savelainen, M., Talvitie, M., Kurki-Suonio, H., & Rusak, S., Constraints on scalar and tensor perturbations in phenomenological and two-field inflation models: Bayesian evidences for primordial isocurvature and tensor modes. 2012, Ap.J., 753, 151, arXiv:1202.2852

Vázquez, J. A., Bridges, M., Hobson, M. P., & Lasenby, A. N., Model selection applied to reconstruction of the Primordial Power Spectrum. 2012, JCAP, 6, 6, arXiv:1203.1252

Vilenkin, A., Classical and Quantum Cosmology of the Starobinsky Inflationary Model. 1985, Phys.Rev., D32, 2511

Wands, D., Bartolo, N., Matarrese, S., & Riotto, A., An Observational test of two-field inflation. 2002, Phys.Rev., D66, 043520, arXiv:astro-ph/0205253

Weinberg, S., Must cosmological perturbations remain non-adiabatic after multi-field inflation? 2004, Phys.Rev., D70, 083522, arXiv:astro-ph/0405397
White, M., Scott, D., & Silk, J., Anisotropies in the Cosmic Microwave Background. 1994, Ann.Rev.Ast.Astro, 32, 319
Zaldarriaga, M. & Seljak, U., An all sky analysis of polarization in the microwave background. 1997, Phys.Rev., D55, 1830, arXiv:astro-ph/9609170
Zeldovich, Y., A Hypothesis unifying the structure and the entropy of the universe. 1972, MNRAS, 160, 1P

[1] APC, AstroParticule et Cosmologie, Université Paris Diderot, CNRS/IN2P3, CEA/lrfu, Observatoire de Paris, Sorbonne Paris Cité, 10, rue Alice Domon et Léonie Duquet, 75205 Paris Cedex 13, France
[2] Aalto University Metsähovi Radio Observatory and Dept of Radio Science and Engineering, P.O. Box 13000, FI-00076 AALTO, Finland
[3] African Institute for Mathematical Sciences, 6-8 Melrose Road, Muizenberg, Cape Town, South Africa
[4] Agenzia Spaziale Italiana Science Data Center, Via del Politecnico snc, 00133, Roma, Italy
[5] Aix Marseille Université, CNRS, LAM (Laboratoire d'Astrophysique de Marseille) UMR 7326, 13388, Marseille, France
[6] Astrophysics Group, Cavendish Laboratory, University of Cambridge, J J Thomson Avenue, Cambridge CB3 0HE, U.K.
[7] Astrophysics & Cosmology Research Unit, School of Mathematics, Statistics & Computer Science, University of KwaZulu-Natal, Westville Campus, Private Bag X54001, Durban 4000, South Africa
[8] Atacama Large Millimeter/submillimeter Array, ALMA Santiago Central Offices, Alonso de Cordova 3107, Vitacura, Casilla 763 0355, Santiago, Chile
[9] CITA, University of Toronto, 60 St. George St., Toronto, ON M5S 3H8, Canada
[10] CNRS, IRAP, 9 Av. colonel Roche, BP 44346, F-31028 Toulouse cedex 4, France
[11] CRANN, Trinity College, Dublin, Ireland
[12] California Institute of Technology, Pasadena, California, U.S.A.
[13] Centre for Theoretical Cosmology, DAMTP, University of Cambridge, Wilberforce Road, Cambridge CB3 0WA, U.K.
[14] Centro de Estudios de Física del Cosmos de Aragón (CEFCA), Plaza San Juan, 1, planta 2, E-44001, Teruel, Spain
[15] Computational Cosmology Center, Lawrence Berkeley National Laboratory, Berkeley, California, U.S.A.
[16] Consejo Superior de Investigaciones Científicas (CSIC), Madrid, Spain
[17] DSM/Irfu/SPP, CEA-Saclay, F-91191 Gif-sur-Yvette Cedex, France
[18] DTU Space, National Space Institute, Technical University of Denmark, Elektrovej 327, DK-2800 Kgs. Lyngby, Denmark
[19] Département de Physique Théorique, Université de Genève, 24, Quai E. Ansermet,1211 Genève 4, Switzerland
[20] Dark Cosmology Centre, Niels Bohr Institute, University of Copenhagen, Juliane Maries Vej 30, 2100 Copenhagen, Denmark
[21] Departamento de Física, Universidad de Oviedo, Avda. Calvo Sotelo s/n, Oviedo, Spain
[22] Department of Astronomy and Astrophysics, University of Toronto, 50 Saint George Street, Toronto, Ontario, Canada
[23] Department of Astrophysics/IMAPP, Radboud University Nijmegen, P.O. Box 9010, 6500 GL Nijmegen, The Netherlands
[24] Department of Physics & Astronomy, University of British Columbia, 6224 Agricultural Road, Vancouver, British Columbia, Canada
[25] Department of Physics and Astronomy, Dana and David Dornsife College of Letter, Arts and Sciences, University of Southern California, Los Angeles, CA 90089, U.S.A.
[26] Department of Physics and Astronomy, University College London, London WC1E 6BT, U.K.
[27] Department of Physics and Astronomy, University of Sussex, Brighton BN1 9QH, U.K.
[28] Department of Physics, Florida State University, Keen Physics Building, 77 Chieftan Way, Tallahassee, Florida, U.S.A.
[29] Department of Physics, Gustaf Hällströmin katu 2a, University of Helsinki, Helsinki, Finland
[30] Department of Physics, Princeton University, Princeton, New Jersey, U.S.A.
[31] Department of Physics, University of California, Berkeley, California, U.S.A.
[32] Department of Physics, University of California, Santa Barbara, California, U.S.A.
[33] Department of Physics, University of Illinois at Urbana-Champaign, 1110 West Green Street, Urbana, Illinois, U.S.A.
[34] Dipartimento di Fisica e Astronomia G. Galilei, Università degli Studi di Padova, via Marzolo 8, 35131 Padova, Italy
[35] Dipartimento di Fisica e Astronomia, ALMA MATER STUDIORUM, Università degli Studi di Bologna, Viale Berti Pichat 6/2, I-40127, Bologna, Italy
[36] Dipartimento di Fisica e Scienze della Terra, Università di Ferrara, Via Saragat 1, 44122 Ferrara, Italy
[37] Dipartimento di Fisica, Università La Sapienza, P. le A. Moro 2, Roma, Italy
[38] Dipartimento di Fisica, Università degli Studi di Milano, Via Celoria, 16, Milano, Italy
[39] Dipartimento di Fisica, Università degli Studi di Trieste, via A. Valerio 2, Trieste, Italy
[40] Dipartimento di Fisica, Università di Roma Tor Vergata, Via della Ricerca Scientifica, 1, Roma, Italy
[41] Dipartimento di Matematica, Università di Roma Tor Vergata, Via della Ricerca Scientifica, 1, Roma, Italy
[42] Discovery Center, Niels Bohr Institute, Blegdamsvej 17, Copenhagen, Denmark
[43] Dpto. Astrofísica, Universidad de La Laguna (ULL), E-38206 La Laguna, Tenerife, Spain
[44] European Southern Observatory, ESO Vitacura, Alonso de Cordova 3107, Vitacura, Casilla 19001, Santiago, Chile
[45] European Space Agency, ESAC, Planck Science Office, Camino bajo del Castillo, s/n, Urbanización Villafranca del Castillo, Villanueva de la Cañada, Madrid, Spain
[46] European Space Agency, ESTEC, Keplerlaan 1, 2201 AZ Noordwijk, The Netherlands
[47] Facoltà di Ingegneria, Università degli Studi e-Campus, Via Isimbardi 10, Novedrate (CO), 22060, Italy
[48] Gran Sasso Science Institute, INFN, viale F. Crispi 7, 67100 L'Aquila, Italy
[49] HGSFP and University of Heidelberg, Theoretical Physics Department, Philosophenweg 16, 69120, Heidelberg, Germany
[50] Helsinki Institute of Physics, Gustaf Hällströmin katu 2, University of Helsinki, Helsinki, Finland
[51] INAF - Osservatorio Astronomico di Padova, Vicolo dell'Osservatorio 5, Padova, Italy
[52] INAF - Osservatorio Astronomico di Roma, via di Frascati 33, Monte Porzio Catone, Italy
[53] INAF - Osservatorio Astronomico di Trieste, Via G.B. Tiepolo 11, Trieste, Italy
[54] INAF/IASF Bologna, Via Gobetti 101, Bologna, Italy
[55] INAF/IASF Milano, Via E. Bassini 15, Milano, Italy
[56] INFN, Sezione di Bologna, Via Irnerio 46, I-40126, Bologna, Italy
[57] INFN, Sezione di Roma 1, Università di Roma Sapienza, Piazzale Aldo Moro 2, 00185, Roma, Italy
[58] INFN, Sezione di Roma 2, Università di Roma Tor Vergata, Via della Ricerca Scientifica, 1, Roma, Italy
[59] INFN/National Institute for Nuclear Physics, Via Valerio 2, I-34127 Trieste, Italy
[60] IPAG: Institut de Planétologie et d'Astrophysique de Grenoble, Université Grenoble Alpes, IPAG, F-38000 Grenoble, France, CNRS, IPAG, F-38000 Grenoble, France
[61] IUCAA, Post Bag 4, Ganeshkhind, Pune University Campus, Pune 411 007, India

[62] Imperial College London, Astrophysics group, Blackett Laboratory, Prince Consort Road, London, SW7 2AZ, U.K.
[63] Infrared Processing and Analysis Center, California Institute of Technology, Pasadena, CA 91125, U.S.A.
[64] Institut Néel, CNRS, Université Joseph Fourier Grenoble I, 25 rue des Martyrs, Grenoble, France
[65] Institut Universitaire de France, 103, bd Saint-Michel, 75005, Paris, France
[66] Institut d'Astrophysique Spatiale, CNRS (UMR8617) Université Paris-Sud 11, Bâtiment 121, Orsay, France
[67] Institut d'Astrophysique de Paris, CNRS (UMR7095), 98 bis Boulevard Arago, F-75014, Paris, France
[68] Institute for Space Sciences, Bucharest-Magurale, Romania
[69] Institute of Astronomy, University of Cambridge, Madingley Road, Cambridge CB3 0HA, U.K.
[70] Institute of Theoretical Astrophysics, University of Oslo, Blindern, Oslo, Norway
[71] Instituto de Astrofísica de Canarias, C/Vía Láctea s/n, La Laguna, Tenerife, Spain
[72] Instituto de Física de Cantabria (CSIC-Universidad de Cantabria), Avda. de los Castros s/n, Santander, Spain
[73] Istituto Nazionale di Fisica Nucleare, Sezione di Padova, via Marzolo 8, I-35131 Padova, Italy
[74] Jet Propulsion Laboratory, California Institute of Technology, 4800 Oak Grove Drive, Pasadena, California, U.S.A.
[75] Jodrell Bank Centre for Astrophysics, Alan Turing Building, School of Physics and Astronomy, The University of Manchester, Oxford Road, Manchester, M13 9PL, U.K.
[76] Kavli Institute for Cosmology Cambridge, Madingley Road, Cambridge, CB3 0HA, U.K.
[77] LAL, Université Paris-Sud, CNRS/IN2P3, Orsay, France
[78] LAPTh, Univ. de Savoie, CNRS, B.P.110, Annecy-le-Vieux F-74941, France
[79] LERMA, CNRS, Observatoire de Paris, 61 Avenue de l'Observatoire, Paris, France
[80] Laboratoire AIM, IRFU/Service d'Astrophysique - CEA/DSM - CNRS - Université Paris Diderot, Bât. 709, CEA-Saclay, F-91191 Gif-sur-Yvette Cedex, France
[81] Laboratoire Traitement et Communication de l'Information, CNRS (UMR 5141) and Télécom ParisTech, 46 rue Barrault F-75634 Paris Cedex 13, France
[82] Laboratoire de Physique Subatomique et Cosmologie, Université Grenoble-Alpes, CNRS/IN2P3, 53, rue des Martyrs, 38026 Grenoble Cedex, France
[83] Laboratoire de Physique Théorique, Université Paris-Sud 11 & CNRS, Bâtiment 210, 91405 Orsay, France
[84] Lawrence Berkeley National Laboratory, Berkeley, California, U.S.A.
[85] Lebedev Physical Institute of the Russian Academy of Sciences, Astro Space Centre, 84/32 Profsoyuznaya st., Moscow, GSP-7, 117997, Russia
[86] Leung Center for Cosmology and Particle Astrophysics, National Taiwan University, Taipei 10617, Taiwan
[87] Max-Planck-Institut für Astrophysik, Karl-Schwarzschild-Str. 1, 85741 Garching, Germany
[88] McGill Physics, Ernest Rutherford Physics Building, McGill University, 3600 rue University, Montréal, QC, H3A 2T8, Canada
[89] National University of Ireland, Department of Experimental Physics, Maynooth, Co. Kildare, Ireland
[90] Niels Bohr Institute, Blegdamsvej 17, Copenhagen, Denmark
[91] Optical Science Laboratory, University College London, Gower Street, London, U.K.
[92] SB-ITP-LPPC, EPFL, CH-1015, Lausanne, Switzerland
[93] SISSA, Astrophysics Sector, via Bonomea 265, 34136, Trieste, Italy
[94] School of Physics and Astronomy, Cardiff University, Queens Buildings, The Parade, Cardiff, CF24 3AA, U.K.
[95] School of Physics and Astronomy, University of Nottingham, Nottingham NG7 2RD, U.K.
[96] Simon Fraser University, Department of Physics, 8888 University Drive, Burnaby BC, Canada
[97] Sorbonne Université-UPMC, UMR7095, Institut d'Astrophysique de Paris, 98 bis Boulevard Arago, F-75014, Paris, France
[98] Space Research Institute (IKI), Russian Academy of Sciences, Profsoyuznaya Str, 84/32, Moscow, 117997, Russia
[99] Space Sciences Laboratory, University of California, Berkeley, California, U.S.A.
[100] Special Astrophysical Observatory, Russian Academy of Sciences, Nizhnij Arkhyz, Zelenchukskiy region, Karachai-Cherkessian Republic, 369167, Russia
[101] Stanford University, Dept of Physics, Varian Physics Bldg, 382 Via Pueblo Mall, Stanford, California, U.S.A.
[102] Sub-Department of Astrophysics, University of Oxford, Keble Road, Oxford OX1 3RH, U.K.
[103] Sydney Institute for Astronomy, School of Physics A28, University of Sydney, NSW 2006, Australia
[104] Theory Division, PH-TH, CERN, CH-1211, Geneva 23, Switzerland
[105] UPMC Univ Paris 06, UMR7095, 98 bis Boulevard Arago, F-75014, Paris, France
[106] Université de Toulouse, UPS-OMP, IRAP, F-31028 Toulouse cedex 4, France
[107] Universities Space Research Association, Stratospheric Observatory for Infrared Astronomy, MS 232-11, Moffett Field, CA 94035, U.S.A.
[108] University of Granada, Departamento de Física Teórica y del Cosmos, Facultad de Ciencias, Granada, Spain
[109] University of Granada, Instituto Carlos I de Física Teórica y Computacional, Granada, Spain
[110] Warsaw University Observatory, Aleje Ujazdowskie 4, 00-478 Warszawa, Poland